THÈSE

En vue de l'obtention du
DOCTORAT DE L'UNIVERSITÉ DE TOULOUSE

Délivré par l'Université Toulouse 3 - Paul Sabatier

Présentée et soutenue par

Paul CRISTOFARI

Le 22 décembre 2022

Caractériser les propriétés atmosphériques de naines rouges à partir de spectres obtenus avec SPIRou

---

Ecole doctorale : **SDU2E - Sciences de l'Univers, de l'Environnement et de l'Espace**

Spécialité : **Astrophysique, Sciences de l'Espace, Planétologie**

Unité de recherche :
IRAP - Institut de Recherche en Astrophysique et Planetologie

Thèse dirigée par
Jean-François DONATI

Jury

M. Thierry FORVEILLE, Rapporteur
Mme Céline REYLÉ, Rapporteure
Mme Gaitee HUSSAIN, Examinatrice
M. Pascal FOUQUE, Examinateur
M. Thomas MASSERON, Examinateur
M. Jean-François DONATI, Directeur de thèse
Mme Claire MOUTOU, Présidente

Abstract

Over the last decades, M dwarfs have attracted increasing attention and were identified as targets of choice for the hunt of exoplanets located in the habitable zone of their host star, and for the study of magnetic fields in cool stars. Nonetheless, their study still represents a great technical and scientific challenge because of the intrinsic faintness of these stars. This thesis is dedicated to the study of M dwarfs, and in particular to their characterization from high-resolution and high signal-to-noise ratio near-infrared spectra acquired with the spectro-polarimeter SPIRou installed at the Canada-France-Hawaï Telescope. We use state-of-the-art synthetic spectra to constrain the atmospheric parameters of M dwarfs, taking advantage of the large wavelength coverage of SPIRou. We show how the different models and line lists considered can lead to significant discrepancies in the estimation of atmospheric parameters. With our process we are able to constrain such parameters with a precision of about 30 K in effective temperature ($T_{\rm eff}$), and 0.1 dex in surface gravity ($\log g$) and metallicity ([M/H]). We also illustrate that the synthetic spectra computed from MARCS model atmospheres can be used to constrain the abundance of α elements, and we derive estimates of atmospheric parameters for 44 M dwarfs observed in the context of the SPIRou Legacy Survey (SLS). Finally, we turn our focus to magnetic targets, and introduce `ZeeTurbo`, our new code based on the extensively-used `Turbospectrum`, to which we added polarized radiative transfer capabilities to include the effect of magnetic fields on spectra in our modeling. With this new code, and an adapted analysis, we constrain the average surface magnetic flux in addition to the atmospheric parameters of several magnetic targets observed in the context of the SLS. Our results and developed tools will guide future projects aimed at characterizing stars, estimating elemental abundances, and constraining magnetic fields, taking advantage of the long lasting observations carried out in the framework of the SLS, and its follow-up SPICE.

Résumé

Au cours des dernières décennies, les naines rouges ont attiré une attention croissante et ont été identifiées comme des cibles de choix pour la chasse aux exoplanètes situées dans la zone habitable de leurs étoiles hôtes, ainsi que pour l'étude des champs magnétiques dans les étoiles froides. Néanmoins, leur étude représente toujours un grand défi technique et scientifique en raison de la faible luminosité de ces étoiles. Cette thèse est dédiée à l'étude des naines rouges, et en particulier à leur caractérisation à partir de spectres proche-infrarouge à haute résolution et à haut rapport signal sur bruit obtenus avec le spectro-polarimètre SPIRou installé au télescope Canada-France-Hawaï. Nous utilisons des spectres synthétiques pour déterminer les paramètres atmosphériques des naines rouges, en utilisant la large couverture en longueur d'onde de SPIRou. Nous montrons comment des modèles différents et des listes de raies différentes peuvent avoir un impact significatif sur les paramètres atmosphériques estimés. Avec notre analyse, nous montrons que nous sommes capables de déterminer ces paramètres avec une précision d'environ 30 K en température effective ($T_{\rm eff}$), et 0.1 dex en gravité de surface $\log g$ et en métallicité ([M/H]). Nous montrons également que les spectres synthétiques calculés à partir des modèles d'atmosphères `MARCS` peuvent être utilisés pour estimer l'abondance des éléments α, et nous déterminons les paramètres atmosphériques de 44 naines rouges observées dans le cadre du SPIRou Legacy Survey (SLS). Enfin, nous nous concentrons sur les étoiles magnétiques et présentons `ZeeTurbo`, notre nouveau code basé sur `Turbospectrum`, auquel nous avons ajouté la résolution de l'équation de transfert radiatif polarisé pour inclure l'effet des champs magnétiques sur les spectres dans nos modèles. Avec ce nouveau code, nous estimons l'intensité moyenne du champ magnétique en plus des paramètres atmosphériques de plusieurs étoiles observées dans le cadre du SLS. Nos résultats et les outils développés guideront de futurs projets visant à caractériser les étoiles M, à estimer les abondances des éléments dans ces étoiles, et à étudier les champs magnétiques, en tirant parti des observations réalisées dans le cadre du SLS, et de son successeur SPICE.

Remerciements

Je voudrais commencer par remercier le programme de recherche et innovation H2020 du conseil de recherche européen (ERC, #740651 NewWorlds) qui a financé les travaux présentés dans ce manuscrit.

Je tiens ensuite à remercier Céline Reylé et Thierry Forveille pour avoir accepté de lire et évaluer ce manuscrit de thèse. Je tiens aussi à exprimer ma gratitude envers tous les membres du jury, Gaitee Hussain, Pascal Fouqué, Thomas Masseron et Claire Moutou, pour leurs questions et pour avoir accepté d'évaluer ce travail. Merci également à mon directeur de thèse, Jean-François Donati, pour m'avoir fait confiance en me proposant d'entreprendre ce vaste projet de recherche. Je veux également remercier tout particulièrement Thomas Masseron et Colin P. Folsom, pour leur aide précieuse qui m'a permis d'apprendre beaucoup et de rapidement développer certains outils utilisés dans ce travail. J'espère avoir l'opportunité de travailler avec vous d'avantage pendant la suite de ma carrière.

Je voudrais ensuite exprimer ma gratitude pour les membres du laboratoire, de l'équipe PS2E, et envers tous ceux qui m'ont aidé de près ou de loin avec ce projet. Merci notamment à Alain Hui-Bon-Hoa et Michel Rieutord pour avoir pris le temps de réfléchir avec moi aux problèmes liés à `PHOENIX`, et à Pascal Petit pour ses précieux conseils.

Ce sont ensuite mes amis que je veux remercier. Baptiste, Louise, pour m'avoir accueilli au laboratoire; Selena, Ben, Sonia, Alix, JS, pour votre soutien permanent et votre bonne humeur constante; Stefano et Bonnie, pour avoir été des amis comme il est rare d'en trouver. Merci à Joey, Anthony, Grégoire, Thea, Florian, Sabrina, Marjorie, Maitrayee, Roberta, et à tous ceux que j'aurai oublié de mentionner ici, pour avoir fait de Toulouse une ville que j'ai aimée.

Je veux ensuite finir en remerciant mes frères, ma soeur, mes parents, pour faire qu'il m'est tout simplement impossible de rêver d'une meilleure famille.

Foreword

Je ne sais pas si les mondes sont habités,
et, comme je ne le sais pas, je vais y voir!
– Michel Ardan,
De la Terre à la Lune, Jules Verne.

Thousands of planets have been detected over the last decades, since the first detection around a Sun-line star (Mayor & Queloz, 1995) to the symbolic threshold of 5000 planets detected in 2022. Because they make up to 75 % of the stars within 25 pc of the Sun (Henry et al., 2006), and because of their relatively low masses (≤ 0.6 $M_\odot$) and radii (≤ 0.6 $R_\odot$), M dwarfs have been identified as ideal targets for the search of exoplanets in the habitable zone of their host stars (Charbonneau et al., 2008). The study of M dwarfs and planets orbiting M dwarfs is a great technical and scientific challenge. Because these stars are less luminous than stars of earlier types, they require the development of dedicated instruments capable of tracking velocity variations of the order of the $m \cdot s^{-1}$ or less (such as HARPS, Bonfils et al., 2013), and ideally observing in the near-infrared domain (nIR). High-resolution in the near-infrared also provides the means to characterize M dwarfs, and to this end, several instruments were built, such as SPIRou (Donati et al., 2020), CARMENES (Quirrenbach et al., 2014) or iSHELL (Rayner et al., 2016), with resolving powers $R \geq 70000$. Nonetheless, observing in the nIR also represents a great scientific challenge, as one needs to disentangle stellar spectra from absorption and emission features caused by the Earth's atmosphere (Artigau et al., 2014; Ulmer-Moll et al., 2019).

The main focus of the work presented here is the characterization of M dwarfs from SPIRou spectra with the use of high-resolution synthetic spectra. The last decades have been marked by the development of several models attempting to synthesize stellar spectra from model atmospheres. Synthetic spectra computed from model atmospheres such as `PHOENIX` (Hauschildt et al., 1999; Allard et al., 2003; Husser et al., 2013), `MARCS` (Gustafsson et al., 2008) or `ATLAS` (Kurucz, 1970) were shown to successfully reproduce spectra of Sun-like stars. Recently, with the availability of high-resolution spectra in the nIR, several studies focused on using these models to analyze M dwarfs

spectra (Rajpurohit et al., 2018; Passegger et al., 2019; Souto et al., 2022). Modeling spectra at high-resolution provides the means to estimate quantities such as the effective temperatures or metallicity of stars with reported precisions of the order of 50 K and a few 0.1 dex, respectively. With accurate models, one can in particular hope to estimate the abundances of individual elements in such stars (Ishikawa et al., 2020, 2022). Modeling stellar spectra requires to account for the diversity of the species forming in the atmosphere of M dwarfs, including many molecules. They also rely on fundamental data for each transition, such as oscillator strengths and Van der Waals parameters, typically acquired through experiments and not always accurately known, especially in the nIR domain for cool stars.

With the work presented in this manuscript, we contribute to recent efforts to characterize M dwarfs from their near-infrared spectra acquired using SPIRou, one of the newest instrument mounted at the CFHT, providing high-resolution spectra (≥ 70000) over the Y, J, H and K bands ($\sim$ 950–2500 nm). Through a brief introductory chapter, we provide the reader with the basic context in which this work stands, and describe our main motivations. With Chapters 2 & 3, we provide more insights on how data is acquired, reduced, and on the theory of spectral synthesis. Focusing first on a sample of weakly active targets, we present our analysis method, calibration, and results in Chapters 4 & 5. We then turn to the study of more active stars, presenting a new tool specifically developed for the inclusion of magnetic fields in spectral modeling. This program, baptized `ZeeTurbo`, and its use for constraining magnetic field strengths of SPIRou targets is presented in Chapter 6. We conclude and outline future perspectives in Chapter 7.

Avant-propos

Des milliers de planètes ont été détectées au cours des dernières décennies, depuis la première détection autour d'une étoile comme le Soleil (Mayor & Queloz, 1995) jusqu'au seuil symbolique des 5000 planètes détectées en 2022. Parce qu'elles constituent ~ 75 % des étoiles situées à moins de 25 pc du Soleil (Henry et al., 2006), et en raison de leurs faibles masses (≤ 0.6 $M_\odot$) et rayons (≤ 0.6 $R_\odot$), les naines rouges sont des étoiles idéales pour la recherche d'exoplanètes dans la zone habitable de leurs étoiles hôtes (Charbonneau et al., 2008). L'étude des naines rouges et des planètes qui orbitent autour d'elles constitue un grand défi technique et scientifique. Parce que ces étoiles sont moins lumineuses que les étoiles plus massives, elles nécessitent des instruments dédiés observant dans le proche infrarouge (nIR) et capables de suivre des variations de vitesse radiale de l'ordre du $m \cdot s^{-1}$ ou plus petites (comme HARPS, Bonfils et al., 2013). Les observations à hautes résolution dans l'infrarouge proche permettent également de caractériser les naines rouges, et dans ce but, plusieurs instruments ont été construits, comme SPIRou (Donati et al., 2020), CARMENES (Quirrenbach et al., 2014) ou iSHELL (Rayner et al., 2016), produisant des spectres à des résolutions $R \geq 70000$. L'observation dans le proche infrarouge est aussi un défi scientifique, car il faut retirer des spectres obtenus les contributions dues à l'atmosphère terrestre (Artigau et al., 2014; Ulmer-Moll et al., 2019). Les travaux présentés dans ce manuscrit se concentrent sur la caractérisation de naines rouges via la comparaison de spectres infrarouges à des modèles de dernière génération. Les dernières décennies ont été marquées par le développement de plusieurs modèles tentant de reproduire les spectres stellaires à partir de modèles d'atmosphères. Des modèles comme `PHOENIX` (Hauschildt et al., 1999; Allard et al., 2003; Husser et al., 2013), `MARCS` (Gustafsson et al., 2008) ou `ATLAS` (Kurucz, 1970) ont permis de modéliser les spectres stellaires d'étoiles semblables au Soleil. Avec l'arrivée de spectres à haute résolution dans le nIR, plusieurs études se sont concentrées sur la modélisation des spectres de naines rouges (Rajpurohit et al., 2018; Passegger et al., 2019; Marfil et al., 2021). Ces modèles permettent entre autre d'estimer la température effective ou la métallicité des étoiles avec une précision rapportée de l'ordre de 50 K et de quelques 0.1 dex, respectivement. Avec ces modèles, certains auteurs ont également essayé d'estimer les abondances de différents éléments dans les naines rouges (Ishikawa et al., 2020, 2022). Les modèles théoriques de spectres stellaires doivent

cependant tenir compte de la complexité de la chimie de l'atmosphère des naines rouges, et en particulier de nombreuses molécules. Ils s'appuient également sur des données fondamentales, telles que la force d'oscillateur et le paramètre d'élargissement par collision pour chacune des transitions considérées, généralement acquises par des expériences, et qui font souvent défaut dans le domaine du proche infrarouge. Avec le travail présenté dans ce manuscrit, nous contribuons aux efforts entrepris pour caractériser les naines rouges à partir de leurs spectres enregistrés avec SPIRou, l'un des plus récents instruments montés au CFHT, fournissant des spectres à haute résolution ($R \geq 70000$) sur les bandes Y, J, H et K ($\sim$ 950 – 2500 nm). A travers un bref chapitre introductif, nous fournissons au lecteur le contexte dans lequel s'inscrit ce travail, et décrivons nos principales motivations. Dans les Chapitres 2 et 3, nous fournissons plus de détails sur la façon dont les données sont acquises, réduites, et sur la théorie de la synthèse spectrale. En nous concentrant d'abord sur un échantillon d'étoiles faiblement actives, nous présentons notre méthode d'analyse et nos résultats dans les Chapitres 4 et 5. Nous nous tournons ensuite vers l'étude d'étoiles plus magnétiques, en présentant un nouvel outil spécifiquement développé pour l'inclusion des champs magnétiques dans la modélisation de spectres stellaires. Ce nouvel outil, baptisé `ZeeTurbo`, et son utilisation pour déterminer les champs magnétiques de plusieurs étoiles, sont présentés dans le Chapitre 6. Nous concluons et exposons les perspectives de nos travaux dans le Chapitre 7.

Contents

Chapter 1

Introduction

Contents

1.1 An introduction to stars

'The remarkable nature of stars is transmitted to us by the light they send' (Gray, 2005). From the first naked-eye observations to modern space-born and ground-based measurements, our understanding of stellar formation, evolution, and death has been constrained by observations of the light they emit. In this chapter, we begin with a brief introduction to stars as we know them today, before discussing the specific case of M dwarfs, the main focus of this research project.

1.1.1 Brief reminder on stars

1.1.1.1 Spectral types and classification

Historically, stars were classified from purely observational features, such as brightness (the amount of light we receive from them), color (where is located the emission peak in their spectrum, intrinsically linked to their temperature), or the presence and shape of lines in their spectra (Gray & Corbally, 2009, chapter 1). One of the most popular spectral classification system, the Harvard spectral classification, assigns to each star a letter based on spectral features that are highly dependent on effective temperature (O, B, A, F, G, K, M in decreasing temperature order). Later, astronomers Hertzsprung and Russell placed observed targets in a magnitude – spectral type diagram, known today as the Hertzsprung–Russell (HR) diagram, which represented an essential step forward in the understanding of stellar classification and evolution (see Fig. 1.1). We identify several groups of stars on the HR diagram, such as the main-sequence (MS) stars, giants, and white dwarfs.

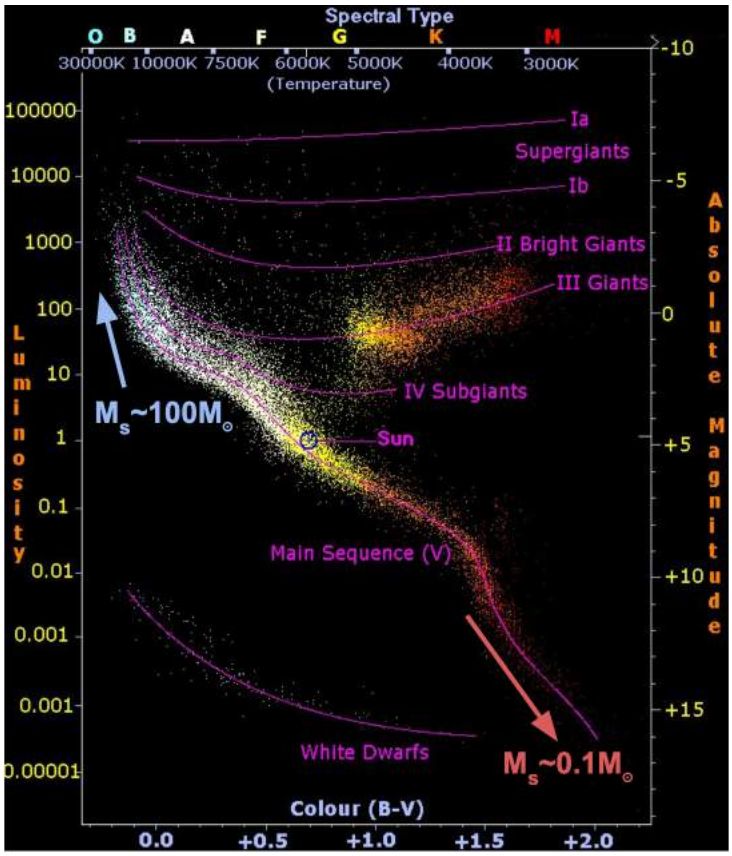

Figure 1.1. HR diagram for over 23000 stars from the Hipparcos and Gliese catalogues. Taken from Dr. Baptiste Klein PhD manuscript (http://thesesups.ups-tlse.fr/5052/), adapted from R. Powell (http://www.atlasoftheuniverse.com/hr.html)

1.1.1.2 Early stages of stellar formation

Stars are believed to form from the collapse of molecular clouds (Lada, 1992), observed as early as 1970 (Wilson et al., 1970). These clouds are mainly composed of Hydrogen molecules (H_2) and Helium (He), with lower amounts of dust and other molecules (such as CO, NH_3, or HCN). Recent observations of the Gould belt, regrouping some of the nearest known star-forming regions in the Galaxy, revealed the filamentary structure of molecular clouds (André et al., 2010, 2019). It is within these filaments that denser regions – baptized pre-stellar cores – are believed to be the first step towards stellar formation.

Within molecular clouds, gravity is typically balanced by other forces arising from turbulence, rotation, or magnetic fields. Several scenarios have been proposed to explain the gravitational collapse at the origin of stellar formation, such as turbulent shocks within clouds (Mac Low & Klessen, 2004), or ambipolar diffusion under the influence of magnetic fields, in which neutral gas and dust contract to the core of the cloud (Nakano & Nakamura, 1978). Several authors have since included both effects in their models (Nakamura & Li, 2005; Tilley & Pudritz, 2007; Crutcher, 2012). The gravitational collapse can also be initiated by external sources, such as supernovae or cloud collisions (Preibisch et al., 2002).

If the perturbation is large enough and the cloud exceeds the Jeans mass, the medium becomes unstable, and the cloud collapses until the formation of a dense object in its center, a protostar. The collapse occurs in two consecutive steps. First, the pre-stellar core collapses until the density reaches about $\rho \sim 10^{10}$ cm^{-3} (Maeder, 2009), at which point the pressure is high enough to initiate the creation of a first core. This first core, supported by thermal pressure, accretes matter from its immediate surrounding environment until the temperature reaches ~ 2000 K, at which point the conditions become favorable to the dissociation of molecular hydrogen. This process triggers the second collapse, which can be as fast as a few years, until the density reaches $\rho \sim 10^{20}$ cm^{-3}, forming a protostar (Tomida et al., 2013).

1.1.1.3 The protostellar phase

From the collapse of molecular clouds to the formation of hydrogen-burning stars, young stellar objects are typically categorized into four classes numbered 0, I, II, and III (André, 2015).

During the first stage of the protostar's life, the class-0 stage, the mass of the core is significantly smaller than that of its surrounding envelope of gas and dust. It is characterized by a spectral energy distribution (SED) compatible with that of a cold black body, with an emission peak located in the far-infrared domain. The angular momentum of the envelope prevents gas and dust from rapidly falling on the central core, but collisions within the could dissipate energy, leading to the formation of a circumstellar disk, which can extend over 100 au (Masunaga & Inutsuka, 2000; Machida & Matsumoto, 2011). The class-0 phase is accompanied by jets of matter (Bachiller & Gomez-Gonzalez, 1992; Bontemps et al., 1996; Bachiller, 1996). The central core continues to accrete matter from its surrounding environment, and within a few tens of thousands of years, becomes more massive than its envelope. The jets weaken and broaden, and the object enters the class-I protostellar stage. The SED is then characterized by the black-body emission of the protostar and a significant far-infrared excess associated with the circumstellar disk. This phase lasts for a few 10^5 yr before the star enters the next phase of its evolution, the pre-main-sequence (PMS).

1.1.1.4 Pre-main-sequence stars

The PMS phase begins with the class-II, when the envelope has been completely depleted and only leaves an optically thick disk surrounding star, which is then called classical T-Tauri star (cTTS). The SED of class-II young stellar objects is mainly dominated by the continuum emission of the star and an excess in the infrared associated with the disk. cTTSs can host complex magnetic fields of strengths reaching several kilogauss (kG, Johns-Krull, 2007), believed to play a significant role in the evolution of PMS stars, by allowing ionized material from the disk to funnel along the fields and fall onto the star (Bouvier et al., 2007), and through rotational braking (Bouvier et al., 2014). During the class-II phase, the star continues to accrete material from its surrounding disk, and within this disk, grains and dust can agglomerate, which can lead to the formation of planets (Armitage, 2011).

Once the inner disk around a cTTS has been depleted via accretion and ejection, the star is known as a weak-line T Tauri star (wTTS), and the system enters the class-III stage of its evolution. The evolution from cTTS to wTTS can range from 1-10 Myr (Bell et al., 2013; Richert et al., 2018). The SED of class-III objects is dominated by the emission of the wTTS, which resembles that of the MS star, and the presence of the disk is detectable only by a slight infrared excess (Hughes et al., 2018). With the inner disk gone, wTTS approach the MS. At the end of the class-III stage, the star loses momentum through the

effect of the magnetized stellar winds and reaches the MS at the zero-age main sequence (ZAMS).

Once the conditions in a PMS star become favorable to onset hydrogen fusion, the star is said to have reached the main sequence (MS). The MS is easily identifiable on an HR diagram, from hot and luminous O stars to cool faint M dwarfs. Stars spend most of their life on the MS, and their lifespan differs for all spectral types. Aside from the MS, several other groups of stars are identifiable on the HR diagram, in particular white dwarfs, red giants, and supergiants. The stars belonging to these groups are believed to be evolved objects, and the different groups are attributed to distinct stages of stellar evolution.

1.1.1.5 Stellar evolution

Stellar mass is the leading property determining the evolution of stars. Stars with masses above 20 $M_\odot$ only live for millions of years, while Sun-like stars can live for about 10 billion years (Maeder, 2009; Kippenhahn et al., 2013). In particular, three main evolutionary scenarios are believed to account for the observed stellar populations. Stars with masses greater than ∼10 $M_\odot$ typically reach the end of their MS phase in less than 100 Myr. In this relatively short time, the star will consume all of the hydrogen present in its core, at which point it begins to inflate. Because the star inflates, its outer layers become cooler and the radius larger. The overall luminosity of the star increases while it moves to later types and joins the super-giant branch of the HR diagram. As a supergiant, the star begins to burn increasingly heavier elements until it develop an iron core. At this point, fusion reactions cannot balance gravitational forces anymore, and the star collapses rapidly until it explodes into a supernova, leaving a neutron star or a black hole at its core.

The evolution of stars between ∼10 and ∼0.9 $M_\odot$ is somewhat similar to the previous case but on different time scales. These stars can stay on the main sequence between 0.1 and 10 Gyr before undergoing inflation and becoming red giants. These stars, however, are not massive enough to onset carbon fusion and develop an iron core. At the end of their life, red giants collapse similarly to super-giants but are not massive enough to turn into supernovae. Instead, they expel their outer layers, contract and turn into white dwarfs, slowly cooling down. This is what is expected to become of the Sun.

Finally, stars below ∼0.9 $M_\odot$ are expected to live lifetimes longer than the age of the Universe (Maeder, 2009).

1.1.1.6 Stellar structure and composition

The Sun is a G-type star and the closest to our observation facilities. It is consequently the most studied and well-known example at our disposal (Robles et al., 2008). Unlike other stars, telescopes can easily probe its surface, and observations at all wavelengths have been carried out for decades, providing a unique insight into its composition and structure (Christensen-Dalsgaard, 2021, for a review). A typical schematic representation of stars between 0.35 and 1.5 $M_\odot$ is presented in Fig. 1.2. In the Sun, the energy generated by the fusion of hydrogen in the core is transported through the radiative zone, which can extend to 45 % of the solar radius and which surface reaches a temperature of $\sim 2 \cdot 10^6$ K. At greater distances from the center, energy is transported by convection, layer in which the temperature decreases with radius, until it reaches $\sim$6000 K at the Sun's surface. The extent of the convective zone depends on stellar mass. In particular, the convective zone grows larger as stellar mass decreases, and stars with masses lower than $\sim$0.35 $M_\odot$ are said to be fully convective (Baraffe et al., 1998).

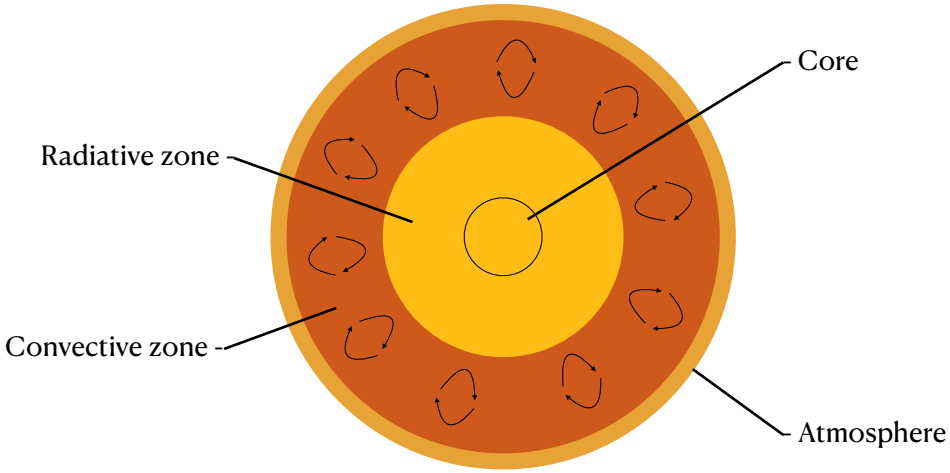

Figure 1.2. Schematic view of a Sun-like star.

Most of the light one can study originates from the stars outer layers: these layers form the stellar atmosphere. The stellar atmosphere is itself divided into several sub-structures. The photosphere is the deepest and brightest region of the stellar atmosphere (Gray, 2005), and is the layer below which the star is opaque (optically thick). It is generally responsible for most of the absorption lines measured with spectrometers. Consequently, many models today focus on this region alone to reproduce stellar spectra (see Chapter 3). The photosphere in the Sun extends on about 300 km. Above the photosphere, the

chromosphere extends on $\sim$4000 km in the Sun, and is at the origin of absorption and emission lines under the influence of magnetic fields (see Sec. 1.2.1). The outermost layer of the stellar atmosphere, the corona, extends on millions of km in the Sun and can be responsible for flares and coronal mass ejection induced by magnetic fields.

In the stellar atmosphere, several elements are responsible for the formation of absorption lines observed in stellar spectra. These can be atoms (such as Fe, Ti, Ca, Al, and Mn, to name a few) or molecules (such as OH, TiO, and CO). The stellar mass, radius, and temperature significantly influence the intensity, width, and shape of these spectral lines, which can therefore be used to constrain the fundamental properties of stars. Molecules can be responsible for the formation of large absorption bands, in particular for the coolest observed stars, and are consequently particularly critical to the study of M dwarfs spectra (see Chapter 4 & 5).

1.1.2 M dwarfs as ideal targets for the search of planets in the habitable zone

1.1.2.1 On the detection of exoplanets

The last decades have been marked by the detection of exoplanets, from the first discovery of a planet orbiting a MS star in 1995 (Mayor & Queloz, 1995) to the symbolic threshold of 5000 detected planets in 2022.

Several techniques for the detection of planets exist (Rice, 2014, for a review). Most methods are said to be indirect, as they infer the presence of a planet by monitoring the light received from the host star. In particular, by tracking the radial velocity (RV) of a star over time, one can detect periodicity and infer the presence of a companion, which can be a planet. Such a technique requires dedicated instruments capable of tracking small fluctuations in the radial velocity signals. For instance, the influence of Jupiter on the Sun induces RV signals of $\sim$12 $\mathrm{m \cdot s^{-1}}$, while that of the Earth induces signals of only $\sim$0.1 $\mathrm{m \cdot s^{-1}}$. RV signals are typically monitored through Doppler shifts measured from stellar spectra. The detection of planets through the radial velocity motion requires the planet to be sufficiently massive with respect to its host star to induce a detectable shift. The amplitude and shape of the observed oscillations also depends on the eccentricity of the system.

Another option to detect planets is to monitor the drop in received flux occurring when a planet passes between the star and the observer. The amplitude of the drop and its shape

directly relates to the ratio between the radii of the planet and the star. Additionally, by masking part of the stellar light, transiting planets can induce shape variations in the stellar lines via the Rossiter-McLaughlin effect (Rossiter, 1924; McLaughlin, 1924). Although the mass of transiting planets is not directly deducible from such observations, they allow for other measurements, such as the orbital periods or radius (relative to that of the star). Other innovative characterization techniques have been explored, such as studying the absorption spectrum of the planet observed during transits.

Aside from indirect methods, planets can be studied by directly detecting light emanating from them (like for the now famous HR8799 system, Marois et al., 2010). Combined with spectroscopy, planetary spectra can be acquired, revealing important information on their composition and properties. This technique remains one of the most challenging, requiring significantly large telescopes, advanced instrumentation, and heavy post-processing steps to disentangle the stellar and planetary light. Direct imaging of exoplanets is limited to massive (i.e. of a few Jupiter masses or more) and self-luminous young planets, sufficiently distant from their host star (typically more than a few au), for the contrast to be favorable. Such a technique is therefore unlikely to reveal the presence of planets in the habitable zone of their host stars in the near future.

The detection of planets, and their characterization, is usually performed by combining different techniques. Radial velocity measurements are often combined with transit follow-ups in order to constrain both the radii and masses of the planets, providing information on their density. The properties of the planets are intrinsically linked to those of the host star. For instance, determining the mass of a planet from radial velocity implies knowledge of the mass of its host star. It is therefore crucial to the field to develop reliable techniques to constrain the fundamental properties of stars.

1.1.2.2 The hunt around M dwarfs and PMS stars

M dwarfs are the coolest stars of the MS and the most numerous stars around us. Their mass span from 0.08 $M_\odot$ and 0.6 $M_\odot$, with effective temperatures ranging from $\sim$2700 K to $\sim$4000 K. They represent over 75 % of the stars located within 25 pc of the Sun (Henry et al., 2006; Winters et al., 2015). They have been identified as some of the most promising targets for searching Earth-like planets located in the habitable zone of their host stars (Charbonneau et al., 2008; Bonfils et al., 2013). Because they are numerous, the probability of detecting planets around them is larger than around stars of earlier types. Furthermore, Earth-like planets induce larger radial velocity signals when orbiting M dwarfs than when orbiting Sun-like stars. Earth-like planets in the

habitable zone of their host stars can induce RV signals of a few meters per second around a M dwarf, rather than a few centimeters per second when orbiting a Sun-like star. Earth-like transiting planets also induce deeper transit depths when orbiting M dwarfs than early-type stars, as the depth increases when the stellar radius decreases. The lower effective temperature of M dwarfs also brings the habitable zone closer to the star making Earth-like planets more likely to transit. The occurrence rate of planets orbiting M dwarfs was found to be 2 to 3 times that of the of planets around Sun-like stars (Dressing & Charbonneau, 2015; Tuomi et al., 2019).

Despite these advantages, detecting exoplanets around M dwarfs remains particularly tricky. Stellar activity in these stars can impact their characterization and induce signals in radial velocity measurements. Moreover, the study of M dwarfs typically requires observing in the nIR domain, which is in itself a technical challenge.

1.2 On the challenging study of M dwarfs

While we established that M dwarfs are among the most promising targets for discovering and studying Earth-like planets in the habitable zone of their host stars, their study remains a technical and scientific challenge. Their observation demands innovative technologies and dedicated instruments, while interpreting their spectra requires modeling the physical processes taking place in their atmospheres. The study of M dwarfs is yet crucial for the characterization of planets and to unveil the complexity of their composition and evolution.

1.2.1 Stellar activity and its impact on stellar spectra

1.2.1.1 Magnetic fields in stars

The first measurements of magnetic fields in stars were performed by the observation of Sun spots (Hale, 1908). Since then, magnetic fields in the Sun have been shown to evolve cyclically, on a scale of $\sim$22 yrs, with a switch in polarity every $\sim$11 yrs (Hathaway, 2015). The origin of these magnetic fields along with their evolution is now believed to be the result of dynamo processes (Parker, 1955; Steenbeck et al., 1966), induced by the motion of fluid in the convective layers of the Sun (see Morin, 2012, for an introduction to dynamo processes). Similarly to the Sun, the detection of activity indicators and the presence of convective layers in low-mass stars suggest that dynamo processes can be at the origin of magnetic fields in M dwarfs and PMS stars. Magnetic fields are at the

origin of a number of phenomena grouped under the term of magnetic activity. The intensity of magnetic fields and related phenomena at the surface of stars scale up with the Rossby number, i.e. the ratio of the inertial to Coriolis forces, hence depending of the rotation period of stars. The larger the rotation period, the larger the Rossby number and the lower is the activity in the star. Activity and magnetic fields at the surface of stars were found to indeed scale up with the Rossby number, as predicted by dynamo theories (Wright et al., 2011; Folsom et al., 2016; Shulyak et al., 2017), and the presence of magnetic fields in M dwarfs, with strengths ranging from a few tens of G to a few kG, is now well established (see Kochukhov, 2021, for a review).

1.2.1.2 Zeeman effect

Magnetic fields in stars influence the shape of spectral lines through the so-called Zeeman effect. If an atom is placed in a uniform magnetic field, the energy levels are split and the number of possible transitions increases (Zeeman, 1897). The presence of magnetic fields in stars therefore induces a splitting of the spectral lines in stellar spectra. In practice, the Zeeman components are not resolved, and magnetic fields of up to a few kG are responsible for the broadening of some spectral lines. This effect depends not only on the field strength but also on the considered transition, and in particular on the Landé factors of each energy level involved in this transition (see Chapter 6 for a more detailed description of the Zeeman effect).

In the case of the so-called normal Zeeman effect, a spectral line at wavelength λ_0 is split into 3 components: one π component, lying at the same wavelength λ_0, and two σ components blue and red shifted by the same amount, so that (Morin, 2012):

$$\Delta\lambda_0 = \frac{\lambda_0^2 e g_{\text{eff}} B}{4\pi m_e c}$$

with $\Delta\lambda_0$ the shift between the π and σ components, e the electron charge, B the magnetic field strength, m_e the electron's mass, c the speed of light, and g_{eff} the effective Landé factor. g_{eff} depends on the Landé factors of the two energy levels involved in the transition, and provides a useful quantification of the sensitivity of a line to the magnetic field. Its value can range from 0 (for an insensitive line) to a few units (for highly sensitive lines). If we consider a line at 1600 nm with a $g_{\text{eff}} = 1$ under the influence of a 1 kG field, then $\Delta\lambda_0 \approx 0.01$ nm. Resolving such separation would require a resolving power $R > 160000$, greater than that of most high-resolution nIR spectrometers in operation today.

The Zeeman effect is also associated with the emission of polarized light, as the π and σ components have different polarization properties, which we can observe depending on the orientation of the magnetic field with respect to the line-of-sight (see Chapter 6). Thus, through the observation of polarized spectra, several teams have been able to map the topology of large-scale magnetic fields at the surface of stars with techniques such as Zeeman Doppler Imaging (ZDI, see e.g., Semel, 1989; Skilling & Bryan, 1984; Donati & Brown, 1997; Morin et al., 2008, 2010). Alternatively, the extraction of polarimetric information from linearly and circularly polarized light has been performed with techniques such as Least-Square-Deconvolution (LSD), which combines the information of thousands of spectral lines to obtain a single, high-SNR profile (Donati & Brown, 1997; Kochukhov et al., 2010).

1.2.1.3 Spots, winds and chromospheric activity

Magnetic fields are believed to be responsible for the formation of bright and dark regions that can appear at the surface of stars (commonly known as plages and spots, respectively) on time scales ranging from days to years (Hale, 1908; Newton et al., 2016). Because the temperature of plages and spots differ from the rest of the photosphere, their presence affects the overall shape of the stellar spectra. For rotating stars, the presence of these spots, cooler and less bright than the rest of the photosphere, can reduce the amount of blue or red-shifted light and induce asymmetries in the line profiles. Such a phenomenon is particularly detrimental to the search for exoplanets via radial velocity measurements and transit photometry as it can introduce additional time-dependent signals (Guenther, 2022).

Through the influence of magnetic fields, the chromosphere can also exhibit variability phenomena (see Hall, 2008, for a review), and be responsible for emission lines such as Hα (Reiners & Basri, 2007; Newton et al., 2017) and Ca II H&K lines (Schrijver et al., 1989; Newton et al., 2017). Magnetic fields can also be at the origin of flares, manifesting as a sudden increase in luminosity which can appear in a few minutes and decay on time scales of several hours (Benz, 2017). Just like in the Sun, several studies reported on the evolution of magnetic activity in M dwarfs (Gomes da Silva et al., 2012; Route, 2016, Bellotti et al., in prep).

1.2.2 Observing in the nIR domain

1.2.2.1 Advantages and motivations

The SED of stars strongly depends on their effective temperature and roughly resembles that of a black body. The maximum luminosity they emit is found at wavelengths that also depend on their temperature: objects cooler than 4000 K emit more light in the red end of the visible spectrum and in the nIR than stars with temperatures above 5000 K, which appear bluer. Figure 1.3 presents modeled spectra for various temperatures. Because M dwarfs are more luminous in the nIR than in the visible domain, observing in the nIR domain allows one to increase the signal-to-noise ratio (SNR). Moreover, with lower effective temperatures, the contrast between bright and dark features induced by stellar activity is lower, limiting their impact on planet detection and stellar characterization. For instance, the temperature difference between spots and the photosphere can go from 2000 K in early G stars, to 200 K in mid-M dwarfs (Berdyugina, 2005).

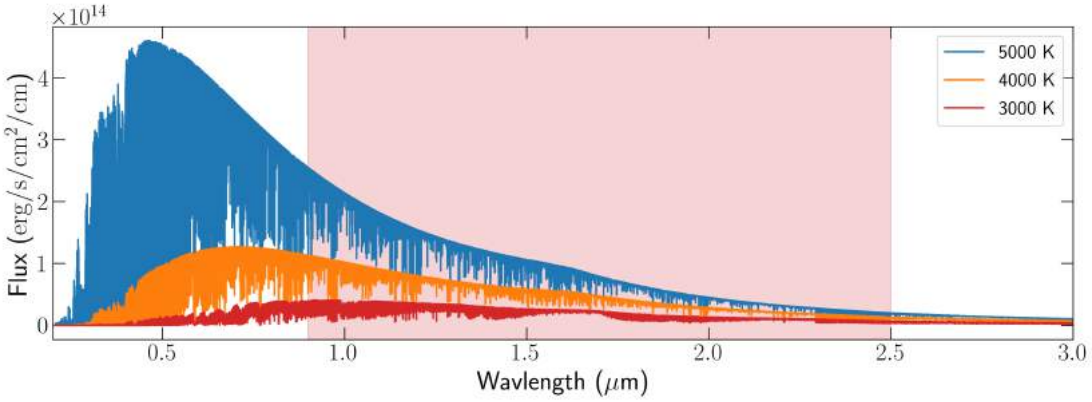

Figure 1.3. `PHOENIX-ACES` synthetic spectra (see Sec. 3.3) for 3 effective temperatures. The red band marks the wavelength domain covered by SPIRou.

1.2.2.2 Limitations and challenges

Observing M dwarfs in the nIR remains a technical challenge despite these advantages. Although cool objects are brighter in the nIR than in the visible, they remain less luminous than stars of earlier types. Their observation requires significant telescope time and dedicated instruments, resulting from years of research and development. Today, high-resolution spectrometers such as iSHELL (Rayner et al., 2016), CARMENES (Quirrenbach et al., 2014), IRD (Kotani et al., 2014, 2018), HPF Mahadevan et al. (2012), GIANO (Claudi et al., 2017), and SPIRou (Donati et al., 2020) already provide data

for M dwarfs, useful to search for exoplanets and to study these stars. Several other instruments are in preparation, such as NIRPS (Wildi et al., 2017) or SPIP (Baratchart et al., 2022), the twin of SPIRou to be installed at the Pic du Midi Observatory.

These instruments are installed on the ground. Consequently, they are sensitive to the Earth's atmosphere, which is responsible for extensive forests of molecular lines in the observed spectra, particularly in the nIR (Ulmer-Moll et al., 2019; Artigau et al., 2014). One of the great challenges observers have to face is to remove the contribution of the Earth atmosphere from the spectra to extract the stellar signal from the data (see Chapter 2).

1.3 On the characterization of stars

As already mentioned, M dwarfs are key targets for the search of habitable exoplanets. To put constraints on the mass, radius, or composition of these planets, it is essential to characterize their host stars as accurately as possible. For transiting planets, knowledge of the radius of the host stars is necessary to constrain the radius of the planets. Constraining the mass of a planet detected via radial velocity techniques requires prior knowledge of the stellar mass. Moreover, the luminosity and temperature of a host star define the position of the habitable zone (Kopparapu et al., 2013). Studying the host star of exoplanetary systems is also essential to disentangle the planetary signals from activity-induced distortions that could lead to false detection (Sarkis et al., 2018).

It is thus important to accurately derive the stellar effective temperature ($T_{\rm eff}$), surface gravity ($\log g$, depending on the stellar radius and mass), and metallicity ([M/H], accounting for the overall abundance of metals in the star). Putting constraints on $T_{\rm eff}$, $\log g$ or [M/H] is particularly challenging for M dwarfs, because these stars are faint, and because rotation, magnetic fields, or spots are likely to affect the various techniques used to estimate stellar properties. In this section, we review some of the most popular methods used by the community to characterize stars and introduce the one at the heart of the present work: the comparison to high-resolution synthetic spectra.

1.3.1 Methods for stellar characterization

1.3.1.1 Photometry and models of low resolution data

One of the most straightforward approaches to study stars is to measure the number of photons received from a given target (photometry). Combined with parallaxes measurements, the magnitude can provide an estimate of the absolute luminosity of a star. Magnitude measurements are routinely performed, and large surveys such as 2MASS (Skrutskie et al., 2006) acquired data for hundreds of millions of objects through filters in the J, H, and K bands. New surveys, such as Gaia, provide new measurements in the optical through its red and blue filters (Gaia Collaboration et al., 2016, 2022). Modern analyses typically combine measurements obtained through several filters covering distinct wavelength domains to get constraints on an the SED of an object. The comparison between magnitudes measured through different filters, commonly referred to as colors, can be used to estimate temperatures or masses from empirically calibrated relations (Ruiz-Dern et al., 2018). Several such relations require to derive bolometric magnitudes, generally computed from bolometric corrections (Code et al., 1976; Mann et al., 2015; Cifuentes et al., 2020). These corrections must be tailored to specific filters. Color–magnitude relations and luminosity estimates can help constrain stellar properties via various applications. They can be used to place the observed targets in the HR diagram and compare them to evolutionary models, or to derive empirical relations linking mass and luminosity (Mann et al., 2019), allowing one to estimate masses with a precision of a few %.

Stellar parameters can also be constrained by fitting the SED with synthetic photometry computed from stellar models (Mann et al., 2015; Vines & Jenkins, 2022). This technique amounts to identifying which model reproduces best the absolute magnitudes computed for several filters, and deducing the properties of stars from them. In particular, such an approach can allow one to derive temperatures with a precision of about a 100 K, but is also model dependent, with differences that can reach up to 500 K depending on the model used (Vines & Jenkins, 2022).

1.3.1.2 Equivalent width and line depth

Mid and high-resolution spectra allow for the study of spectral features in more detail than photometry. Empirically calibrated methods can then be used to derive stellar parameters from the characteristics of lines, such as equivalent width (the width of a rectangle needed to replicate the area of a spectral line, Rojas-Ayala et al., 2010; Neves

et al., 2014). Equivalent widths of lines can be used to estimate $T_{\rm eff}$ or [M/H] from relations that can be calibrated from observations or models (e.g., Ishikawa et al., 2020). Some lines and sets of lines were reported as ideal proxies for the characterization of M dwarfs (Rojas-Ayala et al., 2012), such as TiO and CaH, used to constrain [M/H] in M dwarfs (Gizis, 1997; Woolf & Wallerstein, 2005). Such methods are difficult to apply to low-temperature stars because of the deep and numerous molecular bands rendering normalization difficult (see Sec. 4.2.2) and have driven the development of innovative approaches for the calibration of empirical relations (Pineda et al., 2013; Neves et al., 2013).

Line depth ratios were also proposed as a method to derive temperatures from stars (e.g., Gray & Johanson, 1991; Teixeira et al., 2016). The derivation is typically obtained through calibration on standard stars and was initially applied to FGK types. Still, recent studies explored its use for the characterization of M dwarfs and cool giants (López-Valdivia et al., 2019; Taniguchi et al., 2021).

Here again, the latest generation of models provided new tools to estimate parameters. Hybrid methods relying on equivalent widths measurements and synthetic spectra were proposed as a promising approach to estimating individual abundances in M dwarfs (Ishikawa et al., 2020, 2022).

1.3.1.3 Interferometry

Stellar radii are usually estimated indirectly from quantities such as temperature and luminosity, through evolutionary models or theoretical assumptions. Interferometric measurements of angular diameters, combined with parallaxes, represent today the most accurate method for estimating single-star radii. Such measurements have provided reliable constraints before (Berger et al., 2006), but reported data for M dwarfs remain limited (Boyajian et al., 2012).

1.3.2 Modeling spectra at high resolution

1.3.2.1 On the successes of the approach

Modeling stellar spectra is arguably one of the most reliable approaches to stellar characterization. The shape of absorption lines depends on several parameters. Some of them, such as the oscillator strength or collisional broadening, must be determined for each individual transition (see Chapter 3). Others, such as rotation, turbulence,

temperature, gravity, or chemistry, affect the shape of all spectral lines (see Sec. 3.4). These effects can be accounted for in model atmospheres and synthetic spectra computed from theoretical assumptions and empirical data. The physical properties of stars can then be deduced from the comparison of observed and synthetic spectra.

The first successes of stellar models were reported in the 1970s, with the publication of synthetic spectra tailored to the study of Sun-like stars and hotter objects (Gustafsson et al., 1975; Kurucz, 1979). Since then, remarkable progress has been achieved in estimating the atomic and molecular data required for the computation of such models (Hummer et al., 1993; Seaton et al., 1994; Barklem et al., 1998). As data improved, so did the models, and more detailed descriptions of the stellar atmosphere, radiative transfer, and atomic absorption were proposed. The rapid evolution of computing power over the last decades also significantly contributed to the development and publication of several grids of synthetic spectra with complex physical considerations, such as 3-dimensional hydro-dynamical models (Trampedach et al., 2013; Magic et al., 2013).

Synthetic spectra are today routinely used for the characterization of stars (Valenti & Fischer, 2005; Yee et al., 2017; Marfil et al., 2020), and recent studies explored their use for M dwarfs (Rajpurohit et al., 2013, 2018; Passegger et al., 2019; Schweitzer et al., 2019; Marfil et al., 2021; Sarmento et al., 2021), with reported precision reaching $\sim$50 K in $T_{\rm eff}$ and $\sim$0.1 dex in $\log g$ or [M/H].

1.3.2.2 A set of challenges

Although promising, the modeling of high-resolution spectra remains highly challenging. First, building such models requires a high level of understanding of the physical processes shaping spectral lines. One must precisely describe how a given line forms within a given atmosphere. To this end, years of research have led to the development of increasingly complex models of the stellar atmosphere (Gustafsson et al., 2008; Allard et al., 2011; Husser et al., 2013), which must account for turbulence, rotation, limb darkening, thermal broadening, and natural line shapes, among several other physical processes (see Chapter 3). The complexity of the phenomena occurring in stellar atmospheres is still not fully captured even by the most up-to-date models, which always rely on a set of assumptions and only offer approximate descriptions. These models typically require large computational resources, and each step towards more realistic stellar atmospheres also comes at great computation cost.

The several effects included in the models can also be difficult to disentangle. For instance, rotation and macroturbulence (see Chatper 3) can produce similar effects on the stellar spectra and may be a source of uncertainty. Moreover, multiple descriptions of macroturbulence have been proposed (Takeda & UeNo, 2017, Chapter 3), which can be an additional source of uncertainty, and forces modelers to make assumptions.

Finally, significant improvements to the models were made possible thanks to accurate experimental and observational data, providing realistic descriptions of abundances and line parameters necessary to compute absorption coefficients. In particular, accurate constraints on line parameters, such as their oscillator strength or Van der Waals parameters (see Chapter 3), are essential to compute synthetic spectra that compare well to observations, but are not always accurately known, especially in the nIR domain. Today, lists for millions of lines have been compiled, and current research projects aim at improving such constraints (Barklem et al., 2021; Amarsi et al., 2022).

1.4 SPIRou: a high resolution near infrared spectropolarimeter

1.4.1 High-resolution and polarimetry

SPIRou (spectropolarimètre infrarouge) is a high-resolution instrument installed at the Canada France Hawaï telescope (CHFT) located at the top of Mauna Kea (Donati et al., 2020). Its design, inspired by the previous spectrometers HARPS (Mayor et al., 2003) and ESPaDOnS (Donati, 2003; Donati et al., 2006), was optimized to provide both high precision velocimetry and polarimetry.

Aside from the spectrometer itself, SPIRou is composed of a Cassegrain unit, designed to collect the telescope light, and a calibration unit. These different parts are presented in Fig. 1.4. The Cassegrain unit is itself composed of several structures, including the polarimeter. The latter is composed of two Fresnels and a Wollaston prism splitting the incoming light into two beams of orthogonal polarization states. This system allows SPIRou to monitor circularly or linearly polarized light depending on the orientation of the rhombs.

SPIRou was designed to record spectra on a large wavelength domain (9-2.5 μm) in a single exposure, with a resolving power $R \sim 70000$. The calibration unit is equipped with several calibration lamps, allowing SPIRou to perform radial velocity measurements down to 0.1-0.2 $\mathrm{m \cdot s^{-1}}$ (Donati et al., 2020).

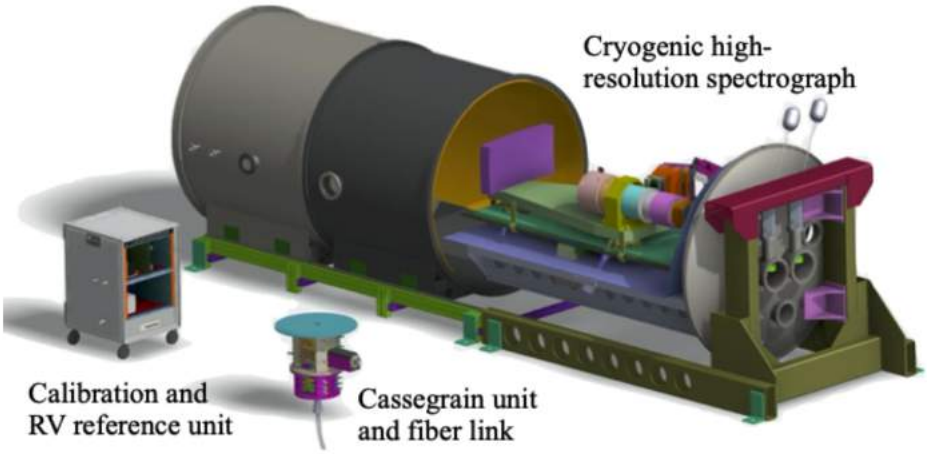

Figure 1.4. Computer aided design of SPIRou, taken from Donati et al. (2020).

1.4.2 The SPIRou legacy survey

For the analysis of SPIRou spectra, the SPIRou Legacy Survey (SLS) large observation program was allocated 310 nights between 2019 and mid-2022. The community regroups more than 150 researchers based in France, Canada and several other countries around the world, promoting international collaborations. The two main science goals of the SLS are the search for exoplanets orbiting M dwarfs, and the study of magnetic activity and planet formation. The high-resolution and spectropolarimetry capabilities of SPIRou place the instrument in an ideal position to fulfill these two goals.

The SLS was divided in 5 work packages (WP) aimed at addressing different aspects of scientific research. These include:

- The **WP1** focusing on planet search around M dwarfs from the SPIRou input catalogs (Moutou et al., 2017; Fouqué et al., 2018). Over 150 nights were allocated to the monitoring of about 70 targets.
- The **WP2** focusing on the monitoring of already-discovered transiting exoplanets, with about 75 allocated nights.
- The **WP3** for the study of magnetism in PMS stars and star/planet formation and interaction, with about 75 allocated nights.
- The **WP4** which goal is the optimization of all the results obtained with WP1-2.
- The **WP5** including all complementary analyses, such as the study of stellar spectra, large and small scale magnetic fields in M dwarfs or telluric correction.

These work packages are far from being independent, and although the results presented in this manuscript are easily categorized in the WP5, they are of crucial importance to planet search and characterization.

With the end of the SLS, a new large program, the SPIRou Legacy Survey - Consolidation & Enhancement (SPICE), was allocated over 174 nights between 2022 and 2024 to focus on new M dwarfs and PMS stars not observed in the context of the SLS.

Chapter 2

Building stellar templates from SPIRou nIR spectra

Contents

SPIRou, like every other ground-based spectrometer, has to face several technical challenges to produce reliable spectra. Several members of the SLS consortium worked on developing a data reduction software (DRS), baptized APERO (A PipelinE to Reduce Observations, Cook et al., submitted), to go from raw recorded data to science products. One essential step to produce stellar spectra is removing the spectrum of the Earth's atmosphere from the data. Absorption and emission lines due to the Earth's atmosphere are particularly deep and numerous in the nIR domain. In this chapter, we briefly summarize the main reduction steps performed by APERO and discuss attempts to improve the telluric correction of SPIRou spectra (Cristofari et al., 2022a).

2.1 Extracting stellar spectra

2.1.1 Extraction steps – APERO

SPIRou frames are recorded on a 4096^2 pixels Hawaii 4RG detector, providing 2D images from which science arrays must be extracted. The optical design of SPIRou makes it possible to fit 50 orders (#80 to #31) on the detector, thus covering the entire range

from 950 to 2500 nm in a single exposure (Donati et al., 2020). Figure 2.1 presents part of a typical image recorded during an observation of AD Leo. Each order on this image consists of three consecutive channels. Two correspond to the spectra of AD Leo in the 2 orthogonal states of the selected polarization, and one corresponds to the reference channel, here fed with the light from the thermally-stabilized Fabry-Perot etalon.

To produce science spectra providing flux as a function of wavelength, several processing steps must be carried out to clean the image, locate the orders, and convert bins to wavelength. SPIRou is equipped with several calibration lamps to carry out flat-field exposures, perform pixel-to-wavelength calibrations, and monitor the performance of the instrument. The reference channel provides additional means to calibrate the data and can be used, among other things, to monitor spectral drifts (of instrumental origin) with respect to the calibration frames recorded at the beginning of the night.

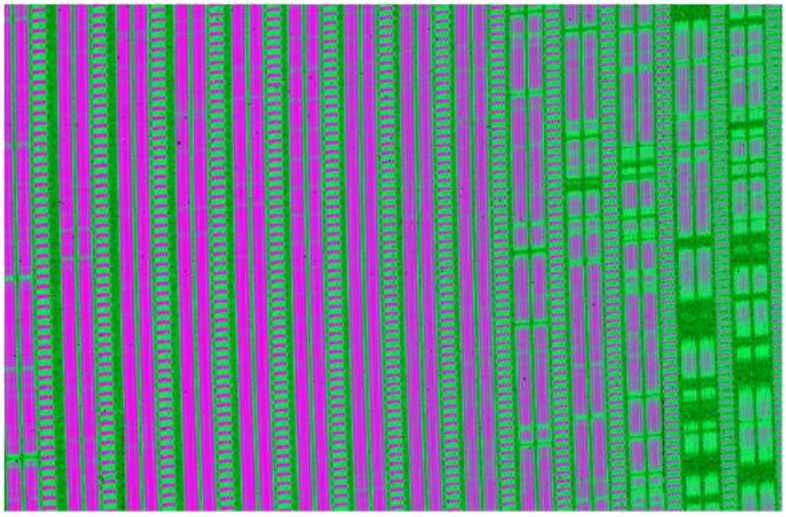

Figure 2.1. Science image on the SPIRou detector. Purple correspond to darker regions on the camera. Three channels are visible for each order, corresponding to the 2 science spectra and the reference Fabry-Perot. Taken from Donati et al. (2020).

`APERO` is a pure `Python` program designed to extract science spectra from raw SPIRou images. It can perform several reduction tasks, which can be run independently on intermediate products, providing flexibility. Such tasks include correcting the thermal background, bad pixel detection, and wavelength calibration, among other things. In particular, APERO identifies the orders on a raw image and extracts blaze profiles from flat-field exposures used to correct each spectral order. Additional recipes were developed to perform telluric correction, compute cross-correlation functions and extract data products for polarimetry.

All SPIRou observations processed with APERO are made available to the principal investigator through the Canada Astronomy Data Center (CADC) website[1]. On top of the science products, raw images and intermediate data are also stored and released to allow for later reprocessing. All processed data are stored in FITS files, with seven main extensions. The r.fits and o.fits files provide raw images of the observation needed for full processing. Three extensions are used to store the spectra before and after telluric correction and with all orders fused in a 1-dimensional array (e.fits, t.fits, and s.fits, respectively). The remaining products provide polarimetric data (p.fits) and order-per-order cross-correlation for radial velocity measurements (v.fits).

The s.fits data products are blaze corrected, normalized, and re-binned on a wavelength solution regularly spaced in wavelength or velocity. For our purposes, we typically rely on e.fits and t.fits files (2D spectra), identifying lines of interest in each order. Because the edges of consecutive orders overlap, some lines may be recorded on two consecutive orders. In such a case, we select the order with the highest flux.

2.1.2 The Earth's atmosphere spectrum

The Earth's atmosphere significantly absorbs in the nIR domain. In the wavelength domain covered by SPIRou, deep absorption features overlap with stellar lines and can bias analyses. It is therefore crucial to disentangle the contribution from Earth's atmosphere and stellar spectrum.

2.1.2.1 The molecules at play

Figure 2.2 presents a typical SPIRou spectrum recorded for Barnard's star (Gl 699) before and after the correction of telluric lines. All orders are shown after individual normalization and blaze corrections are applied. We easily identify deep absorption bands due to the Earth's atmosphere on the uncorrected version of the spectrum. We can, in particular, identify five very deep and dense water absorption regions, spanning from 950 to 1000 nm, from about 1100 to 1200 nm, from 1300 to 1500 nm, from 1800 to 1950 nm, and then again above 2400 nm. These bands alone represent about 40 % of the spectral domain covered by SPIRou. Two additional deep CO_2 bands are visible between 2000 and 2100 nm, and several other smaller bands are the consequence of the presence of O_2, CH_4, and to a smaller extent NO_2. All these molecules leave very few segments of the

[1] https://www.cadc-ccda.hia-iha.nrc-cnrc.gc.ca/

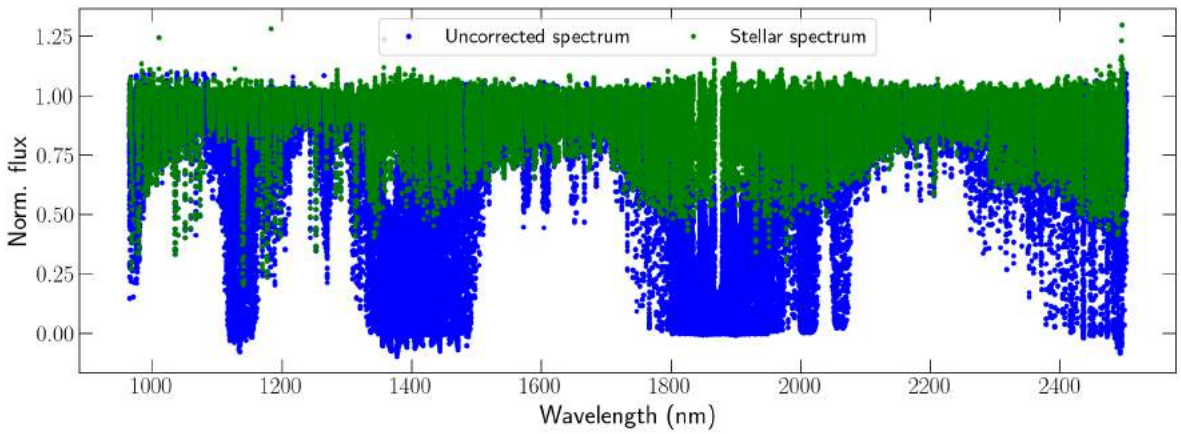

Figure 2.2. Typical SPIRou spectrum for Barnard's star. The raw spectrum containing both the stellar and eath's atmosphere contribution is plotted in blue, while the stellar spectrum obtained after correction of the telluric lines is plotted green.

spectrum unaffected by telluric lines, and even outside of the main absorption bands, thousands of smaller telluric lines can affect stellar lines.

2.1.2.2 Consequences on analysis

Because absorption lines formed by the Earth's atmosphere blend with stellar lines, they are likely to affect spectral analyses if not adequately corrected. Radial velocity estimation through cross-correlation and least-square deconvolution (LSD) profiles can also be affected by the presence of poorly corrected telluric features. Any analysis relying on a spectral line shape, whether via equivalent widths measurements or fits of synthetic spectra to the data, is sensitive to telluric contamination.

Fig. 2.3 presents a small section of the spectrum containing two Na lines of interest to our study before and after the correction of the telluric lines. On top of the deep telluric line observed in the window, several small contributions from the Earth's atmosphere tend to affect the shape of stellar lines, and in particular, their wings, containing crucial information for stellar characterization (see Chapters 4 &5).

2.1.3 Techniques for the correction of telluric lines

Several techniques have been proposed and tested for the correlation of telluric lines. These can be divided into three categories: those relying on observations of standard

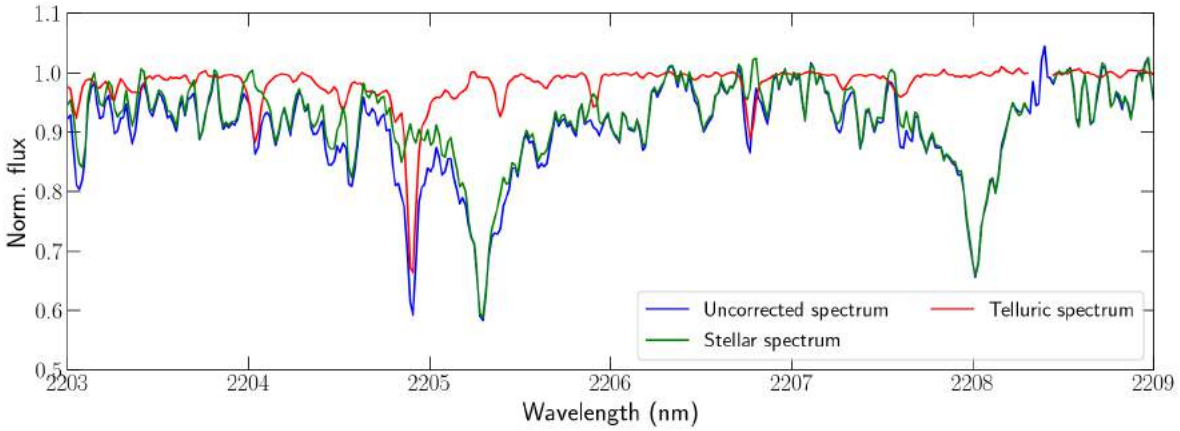

Figure 2.3. Same as Fig. 2.2 for small region of the K band featuring 2 Na lines at 2206.2 and 2208.9 nm.

stars, those attempting to build theoretical models of the atmosphere's transmission, and the data-driven approaches.

Standard stars

The most common approach to telluric lines correction is that relying on the spectra of standard stars. This method consists in observing hot, fast-rotating targets, typically O, B, or A stars (Vacca et al., 2003). The few lines resolved in the spectra of these stars are strongly broadened by rotation, rendering their identification easy. In contrast, telluric lines appear thin and are easily disentangled from stellar features. A typical spectrum of the Earth's atmosphere can therefore be constructed by removing the stellar features from the observation of the standard star. This correction technique is typically reliable and allows one to correct even small absorption features associated with the Earth's atmosphere. For this correction to be accurate, however, the acquisition of the spectrum of the standard and that of the target must be close in time and air mass, as weather conditions impact the relative strengths of telluric lines (Ulmer-Moll et al., 2019).

Theoretical modeling

In an attempt to improve the precision of telluric correction and motivated by the rapid evolution of theory, recent studies have proposed to develop models of the Earth's atmosphere transmission (Lallement et al., 1993; Seifahrt et al., 2010). In the past years, several tools were developed, such as TelFit (Gullikson et al., 2014), Molecfit (Smette et al., 2015) and TAPAS (Bertaux et al., 2014). These programs attempt to reproduce

the transmission spectrum of the Earth from theoretical knowledge of its composition and radiative transfer (Rudolf et al., 2016; Villanueva et al., 2018). Just like for the atmospheres of stars, these models provide many advantages, with the possibility to adjust absorption lines individually and account for various air masses and weather conditions. For the correction to be efficient, these models must accurately reproduce absorption features caused by the Earth's atmosphere, and inaccuracies in the modeling of telluric lines can lead to residuals in the corrected spectra, detrimental to radial velocity measurements and stellar analysis.

Data-driven approaches

Alternative techniques have been proposed to extract the Earth's atmosphere spectrum from data. In particular, Artigau et al. (2014) proposed to use the vast libraries of spectra of standard stars. They demonstrated that a principal component analysis (PCA) was an efficient approach to build models directly from the observation of standard stars. Alternative approaches have also been explored, taking advantage of the relative motion of telluric and stellar features in the observer's reference frame (see Sec. 2.2.3). This is the case of `wobble`, an open-source `Python` package tested for the correction of HARPS data (Bedell et al., 2019) modeling simultaneously the stellar and telluric spectra. Although this tool provides reliable results for M dwarfs spectra in the visible, it requires several tens of high-SNR spectra and has yet to be successfully applied to nIR data on intervals containing dense regions of telluric lines.

2.2 Modeling the Earth's atmosphere transmission

Given that the SPIRou spectra are systematically contaminated by telluric lines throughout the whole domain, singling out unaffected lines is not a viable option for most analyses. Instead, one needs to accurately disentangle the stellar and telluric spectra. `APERO` provides an efficient correction of telluric lines relying on standard stars observations acquired at multiple epochs and air mass. Nonetheless, SPIRou also provides data that are ideal to explore new approaches, as most targets have been monitored several tens of times throughout the years.

In this section, we describe an attempt to develop an alternative technique for telluric lines correction, which does not rely on the observation of standard stars, and inspired by the latest advances in modeling and the PCA-based approach (Artigau et al., 2014). For each observation, a model of the Earth's atmosphere spectrum is obtained in two

main steps: first by fitting a theoretical model (TAPAS; Bertaux et al., 2014) to the data, then by performing data-driven adjustments of the theoretical model with a PCA. The results presented in this section were published in Cristofari et al. (2022a).

2.2.1 The TAPAS model

2.2.1.1 A complete model of the atmosphere

To model the telluric lines, we extensively use TAPAS, a tool capable of computing the Earth's atmosphere transmission for a given line-of-sight and site. This program relies on data from the HITRAN database (Rothman et al., 2009, 2013) and computes the transmission of the atmosphere with the LBLRTM software (Clough & Iacono, 1995). TAPAS was designed to synthesize a telluric spectrum for specified atmospheric conditions but also offers the option to compute the transmission of individual molecules.

We downloaded the typical transmission profiles for O_2, H_2O, O_3, CO_2, CH_4 and NO_2 over the whole SPIRou wavelength domain (see Fig. 2.4). The resulting Earth's absorption spectrum can be computed by taking the product of all individual contributions adjusted by a power law. The spectrum is then convolved with a Gaussian profile to account for instrumental effects, and the expression used to compute it can be written as:

$$T = \left(T_1^{p_1}\ T_2^{p_2}\ T_3^{p_3}\ T_4^{p_4}\ T_5^{p_5}\ T_6^{p_6}\right) * G_\sigma \tag{2.1}$$

where T_X represents the transmission for the molecule X (1: H_2O, 2: CH_4, 3: CO_2, 4: NO_2, 5: O_2, 6: O_3), p_X is the adjusting power for X, and G_σ is the Gaussian broadening function of standard deviation $\sigma = 1.83$ km s^{-1}. To obtain the best possible fit, we also include two radial velocities, We introduce two radial velocities, one for the full spectrum and one specifically for water whose sensitivity to weather conditions is higher and for which high winds can induce shifts of up to 10 m $\cdot$ s^{-1} (Figueira et al., 2012).

2.2.1.2 Simplifying assumptions

With our model, we can obtain a typical synthetic spectrum of the Earth's atmosphere contribution to a given spectrum by fitting all 8 parameters. This process can be slow, and a few simplifying assumptions allow us to perform faster computations. We first assume that O_2, CO_2 and CH_2 are homogeneously distributed in the atmosphere and that their contribution to the spectrum only depends on air mass, which can be estimated for a given line of sight. Water vapor in the atmosphere is typically more sensitive to weather

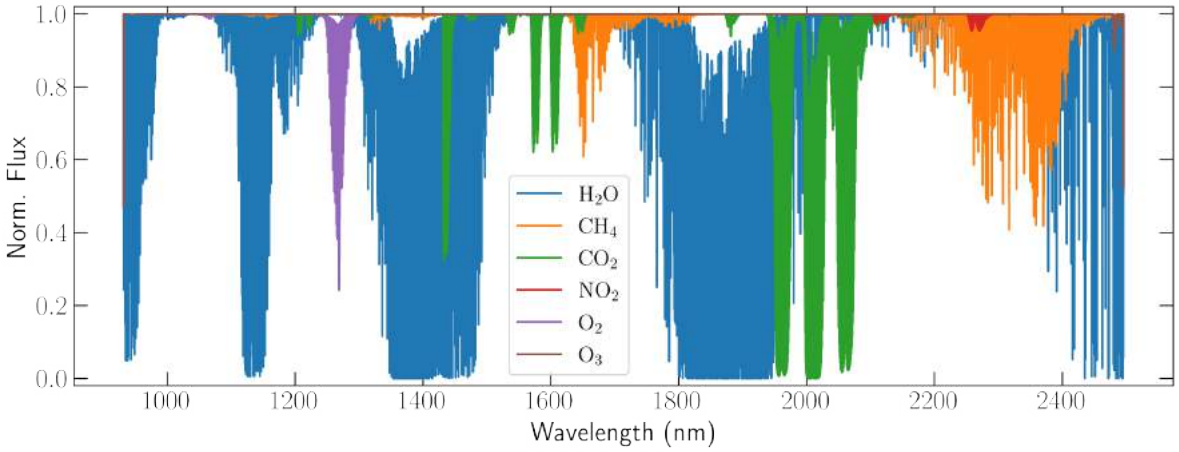

FIGURE 2.4. Typical TAPAS spectrum for each contributing molecule.

conditions, and its distribution is not as homogeneous as that of the other molecules. We consequently fit p_{H_2O}. Because of the small impact of O_3 and NO_2, we also choose not to fit their adjusting power, fixing their value to 1. Therefore, the full model requires to fit only three parameters: the two radial velocities and p_{H_2O}, the others being a function of airmass, or known from calibration spectra (G_σ).

2.2.2 Iterative optimization of the model

A first correction can be obtained by fitting the previously described model on the observed spectra and dividing the observations by the resulting modeled telluric spectrum. This first step is rarely sufficient, however, as the presence of stellar lines can influence the fitting process. To address the issue, we developed an iterative fitting process, illustrated by the first loop of the diagram presented in Fig. 2.5, and relying on the availability of tens of observed spectra acquired with various barycentric earth radial velocities (BERVs). This is the case for most SPIRou targets which are regularly monitored over the years since SPIRou started observing. We then use the fact that the position of telluric lines is expected to remain the same in the Earth's reference frame, while the position of stellar lines is nearly fixed in the barycentric reference frame.

After obtaining a first correction of the spectra, these are shifted to the stellar reference frame, and we compute the median spectrum, which we will refer to as the template spectrum. This template spectrum is expected to contain the typical stellar spectrum with residual contributions from the Earth's atmosphere. For each uncorrected spectra, the template spectrum is then shifted to the observer frame and used to remove the

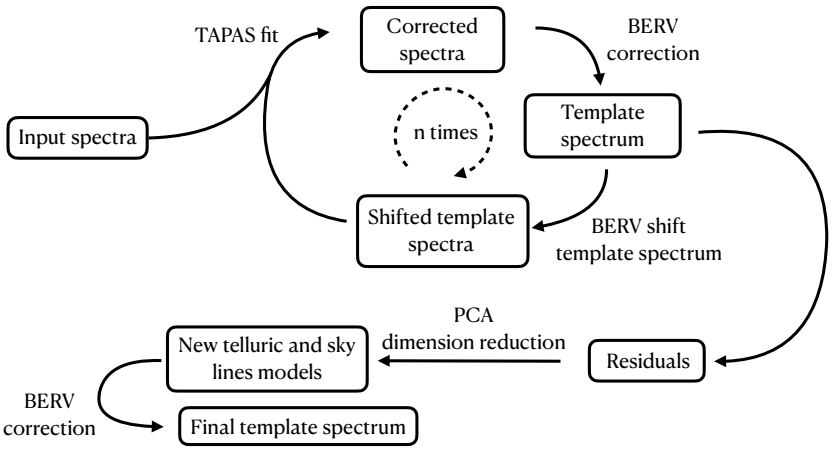

Figure 2.5. Iterative scheme used to derive template spectra from individual SPIRou spectra.

typical stellar spectrum from the observation. A new fit can be performed on the latter, expected to contain primarily telluric lines. The entire process can be repeated several times until the model parameters converge.

2.2.3 Data driven adjustment of the model

The first correction obtained with our model is likely to contain telluric lines residuals, as the shape of the telluric lines is not always ideally modeled. To improve our correction, we implement a second, data-driven step to the procedure.

The second step of the process, illustrated in Fig. 2.5, consists in adjusting the telluric models with a principal component analysis (PCA). PCA is performed on residuals computed by dividing the initial observation spectra by the telluric model and the template. The residuals are expected to contain noise and artifacts caused by improper corrections of telluric lines. Using the fact that we have tens of observations recorded at various BERV at our disposal, the PCA allows us to extract the signal associated with poorly corrected telluric features from the residuals. Taking the 3 to 5 components associated with the highest eigenvalues typically enables us to adjust the telluric model and improve the correction of telluric lines. Additionally, the PCA allows us to remove emission features from the sky (atmospheric airglow) that are not included in the TAPAS models and can be responsible for emission features.

Figure 2.6 presents an example of corrected stellar lines before and after telluric correction.

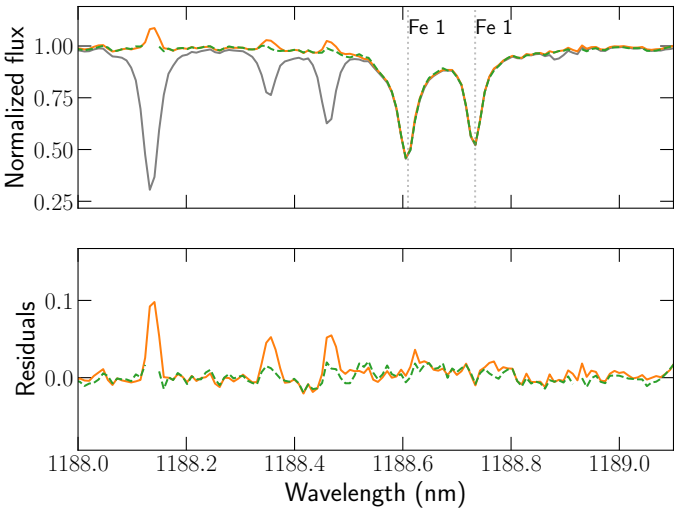

Figure 2.6. Example of correction for one of Gl 15A spectrum before and after correction of the telluric and sky lines. Top panel: The uncorrected spectrum (grey) features telluric lines removed following the TAPAS-based correction (orange). The PCA adjusted correction is shown in green. Telluric lines with absorption larger than 60 % are excluded prior to applying the PCA. Bottom panel: Corresponding residuals before (orange) and after (green) applying PCA.

2.2.4 On the limits of our telluric correction

Our method demonstrates the feasibility of accurately correcting telluric lines from synthetic models and data-driven adjustments without relying on standard stars. Nonetheless, this technique can only be applied to stars monitored several tens of times, with the broadest BERV coverage possible. It is, in particular, not applicable to single observations, for which `APERO` aims at providing corrected spectra.

One by-product of the telluric correction is the derivation of the high-SNR template spectra built from several tens of SPIRou spectra. These templates are built by taking the median of the final telluric-corrected spectra in the barycentric reference frame. In practice, we find that our computed templates agree well with those generated with `APERO`-processed spectra (see Fig. 2.7 for an example), and we choose to use either product for our analyses.

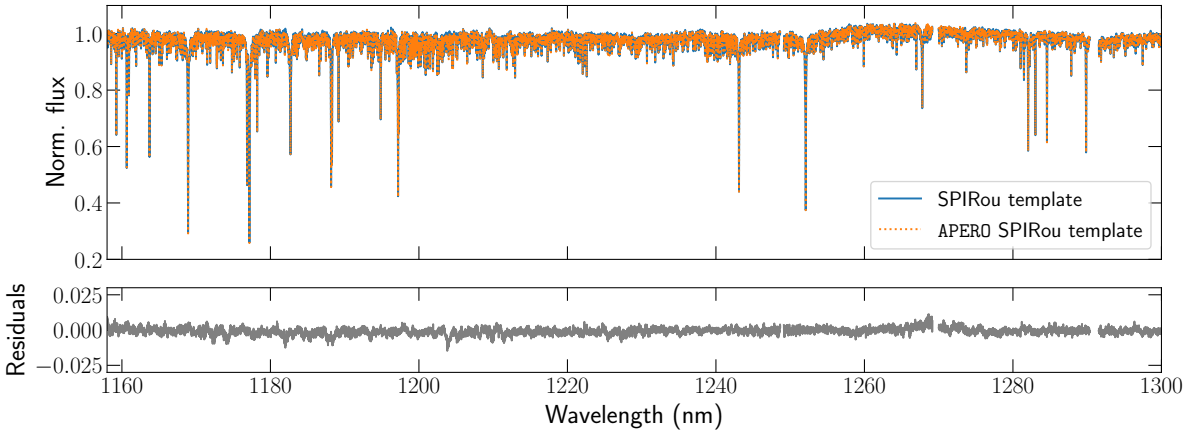

FIGURE 2.7. Comparison between our computed template spectrum and that obtained with APERO for Barnard's star (Gl 699). The bottom plot presents the residuals.

Chapter 3

Modeling stellar spectra

Contents

Stellar spectra carry valuable information on the properties of stars. The strength and shape of emission and absorption lines depend on numerous parameters, in particular on the effective temperature ($T_{\rm eff}$), surface gravity ($\log g$), metallicity ([M/H]), but also turbulence, rotation and magnetic fields. Studying stellar spectra allows astronomers to characterize the stars, but requires advanced models of stellar atmospheres, incorporating most physical processes taking place in these atmospheres. Several such models were developed over the last decades to compute synthetic spectra, relying on experimental data and theoretical results. In this chapter, we very briefly describe the main steps and ingredients needed to model a spectrum, from atmosphere models to instrumental effects, and refer the reader to Gray (2005) for a more detailed description. These steps typically rely on modeling the stellar photosphere (Sec. 3.1), obtaining atomic data (Sec. 3.2) and applying broadening effects to the synthetic spectra (Sec. 3.4).

3.1 Model photosphere

From an observer's point of view, only the outer layers of a star are visible: the light emitted from deep within the star is absorbed before it can escape. We introduce

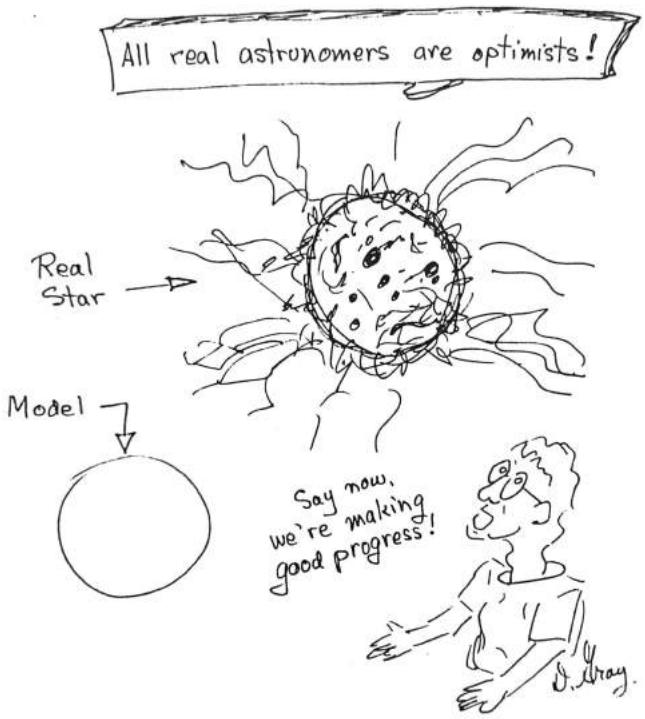

Cartoon by David F. Gray, taken from
Lectures on spectra-line analysis: F, G, and K stars.

the optical depth τ, which is a measure of how much a medium absorbs, as a useful quantity to scale the models. To synthesize spectra, several models concentrate on the stellar photosphere, and models such as `MARCS` were computed for optical depths ranging from $\tau \sim 10^{-5}$ to $\tau \sim 100$, while others, such as `PHOENIX-ACES`, were computed for optical depths ranging from $\tau \sim 10^{-10}$ to $\tau \sim 100$ (see Sec. 3.3). Synthetic spectra are computed by studying the absorption and emission of radiation throughout the photosphere.

3.1.1 Basic assumptions

A model atmosphere consists of a set of physical quantities (such as temperature, electron density, or gas pressure) given as a function of optical depth. Capturing the full complexity of the stellar photosphere can be challenging and requires a large amount of computation time. Several assumptions can simplify the problem. Let us briefly recall some of the most common:

- **Local thermodynamic equilibrium** – One usually assumes that the photospheric plasma is in thermodynamic equilibrium. This assumption does not apply to the photosphere as a whole since there is a substantial temperature gradient throughout the photosphere. Still, it can be used for small volumes of a stellar atmosphere. Within this volume, local thermodynamic equilibrium (LTE) allows one to compute the occupation of energy levels from a Boltzmann distribution, and to estimate the density of ionized atoms through Saha's equation, given a local temperature and pressure. The quantity of light emitted by the medium also obeys Planck's law and only depends on temperature.
- **Hydrostatic equilibrium** – One generally assumes that the photosphere is in hydrostatic equilibrium, as it is not subject to large-scale accelerations inwards or outwards, as the star does not expand or contract.
- **1-dimensional & plane-parallel geometry** – Stars are often assumed to be isotropic, so the pressure and temperature conditions in the photosphere only depend on altitude (or distance below the surface). Thus, these properties can be described for one dimension only. Because the typical photosphere of MS stars is thin compared to the stellar radius, one can additionally represent the stellar photosphere as a succession of parallel planes through which light passes, neglecting any spherical effect.

LTE is typically considered valid as collisions remain the dominant source of atomic transitions. Recent advances in stellar modeling have shown that non-LTE (NLTE) effects can impact stellar spectra (Olander et al., 2021), and several models implemented additional steps to incorporate corrections from LTE computations (Gerber et al., 2022).

In practice, the photosphere is subject to motion caused by convection and differential rotation. Some models today include hydrodynamic considerations in 3D models, requiring significant computation time but allowing for the incorporation of time-dependent phenomena (Magic et al., 2013).

3.1.2 Radiative transfer & model convergence

3.1.2.1 Radiative transfer

Computing a synthetic spectrum from a model atmosphere consists in determining the quantity of light absorbed and emitted by each atmospheric layer. Consider a radiation of frequency ν traveling through a medium of absorption coefficient κ_ν and emission

coefficient j_ν. The theory of radiative transfer states that the change in specific intensity is then the sum of the absorbed and emitted intensities, and can therefore be expressed as (Gray, 2005):

$$\mathrm{d}I_\nu = \kappa_\nu \rho I_\nu \mathrm{d}s + j_\nu \rho \mathrm{d}s$$

with ρ the density of matter in the medium, and $\mathrm{d}s$ is the infinitesimal length element traveled by light. By defining the optical depth as $\tau_\nu = \int_0^s \kappa_\nu \rho \mathrm{d}s$, we can rearrange the previous equation to:

$$\frac{\mathrm{d}I_\nu}{\mathrm{d}\tau_\nu} = -I_\nu + S_\nu$$

where S_ν is the source function, defined as the ratio between the emission and absorption coefficients. This is the general form of the radiative transfer equation one typically needs to solve in order to know how much light will be received from a star. Solving this equation requires some prior knowledge of the absorption coefficients of the photosphere κ_ν (see Sec. 3.2) and of the source function S_ν. Under the LTE approximation, the source function of a small volume can be set to the Planck function, $B_\nu(T)$, which only depends on the local temperature T.

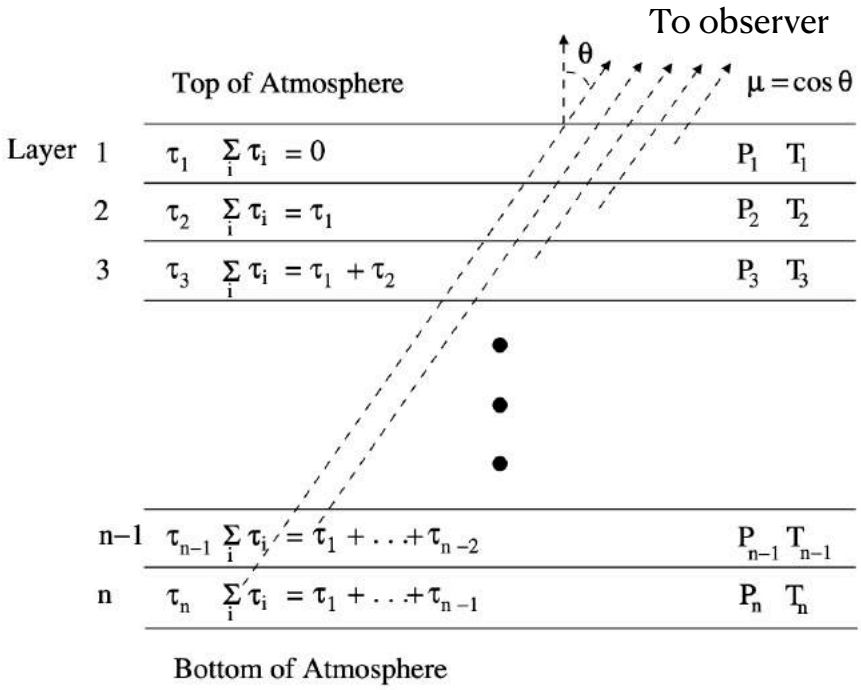

Figure 3.1. Schematic representation of a plane parallel atmosphere. Adapted from Dr. Brigette Emily Hesman's PhD thesis. https://www.researchgate.net/publication/253391065_The_Abundance_of_Carbon_Monoxide_in_Neptune's_Atmosphere

In practice, stars are spherically shaped, and the light received from the center of the stellar disk probes deeper layers of the atmosphere than that received from the edges of the stellar disk. Solving the radiative transfer equation for a star requires to account for geometry: in the case of spherical stars, one needs to express I_ν as a function of the limb angle θ, which is the angle between the normal to the stellar surface and the line-of-sight. The plane-parallel atmosphere allows one to simplify the problem by neglecting spherical effects and only accounting for θ (see Fig. 3.1), re-writing the transfer equation as:

$$\cos\theta \frac{\mathrm{d}I_\nu}{\mathrm{d}\tau_\nu} = I_\nu - S_\nu$$

where the signs of I_ν and S_ν were inverted to comply with usual conventions, defining a depth running from the stellar surface towards the center of the star. One can then estimate the flux of a non-resolved star by dividing the stellar disk into a number of disk elements (typically $\sim 500 - 1000$), and computing the emergent spectrum for each of them, assuming a given limb angle. The stellar flux is then obtained by summing the contributions of all the disk elements.

3.1.2.2 Model convergence

To compute a model atmosphere with the previously mentioned assumptions, one must solve the hydrostatic equation, providing a relation between the pressure and optical depth:

$$\frac{\mathrm{d}P}{\mathrm{d}\tau_\nu} = \frac{g}{\kappa_\nu}$$

with g the gravity and κ_ν the absorption coefficient at frequency ν.

This, however, requires knowledge of the temperature and pressure gradient as a function of optical depth in the photosphere, which is necessary to compute the absorption coefficients. The computation of most models today relies on an iterative process checking for flux constancy:

(1) The model starts from an initial guess on the source function, which can be estimated from a study of the solar disk.
(2) The model then varies the source function slightly, computes the emergent spectrum and compares the flux to that expected from effective temperature.
(3) The previous step is repeated so long as the deviation remains larger than a given threshold (typically a few % of the total flux).

The convergence of model atmospheres can be slow as it requires solving the radiative transfer equation at each step. In order to perform faster computations, some models rely on opacity distribution functions (ODF) (Kurucz, 2017), while others rely on opacity sampling (OS) (Kurucz, 2005). The latter is generally considered to produce more reliable results (Plez, 2011).

3.2 Line lists and opacities

To compute a model atmosphere and an emergent spectrum, it is essential to obtain an estimate of the absorption coefficients of the photosphere. This requires prior knowledge of the composition of stars and of the processes at the origin of absorption. These coefficients are typically divided into two groups, with those contributing to the overall shape of the spectrum on the one hand, that are essential to the proper convergence of the model atmosphere. On the other hand, we have the coefficients responsible for the formation of spectral lines, which may be omitted for the computation of the atmosphere, but are obviously essential to the synthesis of high-resolution synthetic spectra.

3.2.1 Continuous opacity

Two main processes are at the origin of continuum absorption: the free-free transition depicting the acceleration of a charged particle passing by another charge and the bound-free transition corresponding to the ionization process. The total continuous absorption coefficient is the sum of these contributions for the considered elements. Hydrogen is the most abundant element in stars and is responsible for most of the continuous absorption. For stars with $T_{\rm eff} < 4000$ K, the influence of negative hydrogen ions is significant, and shapes the continuum of M dwarfs spectra. Bound-free transitions of H^-, producing neutral H, can only occur for wavelengths shorter than ~ 1644 nm (Doughty et al., 1966). At longer wavelengths, free-free transitions become the main contributor to continuous absorption in cool stars (Doughty & Fraser, 1966). This transition occurs in the middle of the SPIRou wavelength domain and is therefore visible when modeling spectra from 950 to 2500 nm (see Fig. 3.2).

Other sources of continuous absorption can involve hydrogen molecules, helium or even metals (Somerville, 1964; Peach, 1970). Line opacities are not typically included in the computation of continuous absorption coefficients, but may be considered, as the collective effect of absorption lines can influence the computation of temperature profiles in the model

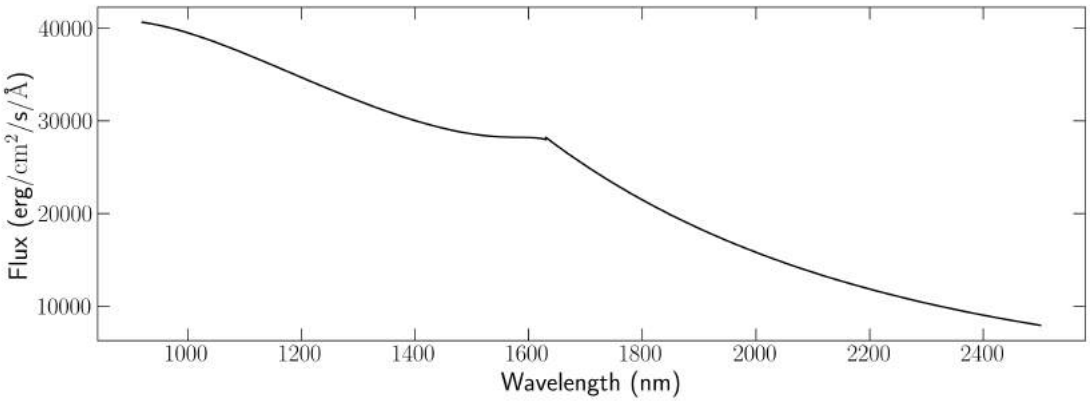

Figure 3.2. Example of continuum flux computed with Turbospectrum from a MARCS model atmosphere over the entire wavelength range covered by SPIRou. The discontinuity observed in the middle of the profile results from the end of H^- bound-free transitions.

atmospheres. For this purpose, data for millions of lines have been compiled (Kurucz, 1979) and revised over the years. Today, the VALD database (Piskunov et al., 1995; Kupka et al., 2000; Pakhomov et al., 2019) provides an extensive compilation of atomic and molecular data.

3.2.2 Line absorption coefficients

Line shapes arise from the specific absorption of light at given wavelengths as the result of bound-bound transitions. Absorption lines are not infinitely narrow: the natural width of these lines can be interpreted as the result of the Heisenberg principle, and the "natural shape" of the line is Lorentzian (Gray, 2005). The width of a line depends on the probability for the associated transition to occur, quantified by a dimensionless parameter called 'oscillator strength' ($\log gf$). The value of $\log gf$ can be predicted by theory for some transitions, but is generally obtained through laboratory experiments, or when data is unavailable, from comparisons of models to observations.

The atoms in the photosphere are located in a medium at high temperature and pressure, and such an environment induces additional broadening of the spectral lines. Four effects are especially relevant:

(1) The thermal broadening resulting from the temperature of the medium, typically modeled by a Gaussian profile.
(2) The microturbulence particularly significant for strong lines, and often considered as turbulence on scales comparable to the length of the 'line forming

region' (Edmunds, 1978; Cantiello et al., 2009). Microturbulence is often modeled by a Gaussian distribution of velocity fields, adding to the effect of thermal broadening (Struve & Elvey, 1934).

(3) The stark broadening, arising from the splitting of energy levels in the presence of an electric field, induced locally by the collision between charged particles.

(4) The Van Der Waals broadening describing the interaction with neutral particles, and in particular with neutral hydrogen. Recent advances in the description of these interactions have given birth to alternative theories meant to replace previous Van Der Waals damping parameters, such as described in Barklem et al. (2000).

Van der Waals parameters (γ_6), like $\log gf$, must typically be derived experimentally, and uncertainties on its value may result in discrepancies between synthetic spectra and observations.

Microturbulent velocity is difficult to constrain and several codes tend to assume a value for the convergence of their model atmospheres (Allard & Hauschildt, 1995; Hauschildt et al., 1999). Recent works have proposed temperature-dependent laws for microturbulent velocity and used these to compute model atmospheres and synthetic spectra (Husser et al., 2013). In the 3000 – 4000 K temperature range, such relations typically suggest a microturbulent velocity lower than 1 km s^{-1}. When computing grids of synthetic spectra from `MARCS` model atmospheres, I therefore adopt a 1 km s^{-1} microturbulent velocity.

Finally, the presence of magnetic fields in stars can also impact line opacities through the so-called Zeeman effect, which will be discussed in Chapter 6 when I present my implementation of `ZeeTurbo`.

3.3 Available tools

A variety of model atmospheres

Several codes were developed and improved in the past decades to compute model atmospheres and synthetic spectra. Let us in particular mention three of the most well-known tools for model atmosphere computations:

- `ATLAS` (Kurucz, 1970) was developed in the 1970s and has been updated several times since. Some of the latest versions of `ATLAS` include `ATLAS9` and `ATLAS12` (Castelli & Kurucz, 2003; Sbordone et al., 2007). The main difference

between the two is that ATLAS9 relies on opacity distribution functions (ODF) while ATLAS12 relies on opacity sampling (OS) with 30000 points.

- MARCS (Gustafsson et al., 1975) was developed in the mid-1970s and largely revised since (Plez, 2008, for a review of the developments). Today MARCS relies on OS with more than 10^5 wavelength points.
- PHOENIX was developed in the 1990s (Hauschildt, 1992; Allard & Hauschildt, 1995; Hauschildt et al., 1997) and is more general than ATLAS or MARCS. Several versions of the codes were developed, and grids of model atmospheres and synthetic spectra were published covering brown dwarfs (Allard et al., 2012) to supernovae (Baron et al., 2009). In order to cover all these cases, PHOENIX allows one to choose between plane-parallel or spherical model atmospheres (Husser et al., 2013).

A variety of spectral synthesis codes

PHOENIX is the only of the three codes designed to compute model atmospheres and emergent spectra at high-resolution. In contrast, complementary codes such as SYNTHE (Kurucz, 2005) and Turbospectrum (Alvarez & Plez, 1998) were developed to compute spectra from ATLAS and MARCS model atmospheres, respectively. Alternative tools were developed for the computation of synthetic spectra from MARCS model atmospheres, such as SPETRUM Gray & Corbally (1994), SME (Valenti & Piskunov, 1996), MOOG (Sneden et al., 2012) or Zeeman (Landstreet, 1988; Wade et al., 2001).

These tools were developed with different assumptions, chemical equilibrium, and numerical approaches (see Blanco-Cuaresma, 2019, for a summary of the main differences). For instance, MOOG does not recompute electron density, while other codes such as Turbospectrum, SME or SYNTHE do. Turbospectrum or MOOG were developed specifically for fast synthesis across large wavelength ranges. While Turbospectrum and SME are capable of handling 1D spherical model atmospheres, SPECTRUM, SME, SYNTHE and Zeeman do not. Finally, most codes do not support NLTE departure coefficients, but SME and the latest version of Turbospectrum (Gerber et al., 2022) do.

Choosing models and computing synthetic spectra

For our purposes, we need high-resolution synthetic spectra with accurate line parameters that best reproduce nIR observations. We choose to focus on MARCS and PHOENIX model atmospheres, as ATLAS models were not computed for $T_{\rm eff} < 3500\ K$, and we aim at

characterizing stars in the range $3000 < T_{\rm eff} < 4000$ K. Furthermore, significant deviations were reported between `ATLAS` and the other two codes for $T_{\rm eff} < 4000$ K (Plez, 2011).

While the `PHOENIX` code is not publicly available, several grids of model atmospheres and synthetic spectra were published and made available to the public[1,2]. For this work, I downloaded synthetic spectra from the latest grid of spectra released (Husser et al., 2013), which was computed from one of the latest versions of the `PHOENIX` code, often referred to as `PHOENIX-ACES`.

`MARCS` model atmospheres are available for public download[3], and its official companion for spectral synthesis, `Turbospectrum`, is freely distributed on GitHub[4]. For this project, I downloaded `Turbospectrum`, and computed a grid of synthetic spectra ranging from 3000 to 4000 K in $T_{\rm eff}$, -1.5 to $+0.5$ dex in [M/H], and 3.0 to 6.0 dex in $\log g$, covering the typical range of parameters expected for M dwarfs. This grid, along with that of `PHOENIX-ACES` models, was used in our initial study published in Cristofari et al. (2022a).

3.4 Broadening

The steps undertaken in Sec. 3.1 allow one to obtain the spectrum expected for a non-rotating star. In order to compare synthetic spectra to observations, we must account for additional broadening of the spectral lines, mainly due to stellar rotation and movements of convective cells in the photosphere. In this Section, we discuss rotation and macroturbulence, assuming non-magnetic models. Magnetic fields will be discussed in Chapter 6 with our implementation of `ZeeTurbo`.

Macroturbulence

Macroturbulence arises from turbulence in the stellar atmospheres. First introduced to explain the observed non-rotational broadening of spectral lines, it was initially described as being isotropic, and approximated by the convolution of synthetic spectra with a Gaussian kernel. It was later proposed that the effect arises from anisotropic velocities as the result of convective cells. This alternative description of macroturbulence, called radial-tangential macroturbulence (Gray, 1975), offers to divide the cells in radial and

[1] http://svo2.cab.inta-csic.es/theory/newov2/
[2] http://phoenix.astro.physik.uni-goettingen.de/
[3] https://marcs.oreme.org/
[4] https://github.com/bertrandplez/Turbospectrum_NLTE

tangential flows, resulting in the following expression:

$$\Theta(\Delta\lambda,\theta) = \frac{\mathrm{A_R}}{\pi^{1/2}\zeta_\mathrm{R}\cos\theta}\exp\left[-\left(\frac{\Delta\lambda}{\zeta_\mathrm{R}\cos\theta}\right)^2\right] + \frac{\mathrm{A_T}}{\pi^{1/2}\zeta_\mathrm{T}\sin\theta}\exp\left[-\left(\frac{\Delta\lambda}{\zeta_\mathrm{T}\sin\theta}\right)^2\right]$$

with θ the angle between the line of sight and the normal to the stellar surface, $\mathrm{A_R}$ and $\mathrm{A_T}$ are the factors accounting for the relative weight of radial and tangential flows, ζ_R and ζ_T are radial and tangential velocities respectively, and $\Delta\lambda$ is the relative distance to the central wavelength of the line.

Because of the dependence on θ, radial-tangential macroturbulence should be applied to each disk element prior to disk integration. A typical disk-integrated profile is shown in Fig. 3.3. However, the value of macroturbulence is not usually known prior to integration, and disk element spectra are not always stored. Radial-tangential macroturbulence is therefore sometimes applied as a post-processing step by convolution of a fiducial profile with the disk-integrated spectrum. One common assumption is to consider the radial and tangential components to be equal in strength, hence writing $\zeta_\mathrm{R} = \zeta_\mathrm{T}$ and $\mathrm{A_R} = \mathrm{A_T}$. In the case where no limb darkening is considered, an analytical calculation of the Fourier transform of radial-tangential macroturbulence was derived by Durrant (1979).

Although radial-tangential macroturbulence was introduced as a more physically motivated alternative to isotropic macroturbulence, recent investigation with comparison to the solar spectrum found discrepancies with observations (Takeda & UeNo, 2017).

Rotation

Macrotuburlence was historically introduced to explain the broadening of spectral lines of slowly rotating stars. Indeed, stellar rotation significantly contributes to line broadening because all points of the stellar disk of rotating stars do not have the same radial velocity. From an observer's point of view, one side of the star is overall blue-shifted, while the other side is red-shifted. In practice, an observer cannot differentiate between a slowly rotating star and a fast rotator with a titled rotation axis. To account for observations, it is therefore useful to define the projection of the equatorial velocity on the line of sight, $v\sin i$, with i the angle between the rotation axis and the line-of-sight.

Just like radial-tangential macroturbulence, a full description of rotation would require to compute the radial shift on each disk element before disk integration. One approximation consists in dividing the stellar disk in a series of stripes and computing the expected profile for rotation (see Gray, 2005, for a detailed derivation). Rotation can then be accounted for by convolving the spectrum with the rotation profile. One can approximate the effect

of limb darkening by assuming a limb darkening law of the form $I_c/I_c^0 = 1 - \epsilon + \epsilon \cos\theta$, with I_c^0 the intensity at the center of the stellar disk, θ the limb angle, and ϵ the limb darkening coefficient.

The full expression of the rotation then becomes (Gray, 2005):

$$G(\Delta v) = \frac{2(1-\epsilon)\sqrt{1-(\Delta v/v_L)^2} + (\pi\epsilon/2)[1-(\Delta v/v_L)^2]}{\pi v_L(1-\epsilon/3)}$$

where Δv is the velocity shift induced by rotation, ϵ is the limb darkening coefficient, and v_L is the projected velocity at the limbs, commonly labeled $v \sin i$.

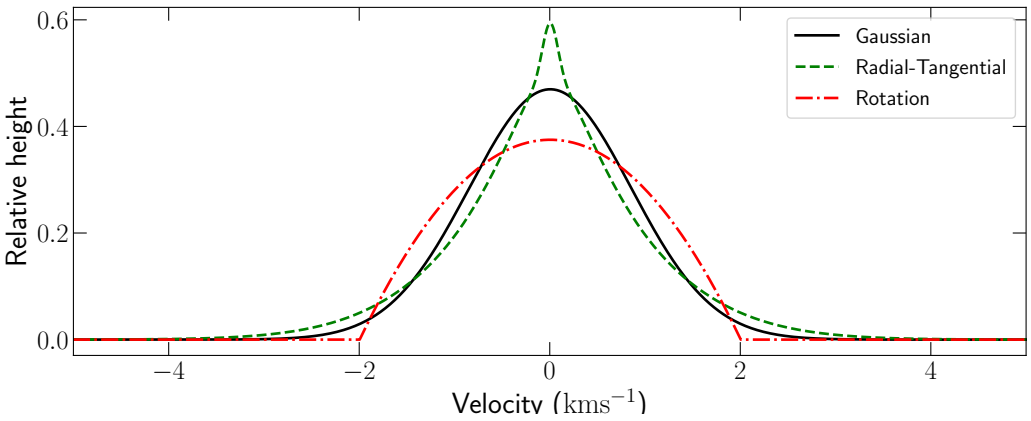

FIGURE 3.3. Comparison between the broadening kernels typically considered. All profiles were normalized. A value of 2 km s^{-1} was assumed for the rotation velocity, radial-tangential macroturbulent velocity and for the full width at half maximum of the Gaussian profile.

Chapter 4

Estimating the fundamental parameters of key reference stars

Contents

4.1 Context

Accurately estimating the fundamental properties of M dwarfs is essential to characterize planets orbiting these stars or to study their magnetic fields. As mentioned in the Chapter 1, several techniques were developed to constrain the effective temperature ($T_{\rm eff}$), surface gravity ($\log g$) and overall metallicity ([M/H]), such as the adjustment of equivalent widths of spectral lines (Rojas-Ayala et al., 2010; Neves et al., 2014; Fouqué et al., 2018), fitting spectral energy distributions (SEDs) on low to mid-resolution spectra (Mann et al., 2013), or fitting synthetic models on high-resolution spectra (Passegger et al., 2018, 2019; Schweitzer et al., 2019; Marfil et al., 2021). The latter is presumably the best option,

especially in the nIR domain which can be contaminated by telluric lines, as it allows us to extract information from the stellar line profiles themselves.

Despite the community's best efforts, significantly different values of $T_{\rm eff}$, $\log g$, and [M/H] were reported in the literature for M dwarfs, as illustrated in Fig. 4.1 and recently discussed in Passegger et al. (2022). Such discrepancies arise from differences in the methods and calibrations used. Interestingly, independent studies performing fits of synthetic spectra on high-resolution data also sometimes report different stellar parameters for the same star. This can be attributed to the choice of model the analysis relies on, assumptions on line broadening sources, normalization, or the selection of lines. The nIR domain is particularly challenging to model because of the large density of atomic and molecular lines for which fundamental parameters (such as oscillator strengths and Van der Waals parameters) are not always accurately known.

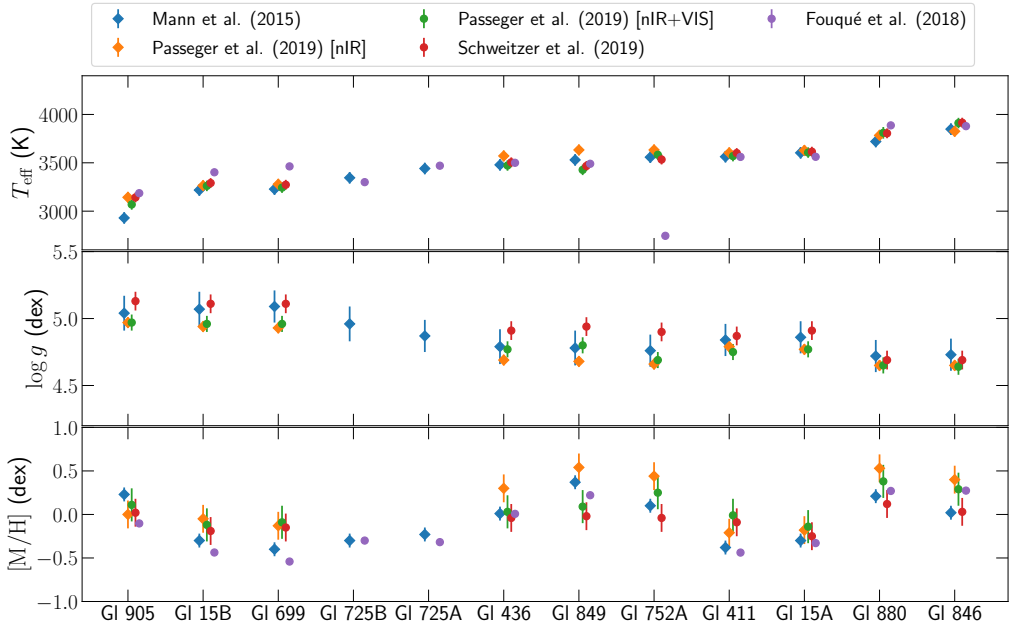

Figure 4.1. Parameters reported by several studies (Mann et al., 2015; Fouqué et al., 2018; Passegger et al., 2019; Schweitzer et al., 2019) for 12 M dwarfs observed in the context of the SLS.

In this chapter, we present an analysis developed for the characterization of M dwarfs from SPIRou spectra, relying on synthetic spectra computed from state-of-the-art model atmospheres (see Sec. 4.2). We select a small sample of extensively studied M dwarfs to guide our modeling strategy and carefully select spectral lines of interest to our work (Sec. 4.3 & 4.4). In Sec. 4.5, we describe a benchmark carried out to simulate the

estimation of M dwarfs atmospheric parameters and to assess the differences between synthetic spectra computed from `PHOENIX` and `MARCS` model atmospheres. We then use our tools to estimate $T_{\rm eff}$, $\log g$, and [M/H] for the stars in our sample and compare our results to those reported in the literature (see Sec. 4.6). The results presented in this chapter were published in Cristofari et al. (2022a, see Appendix A).

4.2 A χ^2 minimization approach

Our analysis relies on the direct comparison of synthetic spectra to SPIRou templates (see Sec. 2). The quality of the fit is estimated by the computation of a χ^2 value after adjusting the continuum and including broadening effects. We then search for the model leading to the best χ^2, and estimate the curvature of the χ^2 hyper-surface at the vicinity of the minimum to estimate error bars on the optimal parameters. To perform this comparison, we must first obtain a grid of synthetic spectra computed for a range of $T_{\rm eff}$, $\log g$ and [M/H].

4.2.1 Two grids of synthetic spectra

We present the results obtained with two grids of synthetic spectra computed from two distinct model atmospheres that we briefly introduce here.

A grid of `PHOENIX-ACES` models

The latest published grid of `PHOENIX` synthetic spectra is described in Husser et al. (2013), often referred to as `PHOENIX-ACES` for its use of the `ACES` equation of state. This grid was published with the specific goal to cover a large range of spectral types, from MS stars to giants; it was therefore computed in spherical geometry to ensure self-consistency throughout the entire parameter space. The published spectra range from 2300 K to 12000 K in $T_{\rm eff}$, from -4.0 to $+1.0$ dex in [M/H] and from 0.0 to 6.0 dex in $\log g$, hence extending way beyond our needs for the study of M dwarfs. In particular, we will focus on models computed with $T_{\rm eff}$ below 4000 K, for which LTE was assumed throughout the entire grid. The published grid of synthetic spectra are *not* normalized, forcing us to perform this normalization manually before using the synthetic spectra.

A grid of MARCS models

A second grid of spectra was computed with Turbospectrum from MARCS model atmospheres. The computations were performed assuming a 1D plane-parallel geometry, for $T_{\rm eff}$ ranging from 3000 K to 4000 K. For each $T_{\rm eff}$ we computed models with $\log g$ ranging from 3.0 to 6.0 dex and [M/H] ranging from -1.5 to +0.5 dex, covering the parameters typically expected for M dwarfs and PMS stars. Table 4.1 summarizes the ranges of parameters covered by both grids.

Table 4.1. Coverage of the synthetic spectra grids in $T_{\rm eff}$, $\log g$, [M/H] and step size on each parameter.

Model	$T_{\rm eff}$ (K)	$\log g$ (dex)	[M/H]
PHOENIX	2300 – 7000 [100]	0.0 – 6.0 [0.5]	-2.0 – $+1.0$ [0.5]
MARCS	3000 – 4000 [100]	3.0 – 6.0 [0.5]	-1.5 – $+0.5$ [0.25]

4.2.2 Fitting synthetic spectra to observation

Instrumental width & normalization

By design, spectrometers are limited by instrumental effects, limiting their resolving power. Optical systems, gratings or slits broaden the spectral lines, and their collective effect gives rise to an instrumental profile. This profile can be estimated experimentally by the observation of intrinsically narrow lines. In the case of SPIRou, with a resolving power estimated to $\sim$ 70000, lines are broadened by a Gaussian-like profile of full width at half maximum (FWHM) $\sim$ 4.3 km s^{-1}. In practice, the instrumental profile of SPIRou is not strictly Gaussian but we work under this hypothesis for our analysis. Furthermore, the instrumental profile varies throughout the SPIRou wavelength domain, but we choose to model it by a single profile of fixed FWHM.

For the purposes of high-resolution spectroscopy, it is convenient to normalize spectra by setting the continuum to 1, in order to compare line depths, widths, and shapes relative to the continuum. This step is however not trivial (Cretignier et al., 2020), particularly for late-type stars in the nIR domain. The high density of spectral lines makes the identification of continuum points difficult. Some regions are so densely populated by spectral lines that the continuum is no longer visible: there are locally no points belonging to the continuum. Such effect is particularly visible in normalized synthetic spectra over the SPIRou domain, where large absorption bands affect the apparent continuum (see

Fig. 4.2). It is therefore important to accurately adjust the continuum of observed spectra to that of the models (Sarmento et al., 2021).

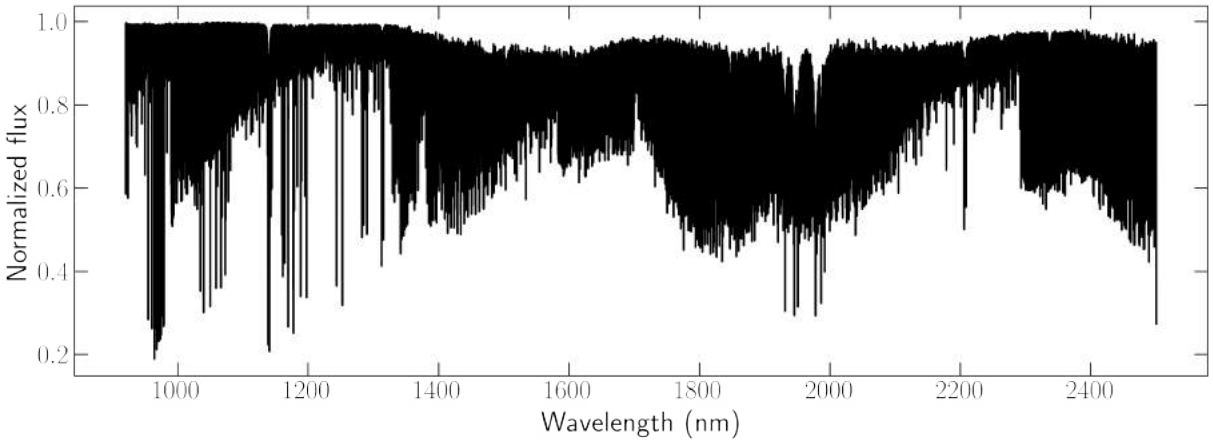

FIGURE 4.2. Example for normalized spectrum computed with Turbospectrum from a MARCS model atmosphere for the full SPIRou wavelength range. This model was computed for $T_{\rm eff} = 3200$ K, $\log g = 5.0$ dex and [M/H] $= -0.5$ dex.

Adjusting the continuum

Because normalization is particularly critical to our work, I implemented an adjustment procedure aimed at locally bringing the continua of SPIRou spectra and synthetic models to the same level. This post-processing step is applied to small spectral regions containing the absorption lines of interest to our analysis (see Sec 4.4). Prior to this correction, all SPIRou templates were normalized by fitting a polynomial on each spectral order.

We define a window around our selected lines (see Sec. 4.4) and assume it is small enough for the local continuum to be approximated by a line. We then search for the points belonging to the continuum within this window. Our process is likely to be affected by emission and absorption features, whether these result from the star or poorly corrected telluric lines. To avoid selecting bins within emission lines, we define 400 bin windows around the targeted absorption lines and reject all points above the $99^{\rm th}$ percentile. We find this threshold is typically sufficient to remove the very thin emission features observed in the spectra. We then divide the window into 40-bin regions, in which we label all points above the $95^{\rm th}$ percentile as belonging to the continuum. The final step of the adjustment consists in fitting a line through the selected continuum points. When comparing SPIRou spectra to synthetic models, the same process is applied to both spectra and used to bring their continua to the same level.

The presented procedure was tailored specifically for M dwarfs spectra recorded with SPIRou, and are the result of several tests and adjustments. The number of bins and choice of upper and lower limits can be adjusted to any specific case.

Obtaining a first estimate

Starting from the initial sparse grid of synthetic spectra computed from either `MARCS` or `PHOENIX` model atmospheres, we compute a 3-dimensional grid of χ^2 values and search for its minimum. This first step allows us to obtain a rough estimate of the atmospheric parameters leading to the best fit. To identify the minimum with greater precision, we interpolate the grid of spectra around the minimum down to steps of 5 K in $T_{\rm eff}$ and 0.01 dex in $\log g$ and [M/H], and compute a new χ^2 grid. For each point of the grid, before computing a χ^2 value, we convolve the synthetic spectrum to account for the instrumental width, macroturbulence, and rotation, and adjust its continuum to fit the observation template as accurately as possible. In practice, we choose to approximate all broadening contributions by a Gaussian profile as we found that the shape of the kernel has little impact on our results with the current setup. Furthermore, we estimate that for most stars, the FWHM of the Gaussian broadening leading to the best χ^2 was of ~ 3 km s^{-1}, and that deviations about this value had a negligible effect on our results at this stage, as most of the stars in our sample have low $v \sin i$. We therefore fixed its value to 3 km s^{-1} for the rest of our analysis.

Estimating error bars

Once a 3-D χ^2 surface is computed around the estimated minimum, we fit a 3-D paraboloid on the 500 points bearing minimal χ^2 values. This number of points was chosen as it is typically sufficient to capture the local curvature of the χ^2 surface around its minimum. From this fit, we derive optimal values of $T_{\rm eff}$, $\log g$ and [M/H] corresponding to the position of the minimum of the paraboloid, and associated error bars from the curvature of the paraboloid (see Fig. 4.3). Assuming that noise obeys a Gaussian distribution, one can estimate the 1 σ confidence intervals by drawing the ellipsoid in which χ^2 increases by no more than 1 around the minimum and projecting the contour on each parameter axis (Press et al., 1992). In practice, the minimum reduced χ^2 (χ^2_r) value is significantly larger than one, as a result of systematic differences between the modeled spectra and the SPIRou templates. In an attempt to account for some of the systematic differences between the models and templates, we divide the χ^2 values by the minimum reduced χ^2 value ($\chi^2_{\rm r,min}$), effectively forcing its value to be 1, and consequently enlarging the

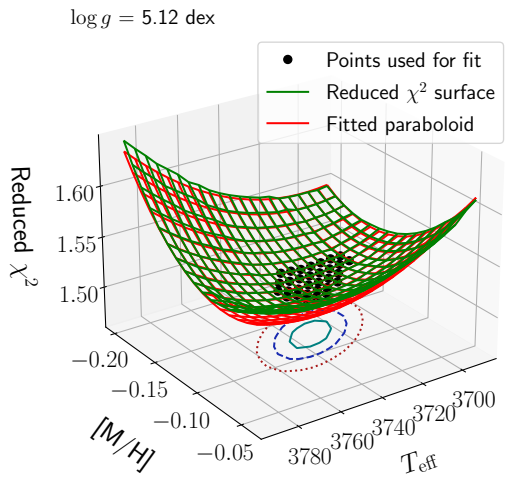

FIGURE 4.3. Typical computed χ^2 surface and the obtained parabolic fit. Projected contours for the 1 σ (solid green), 2 σ (dashed blue) and 3 σ (dotted red) confidence interval are shown on the [M/H]–$T_{\rm eff}$ plane.

error bars estimated from the paraboloid fit by a factor of $\sqrt{\chi^2_{\rm r,min}}$. In the rest of this manuscript, these enlarged error bars will be referred to as 'formal error bars'.

4.3 Choosing a sample of M dwarfs

In this first step, we concentrate our efforts on a small number of reference stars with different parameters, aimed at being a representative sample of the targets monitored with SPIRou. To this end, we select 12 M dwarfs, with effective temperatures ranging from 3000 to 4000 K, which encompasses most stars of interest to the SLS. Our sample also includes targets with high and low metallicities, which is ideal for testing our method. In particular, we include two binary stars whose components are expected to have similar [M/H]. The stars in our sample are expected to be no more than weakly active (Fouqué et al., 2018; Schöfer et al., 2019) and were monitored several tens of times over several months, allowing us to build high-SNR templates for each of them. Finally, for all of these stars, several estimates of $T_{\rm eff}$, $\log g$, and [M/H] were reported by different literature studies. For all 12 reference targets, we summarize the parameters reported by a few recent publications in Table 4.2.

Table 4.2. Atmospheric parameters for our 12 reference stars reported by Mann et al. (2015) (1), Passegger et al. (2019) (2) and Marfil et al. (2021) (3).

Star	$T_{\rm eff}$	$\log g$	[M/H]	Ref.
Gl 846	3848.0 ± 60	4.74 ± 0.05	0.02 ± 0.08	(1)
	3911.0 ± 54	4.64 ± 0.06	0.29 ± 0.19	(2)
	3882.0 ± 12	4.97 ± 0.07	-0.02 ± 0.04	(3)
Gl 880	3720.0 ± 60	4.72 ± 0.05	0.21 ± 0.08	(1)
	3810.0 ± 54	4.65 ± 0.06	0.38 ± 0.19	(2)
	3798.0 ± 21	4.80 ± 0.12	0.03 ± 0.06	(3)
Gl 15A	3603.0 ± 60	4.86 ± 0.05	-0.30 ± 0.08	(1)
	3606.0 ± 54	4.77 ± 0.06	-0.14 ± 0.19	(2)
	3603.0 ± 24	4.99 ± 0.14	-0.75 ± 0.11	(3)
Gl 411	3563.0 ± 60	4.84 ± 0.05	-0.38 ± 0.08	(1)
	3569.0 ± 54	4.75 ± 0.06	-0.01 ± 0.19	(2)
	3557.0 ± 26	4.95 ± 0.14	-0.72 ± 0.10	(3)
Gl 752A	3558.0 ± 60	4.76 ± 0.05	0.10 ± 0.08	(1)
	3583.0 ± 54	4.69 ± 0.06	0.25 ± 0.19	(2)
	3575.0 ± 25	4.88 ± 0.12	-0.14 ± 0.08	(3)
Gl 849	3530.0 ± 60	4.78 ± 0.06	0.37 ± 0.08	(1)
	3427.0 ± 54	4.80 ± 0.06	0.09 ± 0.19	(2)
	3540.0 ± 31	4.81 ± 0.11	-0.02 ± 0.07	(3)
Gl 436	3479.0 ± 60	4.78 ± 0.06	0.01 ± 0.08	(1)
	3472.0 ± 54	4.77 ± 0.06	0.03 ± 0.19	(2)
	3533.0 ± 26	4.83 ± 0.11	-0.19 ± 0.10	(3)
Gl 725A	3441.0 ± 60	4.87 ± 0.05	-0.23 ± 0.08	(1)
	3473.0 ± 34	4.90 ± 0.11	-0.46 ± 0.12	(3)
Gl 725B	3345.0 ± 60	4.96 ± 0.06	-0.30 ± 0.08	(1)
	3393.0 ± 48	4.98 ± 0.12	-0.56 ± 0.18	(3)
Gl 15B	3218.0 ± 60	5.07 ± 0.06	-0.30 ± 0.08	(1)
	3261.0 ± 54	4.96 ± 0.06	-0.12 ± 0.19	(2)
	3318.0 ± 53	5.20 ± 0.11	-0.53 ± 0.17	(3)
Gl 699	3228.0 ± 60	5.09 ± 0.05	-0.40 ± 0.08	(1)
	3243.0 ± 54	4.96 ± 0.06	-0.09 ± 0.19	(2)
	3254.0 ± 32	5.13 ± 0.12	-0.84 ± 0.10	(3)
Gl 905	2930.0 ± 60	5.04 ± 0.06	0.23 ± 0.08	(1)
	3069.0 ± 54	4.97 ± 0.06	0.11 ± 0.19	(2)
	3186.0 ± 41	5.15 ± 0.18	0.04 ± 0.17	(3)

4.4 Line selection

One essential part of this work consists in selecting lines of interest exhibiting features allowing us to constrain stellar parameters. In particular, these lines must be well

modeled across the entire range of covered parameters and sensitive to $T_{\rm eff}$, $\log g$, or [M/H]. Ideally, we must include lines that are not sensitive to all of them in order to lift off potential degeneracies between parameters. For M dwarfs in the nIR, identifying such lines is non-trivial because the models do not always correctly reproduce observations and because very few lines are isolated, forcing us to select features that are sometimes blended with surrounding atomic and molecular lines. Let us illustrate these challenges by comparing models to observations and discuss our spectral lines selection.

4.4.1 Large differences between models and observations

Figure 4.4 presents a comparison between synthetic spectra computed from `PHOENIX-ACES` and `MARCS` model atmospheres, and the SPIRou template for Barnard star (Gl 699). This star has been extensively studied over the last years, and its parameters are expected to be fairly close to $T_{\rm eff} \approx 3200$ K, [M/H] ≈ -0.4 dex and $\log g \approx 5.0$ dex. Moreover, the spectra of Gl 699 were acquired over hundreds of visits, allowing us to derive a reliable high-SNR template. In Fig. 4.4, we show a tiny fraction of the SPIRou wavelength domain for which the synthetic spectra do not match the observed one. From such a comparison, we draw three main conclusions:

- We find significant discrepancies between the models and the SPIRou template. Some absorption features observed in the template do not appear in the synthetic spectra, and some modeled features are missing from the template.
- Some of the lines found in both the synthetic spectra and the template are not well reproduced, with significant differences in depth and width.
- The synthetic spectra computed from both models give significantly different profiles, with differences in line depths, width, and shape.

These discrepancies between templates and models are observed throughout the entire SPIRou wavelength range. To analyze SPIRou spectra, we must therefore carefully pick the spectral lines that are best modeled. Moreover, the large differences observed between the models are likely to impact the results of our analysis. In this first step, we select lines that are best reproduced by both sets of models.

4.4.2 A careful selection of lines

Identifying the best lines for our analysis is no trivial task. The solar spectrum would in principle be a good reference, but its IR lines are so different from those of our reference

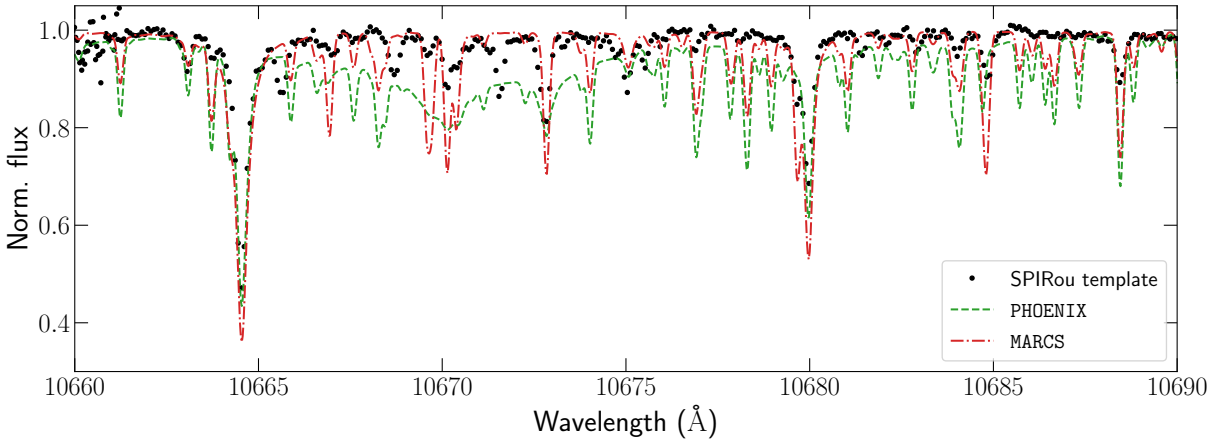

Figure 4.4. Gl 699 template spectrum compared to synthetic models for $T_{\rm eff} = 3200$ K, $\log g = 5.0$ dex and [M/H] $= -0.4$ dex for a tiny chunck of the SPIRou domain (1066 – 1069 nm).

stars (as a result of the difference in spectral type) that it is not very helpful in practice. We thus choose to rely on M dwarfs for which parameters were derived by previous studies, such as Gl 699 or Gl 15A, and compare their SPIRou template to synthetic spectra computed for the expected parameters.

We began by searching for lines already used for high-resolution spectral analysis by other studies (Rajpurohit et al., 2018; Passegger et al., 2019; Flores et al., 2019; López-Valdivia et al., 2021). For each of them, we compared the line profiles of the template and the synthetic spectra and kept the lines if both models agreed well with the observation. We also defined a specific window for each line, to avoid neighboring features that may contaminate our analysis. To complete our line selection, we relied on VALD data to list stellar lines and their expected depth at a given temperature. We automatically scanned the SPIRou wavelength domain, computing a RMS value to identify the lines that were best reproduced by the models. We then visualized each selected line and rejected those for which the fit was suboptimal.

A second aspect of the line selection is to locate features that are sensitive to $T_{\rm eff}$, $\log g$, or [M/H]. This was performed by searching for large variations of the modeled spectral lines as a function of one parameter. Figure 4.5 presents two selected Ti lines, compared to synthetic spectra computed for various $T_{\rm eff}$ and $\log g$. Their sensitivity to either parameter is larger than the discrepancies between the SPIRou template and the expected best model, and we therefore deduce that these lines can be used to constrain $T_{\rm eff}$ and $\log g$.

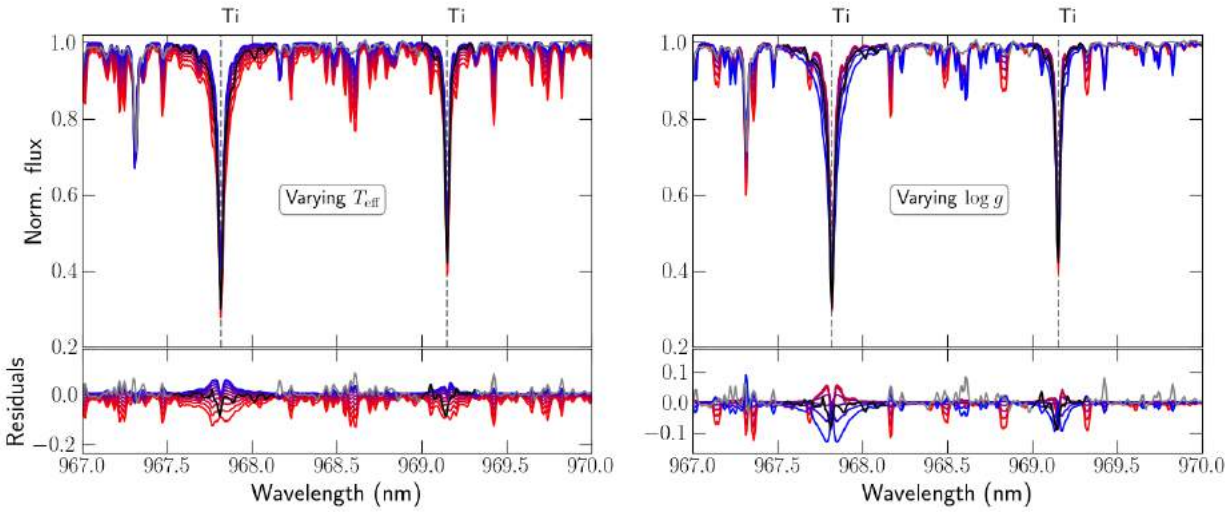

FIGURE 4.5. Comparison between synthetic spectra computed from PHOENIX model atmospheres and the template spectrum of Gl 15A (gray). The color codes the effective temperature from coolest (red) to hottest (blue). Bottom plots show the residuals.

For each spectral line, if the discrepancy between the template and the model is larger than the line's sensitivity to the atmospheric parameters, we reject it.

With our criteria, we built a list of about 30 atomic lines and 40 molecular lines. This list contains lines from several atoms (Ti, Ca, Fe, K, Mn, Al, Mg, Na), as well as molecular lines, mainly from CO lines (belonging to one molecular band located between ∼2290 and 2320 nm), and 3 OH lines. All lines used in this analysis are reported in Table 4.3.

4.5 A comparison between models

To quantify the influence of the model choice on the results and to assess the precision of our study, we built a benchmark allowing us to simulate the analysis from a modeled template.

4.5.1 Simulating the estimation of atmospheric parameters

The simulation framework, illustrated in Fig. 4.6, runs as follows. We draw a random set of $T_{\rm eff}$, $\log g$, and [M/H] values, which we call input parameters, and select the corresponding synthetic spectrum from one grid of models (either MARCS or PHOENIX), interpolating through the spectra if needed. The spectrum is then convolved with a Gaussian kernel of

Table 4.3. Selected lines for the analysis. Vacuum wavelengths were extracted from the VALD database.

Species	Wavelength (nm)
Ti I	967.8198, 969.15274, 970.83269, 972.16252, 1058.7534, 1066.4544, 1189.6132, 1197.7124, 1281.4983, 1571.9867, 2296.9597
Ca I	1034.6654
Fe I	1169.3173, 1197.6323
K I	1169.342, 1177.2861, 1177.6061, 1243.5675, 1516.7211
Mn I	1297.9459
Al I	1315.435, 1672.3524, 1675.514
Mg I	1504.4357
Na I	2206.242, 2208.969
OH	1672.3418, 1675.3831, 1675.6299
CO	2293.5233, 2293.5291, 2293.5585, 2293.5754, 2293.6343, 2293.6627, 2293.7511, 2293.7900, 2293.9094, 2293.9584, 2294.1089, 2294.1668, 2294.3494, 2294.4163, 2294.6311, 2294.7059, 2294.9544, 2295.3195, 2295.4059, 2295.7263, 2295.8159, 2296.1743, 2296.2671, 2296.6648, 2296.7576, 2297.1971, 2297.2884, 2297.7719, 2297.8596, 2298.3888, 2298.4707, 2299.0488, 2299.1222, 2311.2404, 2312.4542, 2315.0029, 2316.3381

FWHM 4.3 km s^{-1} to account for instrumental width and resampled on a typical SPIRou wavelength grid. Noise is added to the spectrum, according to the typical blaze function in each order and the SPIRou throughput (Donati et al., 2020). The resulting modeled template is referred to as 'input model'. We then run the analysis described in Sec. 4.2 on the input model, relying on either the grid of `MARCS` or `PHOENIX` models, and derive estimates of $T_{\rm eff}$, $\log g$ and [M/H], which we refer to as output parameters.

The simulation framework allows us to compare the input and output parameters and check the consistency between the two sets of values. We run the analysis 100 times with randomly drawn parameters in order to obtain estimates of the dispersion in the results and to cover the full parameter space. When the same model is used to generate the input model and run the analysis, we expect to recover the parameters with a precision that is directly correlated to the level of noise added to the input model. In practice, the scattering on the recovered parameters is larger (see Fig. 4.7), and most of the dispersion can be attributed to the adjustment of the continuum.

A second set of simulations was carried out using either `PHOENIX` or `MARCS` models to generate the input model and the other to perform the analysis. Figure 4.8 presents the results obtained on 100 simulations carried out with `MARCS` as an input model and using `PHOENIX` for the analysis, and vice versa. In the first case, we systematically recover

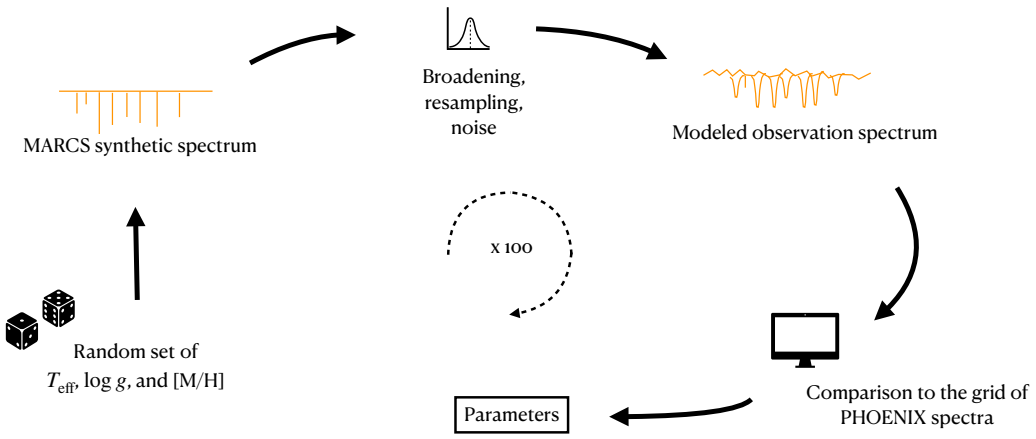

FIGURE 4.6. Illustration of the simulation process. In this example, the grid of `MARCS` spectra is used to generate the input models, and the `PHOENIX` spectra are used to perform the analysis. We used the same approach for the 4 possible combinations of models, `MARCS`/`MARCS`, `MARCS`/`PHOENIX`, `PHOENIX`/`MARCS`, and `PHOENIX`/`PHOENIX`.

larger $T_{\rm eff}$, $\log g$ and [M/H] than used to generate the input model, with average shifts of about 50 K in $T_{\rm eff}$, 0.4 dex in $\log g$ and 0.3 dex in [M/H]. Conversely, if the analysis is performed with the grid of `MARCS` synthetic spectra on input models generated from the `PHOENIX` models, we find that our output parameters are smaller than our input parameters. Furthermore, we observe trends in the recovered parameters, with slopes that are not equal to 1. These results likely arise from systematic differences in line shapes (see Sec. 4.5.2). On top of these systematic shifts, we find that the dispersion on all three parameters is larger than our computed formal error bars. The RMS on the residuals is of about 30 K in $T_{\rm eff}$, 0.05 dex in $\log g$, and 0.10 dex in [M/H], significantly larger than the computed formal error bars, of the order of 8 K in $T_{\rm eff}$, and 0.02 dex in $\log g$ and [M/H]. These results show that systematic differences between models can lead to significant uncertainties, unaccounted for by our formal error bars. To provide the community with better confidence levels on our retrieved parameters, we choose to quadratically add the typical RMS previously computed to our formal error bars.

Our benchmark therefore serves two purposes. First, it provides confirmation that our process performs as expected, allowing us to constrain the atmospheric parameters from

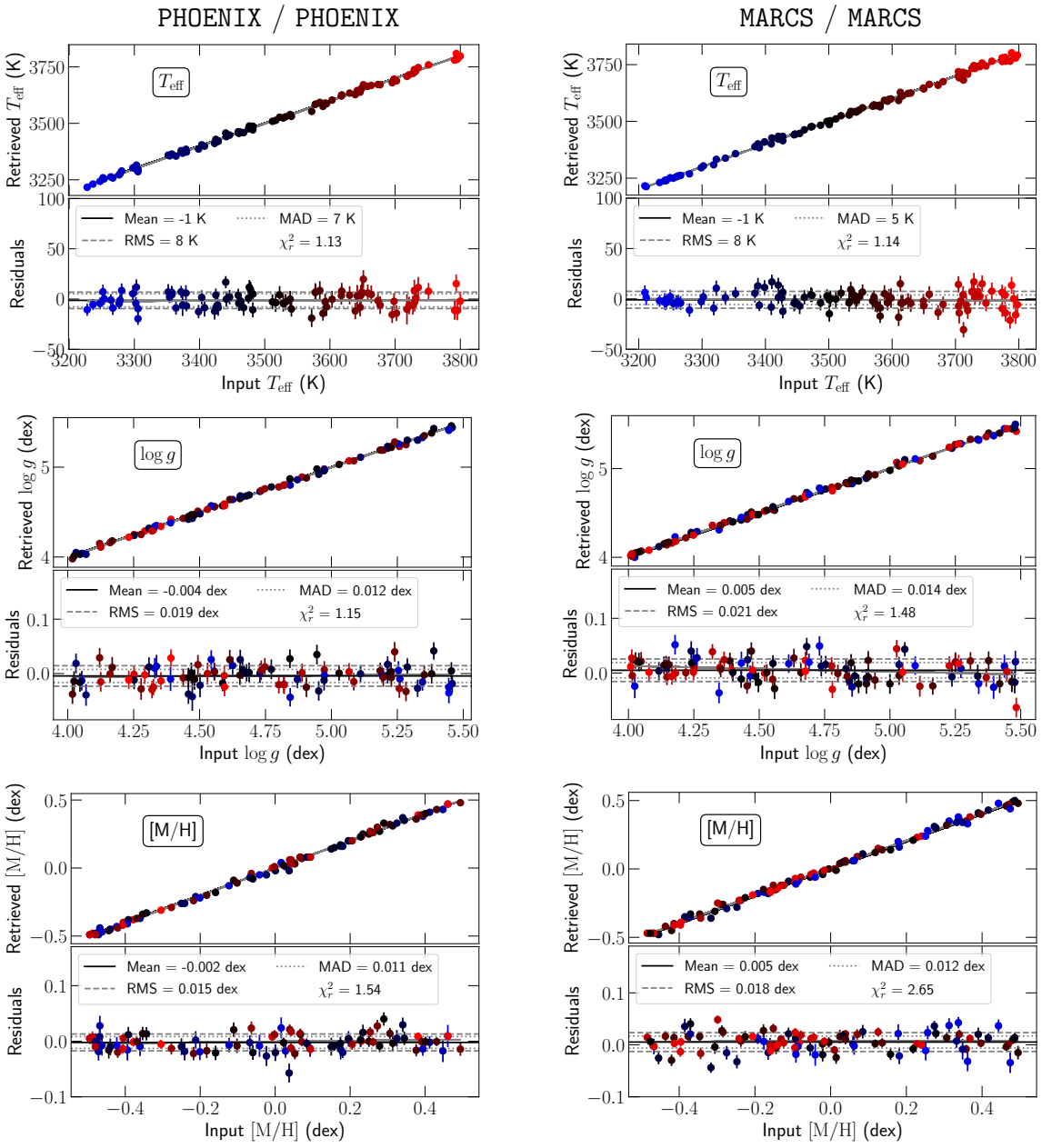

FIGURE 4.7. Simulation of parameters estimation. Retrieved $T_{\rm eff}$ log g and [M/H] are plotted against input parameters. The left column presents the results obtained with PHOENIX used to generate the input model and analyze the model templates. The right column presents the results obtained with the grid of MARCS models. Residuals are presented on the bottom plots, along with their average, RMS, median absolute deviation (MAD) and the reduced χ^2 of series of points. Data points are color coded as a function of temperature, with blue the lowest temperature, and red the highest temperature.

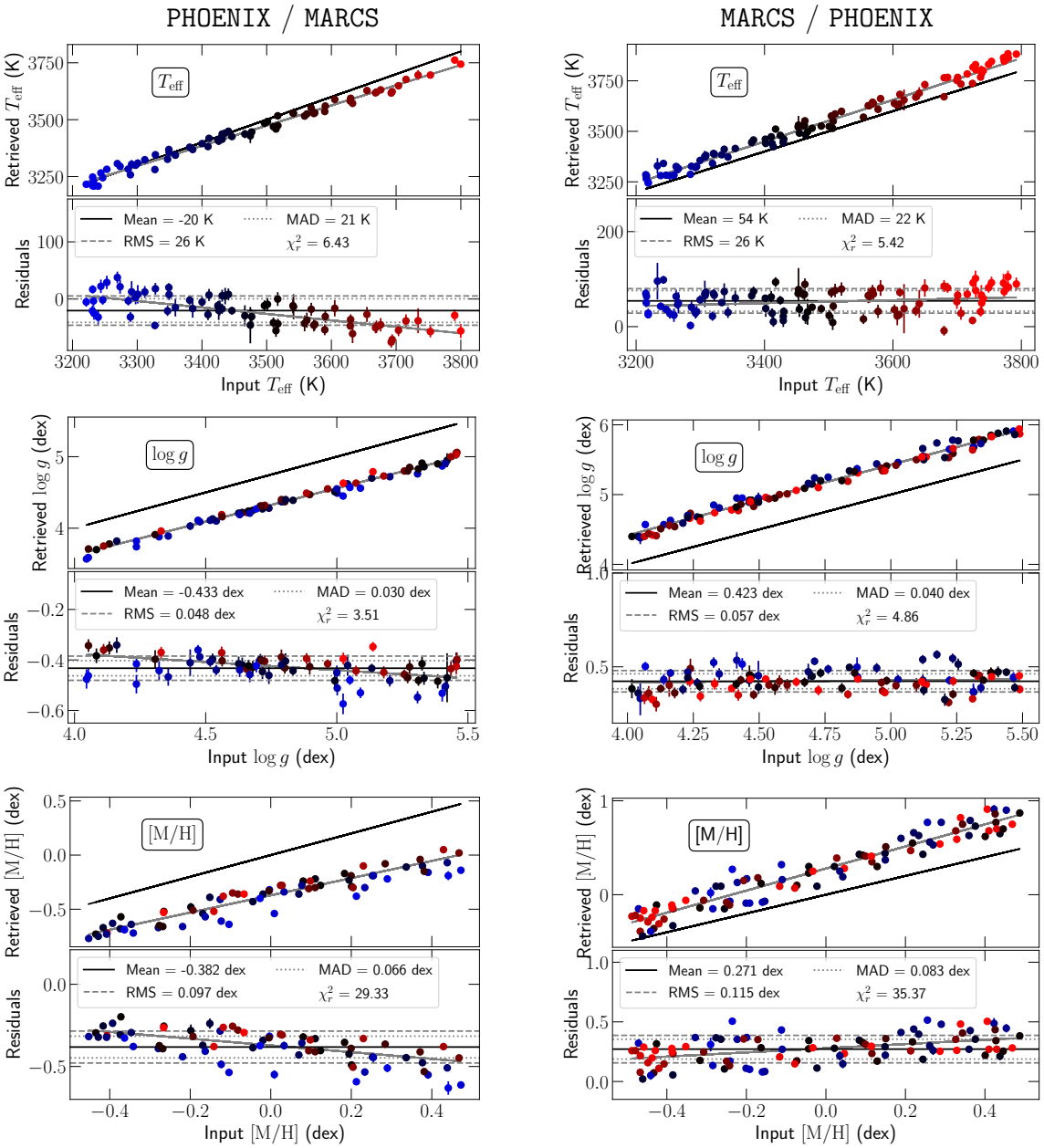

FIGURE 4.8. Same as Fig. 4.7 but using the PHOENIX models to generate input models analyzed with the grid of MARCS spectra (left), and using the MARCS models to generate input models analyzed with the grid of PHOENIX spectra (right).

our selected lines. Secondly, it allows us to assess the significant impact of the model choice on the analysis. We may, in particular, expect to derive lower parameters with the grid of PHOENIX-ACES synthetic spectra than with that computed from MARCS models.

4.5.2 Investigating the differences between models

The systematic differences in the results presented in Sec. 4.5.1 are the consequence of significant discrepancies in the line shapes computed with both models. Figure 4.9 presents a comparison between the synthetic spectra computed from `PHOENIX` and `MARCS` model atmospheres, for one Ca line and two K lines, at $T_{\rm eff} = 3100$ K and $T_{\rm eff} = 3500$ K. We find that the wings of the line profiles tend to be systematically larger when computed from `MARCS` models than when synthesized with `PHOENIX`. We also observe that some differences are temperature-dependent, as is visible for the K lines. For these lines, the models are in better agreement at 3500 K than at 3100 K.

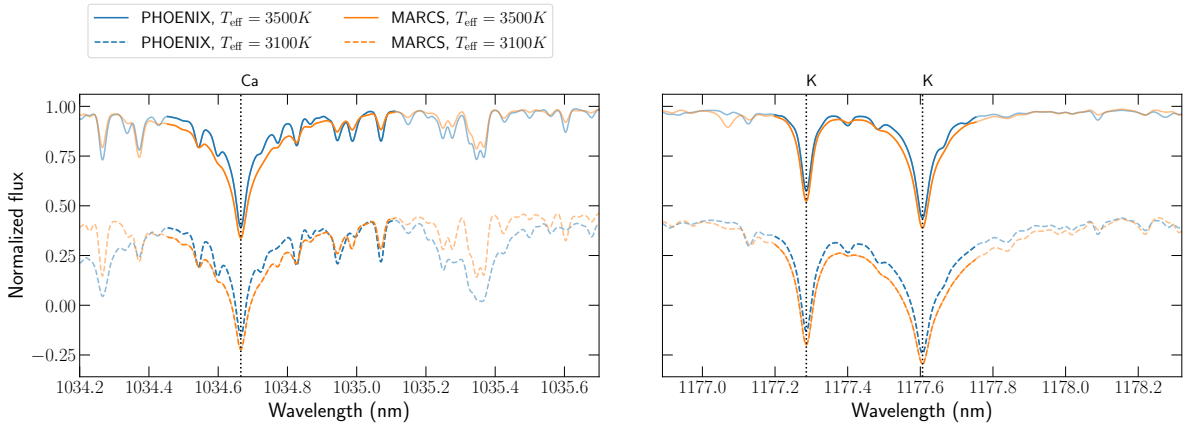

FIGURE 4.9. Comparison between line profiles computed from PHOENIX (blue) and MARCS (orange) model atmospheres. In each panel, models are plotted for two temperatures: 3100 K (dashed lines) and 3500 K (solid lines). The regions selected for our analysis are plotted in bold. For all models, the values of $\log g$ and [M/H] are fixed to 5.0 dex and 0.0 dex respectively.

Fig. 4.10 presents a comparison of the temperature, electronic pressure and gas pressure as a function of optical depth predicted by `PHOENIX-ACES` and `MARCS`. We observe significant differences in the model structures, especially at low $T_{\rm eff}$. Such differences, originating from the physical assumptions made in both models, are likely to impact the shape of spectral lines. Furthermore, the line lists used by both codes differ, as our grid of spectra computed with `Turbospectrum` relies on some of the latest available data, while the `PHOENIX-ACES` synthetic spectra used an old list available in 2016. By inspecting the line lists used by both codes, we also find significant differences in the oscillator strengths of several lines used in our analysis.

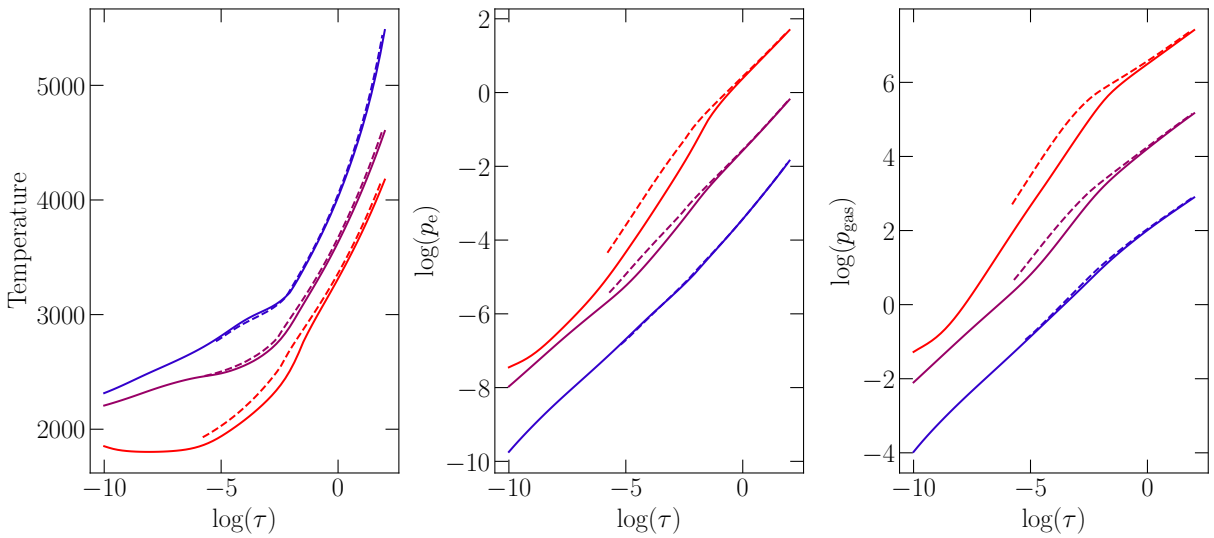

FIGURE 4.10. Comparison between the model atmosphere structure of `PHOENIX-ACES` (solid lines) and `MARCS` (dashed lines). Structures are displayed for a $T_{\rm eff}$ of 3000, 3400 and 3800 K, displayed in red, purple and blue respectively. Arbitrary offsets were applied on $\log p_{\rm e}$ and $\log p_{\rm gas}$ for better readability.

Since we have no means to know which model is best, we choose to stick with both of them for now and to use the observed discrepancies to adjust our error bars.

4.5.3 Incorporating systematics within error bars

The formal error bars reflect uncertainties that are intrinsic to our method: they provide a confidence level assuming that the uncertainties on data points are well estimated, and that photon noise dominates over other sources of error. By comparing models, we found that these error bars are insufficient to account for the dispersion induced by systematic differences throughout the entire parameter space, but rather give a confidence level on the derived parameters for a given set of $T_{\rm eff}$, $\log g$ and [M/H].

Because we are unable at this stage to identify one model as being unarguably better than the other, we use the discrepancies between the two models to provide the community with more conservative error bars. This is done by quadratically adding the typical RMS computed through simulations on each parameter, i.e., 30 K in $T_{\rm eff}$, 0.05 dex in $\log g$ and 0.1 dex in [M/H], to the computed formal error bars. For the sake of clarity, we will refer to these enlarged error bars as 'empirical error bars' in the rest of this manuscript.

4.6 Recovering Stellar parameters

We perform the analysis described in this chapter on our 12 targets of reference and retrieve a value of $T_{\rm eff}$, $\log g$, and [M/H] for each of them, with both the `PHOENIX` and `MARCS` models. Both sets of estimates are compared to literature values for each star. In particular, we choose to confront our estimates to those published by Mann et al. (2015), because this reference relies on methods that are largely independent from ours, reducing the risk of potential biases. In particular, Mann et al. (2015) derived stellar parameters from empirical mass-magnitude relations, equivalent widths and fits of `PHOENIX BT-settl` models to low resolution spectra. Figure 4.11 presents our estimates of $T_{\rm eff}$, $\log g$ and [M/H] compared to those published in this reference study.

4.6.1 Results

Effective temperature

With both the `PHOENIX` and `MARCS` models, we recover $T_{\rm eff}$ in good agreement with those reported by Mann et al. (2015), with a dispersion of about 40 K, consistent with the typical uncertainty published by Mann et al. (2015) on $T_{\rm eff}$ of about 60 K. We find that the parameters recovered with the grid of `PHOENIX` models are on average 30 K larger than those obtained with the `MARCS` models. This offset is consistent with the results of our simulations presented in Sec. 4.5. Furthermore, the comparison to Mann et al. (2015) reveals trends in our retrieved $T_{\rm eff}$, with slopes that are not equal to one. With the grids computed from `MARCS` models, the slope is 0.85 ± 0.03, while it is 1.02 ± 0.04 when relying on the grid of `PHOENIX` models. These trends are consistent with the results of our simulations. The dispersion about these trends is of the order of ~ 30 K with both models, consistent with our empirical error bars.

Metallicity

Our retrieved [M/H] are also found to be in relatively good agreement with those reported by Mann et al. (2015). The dispersion on the values retrieved with the grid of `MARCS` models is nonetheless larger than that computed with the grid of `PHOENIX-ACES` models, with RMS of 0.23 dex and 0.13 dex, respectively. This dispersion, in particular with the grid of `MARCS` models, is larger than our empirical error bars, estimated to be about 0.10 dex. Furthermore, we find that our estimates obtained with the grid of `MARCS` models

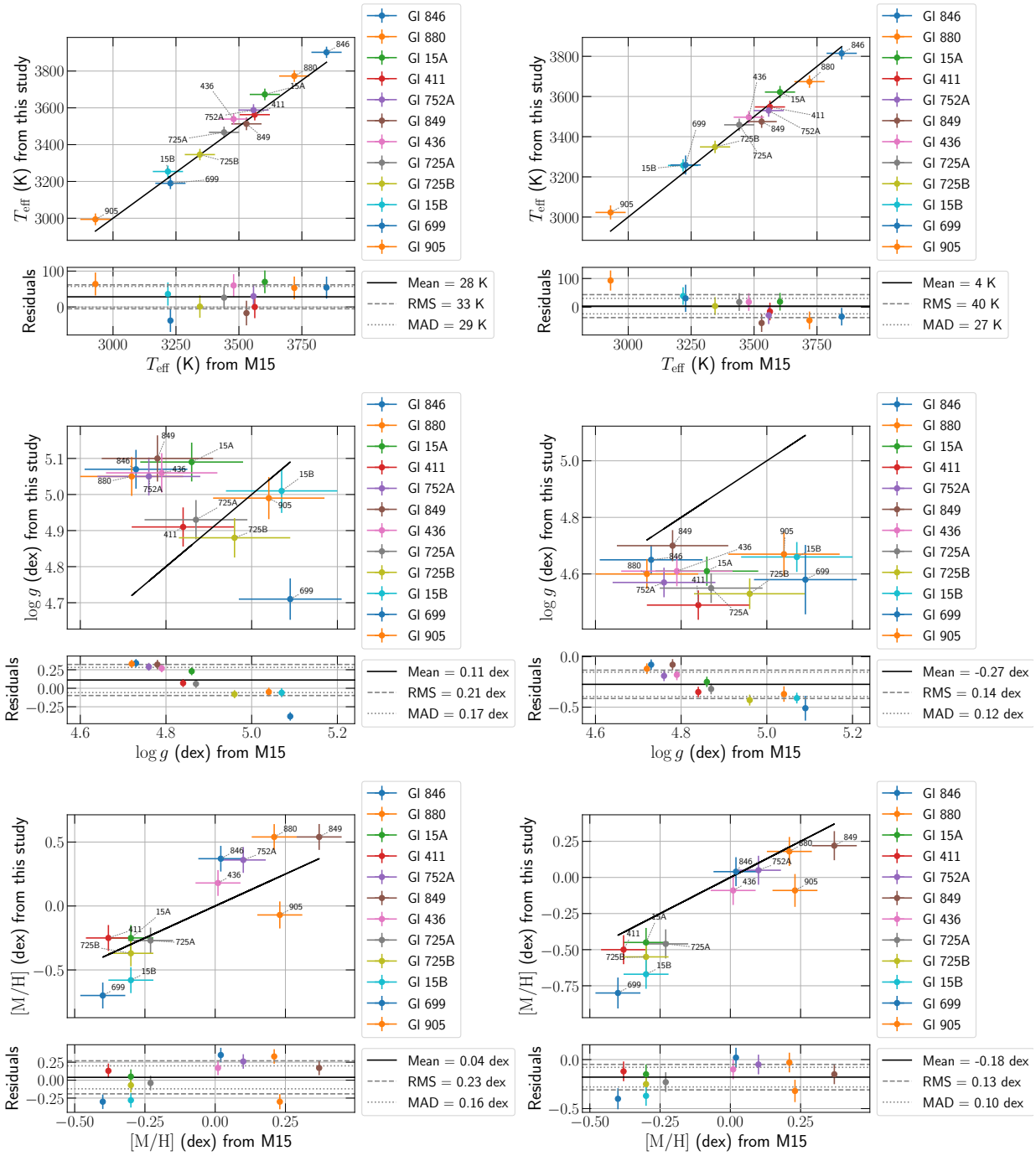

FIGURE 4.11. From top to bottom we present our retrieved $T_{\rm eff}$, $\log g$ and [M/H] using the grid of PHOENIX (left) and MARCS (right) spectra plotted against values published by Mann et al. (2015). The solid black line marks the equality. The bottom plots present the residuals, i.e. the retrieved values minus literature values. RMS and median absolute deviation (MAD) values are computed after application of a sigma clipping function on the residuals with a threshold at 5 σ.

are on average 0.20 dex lower than those derived from the PHOENIX-ACES models, which is again consistent with our simulations.

Our sample of stars includes two binaries: Gl 15AB and Gl 725AB. Binary stars are usually expected to have a similar composition, as they are likely to have formed together within a same star-forming region. With both grids of synthetic spectra, our retrieved [M/H] for Gl 725A and Gl 725B are in good agreement, with a difference of about 0.10 dex, consistent with our empirical error bar. With the grid of PHOENIX spectra, the difference in [M/H] estimated for Gl 15A and Gl 15B reaches 0.33 dex, 3.3 times larger than our empirical error bars. A 2 σ difference is also found between the values obtained with the grid of MARCS spectra for this binary. It is worth noting that while we derive similar $T_{\rm eff}$ for Gl 725A and Gl 725B, Gl 15B is estimated to be over 300 K cooler than Gl 15A. The significant difference in recovered metallicities could therefore reflect further uncertainties in the modeled spectra, which fail to accurately reproduce spectra at low $T_{\rm eff}$. Such discrepancies have since been reduced thanks to improvements in our method, described in Chapter 5.

Surface gravity

Surface gravity is notoriously tricky to constrain, to the point where several studies chose to set its value based on empirical or theoretical relations (Passegger et al., 2018; Schweitzer et al., 2019). Fixing the value of $\log g$ however requires one to have a priori estimates of, e.g., the mass and radius of the star, whose accuracy is not necessarily guaranteed. In this work, we therefore chose to fit this parameter. The dispersion on our retrieved $\log g$ is of about 0.15 dex with the grid of spectra computed from MARCS model atmospheres and of about 0.20 dex with the one computed from PHOENIX models. These are larger than our estimated empirical error bars, of 0.05 dex.

Fixing $\log g$ impacts the estimation of $T_{\rm eff}$ and [M/H]. By fixing the value of $\log g$, we found that our retrieved $T_{\rm eff}$ and [M/H] were not in better agreement with those reported in the literature, but rather led to an increase in the dispersion on temperatures, particularly with the grid of MARCS models. In particular, fixing the values of $\log g$ did not significantly reduce the discrepancy between the metallicities of Gl 15A and Gl 15B.

Investigating the significance of error bars

We can further investigate the precision of our formal error bars by performing our analysis on individual high-resolution spectra of a same star. We find that our formal

error bars do account for most of the dispersion on the retrieved values (see Fig. 4.12). These results suggest that our formal error bars properly account for the uncertainty on the parameters for a given star, i.e. at a given point of the $T_{\rm eff}$-log g-[M/H] parameter space.

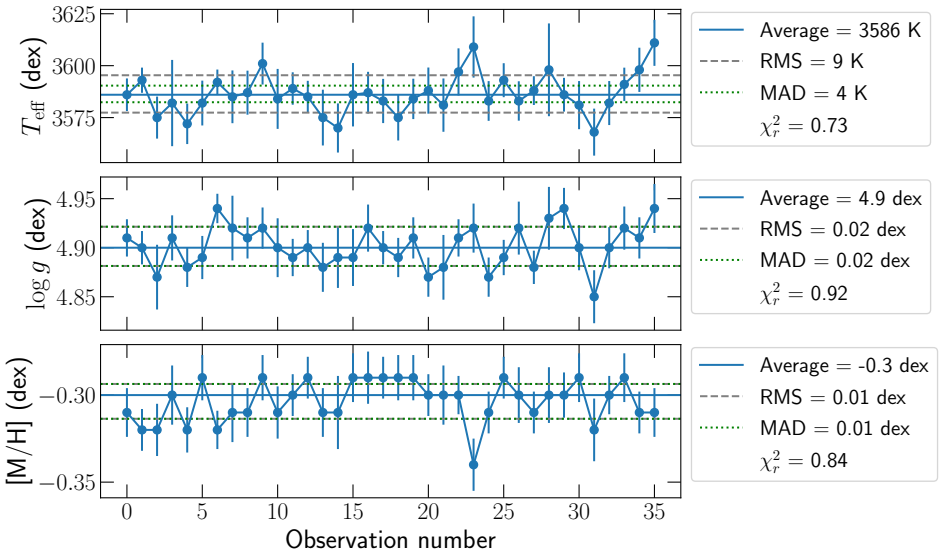

Figure 4.12. Optimal estimates and corresponding formal error bars retrieved for a series spectra of Gl 411. For each parameter we display the average, RMS, median absolute deviation(MAD) and χ^2 on the series of points.

4.6.2 Comparison to other literature studies

In the previous sections, we presented our results compared to the parameters reported by Mann et al. (2015). We do not, however, have an absolute reference for stellar parameters, and other studies may report different values for our sample of stars. In particular, recent works attempted to estimate atmospheric parameters for 10 of these 12 stars from fits of `PHOENIX` models to high-resolution CARMENES spectra. Let us briefly comment on how our results compare to those of such studies, and how literature references compare one to another.

Comparing our results to other studies

Figure 4.13 presents our $T_{\rm eff}$ and log g estimates derived with the grid of `MARCS` models compared to those reported by Passegger et al. (2019), obtained by performing fits of `PHOENIX` synthetic spectra to high-resolution CARMENES data. We find the dispersion

on $T_{\rm eff}$ and [M/H] is compatible with those computed when comparing our results to Mann et al. (2015), with RMS values of about 50 K and 0.16 dex, respectively. The larger dispersion on $T_{\rm eff}$ can, in particular, be attributed to the reported $T_{\rm eff}$ of Gl 905, about 200 K smaller in Mann et al. (2015) than Passegger et al. (2019). Furthermore, we find differences in the overall offsets computed when comparing our results to the latter, suggesting that the two references provide significantly different results.

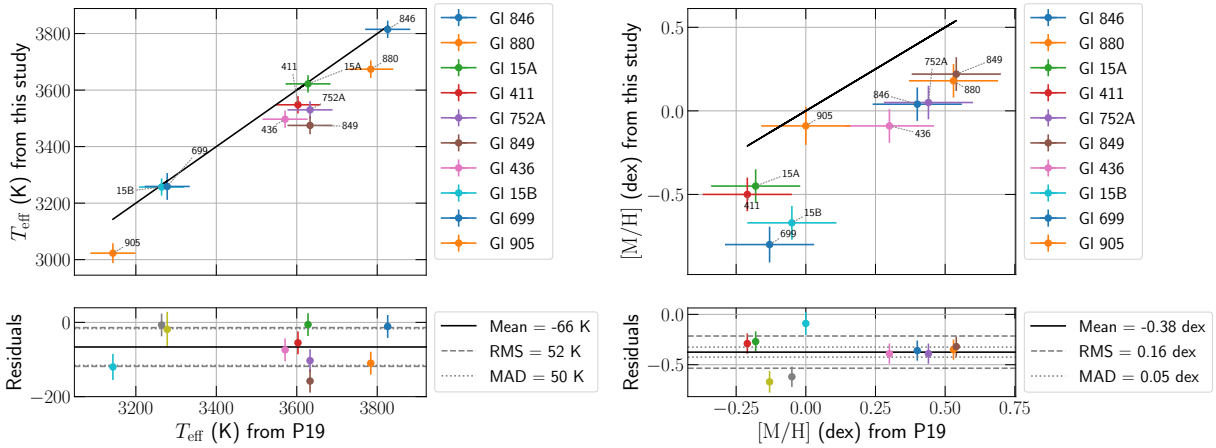

FIGURE 4.13. Comparison between our retrieve $T_{\rm eff}$ (left panel) and [M/H] (right panel) to those reported by Passegger et al. (2019) (P19). The solid black line marks the equality. The bottom panels show the residuals.

Comparing results from different studies

Figure 4.14 presents a comparison between the values reported by Passegger et al. (2019) and those of Mann et al. (2015). The discrepancies between the two studies are comparable to those observed with our results. In particular, the comparison shows that the $T_{\rm eff}$ and $\log g$ published in Passegger et al. (2019) are on average 70 K and 0.20 dex larger than those of Mann et al. (2015), respectively. Moreover, the dispersion between the two studies is about 60 K in $T_{\rm eff}$ and about 0.20 dex in [M/H].

4.7 What have we learned?

The results of this study, published in Cristofari et al. (2022a, see Appendix A), correspond to the first step in our effort to characterize M dwarfs from SPIRou spectra. We selected spectral lines for our analysis, driven by the comparison of models to the spectra of key reference stars. We then implemented a code for the computation of stellar parameters from a χ^2 minimization and tested it through simulations. Our benchmark allowed

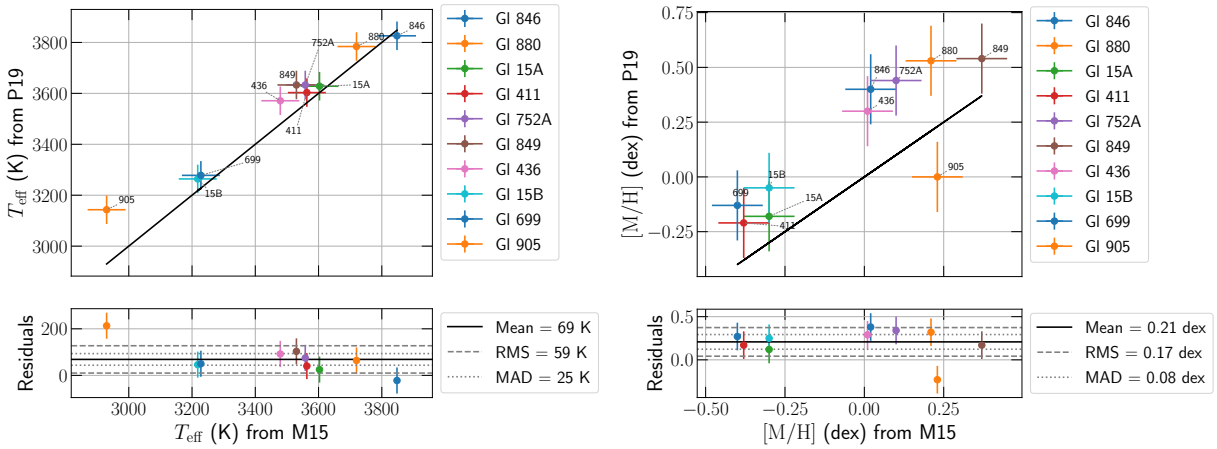

FIGURE 4.14. Same as Fig. 4.13 comparing results reported by Passegger et al. (2019) (P19) and Mann et al. (2015) (M15).

us to assess the performances of our tools and to estimate the impact of the model choice on the results. In particular, we found that when confronting two state-of-the-art models, `PHOENIX-ACES` and `MARCS`, systematic differences led to significant dispersion in the results. Consequently, we used these results to adjust our error bars and performed our analysis on 12 reference targets with both models. The results of our analysis are in good agreement with the literature, although we found that $\log g$ was especially difficult to constrain. Systematic shifts in the retrieved parameters are consistent with the results of simulations, further confirming that the choice of model does significantly impact the estimation of the parameters. Pinpointing the physical origin of these differences is not trivial and calls for a complete and in-depth investigation of both codes.

The analysis performed so far was carried out on 12 reference stars. SPIRou monitored over 70 targets, most of them several tens of times. As a natural continuation to this work, we therefore expanded and improved our analysis to derive the parameters of a larger sample of stars (see Chapter 5).

Chapter 5

Expanding and improving our analysis to M dwarfs within the SLS sample

Contents

5.1 Context

In Chapter 4, we presented the results of our analysis of 12 reference M dwarfs to test and assess the performances of our method. Our next step is to improve our analysis and apply it to a larger number of targets. We tried to refine our analysis to increase the precision and reliability of the measurements.

It is now well established that the Galactic disk is composed of several components (see Fig. 5.1) with different abundances of the so-called α elements. In particular, it can be divided into a thin disk, mainly composed of α-poor stars, and a thick disk, composed of

stars with larger α abundances (Fuhrmann, 1998; Reddy et al., 2006; Adibekyan et al., 2013). Some authors tried to derive individual elemental abundances of M dwarfs, relying on high-resolution spectra (Souto et al., 2022), or equivalent widths (Ishikawa et al., 2020, 2022). Although promising, setting constraints on the composition of M dwarfs remains difficult and likely sensitive to modeling strategies.

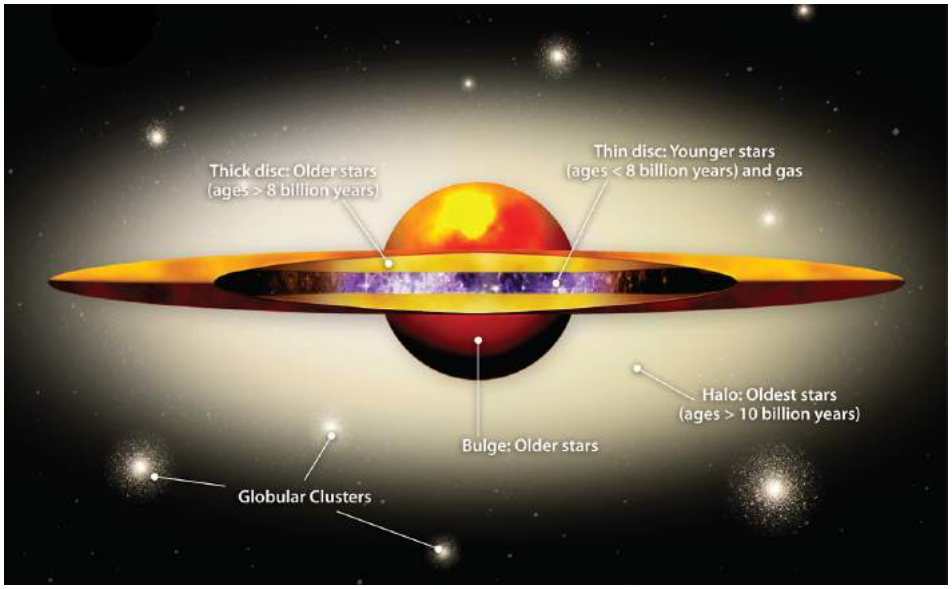

Figure 5.1. Schematic representation for the Milky way. Credit: Amanda Smith, IoA graphics officer. https://www.universetoday.com/83315/thick-stellar-disk-isolated-in-andromeda/

In Chapter 4, the `PHOENIX-ACES` and `MARCS` models were computed assuming that the chemical composition of the stars relative to iron varies by the same amount for all elements, i.e., that a single [M/H] parameter controls the total abundances of metals. Because the abundance of α elements is known to differ from star to star, these models have included an α-enhancement parameter ([α/Fe]) to their modeling.

In this chapter, we present a follow-up to the analysis presented in Chapter 4. We improved our modeling strategy by adding the [α/Fe] parameter and calibrated our analysis on a few key reference targets. We then applied our analysis to a sample of 44 M dwarfs monitored in the context of the SLS, providing estimates of $T_{\rm eff}$, $\log g$, [M/H], [α/Fe], masses, and radii. The results presented in this chapter were published in Cristofari et al. (2022b, see Appendix A).

5.2 The influence of α-elements abundances on retrieved parameters

5.2.1 On the origin of α-elements

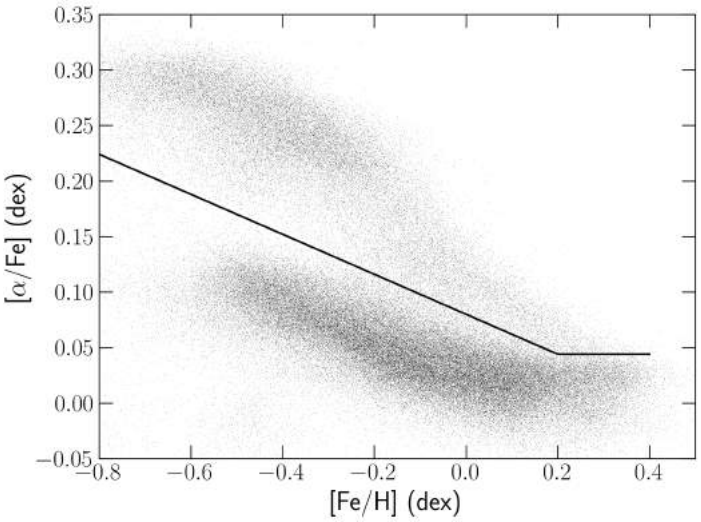

FIGURE 5.2. p
lane]Giants studied with APOGEE in the [α/Fe]–[Fe/H] plane (Jönsson et al., 2020). The solid black line marks the fiducial boundary between α-rich and α-poor stellar populations.

Alpha-elements are primarily produced through the so-called α process, one of the two chains of reactions burning helium in massive stars (Blancato et al., 2019). This reaction chain begins with the fusion of carbon and helium, and goes on to fuse helium with the result of the previous reaction, forming O, Ne, Si, S, Ar, Ca, and Ti. Such fusion processes can only occur in massive stars, and consequently, α elements are mainly released in the interstellar medium (ISM) by core-collapse supernovae. Other elements such as Fe, Mn, Na, or Cr, are released by both core-collapse and type Ia supernovae. Because of the time delay between core-collapse and Type Ia supernovae, α elements have been proposed as a marker of choice in the field of Galactic archaeology. As the number of type Ia supernovae increases, the relative abundance of α elements with respect to iron decreases. The observed abundances in stars should consequently capture the epoch at which their formation occurred.

To account for the relative abundance of α elements with respect to the abundance of iron, we introduce the [α/Fe] parameter, so that [α/H] = [M/H] + [α/Fe] for each element

α. A trend is observed within the Milky Way between [α/Fe] and [Fe/H]. Several works have also revealed that the disk of the Milky Way is composed of at least two populations, consisting of α-rich and α-poor stars, first observed in the solar vicinity (Fuhrmann, 1998; Reddy et al., 2006; Adibekyan et al., 2013). These observations were later confirmed by large science surveys such as APOGEE (Jönsson et al., 2020). Figure 5.2 presents the position of giants studied with APOGEE in the [α/Fe]–[Fe/H] plane, for which precise estimates of [α/Fe] and [Fe/H] are available. The α-rich and α-poor populations are easily identifiable, and for both groups, we observe an anti-correlation between [α/Fe] and [M/H] for metal-poor stars.

5.2.2 Disk populations and cinematic

On top of differences in composition, large surveys unveiled correlations between [α/Fe] and velocities in the Galactic coordinate system. In Fig. 5.3, we place the giants studied

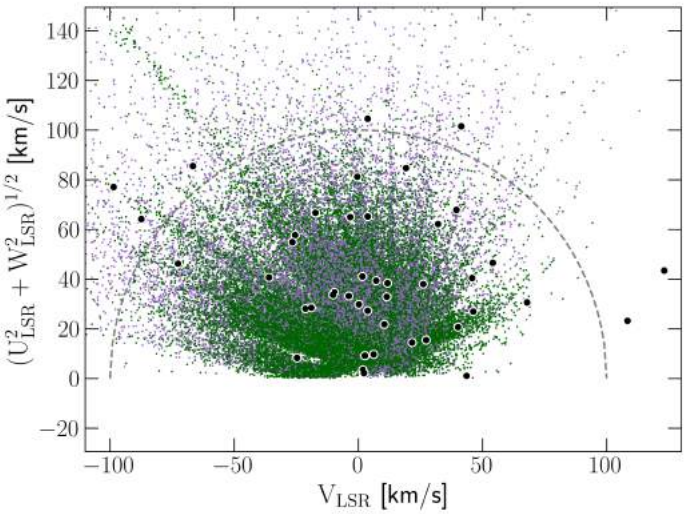

Figure 5.3. Toomre diagram for the giants studied with APOGEE. Green points presents α-poor thin disk stars, while the purple points present α-rich thick disk stars. Black dots present the position of the 44 M dwarfs included in our sample (see Fig. A1 of Cristofari et al., 2022b, for a figure with the star names). The dashed circle marks the fiducial boundary at 100 km s^{-1}.

with APOGEE in a Toomre diagram, computing their velocity in the Galactic coordinate system from Gaia DR3 proper motion and parallaxes. We label each star as belonging to the α-rich or α-poor population based on their position in Fig. 5.2. The thin and thick

disks are composed of a majority of α-poor and α-rich stars, respectively, and modern theories on the formation of the Milky Way propose that the thick disk formed before the thin disk. The Toomre diagram reveals that stars with overall velocities larger than 100 km s^{-1} are mostly α-rich, while most stars with lower velocities are α-poor. Placing the 44 M dwarfs we aim at studying on the diagram, we see that most of them are found within the fiducial 100 km s^{-1} boundary. A few targets, however, are found with higher velocities and likely belong to the thick disk. Because velocity is not an absolute marker of population, a few targets found within the 100 km s^{-1} boundary could belong to the thick disk as well.

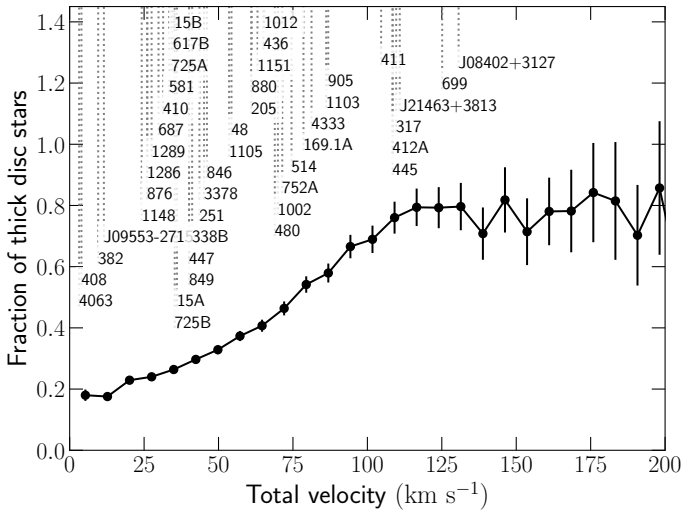

FIGURE 5.4. Fraction of thick disk stars per velocity bin estimated from APOGEE data for giants. The position of each target in our sample is marked on the horizontal axis.

From this correlation, we can derive a probability for stars to belong to the thin or thick disk based on their total velocity. Based on APOGEE data for giants, we compute the fraction of α-rich stars as a function of total velocity (see Fig. 5.4). This ratio can then be interpreted as the probability that a star with a given total velocity belongs to the α-rich thick disk. We use this ratio to check the consistency of our results, presented later on. One should note that the abundance of α elements is not an absolute marker for thin and thick disk populations (Fuhrmann, 2008; Lee et al., 2011; Adibekyan et al., 2013), but we label thin and thick disk stars based on [α/Fe]. This is because [α/Fe] has a significant impact on the stellar spectra of M dwarfs and is, therefore, the parameter of interest to our analysis.

5.2.3 How does [α/Fe] impact model atmospheres and stellar spectra?

By modifying the abundance of oxygen, one also modifies the chemical equilibrium within the model atmosphere, leading to significant changes in pressure, temperature, and density. Indeed, the impact of [α/Fe] is not limited to atomic lines, as the abundance of α-elements, and in particular that of oxygen, strongly impacts the formation of molecular lines (such as TiO, CO, and OH, to name a few). These molecules are responsible for large absorption bands, numerous in the nIR domain for cool stars.

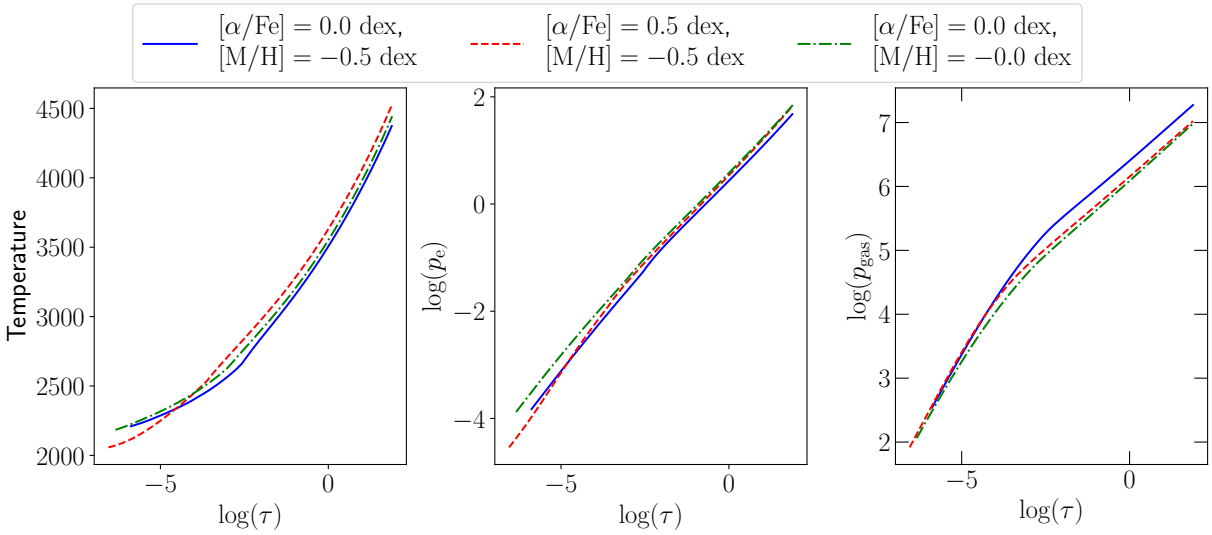

FIGURE 5.5. `MARCS` atmosphere model structure for different [α/Fe] and [M/H]. The figure shows the temperature, electronic pressure and gas pressure (left, middle and right panels respectively), [M/H] = −0.5 dex & [α/Fe] = 0.0 dex; [M/H] = −0.5 dex & [α/Fe] = 0.5 dex and [M/H] = 0.0 dex & [α/Fe] = 0.5 dex (solid blue, dashed red and dashed green lines respectively). All models are presented for $T_{\rm eff}$ = 3200 K and $\log g$ = 5.0 dex.

Figure 5.5 presents the impact of the [α/Fe] parameter on the temperature, electronic pressure, and gas pressure of the `MARCS` model atmospheres. A change in [α/Fe] leads to significant temperature variations as a function of the optical depth, which can be at the origin of large differences in the emergent spectra. Such differences are clearly visible in the spectra computed from `MARCS` models (see Fig. 5.6).

Because of the significant impact α element abundances have on the spectra, several models incorporated [α/Fe] as a parameter to compute atmospheres and synthesize spectra (Allard et al., 2011; Husser et al., 2013; Gustafsson et al., 2008). Consequently, some

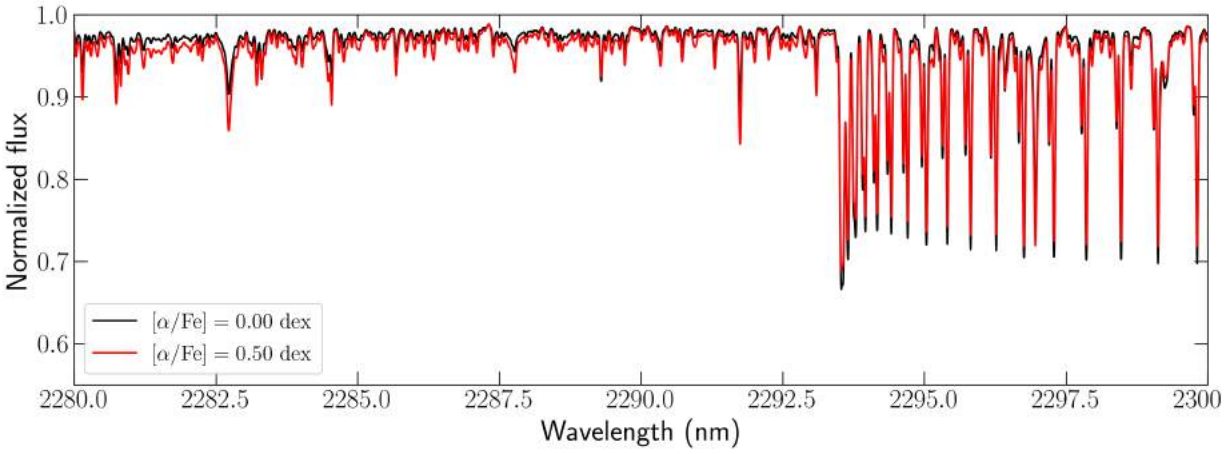

FIGURE 5.6. Example of spectra computed with $[\alpha/\mathrm{Fe}] = 0.00$ dex and $[\alpha/\mathrm{Fe}] = 0.50$ dex, with $T_{\mathrm{eff}} = 3200$ K, $\log g = 5.0$ dex and $[\mathrm{M/H}] = 0.0$ dex.

published grids of models provide spectra computed with multiple values of $[\alpha/\mathrm{Fe}]$ (Husser et al., 2013), or with fixed values of $[\alpha/\mathrm{Fe}]$, estimated from empirical on $[\mathrm{M/H}]$-$[\alpha/\mathrm{Fe}]$ relations (Allard & Hauschildt, 1995). In this work, we choose to fit $[\alpha/\mathrm{Fe}]$ as an additional parameter to improve constraints on T_{eff}, $\log g$, and $[\mathrm{M/H}]$. The `PHOENIX-ACES` models were only published with $[\alpha/\mathrm{Fe}] \neq 0$ for $T_{\mathrm{eff}} < 3500$ K, which limits their use. We thus focus on the `MARCS` models computed with multiple $[\alpha/\mathrm{Fe}]$ values for T_{eff} ranging between 3000 and 4000 K.

5.3 Adjusting atomic line parameters

For this extended study, we revised the line selection presented in Chapter 4. Because we now only focus on synthetic spectra computed with `Turbospectrum` from `MARCS` model atmospheres, some lines which were not previously selected were added. To refine our selection, we compared the synthetic spectra to those of 3 key reference stars (Gl 699, Gl 15A, and Gl 411), assuming the parameters published by (Mann et al., 2015) for these targets. This comparison allowed us to calibrate our line selection on these targets by removing lines that pulled the analysis away from the expected parameters. Furthermore, it showed that our grid of models did not accurately reproduce the wings of several lines. In particular, a few Ti lines present larger wings than observed in the SPIRou templates for our calibration stars. To improve our fits and calibrate our method, we adjusted the Van der Waals broadening parameters of these lines to obtain the best match for the expected parameters (see Fig. 5.7). We found these adjustments improve

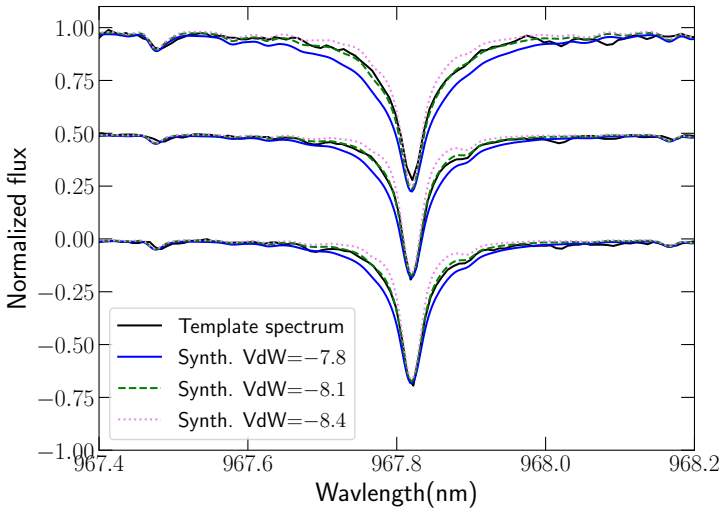

FIGURE 5.7. Effect of the Van der Waals parameters on the line shape. The spectra of our 3 references stars are displayed (Gl 699, Gl 15A, Gl 411 from top to bottom), with the associated models computed for different values of the Van der Waals parameters.

the derivation of stellar parameters of the 12 stars included in our first study, particularly for the constraints on $\log g$.

5.4 A larger sample of stars

For this study, we extended our sample to 44 M dwarfs regularly observed in the context of the SLS, favoring stars with moderate to low activity and monitored over at least 20 visits. These stars are all relatively slow rotators — slow enough for rotation and activity to have a limited impact on the spectral lines. The typical number of observations and SNR for each target is listed in Table 5.1. Templates are built for each target using all available telluric-corrected observations with SNR above 50.

5.5 Deriving stellar properties

5.5.1 Error estimation on $[\alpha/\mathrm{Fe}]$

Formal and empirical error bars were defined in Sec. 4.5.3. Following a similar procedure, we estimate formal error bars on T_{eff}, $\log g$, [M/H], and $[\alpha/\mathrm{Fe}]$ from the curvature of the

Table 5.1. Number of spectra, number of visits and typical SNR for the 44 stars included in our sample.

Star	Nb. spectra	Nb. epochs	Med. SNR [SNR range]
Gl 338B	124	31	250 [150 - 300]
Gl 410	472	112	130 [50 - 150]
Gl 846	792	194	160 [50 - 230]
Gl 205	593	143	290 [50 - 350]
Gl 880	634	155	200 [70 - 250]
Gl 514	740	152	160 [50 - 280]
Gl 382	238	59	150 [50 - 220]
Gl 412A	884	148	180 [60 - 350]
Gl 15A	1040	198	280 [60 - 360]
Gl 411	592	143	360 [200 - 440]
Gl 752A	523	129	170 [50 - 230]
Gl 48	786	195	130 [60 - 150]
Gl 617B	546	133	120 [50 - 150]
Gl 480	283	70	110 [60 - 120]
Gl 436	188	38	150 [70 - 220]
Gl 849	771	189	120 [50 - 140]
Gl 408	495	117	140 [50 - 170]
Gl 687	898	214	200 [60 - 240]
Gl 725A	889	213	210 [50 - 260]
Gl 317	108	27	100 [70 - 130]
Gl 251	749	175	140 [50 - 170]
GJ 4063	784	190	100 [50 - 120]
Gl 581	124	31	120 [60 - 150]
Gl 725B	855	211	160 [70 - 200]
PM J09553-2715	172	43	110 [80 - 140]
Gl 876	369	88	160 [70 - 220]
GJ 1012	522	129	100 [50 - 120]
GJ 4333	734	181	100 [50 - 120]
Gl 445	171	43	110 [50 - 140]
GJ 1148	399	98	100 [50 - 110]
PM J08402+3127	462	115	100 [50 - 110]
GJ 3378	725	179	100 [50 - 130]
GJ 1105	515	128	100 [50 - 130]
Gl 699	950	231	200 [60 - 240]
Gl 169.1A	673	165	100 [50 - 130]
PM J21463+3813	718	177	100 [50 - 120]
Gl 15B	755	188	100 [50 - 120]
GJ 1289	812	202	100 [50 - 110]
Gl 447	180	45	120 [60 - 170]
GJ 1151	568	141	100 [50 - 120]
GJ 1103	254	62	100 [50 - 110]
Gl 905	484	117	110 [50 - 130]
GJ 1002	524	130	100 [60 - 120]
GJ 1286	438	113	100 [50 - 120]

paraboloid fitted on the χ^2 surface. These formal error bars are typically of the order of $\sim$10 K in $T_{\rm eff}$, $\sim$0.02 dex in $\log g$ and [M/H] and $<$ 0.01 dex in [α/Fe].

In Cristofari et al. (2022a), empirical error bars were estimated by comparing the results of simulations carried out with both the `PHOENIX` and `MARCS` models. To account for some of the systematics, we rely on the results of Cristofari et al. (2022a) and increase our formal error bars by quadratically adding 30 K, 0.05 dex, and 0.10 dex to those estimated for $T_{\rm eff}$, $\log g$ and [M/H] respectively. Given that we have no empirical estimate for [α/Fe], we choose to enlarge the error bar on this parameter by an amount proportional to that estimated for [M/H]. In particular, we find that the dispersion on [α/Fe] is generally 40 % that of the dispersion on [M/H]. We therefore choose to enlarge our formal error bars on [α/Fe] by quadratically adding 0.04 dex to them. These enlarged error bars are referred to as 'empirical error bars'.

5.5.2 $T_{\rm eff}$, $\log g$, [M/H], [α/Fe]

In contrast to Cristofari et al. (2022a), we revised a few aspects of our process to improve the estimation of parameters, including the adjustment on the continuum and the spectral line selection. With our updated process, we retrieve parameters in good agreement with the literature and provide updated stellar parameters for our initial sample of 12 stars. The results presented here were published Cristofari et al. (2022b).

To assess the accuracy of our retrieved atmospheric parameters, we compare them to those reported by Mann et al. (2015) for the 28 stars included in both studies. Figure 5.8 presents such comparison for $T_{\rm eff}$, $\log g$ and [M/H].

Effective temperature

We retrieve $T_{\rm eff}$ estimates in good agreement Mann et al. (2015), with a dispersion of about 40 K, consistent with our previously derived empirical error bars. Similarly to Cristofari et al. (2022a), we find the largest disagreement with our reference study for the coolest stars in our sample, with a difference of up to about 140 K for Gl 905. It is worth pointing out that several other studies, including some performing fits of high-resolution spectra to observation (Passegger et al., 2019; Marfil et al., 2021), reported larger $T_{\rm eff}$ for these stars than Mann et al. (2015).

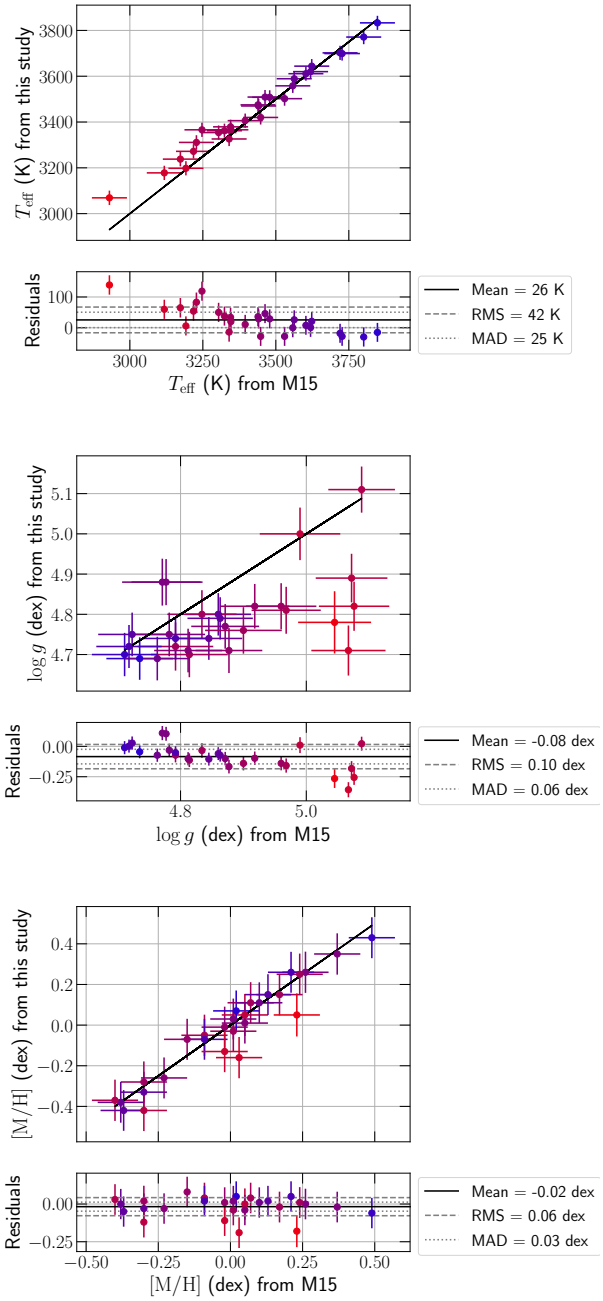

FIGURE 5.8. Retrieved parameters of our stellar sample plotted against those of Mann et al. (2015, M15). The color of the points codes the temperature from cold (red) to hot (blue). The bottom plots show the residuals with the associated average value, RMS and median absolute deviation (MAD).

Metallicity and α-enhancement

With our revised analysis, we obtain an excellent agreement between our retrieved [M/H] and those reported by Mann et al. (2015), with a dispersion of 0.06 dex, smaller than our estimated empirical error bars on this parameter. The most significant deviations from our reference are, here again, observed for the coolest stars of our sample, with shifts up to 0.2 dex. Larger dispersions are computed when comparing our results to other studies, with RMS of about 0.13 dex and 0.16 dex when comparing our results to those of Marfil et al. (2021) and Passegger et al. (2019), respectively. These discrepancies between studies further illustrate the challenges of deriving accurate stellar parameters, which depend on the adopted models and methods.

Significant discrepancies were found in Cristofari et al. (2022a) for the binary stars included in our sample, mainly for Gl 15AB. With our new analysis, the [M/H] values are found in good agreement, with a difference of 0.09 dex between that of Gl 15A and Gl 15B, compatible with our estimated empirical error bars.

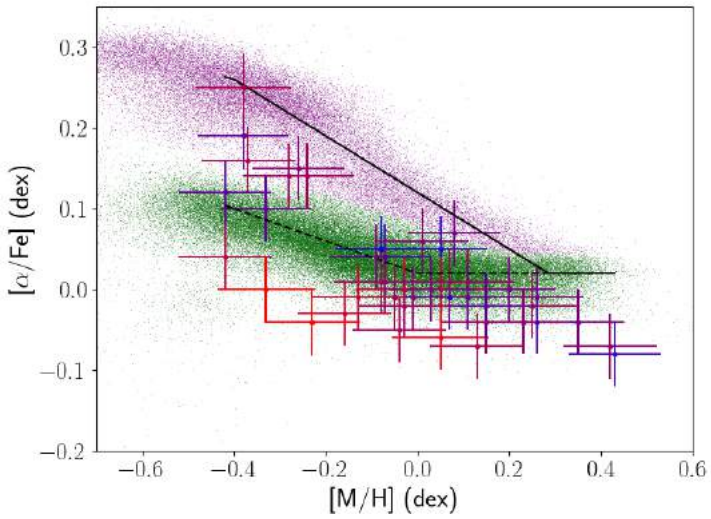

Figure 5.9. Estimated [α/Fe] plotted against [M/H]. Purple and green points mark the position of thick and thin disk giants observed with APOGEE, respectively. The solid and dashed lines present fiducial relations for the thick and thin disk, respectively. The color of the points codes the temperature, from cold (red) to hot (blue).

For the stars in our sample, our reference studies do not typically provide estimates of [α/Fe]. To ensure that our retrieved values are consistent with those expected from empirical [α/Fe]-[M/H] relations, we place our 44 targets in the [M/H]-[α/Fe] plane (see

Fig 5.9). We compare their position in this plane to the empirically estimated trends for thin and thick disk stars. We find that our estimates agree with these trends, with most of our stars located in the thin disk population. We derive larger [α/Fe] values for a few stars, suggesting they could belong to the thick disk. This is, in particular, the case for Gl 699, Gl 411, PM J21463+3813, and Gl 445, which is compatible with the high velocity of these 4 targets. These results also agree with previous studies which classified these stars in the thick disk (Cortés-Contreras, 2016; Schöfer et al., 2019).

Surface gravity

We illustrated in Chapter 4 the difficulty to constrain $\log g$ from fits of synthetic spectra. In this follow-up study, we continue the previous efforts and fit this parameter. We obtain$\log g$ estimates in better agreement with the literature and empirical relations than those previously derived – except for a few of our coolest targets – proving that our various improvements, including line selection and line parameters adjustments, helped to fix the issue.

5.6 Estimating Masses and radii

Estimating the atmospheric parameters of M dwarfs is essential to many kinds of studies, including those aimed at characterizing orbiting planets. The properties of planets are entangled with those of the host star, and putting constraints on the atmospheric parameters of stars can help to put constraints on the properties of the planets. To complete our analysis, we use our derived atmospheric parameters to compute the masses and radii of the targets in our sample. To do so, we must first obtain estimates of the bolometric luminosity for each of them.

5.6.1 Comparing $T_{\rm eff}$ to luminosity

5.6.1.1 Bolometric luminosity

Bolometric luminosity can be estimated from absolute magnitudes and bolometric corrections. For the latter, several relations were proposed, tailored to specific filters (Pecaut & Mamajek, 2013; Mann et al., 2015; Cifuentes et al., 2020). Most relations typically rely on colors computed from combinations of magnitudes obtained through different filters. Using colors usually provides more reliable corrections, as these implicitly account for

$T_{\rm eff}$ dependence. Some authors, such as Mann et al. (2015), also proposed metallicity-dependent relations for bolometric corrections, which were used to verify that for our sample of stars, the influence of metallicity on the correction was limited. These relations, however, depend on 2MASS V band magnitudes, for which measurements are sometimes missing or labeled as unreliable for our targets.

To compute the bolometric luminosities of the M dwarfs in our sample, we extensively used SIMBAD[1], extracting parallaxes, 2MASS J, and Gaia (DR2) G band apparent magnitudes. We then used the magnitude–color bolometric corrections proposed by Cifuentes et al. (2020) to obtain bolometric magnitudes (Cristofari et al., 2022b).

5.6.1.2 Locating our stars on a HR diagram

With our estimated luminosities and $T_{\rm eff}$, we place our stars in the HR diagram and compare their position to that expected from models.

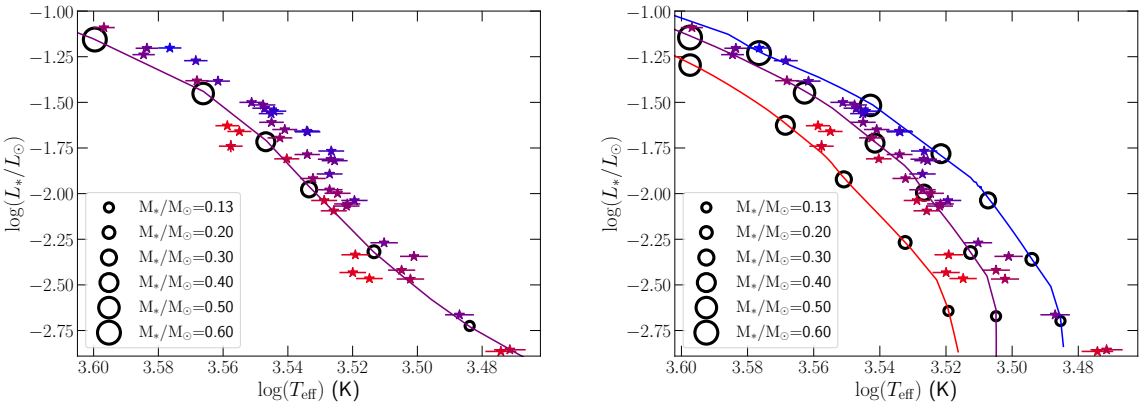

Figure 5.10. HR diagram showing the position of the stars in our sample. On both panels, the color of the points code the metallicity from red to blue (low to high metallicity respectively). On the left panel: comparison to the solar-metallicity isochrone computed by Baraffe et al. (2015) (purple line). On the right panel: comparison to the DSEP isochrones computed for [M/H] = −0.5 dex, [M/H] = 0.0 dex and [M/H] = +0.5 dex (red, purple and blue solid lines respectively). Black open circles mark the position of various stellar masses on each isochrone.

Figure 5.10 presents a comparison between our estimated $T_{\rm eff}$ and bolometric luminosities and two distinct sets of modeled isochrones computed by (Baraffe et al., 2015), and with the Dartmouth stellar evolution program (DESP, Dotter et al., 2008). We note that

[1] http://simbad.cds.unistra.fr/simbad/

the tracks predicted by the two models significantly differ, particularly for the coolest stars (below ∼3300 K). We also point out that the DSEP models are quite sensitive to metallicity. On the HR diagram, our targets are scattered around the solar-metallicity isochrones. Most of them are located between the low and high-metallicity DSEP models (computed with [M/H] = -0.5 dex and [M/H] = +0.5 dex, respectively), which is consistent with our estimated metallicities.

5.6.2 Masses and radii

We compute the masses for all of our targets using a K band magnitude – mass – metallicity relation proposed by Mann et al. (2019). We compute stellar radii from the Stefan-Boltzman law given our $T_{\rm eff}$ estimates and bolometric luminosities. Few interferometric measurements have been published for M dwarfs, and Boyajian et al. (2012) reported data for only 9 targets included in our sample. Nonetheless, interferometric measurements remain one of the most accurate approaches to stellar radius estimation, and we compare our values to those of Boyajian et al. (2012) (see Fig. 5.11). We find that

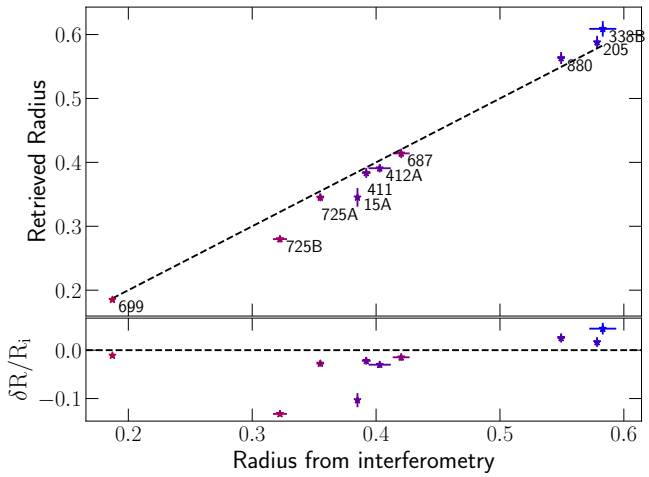

Figure 5.11. Comparison between our estimated radii and those computed from interferometric data. The dashed line marks the equality. The color of the points reflect the temperature from red (coolest) to blue (hottest).

our radii ($R_{\rm f}$) are in good agreement with those estimated from interferometric data ($R_{\rm i}$), with a dispersion on $\delta R/R_{\rm i}$ of about 5 %, with $\delta R = R_{\rm f} - R_{\rm i}$. Our estimated radius for Gl 725B is significantly smaller than that obtained from interferometry. Assuming that the bolometric luminosity computed for this target is correct, the interferometric radius

of ∼0.32 $R_\odot$ would lead to an estimated effective temperature of $T_{\rm eff}$ = 3145 ± 10 K, about 200 K lower than that reported by several studies (Fouqué et al., 2018; Marfil et al., 2021; Mann et al., 2015; Cristofari et al., 2022a). This discrepancy, also discussed in Mann et al. (2015), calls for an in-depth study of Gl 725B.

Figure 5.12 compares our estimated masses and those expected from mass-radius relations predicted by the evolutionary models mentioned in Sec. 5.6.1.2. We find a good agreement between our masses and these relations, which also agree with the values reported by Mann et al. (2015). We note a slight tendency to estimate larger radii than those predicted by the DSEP models and those of (Baraffe et al., 2015). Such tendency was previously reported in the literature (Feiden & Chaboyer, 2014; Jackson et al., 2018), and different hypothesizes were proposed to explain it, attributing the phenomenon to metallicity, modeling assumptions, or radius inflation induced by the presence of magnetic fields.

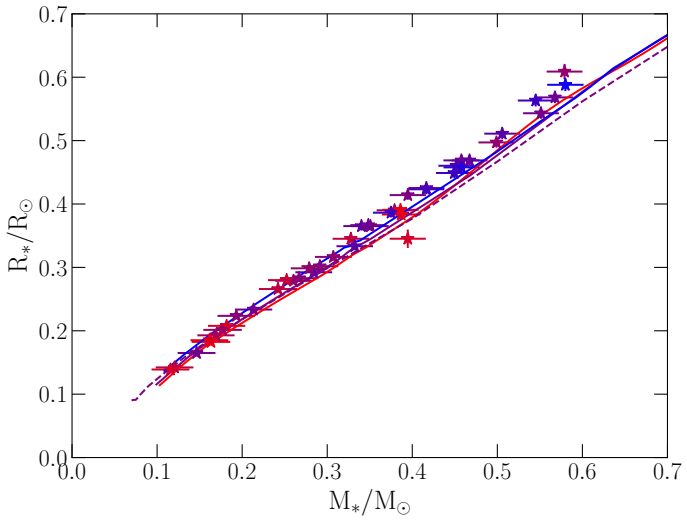

Figure 5.12. Comparison between our estimated masses and mass – radius relations derived from evolutionary models. The color of the points codes the temperature from coldest (red) to hottest (blue). The red, purple and blue solid lines present the relations predicted by the DSEP models for [M/H] = −0.5 dex, [M/H] = 0.0 dex and [M/H] = +0.5 dex respectively. The dashed purple line presents the relation computed by the models of Baraffe et al. (2015) at solar metallicity.

5.7 What have we learned?

With this new study, we improved our analysis procedure and demonstrated our ability to retrieve atmospheric parameters for M dwarfs from SPIRou spectra. Continuing the work undertaken in Cristofari et al. (2022a), we extended our analysis to 44 weakly-active M dwarfs regularly monitored in the context of the SLS and provide estimates of $T_{\rm eff}$, $\log g$, [M/H] and [α/Fe] for all of them. In particular, we show that [α/Fe] can significantly impact the derivation of other atmospheric parameters and consequently choose to fit this parameter. We find our $T_{\rm eff}$, $\log g$, and [M/H] estimates to be in good agreement with those reported in the literature and that our derived [α/Fe] are consistent with empirical relations. We then computed masses and radii, providing the community with a complete set of parameters for the targets in our sample (Cristofari et al., 2022b, see Appendix A).

The recovered parameters were obtained with several assumptions, one of them being that the effect of magnetic fields could be neglected for the targets in our sample. In practice, these stars may be weakly active, and magnetic fields can have a small impact on their spectra. Furthermore, several targets monitored with SPIRou are known to be active, and our assumption will not hold for these stars. To study more active M dwarfs and PMS stars, it is crucial to account for the impact of magnetic fields on the stellar spectra.

Chapter 6

Magnetic characterization of M dwarfs

Contents

6.1 Context

Throughout Chapters 3 to 5, we purposely neglected the impact of magnetic fields on stellar spectra. Although this assumption is viable for weakly active stars, several targets monitored with SPIRou are known to host magnetic fields.

Stellar magnetic fields can trigger a number of observational features. Cool spots and plages can appear at the surface as a consequence of the local magnetic field and generate radial velocity fluctuations. The presence of magnetic fields, more generally, can be responsible for the broadening and intensification of spectral lines through the so-called Zeeman effect. This effect, in particular, can strongly impact the shape of absorption

lines and is easily noticeable for some of the most magnetic stars monitored by SPIRou. Therefore, more advanced tools, taking into account the effect of magnetic fields on spectral lines, are required to model the spectra of magnetic stars.

In this chapter, we describe a new approach, building on our previous works, to extend the analysis to magnetic stars, and attempt to derive the average magnetic flux of some SLS targets. The results presented in this chapter are part of Cristofari et al. (in prep, see Appendix A).

6.2 Zeeman effect and polarized radiative transfer

In this section, we provide a very brief overview of the Zeeman effect and its impact on the spectrum of stars. We then briefly describe how the modeling approach presented in Chapter 3 is revised to account for the presence of magnetic fields in stars monitored with SPIRou.

6.2.1 Zeeman splitting of energy levels

Energy levels of atoms placed in a uniform magnetic field described by the vector $\boldsymbol{B}$ are split into several components. This effect is commonly known as the Zeeman effect (Zeeman, 1897), and the number of levels depends on the atomic structure and the considered transition. Under the weak-field approximation, meaning that the spin-orbit interaction dominates over the effect of the external magnetic field (Landi Degl'Innocenti & Landolfi, 2004), each energy level E_J, with J the total angular momentum, splits into $2J+1$ sub-levels, each with an energy of:

$$E_{J,M} = E_{J,0} + \mu_0 g B M$$

with M ranging from $-J$ to J in steps of 1, B the field intensity, μ_0 the Bohr magneton, and g the Landé factor of the corresponding energy level. With this expression, we see that the energy levels are distributed around that of the transition with no magnetic field. Moreover, the energy levels depend on the magnetic field strength, and the Landé factor. The latter can be computed from the weak-field approximation as:

$$g = 1 + \frac{1}{2}\frac{J(J+1) + S(S+1) + L(L+1)}{J(J+1)}$$

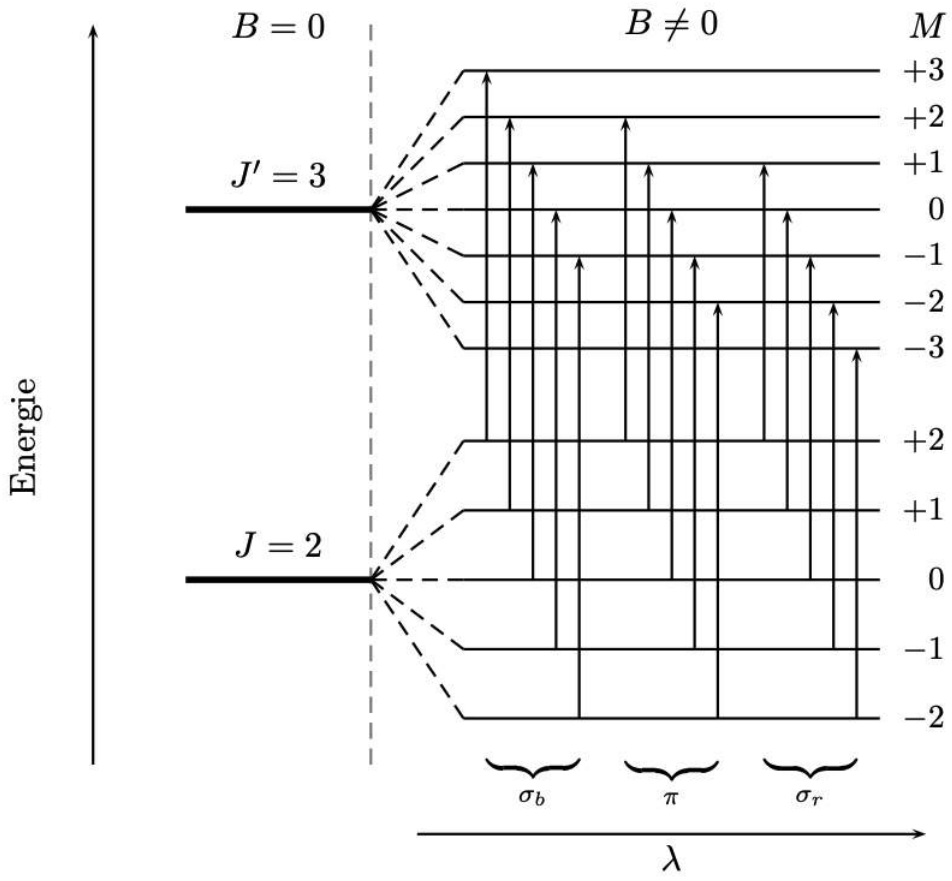

Figure 6.1. Splitting of energy levels within a magnetic field. Taken from Dr. Julien Morin's PhD thesis (http://thesesups.ups-tlse.fr/816/). The resulting line profile is illustrated in Fig. 6.2.

for $J \neq 0$, and with L and S the angular momentum and the particle's spin, respectively. The Landé factor only depends on J, L and S, and relates to the sensitivity of one specific energy level to the magnetic field.

Let us then consider a transition occurring between two energy levels, $E_{J,0}$ and $E_{J',0}$. Placed within a uniform magnetic field, both levels are split, and all transitions between $E_{J,M}$ and $E_{J',M}$ such that $M - M' \in \{-1, 0, 1\}$ are allowed. This results in (if $J' > J$) $2J + 1$ transition with $M = 0$, referred to as π transitions, and $2(J + J')$ transitions with $M \in \{-1, 1\}$, referred to as σ transitions, amounting to a total of $4J + 2J' + 1$ allowed transitions (see Fig. 6.1 for an example).

In the presence of a non-zero magnetic field, π and σ transitions are shifted in energy, and the different Zeeman components consequently absorb at different wavelengths, which

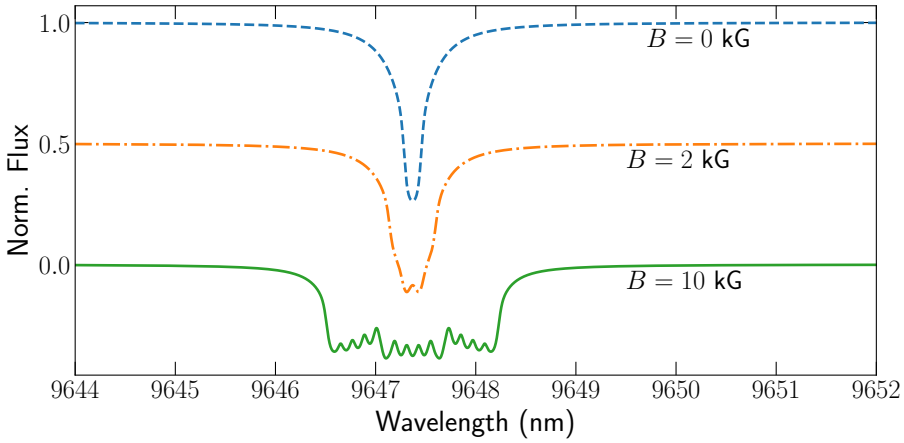

Figure 6.2. Impact of the magnetic field strength of the profile of one Ti line at 965.0 nm. The Ti line was modeled with `ZeeTurbo` (see Sec. 6.3) with a purely radial magnetic field configuration (monopole). An arbitrary offset is applied for better readability. The line is a results from a transition between two energy levels with $J = 2$ and $J' = 3$.

can be blue or red-shifted with respect to the position of the absorption line in a $B = 0$ magnetic field (see Fig. 6.2). The σ transitions are generally separated into two groups: those with $M = 1$ which absorb at shorter wavelengths and labeled σ_b; and those with $M = -1$ which absorb at longer wavelengths and labeled σ_r. The splitting of energy levels is, in most cases, insufficient for these transitions to be resolved and leads to an apparent broadening and intensification (Landi Degl'Innocenti & Landi Degl'Innocenti, 1981; Stift & Leone, 2003) of the spectral lines (see, for example, the 2 kG case in Fig. 6.2). The broadening is directly related to the Landé factors of the transitions and, consequently, differs for each spectral line.

The different transitions induced by the presence of magnetic fields are polarized, and the polarization of the light viewed by an observer depends on the orientation of the magnetic field with respect to the line-of-sight (see Fig. 6.3). In particular, if the magnetic field is aligned with the line-of-sight, an observer would only see circularly polarized σ transitions. If the line-of-sight is perpendicular to the field, however, the observer would only see linearly polarized transitions, but would see both π and σ components. A useful description of the polarization of light is obtained through the definition of the Stokes vectors I, Q, U, and V, with I the unpolarized light intensity, Q the difference between light beams observed through 2 linear polarizers with orientations at 90° from one another, U the same than Q but with an orientation tilted by 45°, and V the difference between orthogonal circularly polarized beams.

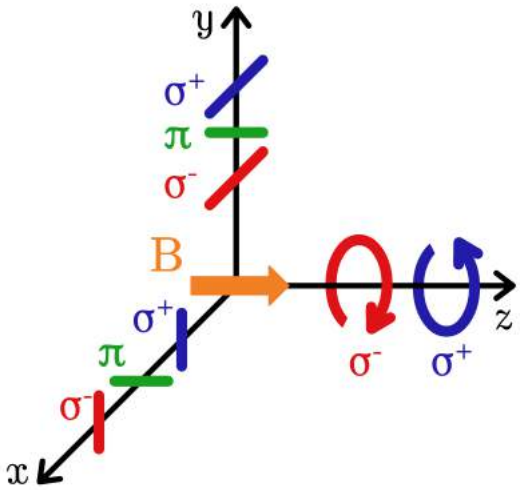

Figure 6.3. Polarization of the Zeeman components. Taken from Dr Lisa Lehmann's PhD thesis (https://doi.org/10.17630/10023-20354).

6.2.2 Including the magnetic fields in stellar synthesis models

6.2.2.1 Modified opacities and magnetic field geometry

Because the Zeeman effect splits the energy levels, it is necessary to consider each Zeeman sub-component in the opacity computation for a given magnetic field. To account for magnetic fields in the photosphere, the absorption coefficients for the σ and π Zeeman components must be computed for each element of the stellar disk, given the local magnetic field and intensity for that element (see Fig. 6.4 for a schematic representation of the synthesis process). Computing the absorption coefficient for each element of the stellar disk also allows us to compute the emergent spectrum assuming different magnetic field topologies.

6.2.2.2 Polarized transfer equation

Considering partially polarized light requires to revisit the classical radiative transfer equation mentioned in Sec 3.1.2.1. Introducing the Stokes vector $\boldsymbol{I}$, the source function vector $\boldsymbol{S}$ and the opacity matrix $\boldsymbol{K}$, the equation becomes (Landi Degl'Innocenti & Landi Degl'Innocenti, 1985):

$$\frac{\mathrm{d}\boldsymbol{I}}{\mathrm{d}s} = -\boldsymbol{K}(\boldsymbol{I} - \boldsymbol{S})$$

In this equation, $\boldsymbol{I} = (I, Q, U, V)^T$ where I, Q, U and V are the Stokes components and $\boldsymbol{S} = (S_I, S_Q, S_U, S_V)^T$ is the source function for the various Stokes parameters. Neglecting

the effect of polarization on the source function, one has $\boldsymbol{S} = (S_I, 0, 0, 0)^T$, and under LTE, one can approximate S_I by the Planck function (see Landi Degl'Innocenti & Landolfi, 2004, for a detailed derivation). The opacity matrix can then be written as (Landi Degl'Innocenti & Landi Degl'Innocenti, 1981):

$$\boldsymbol{K} = \begin{pmatrix} \eta_I & \eta_Q & \eta_U & \eta_V \\ \eta_Q & \eta_I & \rho_V & -\rho_U \\ \eta_U & -\rho_V & \eta_I & \rho_Q \\ \eta_V & \rho_U & -\rho_Q & \eta_I \end{pmatrix}$$

where η_I, η_Q, η_U, η_V relate to the absorption for different polarization states, and ρ_Q, ρ_U, ρ_V describe the coupling of Stokes components resulting from anomalous dispersion effects. The computation of synthetic spectra therefore requires to solve this new version of the radiative transfer equation, for which solutions have been published (Martin & Wickramasinghe, 1979).

6.3 Modeling the Zeeman effect

We mentioned in Chapter 3 the multiple spectral synthesis tools available today, several of which are freely accessible. The number of codes designed to incorporate Zeeman splitting is much more limited, and very few of these tools are public. In this Section, we briefly introduce the `Zeeman` code and its limitations, before describing our implementation of the Zeeman effect in `Turbospectrum`.

6.3.1 The `Zeeman` code

`Zeeman` is a spectral synthesis code originally developed by Landstreet (1988); Wade et al. (2001), and later updated by Folsom et al. (2012, 2016). This `FORTRAN` program has been widely used in recent studies (Folsom et al., 2018, 2020; Petit et al., 2021; Folsom et al., 2022), and performs fast spectral synthesis from `MARCS` model atmospheres.

The `Zeeman` code contains several `FORTRAN` subroutines allowing one to perform synthesis on small spectral windows and to read data directly from VALD line lists. The resolution of the radiative transfer equation follows the solution of Martin & Wickramasinghe (1979) and `Zeeman` allows for the computation of opacities for multipolar magnetic topologies.

We attempted to use `Zeemann` to analyze stars in our sample. We found significant differences between synthetic spectra computed with `Zeemann` and `Turbospectrum` in the

non-magnetic case, particularly at low temperatures (< 3500 K). Part of these differences are likely related to the fact that the `Zeemann` code does not consider molecules at all, which limits its capability to model spectra of cool stars.

To properly analyze the stars in our sample, we need a code capable of handling molecules and polarized radiative transfer. Given the good results obtained so far with `Turbospectrum` (see Chapter 5), we undertook to modify `Turbospectrum` to include the Zeeman effect and polarized radiative transfer to its functionalities.

6.3.2 `ZeeTurbo` – Incorporating the polarized radiative transfer and the Zeeman effect within `Turbospectrum`

Building from `Turbospectrum` and `Zeeman`, borrowing code from both programs, we introduce a new version of `Turbospectrum`, baptized `ZeeTurbo` in the rest of this manuscript.

6.3.2.1 Code structure and functionalities

`ZeeTurbo` borrows line opacity computations and chemical equilibrium routines from `Turbospectrum`, and computes Zeeman components, solves the polarized radiative transfer equation and performs disk integration with routines inspired and adapted from the `Zeeman` code. Figure 6.4 presents the overall process of `ZeeTurbo` to provide the reader with an overview of the main program blocks.

Let us briefly describe the main modifications and additions to the original code. `ZeeTurbo`, like `Zeeman`, requires lower and upper Landé factors for the computation of all the σ and π components. We therefore adapted the line list format used by `Turbospectrum` to include Landé factors reported in the VALD line lists when available. If Landé factors are missing, `ZeeTurbo` will parse the atomic structure to compute g-factors for the upper and lower energy levels assuming LS coupling. To ensure backward compatibility, if the line list format does not allow for the computation of the Zeeman components, the line is treated as insensitive to the magnetic field. This is the case of molecular line lists for which Landé factors are often missing and which are for now assumed to be insensitive to the magnetic field (which is a good assumption for some molecular lines, such as the CO band redward of ~ 2.3 μm).

The main program of `Turbospectrum`, bsyn, was slightly modified to comply with the scheme presented in Fig. 6.4. For each stellar disk element, before entering opacity calculations, we compute the local magnetic field given a requested geometry, and the

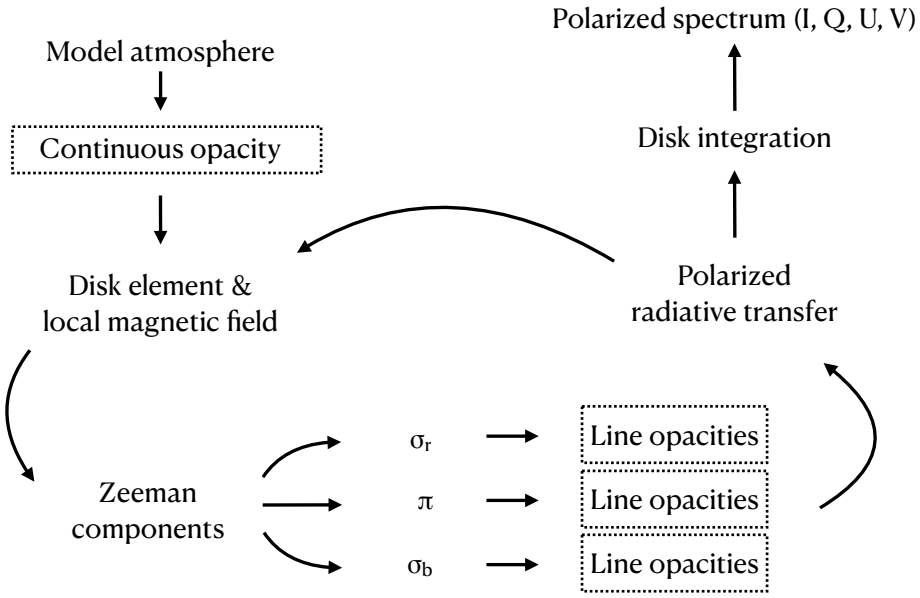

Figure 6.4. `ZeeTurbo` schematic. The dashed boxes indicate the `Turbospectrum` routines.

resulting local splitting. The opacity computations are kept identical to that used in `Turbospectrum` but are called three times, once for the σ_r, σ_b, and π components. The polarized radiative transfer routine, adapted from that of the `Zeeman` code, is called for each disk element.

6.3.2.2 Benchmark and performances

Before using `ZeeTurbo` for Science purposes, it is essential to ensure that it behaves as expected. We therefore run a few tests and comparisons. First, because line opacity computations are the same, `ZeeTurbo` should be able to synthesize spectra comparable to those computed with `Turbospectrum` in non-magnetic cases. Second, when considering a given magnetic field topology and strength, the number of components and their relative strengths computed with `ZeeTurbo` should be compatible with those predicted by the `Zeeman` code. We therefore test our program by comparing the outputs of the three programs.

Figure 6.5 presents a comparison between spectra synthesized with `Turbospectrum` and `ZeeTurbo` using the same model atmosphere and line lists. We find excellent agreement between the spectra in both molecular and atomic lines. This illustrates the ability of

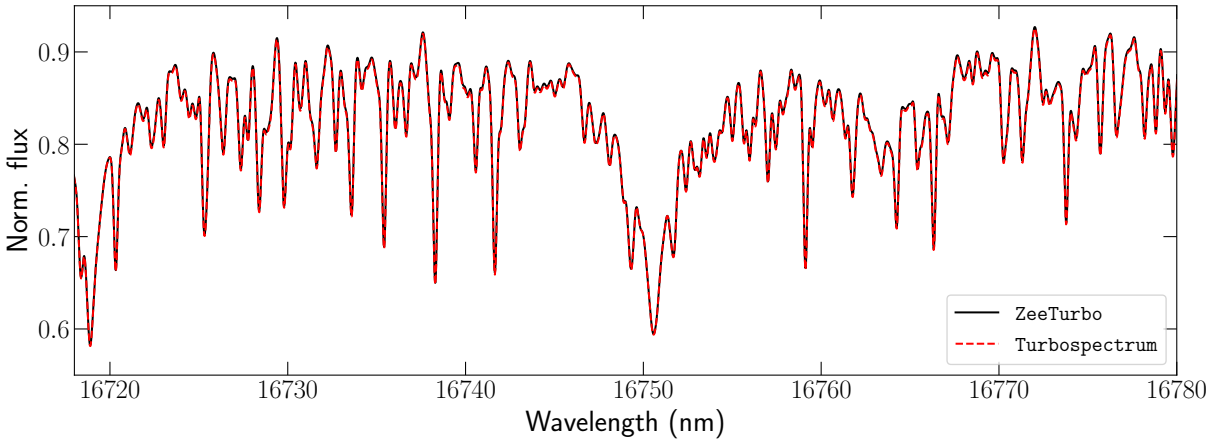

FIGURE 6.5. Comparison between `ZeeTurbo` and `Turbospectrum` spectra. Models were computed assuming $T_{\rm eff} = 3200$ K, $\log g = 5.0$ dex and [M/H] = 0.0 dex.

our program to properly reproduce non-magnetic spectra, and shows that the change of radiative transfer routine and disk integration induces negligible differences in the output spectra.

We then compare the spectra computed with our code and those obtained with `Zeeman`. For this comparison to be meaningful, we made sure to compare spectra at higher temperatures (e.g. $T_{\rm eff} > 5000$ K), where `Zeeman` and `Turbospectrum` agree best. We consider a magnetic monopole with given field strength in both `ZeeTurbo` and `Zeeman`, using the same input line lists. Figure 6.6 presents such comparison for a few magnetic-sensitive lines. Here again, we find excellent agreement between the two codes, demonstrating that the computation of the Zeeman components is properly implemented.

The multiple tests we performed allowed us to confirm that `ZeeTurbo` is behaving as expected. We can now use `ZeeTurbo` for scientific purposes.

6.4 A simple model for the characterization of magnetic M dwarfs

Inspired by previous works (Kochukhov & Reiners, 2020; Reiners et al., 2022), we attempt to reproduce the overall effect of magnetic fields on the template spectra by combining synthetic models.

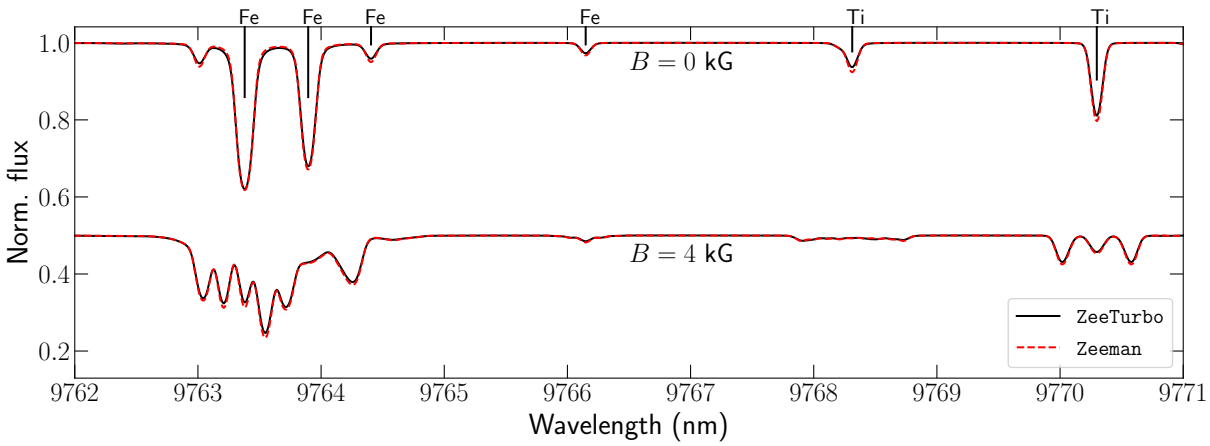

Figure 6.6. Comparison between `ZeeTurbo` and `Zeeman` spectra. Models were computed assuming $T_{\rm eff} = 6000$ K, $\log g = 4.5$ dex and [M/H] = 0.0 dex.

6.4.1 Modeling stellar spectra with multiple magnetic fields

We compute synthetic spectra for field strengths of 0, 2, 4, 6, and 8 kG. Following Shulyak et al. (2014); Kochukhov & Reiners (2020); Reiners et al. (2022), we choose to model a spectrum as the combination of non-magnetic and magnetic stellar spectra computed with a simple topology, i.e., assuming that the magnetic field is always radial to the stellar surface (monopoles). For a given observation, the spectra are then modeled by a linear combination of the spectra computed for various field strengths, so that:

$$S = a_0 S_0 + a_2 S_2 + a_4 S_4 + a_6 S_6 + a_8 S_8$$

where $S_{\rm X}$ is the spectrum computed for a field strength of X kG, and a_0 to a_8 are the corresponding filling factors so that $a_0 + a_2 + a_4 + a_6 + a_8 = 1$ and $a_{\rm X} > 0$ for any field X. To fit a spectrum to an observation spectrum then consists in deriving the filling factors that lead to the lowest χ^2.

6.4.2 Revised analysis, an MCMC approach

In Chapters 4 & 5, the best fits were estimated by studying the χ^2 surface spanning a given range of all parameters around the minimum. For a small number of dimensions, this method presents the great advantage of being fast and reliable. If the number of dimensions becomes too large, however, the number of points that must be computed around the grid minimum becomes prohibitive.

We revise our analysis, replacing the grid fit by a Markov chain Monte Carlo (MCMC). While such a process is slower than a simple grid search, optimization of our codes allowed us to significantly reduce computation time[1]. The implementation relies on the `emcee`[2] `Python` package (Foreman-Mackey et al., 2013), and allows us to derive $T_{\rm eff}$, $\log g$, [M/H], [α/Fe] and the filling factors from posterior distributions. Priors are set to ensure that the filling factors are all positive and that their sum is equal to one, while no additional constraints are set on the atmospheric parameters. Our analysis relies on the comparison of Stokes I profiles only (unpolarized spectra) to SPIRou templates, with continuum adjustment, broadening unctions and χ^2 scaling similar to those used in our previous studies.

6.5 Application to the characterization of stars

In this section, we present the results of our new method aimed at estimating both the atmospheric parameters of the stars and the average magnetic field strength of active targets. We first conduct a set of simulations to assess the performances of our revised approach before applying our technique to stars monitored within the SLS.

6.5.1 Estimating filling factors

Our process must be able to recover input filling factors. To assess our capability to do so, we model template spectra and attempt to estimate the filling factors from the models. We proceed with the following method:

(1) We first draw a given set of filling factors, and compute a synthetic spectrum as the combination of synthetic spectra with fixed monopolar magnetic fields (see Sec. 6.4.2).
(2) Noise is added to the synthetic spectrum, given the typical blaze and SPIRou throughput, and is then projected on a typical wavelength grid for SPIRou.
(3) We perform an MCMC with 200 walkers and 2000 steps, which is found to be typically sufficient for walkers to converge towards the best solution.
(4) We then run our process on the modeled template spectrum, estimate atmospheric parameters and filling factors from posterior distributions, and compare them to those used to produce the model.

[1] Optimization of our `Python` codes was possible thanks to the `Numba` just-in-time compilation module.
[2] https://emcee.readthedocs.io/

Figure 6.7 presents the result of a simulation on a model generated with SNR in the H band of 500. The retrieved parameters agree well with those used to generate the model template. We observe some correlation between the filling factors. To assess

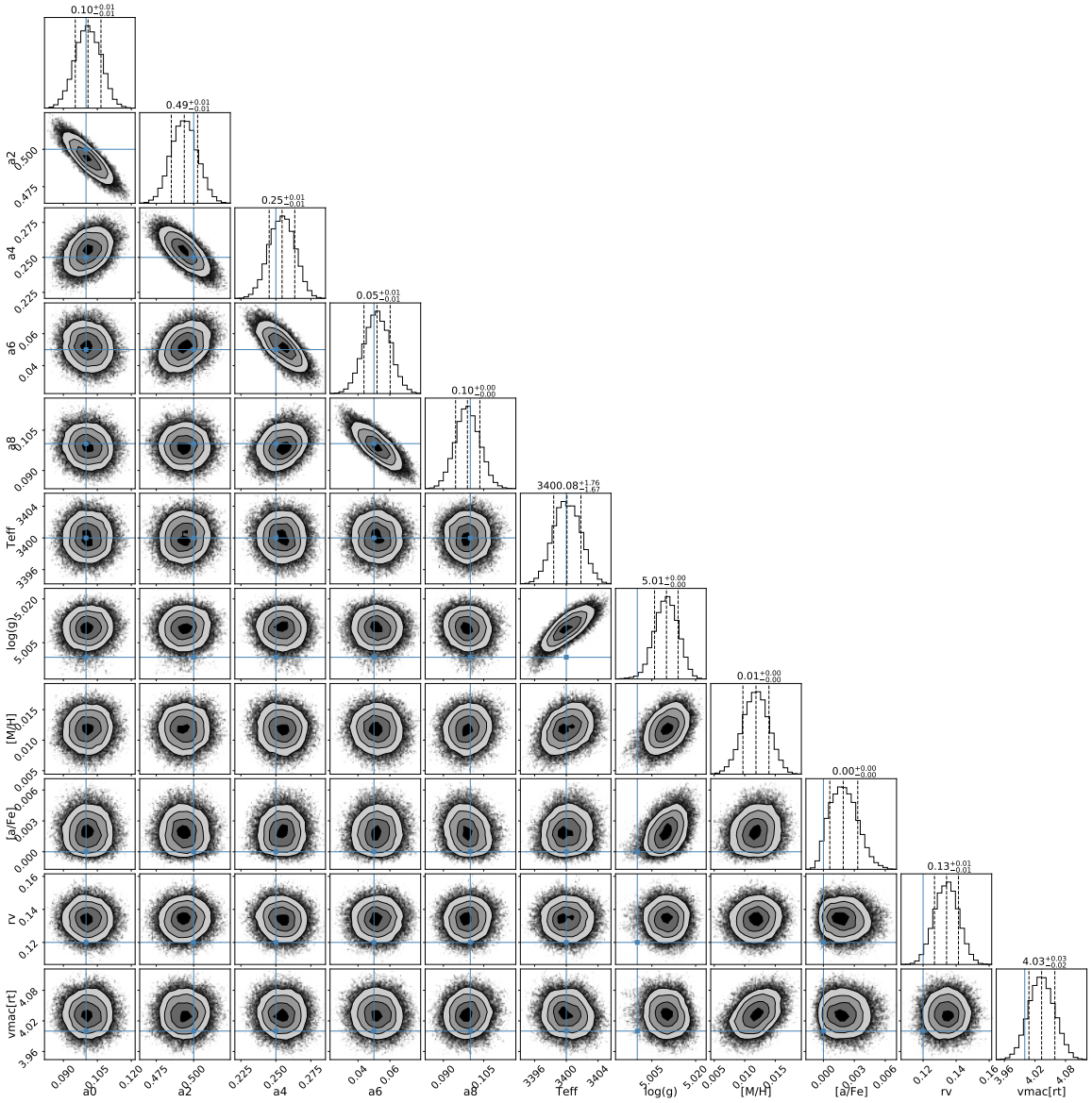

Figure 6.7. Corner plots showing the posterior distribution on all fitted parameters. The input parameters are located by the blue lines.

the precision of our tools, we repeat the simulations with 50 realizations of noise, and compare for each simulation the retrieved parameters to those used to compute the input models (see Fig. 6.8). For each parameter, we compute the reduced χ^2 on the residuals to assess the precision of our method. We find that our method achieves satisfactory precision. A comparison between an analysis performed with and without adjustment

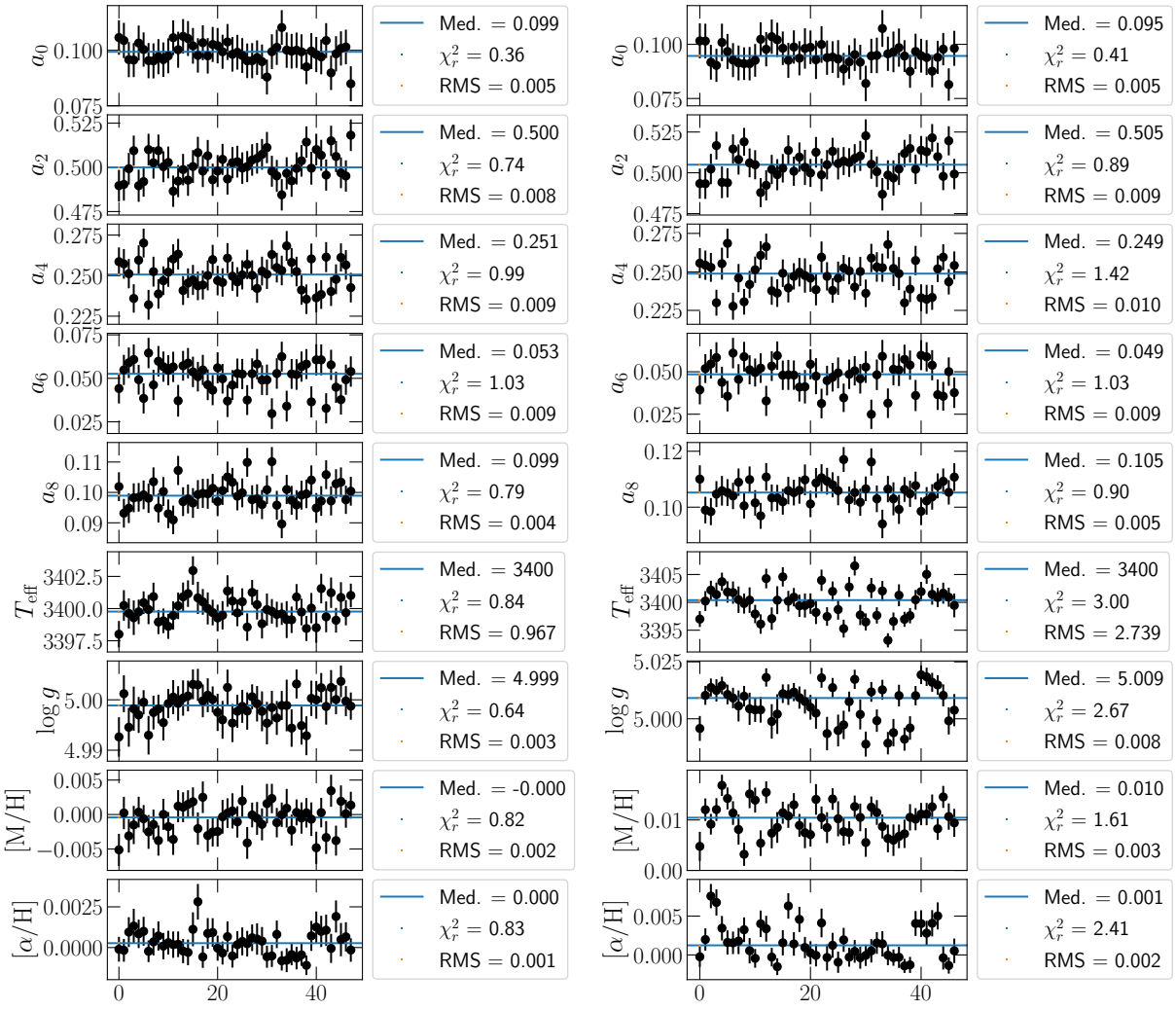

FIGURE 6.8. Results of 50 simulations. We present the residuals between the retrieved parameters and those used to generate the model. For each series of points, we compute the median and RMS. We also compute a reduced χ^2 on the residuals. The left column presents the results of the analysis with no adjustment of the continuum, while the right column presents the results of the analysis performing the adjustment of the continuum.

of the continuum allows us to assess the impact of the latter. In particular, we see that the adjustment step leads to larger scattering in the retrieved parameters, and offsets reaching up to 0.01 dex in $\log g$ and [M/H]. We find that these offsets depend on the SNR, and can reach up to 0.1 dex in $\log g$ and 20 K in $T_{\rm eff}$ if the SNR is assumed to be 100. In practice, these levels are much lower than those expected for our template spectra, reaching a SNR of a few thousand. These results, in particular, illustrate that the

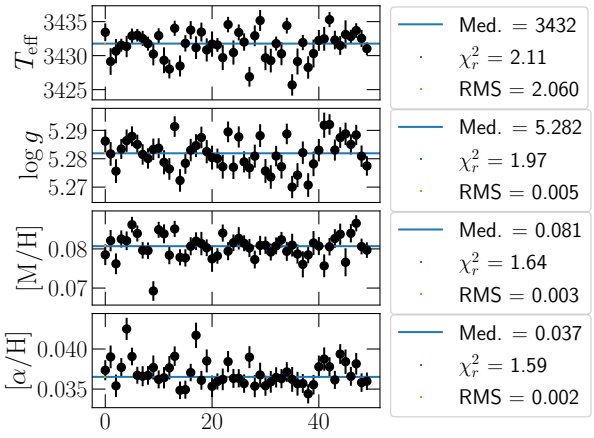

Figure 6.9. Same as Fig. 6.8 but with no field considered in the analysis.

error bars estimated from posterior distributions only partly account for the uncertainty associated with our method.

Additionally, our simulation framework allows us to assess the impact of performing an analysis on an active star with non-magnetic models. To do so, we run once again the analysis on the previously computed modeled templates, but omit the filling factors in the fitting procedure, hence deriving only atmospheric parameters (see Fig. 6.9). In the currently presented case, we recover systematic shifts in the atmospheric parameters of up to $\sim$ 30 K in $T_{\rm eff}$, $\sim$ 0.28 dex in $\log g$. Smaller biases are observed on [M/H] and [α/Fe], with shifts of $\sim$ 0.08 dex and $\sim$ 0.04 dex, respectively.

6.5.2 Deriving the magnetic field strengths of SLS targets

We applied our code to a few strongly magnetic targets monitored with SPIRou, namely AU Mic, AD Leo and EV Lac. All results presented in this section are part of Cristofari et al. (in prep, see Appendix A).

6.5.2.1 The case of AU Mic = Gl 803

AU Mic is a young star that attracted significant attention in the past years (Boccaletti et al., 2018; Kochukhov & Reiners, 2020; Martioli et al., 2020, 2021; Klein et al., 2021, 2022). Its magnetic field has been studied through various approaches, and recently, through the modeling of spectral lines (Kochukhov & Reiners, 2020; Reiners et al., 2022). Using our new model, we estimate its average magnetic flux and atmospheric parameters.

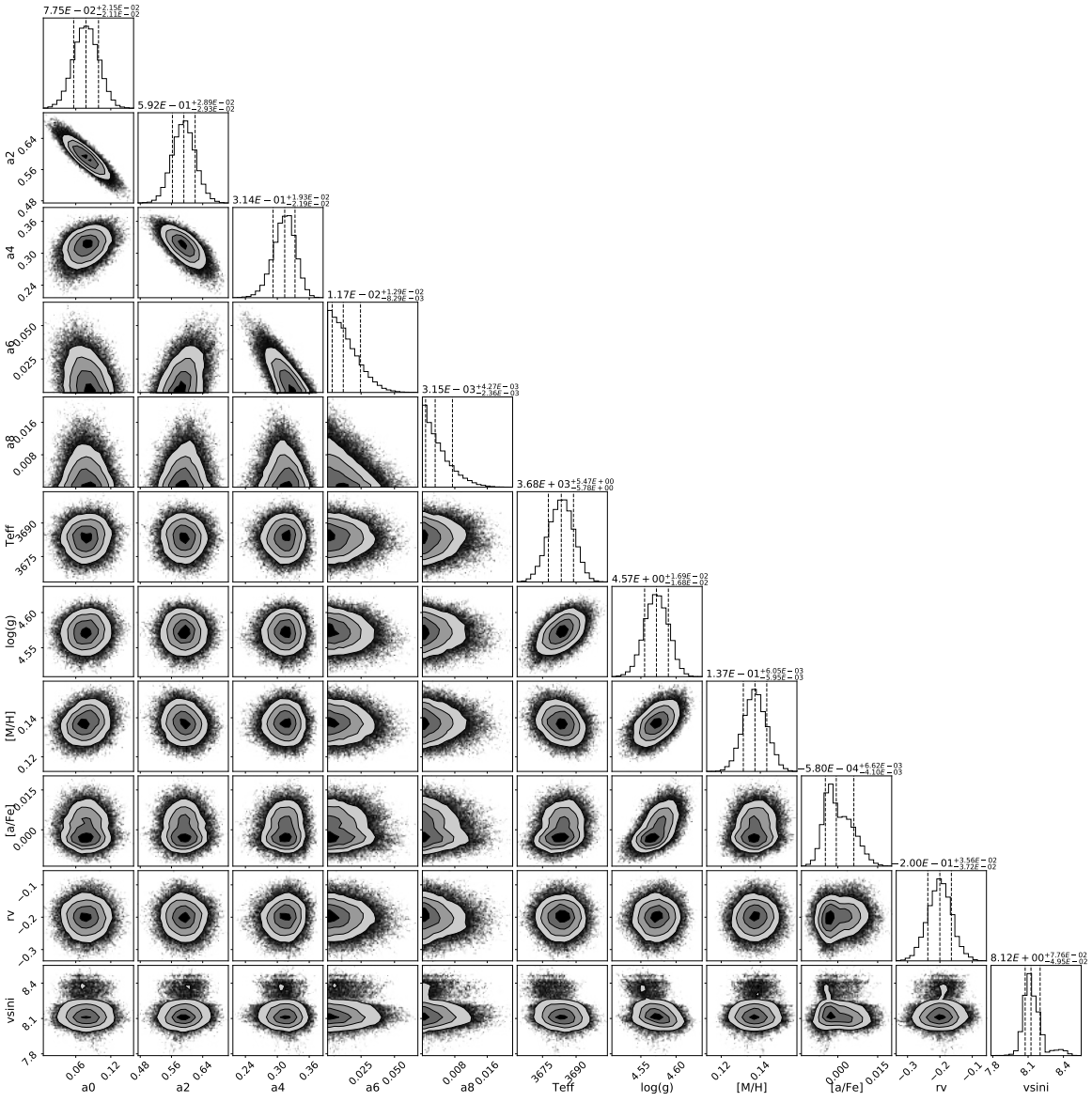

Figure 6.10. Same as Fig. 6.7 for AU Mic

Previous studies have provided constraints on AU Mic rotation velocity, atmospheric parameters and magnetic field strength. For instance Kochukhov & Reiners (2020) discussed the impact of radial-tangential macroturbulence ($\zeta_{\rm RT}$) on the estimation of $v \sin i$. In our previous works, we modeled all broadening contributions by a Gaussian, including the macroturbulence. In an attempt to reproduce these results, we fix the value of $\zeta_{\rm RT} = 4.5$ km s^{-1} and fit $v \sin i$. Figure 6.10 presents the resulting corner plot for this star. From posterior distributions, we estimate $T_{\rm eff} = 3683 \pm 6$ K, $\log g = 4.57 \pm 0.02$ dex, [M/H] $= 0.13 \pm 0.01$ dex and $[\alpha/{\rm Fe}] = 0.00 \pm 0.01$ dex. Following our previous results,

we estimate empirical error bars by quadratically adding 30 K, 0.05 dex, 0.10 dex and 0.04 dex to the these error bars on $T_{\rm eff}$, $\log g$, [M/H] and [α/Fe], respectively. The results are presented with empirical error bars in Table 6.1. We note that the error bars estimated from posterior distributions are closer to the formal error bars introduced in Chapter 4 than our empirical error bars. Our retrieved $T_{\rm eff}$ is in good agreement with previous estimates (Afram & Berdyugina, 2019). Recent interferometric measurements (White et al., 2015; Gallenne et al., 2022) of the star have provided values of angular diameters and allowed us to put constraints on its radius and $\log g$. The latter is expected to be closer to 4.4 dex than 4.6 dex. We also recover a projected rotational velocity $v \sin i = 8.1 \pm 0.1$ km s^{-1}, in good agreement with that reported in Kochukhov & Reiners (2020) when fixing $\zeta_{\rm RT} = 4.5$ km s^{-1}. If we substitute the radial-tangential macroturbulence for an isotropic Gaussian macroturbulence of FWHM $\zeta_{\rm G} = 4.5$ km s^{-1}, the rotational velocity is then found to be $v \sin i = 8.5 \pm 0.1$ km s^{-1}. We estimate the average magnetic field of AU Mic to be $\sim 2.55 \pm 0.05$ kG. This value compares well to values reported in the literature of, for instance, 2.1–2.3 kG (Kochukhov & Reiners, 2020) and 3.01 ± 0.22 kG (Reiners et al., 2022). We also find that the distribution of the field strength across filling factors to be consistent with the results of Kochukhov & Reiners (2020), with most of the magnetic power distributed on the 2 kG and 4 kG components (see Fig. 6.11), and about 8 % of non-magnetic flux.

We run an additional analysis on AU Mic, this time fixing the value of $\log g$ to 4.4 dex. In that case, we retrieve a $T_{\rm eff} = 3648 \pm 4$ K and [M/H] $= 0.10 \pm 0.01$ dex, $v \sin i = 8.5 \pm 0.1$ km s^{-1}, and $< B >= 2.69 \pm 0.05$ kG. These values are still somewhat consistent with those reported in the literature. We note, in particular, that fixing $\log g$ to a lower value results in a larger $v \sin i$ estimate.

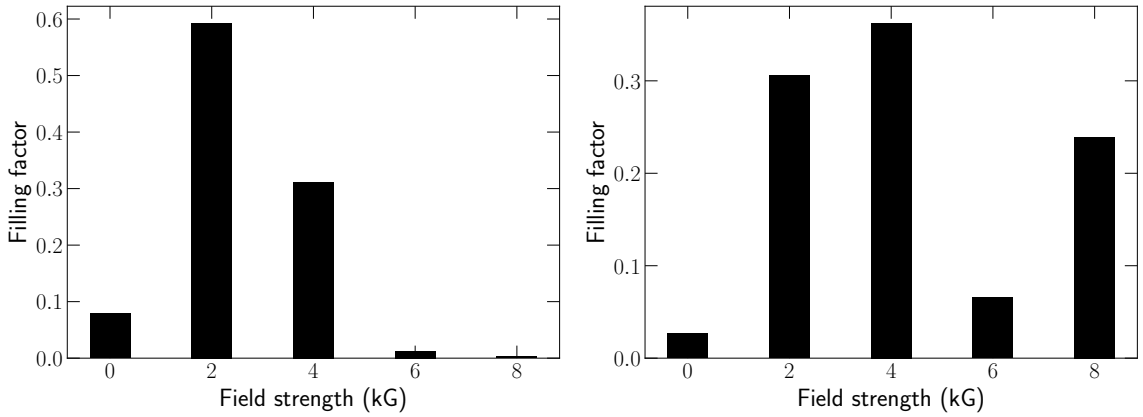

Figure 6.11. Retrieved filling factors for AU Mic (left) and EV Lac (right).

Table 6.1. Retrieved stellar parameters and magnetic fields for our sample of targets. Values given with no associated uncertainties were fixed.

Star	Gliese ID	$T_{\rm eff}$ (K)	$\log g$ (dex)	[M/H] (dex)	[α/Fe] (dex)	$v \sin i$ (km s^{-1})	$\zeta_{\rm RT}$ (km s^{-1})	$\zeta_{\rm G}$ (km s^{-1})	$< B > (kG)$
AU Mic	Gl 803	3683 ± 31	4.57 ± 0.05	0.13 ± 0.10	0.00 ± 0.04	8.1 ± 0.1	4.5	–	2.53 ± 0.05
AD Leo	Gl 388	3463 ± 31	4.89 ± 0.05	0.23 ± 0.10	0.00 ± 0.04	3	1.9 ± 0.2	–	2.97 ± 0.05
EV Lac	Gl 873	3343 ± 31	4.88 ± 0.05	0.01 ± 0.10	0.02 ± 0.04	4	2.3 ± 0.2	–	4.37 ± 0.06
DS Leo	Gl 410	3824 ± 31	4.79 ± 0.05	0.01 ± 0.10	0.04 ± 0.04	2	0.4 ± 0.3	–	0.70 ± 0.04
AU Mic	Gl 803	3685 ± 31	4.58 ± 0.05	0.13 ± 0.10	0.00 ± 0.04	8.5 ± 0.1	–	4.5	2.53 ± 0.05
AD Leo	Gl 388	3465 ± 31	4.90 ± 0.05	0.23 ± 0.10	0.00 ± 0.04	3	–	2.2 ± 0.2	2.97 ± 0.05
EV Lac	Gl 873	3346 ± 31	4.89 ± 0.05	0.03 ± 0.10	0.01 ± 0.04	4	–	2.5 ± 0.2	4.31 ± 0.06
DS Leo	Gl 410	3825 ± 30	4.79 ± 0.05	0.01 ± 0.10	0.04 ± 0.04	2	–	0.4 ± 0.3	0.69 ± 0.03

The reliable constraint on magnetic field strength can be explained because our process relied on sensitive atomic lines, and insensitive atomic and molecular lines. These are illustrated with the best obtained fit in Fig 6.12 (see Cristofari et al., in prep, Appendix A, for additional examples). From this figure, the impact of the magnetic field is clear and its inclusion obviously improves the fit quality. This is particularly visible with the peculiar shape of the Na line at 22089.7 Å. The comparisons of the best fit to the templates demonstrate further the need to include magnetic fields in the modeling of active stars, and the ability to do so with `ZeeTurbo`.

We note that the filling factors computed for AU Mic are mainly distributed on the 2 and 4 kG components. In particular, the filling factor derived for the 8 kG component is close to 0. We therefore carry out a new analysis, this time omitting the 6 and 8 kG models. For this test, we fix $\zeta_{\rm RT}$ to 4.5 dex, and fit $v \sin i$. We find that the retrieved atmospheric parameters are almost unchanged, with $T_{\rm eff} = 3682 \pm 6$ K, $\log g = 4.57 \pm 0.02$ dex, [M/H] $= 0.13 \pm 0.01$ dex and [α/Fe] $= 0.00 \pm 0.01$ dex. We obtain slightly lower values for the magnetic field, of about 2.50 ± 0.04 kG, which can be expected as the filling factor a_6 was not strictly 0 in the previous case. We also recover a $v \sin i = 8.2 \pm 0.1$ km s^{-1}, similar to our previous estimate.

6.5.2.2 The case of EV Lac = Gl 873

EV Lac is a well-known strongly magnetic target extensively monitored in the context of the SLS, with an estimated $v \sin i$ of ~ 4 km s^{-1} (Morin et al., 2008). In this case, we therefore fix the value of $v \sin i$ and fit $\zeta_{\rm RT}$. For this star, we retrieve atmospheric parameters such that $T_{\rm eff} = 3343 \pm 6$, $\log g = 4.88 \pm 0.02$, [M/H] $= 0.03 \pm 0.01$ and [α/Fe] $= 0.02 \pm 0.01$. These are in good agreement with previously reported estimates (Fouqué et al., 2018; Maldonado et al., 2020). Our $\log g$ is also in good agreement with reported masses and radii ($M = 0.369 \pm 0.005$ M$_\odot$ & $R = 0.365 \pm 0.005$ R$_\odot$ Schweitzer et al., 2019). For this star we recover an average magnetic field $< B >= 4.37 \pm 0.06$ kG,

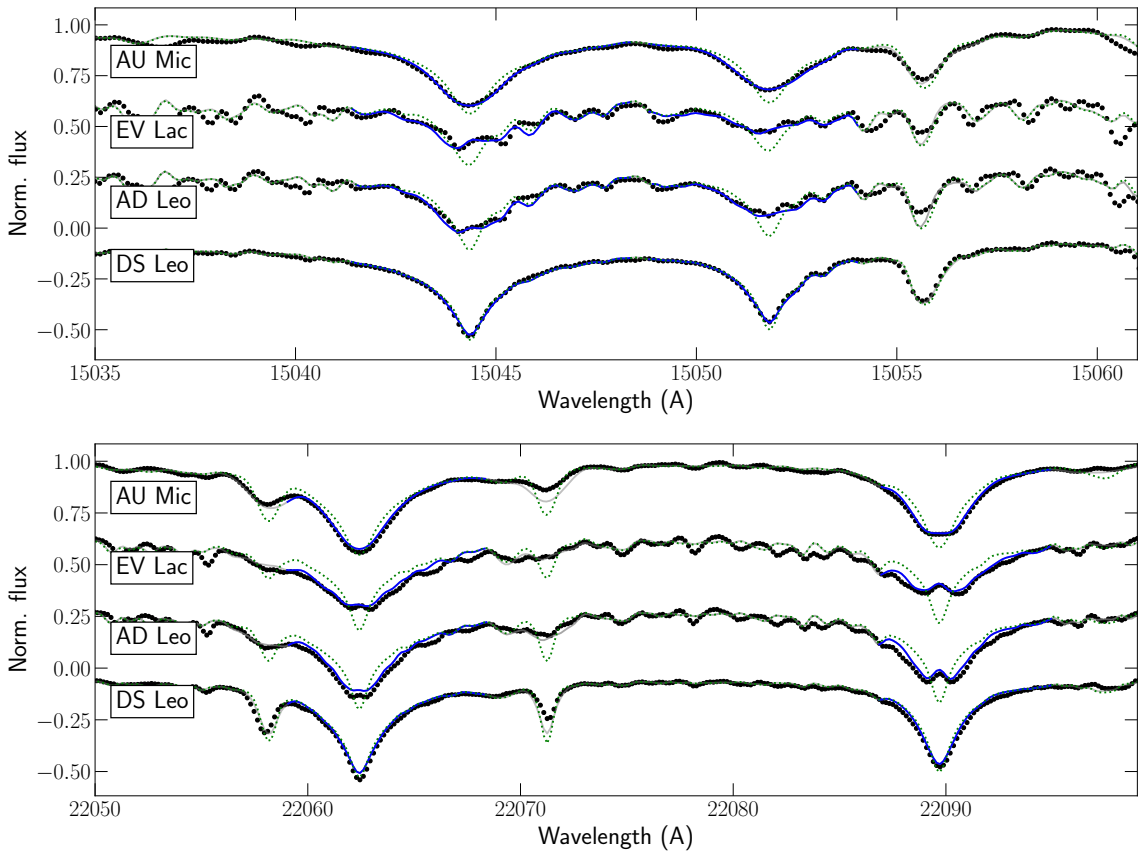

Figure 6.12. Best fit obtained for AU Mic, EV Lac, AD Leo and DS Leo with `ZeeTurbo` for two Mg lines (15044.3 & 15051.8 Å), and two Na lines (22062.4 & 22089.7 Å). Black points present the data. The gray solid line shows the best fit, and the blue solid blue line presents the part of the windows used for the fit. The green dotted line shows the model obtained for the same atmospheric parameters but with a zero magnetic field.

consistent with values reported in the literature, of 3.8 ± 0.5 kG (Shulyak et al., 2014) or 4.32 ± 0.11 kG (Reiners et al., 2022), and find that the distribution of the magnetic energy on the filling factor differs from that of AU Mic (see Fig. 6.11). With our setup, we retrieve $\zeta_{\rm RT} = 2.3$ km s^{-1}.

We repeat the analysis of EV Lac, this time assuming that the macroturbulence is Gaussian. The atmospheric parameters are found to be almost unaffected, with estimates of $T_{\rm eff} = 3346 \pm 6$, $\log g = 4.89 \pm 0.02$, [M/H] $= 0.03 \pm 0.01$ and [α/Fe] $= 0.01 \pm 0.01$. The value of the macroturbulent velocity is also found to be similar, with FWHM $\zeta_{\rm G} = 2.5 \pm 0.1$ km s^{-1}. The computed average magnetic field of $< B >= 4.31 \pm 0.06$ kG is also in excellent agreement with our previous estimate, and we conclude that the change

of the macroturbulence model did not significantly impact the results for this star. The results are reported in Table 6.1

6.5.2.3 The case of AD Leo = Gl 388

AD Leo is another magnetic M dwarf, with an estimated $v \sin i = 3$ km s^{-1} (Morin et al., 2008). Just like for EV Lac, we begin by fixing the value of $v \sin i$ and fitting $\zeta_{\rm RT}$. We retrieve atmospheric parameters of $T_{\rm eff} = 3463 \pm 7$, $\log g = 4.89 \pm 0.02$, [M/H] $= 0.23 \pm 0.01$ and [α/Fe] $= 0.00 \pm 0.01$. These values compare well with previous estimates (Mann et al., 2015), with the exception of a few recent studies suggesting that this star may be metal-poor Marfil et al. (2021). Our $\log g$ is in good agreement with previous mass and radius estimates ($M = 0.42$ M$_\odot$ & $R = 0.38$ R$_\odot$ Morin et al., 2008). We derive an average magnetic field of 2.97 ± 0.05 kG, which compares well with some reported average field strengths, of 2.9 ± 0.2 kG (Reiners & Basri, 2007) and 3.57 ± 0.09 kG (Reiners et al., 2022). The distribution of filling factors are presented in Fig. 6.13. We also retrieve a value for the macroturbulence of $\zeta_{\rm RT} = 1.9 \pm 0.2$ km s^{-1}.

Here again, we perform a new analysis, this time fitting a Gaussian macroturbulence. We find no significant change in the atmospheric parameters nor in the average magnetic field, but recover a value for the Gaussian macroturbulence of $\zeta_{\rm G} = 2.2 \pm 0.2$ km s^{-1}. Our estimates are summarized in Table 6.1.

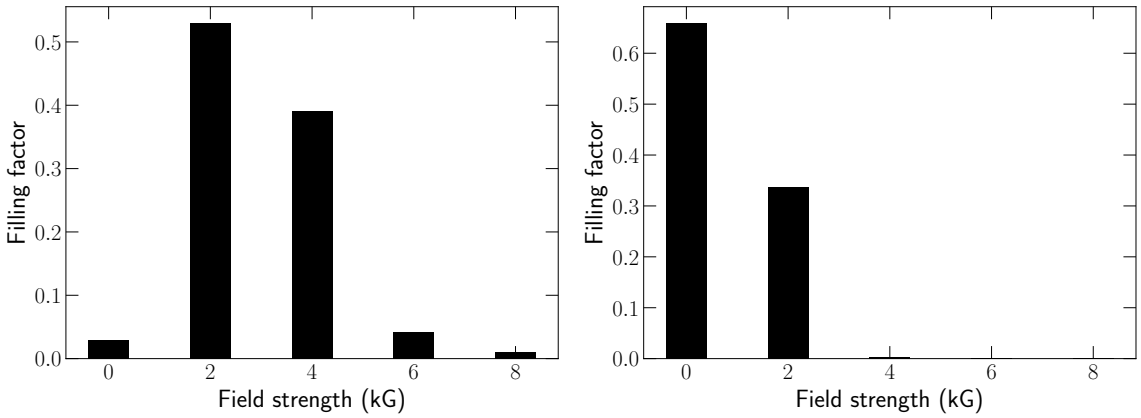

Figure 6.13. Same Fig. 6.11 for AD Leo (left) and DS Leo (right).

6.5.2.4 The case of DS Leo = Gl 410

We conclude with the analysis of a less magnetic star, DS Leo, which was also included in our previous studies (see Chapter 5). For this target, we fix $v \sin i$ to 2 km s^{-1} (Donati et al.,

2008), and retrieve atmospheric parameters of $T_{\rm eff} = 3824 \pm 6$ K, $\log g = 4.79 \pm 0.02$ dex, [M/H] $= 0.01 \pm 0.01$ dex and [α/Fe] $= 0.04 \pm 0.01$ dex. These results are in good agreement with previously reported estimates, including ours (Mann et al., 2015; Cristofari et al., 2022b). Our estimated $\log g$ is slightly larger than that implied by previous mass and radius estimates ($M = 0.570 \pm 0.004$ M$_\odot$ & $R = 0.568 \pm 0.008$ R$_\odot$, Schweitzer et al., 2019), but in good agreement within the typical empirical error bars estimated in Chapter 4. We estimate an average magnetic field of $< B >= 0.70 \pm 0.04$ kG, close to previously reported estimates ($< B >= 1.04 \pm 0.06$ kG, Reiners et al., 2022). These values are reported in Table 6.1. The corresponding filling factors are presented in Fig. 6.13.

We find that most of the magnetic power is distributed on the 2 kG component, with $a_2 = 0.33$. Consequently, just like for AU Mic, we carry out a second analysis, this time only using models computed for 0 and 2 kG. We find this constraint to have negligible impact on the results, of less than 1 K in $T_{\rm eff}$, less than 0.01 dex on $\log g$, [M/H] and [α/Fe], and 0.01 kG on $< B >$.

6.6 What have we learned?

It is now well established that magnetic fields influence the shape of spectral lines in non-trivial ways. While magnetic fields can be neglected to estimate the atmospheric parameters of some targets, several stars monitored in the context of the SLS are simply too active for these fields to be ignored.

The analysis presented in Chapters 4 & 5, if blindly applied to magnetic stars, could lead to incorrect estimates of their atmospheric parameters, and to a poor fit. Nonetheless, synthetic spectra computed with `Turbospectrum` gave us reliable results for weakly active stars, allowing us to rely on atomic and molecular features. Other codes, such as `Zeeman`, solve the polarized radiative transfer equation, but do not perform ideally for cool stars. In order to build on our previous successes while improving our approach and expanding our analysis, we developed a new code, `ZeeTurbo`, built on `Turbospectrum` and capable of solving the polarized radiative transfer equation.

With our newly developed tool, we built a new grid of synthetic spectra, computed for various atmospheric parameters and magnetic fields. Through simulations, we demonstrated the necessity to include magnetism in the modeling of stellar spectra, and our ability to constrain $T_{\rm eff}$, $\log g$, [M/H], [α/Fe] and the magnetic field at once (Cristofari et al., in prep, see Appendix A). This promising approach will allow us to perform extensive

analyses of active and inactive M dwarfs monitored in the context of the SLS, extending and improving our study. Follow-up works will allow us to monitor the evolution of the field through time, taking advantage of the long monitoring of SPIRou targets.

Chapter 7

Conclusions and perspectives

The work presented here focuses on constraining atmospheric parameters of M dwarfs through the analysis of high-resolution nIR spectra. We demonstrated that by comparing high-SNR SPIRou templates to modeled spectra computed from some of the latest state-of-the-art model atmospheres, we were capable of constraining $T_{\rm eff}$, $\log g$, [M/H] and [α/Fe]. To study magnetic stars, we implemented a new code, `ZeeTurbo`, and used it to estimate the average magnetic field of a few targets. These results and the developed tools (i) helps better understand the properties of M dwarfs, (ii) provides the community with necessary parameters for the characterization of exoplanets, and (iii) helps identify short-term (2-3 years) and long-term (>3 years) research prospects.

7.1 Characterizing M dwarfs from high-resolution spectra

Accurately characterizing M dwarfs is essential to both the search and characterization of planets, and the study of magnetic fields in these stars. Of all the techniques available to characterize stars, modeling high-resolution spectra was identified as one of the best options, allowing us to rely on the shape of individual absorption features rather than integrated quantities (such as equivalent widths or SEDs). Our results and previous studies (Rajpurohit et al., 2018; Passegger et al., 2019) illustrate the viability of such approach for the characterization of M dwarfs, as we explored its application to the nIR domain, especially relevant because of the substantially enhanced brightness (several magnitude) compared to the optical domain.

This approach is however inherently limited by the accuracy of the model atmospheres and by the approximations used in spectral synthesis codes. With our work, we confirm that different models can result in significantly disparate estimates of atmospheric parameters (Cristofari et al., 2022a). Such discrepancies have now been reported by several works (Plez, 2011; Blanco-Cuaresma, 2019) and find their origin deep in the physical assumptions made to compute model atmospheres, and in the accuracy of the

molecular and atomic data used to synthesize spectra. Several physical quantities used as inputs, such as Van der Waals parameters and oscillator strengths must indeed be accurately estimated for spectral line profiles to match observations. However, these quantities remain poorly constrained or missing for many lines, especially in the nIR domain. Some recent works attempted to adjust the line parameters in order to improve the fits of spectra to observations (Petit et al., 2021), and similarly, we found that adjusting the Van der Waals parameters of some Ti lines can help us derive atmospheric parameters in closer agreement with the literature.

By estimating the atmospheric properties of 44 M dwarfs observed in the context of the SLS, we contribute to the effort that aims at providing the community with accurate constraints for such stars (Cristofari et al., 2022b). In particular, we provided constraints on [α/Fe] in good agreement with empirical [M/H]–[α/Fe] trends within the Galaxy, suggesting that while most of our observed targets belong to the thin Galactic disk, a few could belong to the thick Galactic disk. These results are in line with previous classifications (Cortés-Contreras, 2016; Schöfer et al., 2019), and enabled us to improve the characterization of these stars.

Moreover, the characterization of M dwarfs is influenced by the presence of magnetic fields (Shulyak et al., 2014; Kochukhov & Reiners, 2020; Reiners et al., 2022). Constraining the magnetic flux of M dwarfs is thus essential to better understand how these fields impact stellar formation and evolution. While large scale magnetic fields have been studied from polarized spectra through techniques such as Zeeman Doppler Imaging, magnetic fields are known to have an impact on unpolarized spectra (Kochukhov & Reiners, 2020; Reiners et al., 2022). With our newly developed tool, `ZeeTurbo`, we implemented a process capable of constraining the average magnetic field and atmospheric parameters of M dwarfs, simultaneously. We thereby confirm the necessity of including magnetic fields in the modeling of stellar spectra to derive the atmospheric parameters of magnetic M dwarfs monitored with SPIRou. In a subsequent study, we will focus on expanding our new analysis to a larger sample of targets observed in the context of the SLS, re-processing those already included in our previous works (Cristofari et al., 2022b), to refine constraints of their properties and further investigate the impact of magnetic fields on their characterization. Furthermore, we will apply our tools to the spectra of PMS stars, for which systematic analyses have not been carried out yet. The study of PMS stars, and in particular of their magnetic fields, can help us better understand the processes at the origin of the formation of stars and planets.

7.2 Future prospects

Our results, and the newly developed tools, will help to support major research projects that aim at constraining further the fundamental properties of M dwarfs, and to better understand the structure and the role of magnetic fields in cool stars.

Improving the characterization of M dwarfs

The dynamo processes, proposed to be at the origin of magnetic fields in M dwarfs, result from complex theoretical works and predict activity cycles or polarity reversals evolving on different timescales (typically from years to a few tens of years). Observational data is crucial to constrain these models. In the short term, our tools, and in particular `ZeeTurbo`, can help us to track the evolution of the magnetic flux in stars monitored across several years in the context of the SLS. Such estimates will come to complement other activity indicators and measurements, and can help us to search for constraints on activity cycles. Moreover, M dwarfs tend to have complex field topologies, which origin is not entirely clear, and could derive from specific dynamo processes, or strong-field spots at the surface of M dwarfs (Kochukhov, 2021). `ZeeTurbo` will allow us to assess the role of topology on our derived average magnetic field and on the distribution of filling factors. We will be able to synthesize spectra of rotating stars with a given topology, and use our developed process to analyze the generated models. Minor modifications to the code will also allow us to perform similar simulations for spotted stars, and provide us with insights on the influence of spots and topology on the derived filling factors.

The magnetic activity was shown to have a significant impact on RV measurements (Gomes da Silva et al., 2012), which is detrimental to the search and characterization of planets orbiting M dwarfs. By tracking the evolution of magnetic fields, we will be able to confront our estimation for the magnetic field strength to radial velocity signals, and search for potential biases in the RV measurements, taking advantage of the several years of data recorded with SPIRou. Correlations between RV measurements and measurements of the average magnetic fields could in particular help us to better understand the origin of the activity jitters, and provide better constraints on the properties of the detected planets.

Our developed tools can also help us to derive individual elemental abundances of M dwarfs in the line of the work of Ishikawa et al. (2020, 2022). Such measurements were shown to be particularly challenging for cool stars, but provide additional constraints on the composition of their photosphere, and help us to better characterize M dwarfs. With the recent evolution of transit spectroscopy, such estimates can also provide useful

information on the host star, and allow one to refine the detection of molecules in the atmospheres of habitable planets.

The future of stellar models and observation facilities

In spite of the latest advances in spectral modeling, our work confirms that significant discrepancies are still found between synthetic spectra computed from different model atmospheres. Our work and subsequent studies would greatly benefit from an in-depth review of the differences between the latest `PHOENIX` and `MARCS` model atmospheres, and of the associated spectral synthesis programs. The comparison of the synthesized spectra to the now available nIR high-resolution spectra of reference targets would help identify which model best reproduces observations of M dwarfs, and to better identify the source(s) of errors and uncertainties associated to the various models.

Our analyses will also benefit from new observations, from current and future nIR spectrometers. In particular, SPIP (Baratchart et al., 2022), the twin of SPIRou to be installed on the 2-m Telescope Bernard Lyot (TBL) at the Pic du Midi (France) will provide additional data for stellar characterization and for the search for Earth-like planets orbiting M dwarfs. NIRPS (Wildi et al., 2017), installed at the ESO 3.6-m telescope at La Silla Observatory will provide $R \sim 100000$ nIR spectra in the 0.9–1.8 μm wavelength range, and will come to complement the data collected by HARPS.

Moreover, other instruments will complement these high-resolution spectrographs, such as for instance WINERED, the Warm INfrared Echelle spectrograph to REalize Decent high-resolution spectroscopy, installed at the 6.5-m Magellan Clay telescope at Las Campanas Observatory and covering a 0.9–1.3 μm wavelength range with a resolving power $R \sim 70000$ (Ikeda et al., 2022), specifically designed to record high-SNR spectra.

SPIRou was designed to focus on two main topics: 1) the search and characterization of habitable Earth-like planets around nearby M dwarfs; 2) the role of the magnetic fields on low-mass stars and planets formation. SPIRou is thus directly connected to key Science projects of several major facilities. It complements observations at various wavelength, in space and on the ground, from current and next generation instruments, such as the VLA[1] (Very Large Array, centimeter domain, 1980) (Andre et al., 1993), ALMA[2] (the Atacama Large Millimeter/submillimeter Array, mm/sub mm domain, 2013) (Ricci et al., 2014),

[1] https://public.nrao.edu/visit/very-large-array/
[2] https://www.almaobservatory.org/

JWST[3] (The James Webb Space Telescope, IR, 2021) (Gardner et al., 2006), ARIEL[4] (Atmospheric Remote-sensing Infrared Exoplanet Large-survey, IR, 2029) (Tinetti et al., 2016), TESS[5] (Transiting Exoplanet Survey Satellite, optical, 2018) (Ricker et al., 2015), PLATO [6] (Planetary transits and oscillations of stars, in the optical domain, 2026) (Rauer et al., 2014), the ELT[7] (The Extremely Large Telescope, optical/nIR domain) (Gilmozzi & Spyromilio, 2007), the GMT[8] (Giant Magellan Telescope, optical domain, 2029) (Johns et al., 2012). For instance, while ALMA will complement SPIRou observations probing protoplanetary disks of pre-main-sequence stars, TESS/PLATO will characterize the planets transiting across M stars, and JWST will probe the atmospheres of planets.

These instruments and the associated analyses are aimed at addressing fundamental questions that are still open: How do stars and planets form and evolve? Is there life outside of the solar system? How do magnetic fields impact stellar formation and evolution? How do stellar magnetic fields impact the formation and evolution of planets?

[3]https://webb.nasa.gov/
[4]https://arielmission.space/
[5]https://www.nasa.gov/tess-transiting-exoplanet-survey-satellite/
[6]https://platomission.com/
[7]https://elt.eso.org/
[8]https://giantmagellan.org/

Chapter 8

Conclusions et perspectives

Ce chapitre présente les mêmes conclusions et perspectives que le Chapitre 7, en Français.

Le travail présenté ici se concentre sur la détermination des propriétés atmosphériques des naines rouges via l'analyse de spectres proche-infrarouge (nIR) à haute résolution. Nous avons montré qu'en comparant des spectres SPIRou à haute résolution à des spectres synthétiques calculés à partir de modèles d'atmosphères, nous sommes en mesure de déterminer $T_{\rm eff}$, $\log g$, [M/H] et [α/Fe]. Pour étudier les étoiles magnétiques, nous avons développé un nouveau code, `ZeeTurbo`, et nous l'avons utilisé pour estimer le champ magnétique moyen de plusieurs étoiles. Ces résultats et les outils développés (i) aident à mieux comprendre les propriétés des naines rouges, (ii) fournissent à la communauté les paramètres nécessaires à la caractérisation des exoplanètes, et (iii) aident à identifier les perspectives de recherche à court (2-3 ans) et long terme (>3 ans).

8.1 Caractériser les étoiles M à partir de leurs spectres infrarouges

Caractériser les étoiles M avec précision est essentiel à la fois pour la recherche et la caractérisation de planètes, et pour l'étude des champs magnétiques dans ces étoiles. Parmi toutes les techniques disponibles pour caractériser des étoiles, la modélisation de spectres à haute résolution a été identifiée comme l'une des meilleures options, nous permettant de nous appuyer sur la forme des raies d'absorption, plutôt que sur des quantités intégrées (telles que les largeurs équivalentes ou les distributions spectrales en énergie). Nos résultats et les études précédentes (Rajpurohit et al., 2018; Passegger et al., 2019) montrent que cette approche est valide pour les naines rouges, et notamment dans le domaine du proche infrarouge, particulièrement intéressant en raison de la plus forte luminosité (plusieurs magnitudes) des étoiles M dans ce domaine par rapport au visible.

Cette approche est cependant limitée par la précision des modèles d'atmosphères et par les approximations utilisées dans les codes de synthèse spectrale. Avec notre travail, nous confirmons que différents modèles peuvent donner lieu à des estimations significativement différentes des paramètres atmosphériques (Cristofari et al., 2022a). Ces différences ont maintenant été rapportées par plusieurs travaux (Plez, 2011; Blancato et al., 2019) et trouvent leur origine dans les hypothèses physiques faites pour calculer les modèles d'atmosphères, et dans la précision des données moléculaires et atomiques utilisées pour synthétiser les spectres. Plusieurs quantités physiques utilisées par ces modèles, telles que les paramètres de Van der Waals et les forces des oscillateurs, doivent en effet être estimées avec précision pour que les profils des raies collent aux observations. Cependant, ces quantités restent peu contraintes ou manquantes pour de nombreuses raies, en particulier dans le domaine du proche infrarouge. Certains travaux récents ont tenté d'ajuster les paramètres des raies afin d'améliorer les analyses (Petit et al., 2021), et de la même manière, nous avons trouvé que l'ajustement des paramètres de Van der Waals de certaines raies du Titane nous aide à dériver des paramètres atmosphériques en meilleur accord avec la littérature.

En estimant les propriétés atmosphériques de 44 naines rouges observées dans le cadre du SLS, nous contribuons à fournir à la communauté des paramètres précis pour ces étoiles (Cristofari et al., 2022b). En particulier, nous avons obtenu des contraintes sur [α/Fe] en bon accord avec les relations empiriques observées entre [M/H] et [α/Fe] au sein de la Galaxie, et suggérant que la plupart des étoiles étudiées appartiennent au disque galactique mince, avec quelques exceptions. Ces résultats sont en accord avec de précédentes études (Cortés-Contreras, 2016; Schöfer et al., 2019), et nous ont permis d'améliorer la caractérisation de ces étoiles. De plus, la caractérisation des étoiles M est influencée par la présence de champs magnétiques (Shulyak et al., 2014; Kochukhov & Reiners, 2020; Reiners et al., 2022). Il est essentiel de contraindre la valeur du champ magnétique des étoiles M pour mieux comprendre son impact sur la formation et l'évolution stellaire. Les champs magnétiques à grande échelle ont été étudiés à partir de spectres polarisés grâce à des techniques telles que l'imagerie Doppler Zeeman, mais on sait également que les champs magnétiques ont un impact sur les spectres non polarisés (Kochukhov & Reiners, 2020; Reiners et al., 2022). Avec notre nouvel outil, `ZeeTurbo`, nous avons mis en oeuvre un processus capable d'estimer le champ magnétique moyen et les paramètres atmosphériques des naines M. Nos résultats montrent la nécessité d'inclure les champs magnétiques dans la modélisation des spectres stellaires. Dans une prochaine étude, nous étendrons notre analyse à un plus grand échantillon d'étoiles observées dans le cadre du SLS, et feront une nouvelle analyse

des naines rouges déjà incluses dans nos travaux précédents (Cristofari et al., 2022b), afin d'affiner leur caractérisation, et d'étudier l'impact des champs magnétiques sur les résultats de notre analyse. Nous étudierons également les spectres d'étoiles PMS, pour lesquelles des analyses systématiques n'ont pas encore été réalisées. L'étude des étoiles PMS, et en particulier de leurs champs magnétiques, peut nous aider à mieux comprendre les processus à l'origine de la formation des étoiles et des planètes.

8.2 Perspectives

Nos résultats, et les outils nouvellement développés, aideront à soutenir des projets de recherche majeurs qui ont pour but de contraindre davantage les propriétés fondamentales des naines M, et de mieux comprendre la structure et le rôle des champs magnétiques dans les étoiles froides.

Améliorer la caractérisation des étoiles M

Les processus dynamo, proposés comme étant à l'origine des champs magnétiques dans les naines rouges, résultent de travaux théoriques complexes et prédisent des cycles d'activité ou des inversions de polarité sur des échelles de temps différentes (typiquement de quelques années à quelques dizaines d'années). Les observations sont cruciales pour contraindre ces modèles. A court terme, nos outils, et en particulier `ZeeTurbo`, peuvent nous aider à suivre l'évolution du champ magnétique des étoiles observées sur plusieurs années dans le cadre du SLS. Ces données viendront compléter d'autres indicateurs et mesures d'activité, et pourront nous aider à contraindre les cycles d'activité. De plus, les champs magnétiques dans les naines rouges peuvent avoir des topologies complexes, dont l'origine n'est pas toujours claire, et qui pourraient provenir de processus dynamo spécifiques, ou de zone de champs magnétique intense à la surface des étoiles M (Kochukhov, 2021). `ZeeTurbo` nous permettra d'évaluer le rôle de la topologie sur notre estimation du champ magnétique moyen. Nous pourrons synthétiser les spectres d'étoiles en rotation avec une topologie donnée, et utiliser nos outils pour analyser les modèles générés. Quelques modifications du code nous permettront également d'effectuer des simulations similaires pour les étoiles tachetées, et nous fourniront un aperçu de l'influence des taches et de la topologie sur l'estimation du champ magnétique moyen.

Il a été montré que l'activité magnétique avait un impact significatif sur les mesures de vitesse radiale (Gomes da Silva et al., 2012), qui affecte la recherche et la caractérisation de planètes en orbite autour de naines rouges. En suivant l'évolution des champs magnétiques,

nous pourrons comparer l'évolution du champ magnétique moyen aux courbes de vitesse radiale, et chercher de possibles biais, en tirant parti des données obtenues avec SPIRou sur plusieurs années. Nos outils développés peuvent également nous aider à dériver les abondances des éléments dans les naines rouges, poursuivant les travaux entrepris par Ishikawa et al. (2020, 2022). Ces mesures sont particulièrement difficiles pour les étoiles froides, mais fournissent des contraintes supplémentaires sur la composition de la photosphère des naines rouges. Avec l'évolution récente de la spectroscopie de transit, ces données peuvent également aider à la caractérisation des atmosphères de planètes habitables.

La prochaine génération de modèles et d'instruments

Malgré les dernières avancées en matière de modélisation de spectres stellaires, notre travail montre qu'il reste des différences significatives entre les spectres synthétiques calculés à partir de différentes modèles d'atmosphères. Notre travail et les études ultérieures pourraient bénéficier d'un examen approfondi des différences entre les dernières versions des modèles `PHOENIX` et `MARCS`, et des codes de synthèse spectrale associés. La comparaison des spectres synthétisés aux spectres nIR à haute résolution qui sont maintenant disponibles pour des étoiles de référence aiderait à identifier le modèle qui reproduit le mieux les observations des naines rouges, et à mieux quantifier les erreurs associées au choix du modèle.

Nos analyses bénéficieront également de nouvelles observations obtenues avec les instruments actuels et leurs successeurs. En particulier, SPIP (Baratchart et al., 2022), le jumeau de SPIRou qui sera installé sur le télescope Bernard Lyot (TBL) de 2 m au Pic du Midi (France), fournira des données supplémentaires pour la caractérisation stellaire et la recherche de planètes semblables à la Terre en orbite autour de naines M. NIRPS (Wildi et al., 2017), installé sur le télescope de 3,6 m de l'ESO à l'Observatoire de La Silla, fournira des spectres nIR avec une résolution $R \sim 100000$ pour des longueurs d'ondes allant de 0,9 à 1,8 μm, et viendra compléter les données collectées par HARPS.

D'autres instruments permettront de compléter ces spectrographes à haute résolution, comme par exemple WINERED, le Warm INfrared Echelle spectrograph to REalize Decent high-resolution spectroscopy, installé sur le télescope de 6.5-m Magellan Clay à l'observatoire de Las Campanas Observatory et couvrant un domaine de longueur d'onde de 0.9–1.3 μm avec une résolution $R \sim 70000$,(Ikeda et al., 2022), spécifiquement conçu pour enregistrer des spectres à haut rapport signal sur bruit.

SPIRou a été conçu pour se concentrer sur deux sujets principaux : 1) la recherche et la caractérisation de planètes habitables semblables à la Terre autour d'étoiles M; 2) l'étude des champs magnétiques dans les étoiles de faible masse et la formation de planètes. SPIRou est ainsi lié aux projets scientifiques clés d'autres grandes installation. Il complète les observations effectuées à diverses longueurs d'onde, dans l'espace et au sol, avec les instruments actuels et de prochaine génération, tels que le VLA[1] (Very Large Array, centimeter domain, 1980) (Andre et al., 1993), ALMA[2] (the Atacama Large Millimeter/submillimeter Array, mm/sub mm, 2013) (Ricci et al., 2014), JWST[3] (The James Webb Space Telescope, IR, 2021) (Gardner et al., 2006), ARIEL[4] (Atmospheric Remote-sensing Infrared Exoplanet Large-survey, IR, 2029) (Tinetti et al., 2016), TESS[5] (Transiting Exoplanet Survey Satellite, optique, 2018) (Ricker et al., 2015), PLATO [6] (Planetary transits and oscillations of stars, dans l'optique, 2026) (Rauer et al., 2014), l'ELT[7] (The Extremely Large Telescope, optique/nIR) (Gilmozzi & Spyromilio, 2007), le GMT[8] (Giant Magellan Telescope, optique, 2029) (Johns et al., 2012). Par exemple, ALMA complétera les observations de SPIRou qui sondent les disques protoplanétaires des étoiles jeunes, TESS/PLATO caractériseront les planètes qui transitent autour d'étoiles M, et JWST sondera les atmosphères des planètes.

Ces instruments et les analyses associées visent à répondre à des questions fondamentales qui restent encore ouvertes : Comment les étoiles et les planètes se forment-elles et évoluent-elles ? Existe-t-il de la vie en dehors du système solaire ? Quel est l'impact des champs magnétiques sur la formation et l'évolution des étoiles ? Comment les champs magnétiques stellaires influent-ils sur la formation et l'évolution des planètes ?

[1] https://public.nrao.edu/visit/very-large-array/
[2] https://www.almaobservatory.org/
[3] https://webb.nasa.gov/
[4] https://arielmission.space/
[5] https://www.nasa.gov/tess-transiting-exoplanet-survey-satellite/
[6] https://platomission.com/
[7] https://elt.eso.org/
[8] https://giantmagellan.org/

Bibliography

Adibekyan V. Z., et al., 2013, A&A, 554, A44

Afram N., Berdyugina S. V., 2019, A&A, 629, A83

Allard F., Hauschildt P. H., 1995, ApJ, 445, 433

Allard F., Guillot T., Ludwig H.-G., Hauschildt P. H., Schweitzer A., Alexand er D. R., Ferguson J. W., 2003, in Martín E., ed., IAU Symposium Vol. 211, Brown Dwarfs. p. 325

Allard F., Homeier D., Freytag B., 2011, in Johns-Krull C., Browning M. K., West A. A., eds, Astronomical Society of the Pacific Conference Series Vol. 448, 16th Cambridge Workshop on Cool Stars, Stellar Systems, and the Sun. p. 91 (arXiv:1011.5405)

Allard F., Homeier D., Freytag B., Sharp C. M., 2012, in Reylé C., Charbonnel C., Schultheis M., eds, EAS Publications Series Vol. 57, EAS Publications Series. pp 3–43 (arXiv:1206.1021), doi:10.1051/eas/1257001

Alvarez R., Plez B., 1998, A&A, 330, 1109

Amarsi A. M., Liljegren S., Nissen P. E., 2022, arXiv e-prints, p. arXiv:2209.13449

André P., 2015, in Gargaud M., et al., eds, , Encyclopedia of Astrobiology. pp 2308–2313, doi:10.1007/978-3-662-44185-5_504

Andre P., Ward-Thompson D., Barsony M., 1993, ApJ, 406, 122

André P., et al., 2010, A&A, 518, L102

André P., Arzoumanian D., Könyves V., Shimajiri Y., Palmeirim P., 2019, A&A, 629, L4

Armitage P. J., 2011, ARA&A, 49, 195

Artigau É., et al., 2014, in Proc. SPIE. p. 914905 (arXiv:1406.6927), doi:10.1117/12.2056385

Bachiller R., 1996, ARA&A, 34, 111

Bachiller R., Gomez-Gonzalez J., 1992, A&ARv, 3, 257

Baraffe I., Chabrier G., Allard F., Hauschildt P. H., 1998, A&A, 337, 403

Baraffe I., Homeier D., Allard F., Chabrier G., 2015, A&A, 577, A42

Baratchart S., et al., 2022, in Evans C. J., Bryant J. J., Motohara K., eds, Society of Photo-Optical Instrumentation Engineers (SPIE) Conference Series Vol. 12184, Ground-based and Airborne Instrumentation for Astronomy IX. p. 121844Q, doi:10.1117/12.2629347

Barklem P. S., Anstee S. D., O'Mara B. J., 1998, Publ. Astron. Soc. Australia, 15, 336

Barklem P. S., Piskunov N., O'Mara B. J., 2000, A&AS, 142, 467

Barklem P. S., et al., 2021, ApJ, 908, 245

Baron E., Chen B., Hauschildt P. H., 2009, in Hubeny I., Stone J. M., MacGregor K., Werner K., eds, American Institute of Physics Conference Series Vol. 1171, Recent Directions in Astrophysical Quantitative Spectroscopy and Radiation Hydrodynamics. pp 148–160 (arXiv:0908.4273), doi:10.1063/1.3250055

Bedell M., Hogg D. W., Foreman-Mackey D., Montet B. T., Luger R., 2019, AJ, 158, 164

Bell C. P. M., Naylor T., Mayne N. J., Jeffries R. D., Littlefair S. P., 2013, MNRAS, 434, 806

Benz A. O., 2017, Living Reviews in Solar Physics, 14, 2

Berdyugina S. V., 2005, Living Reviews in Solar Physics, 2, 8

Berger D. H., et al., 2006, ApJ, 644, 475

Bertaux J. L., Lallement R., Ferron S., Boonne C., Bodichon R., 2014, A&A, 564, A46

Blancato K., Ness M., Johnston K. V., Rybizki J., Bedell M., 2019, ApJ, 883, 34

Blanco-Cuaresma S., 2019, MNRAS, 486, 2075

Boccaletti A., et al., 2018, A&A, 614, A52

Bonfils X., et al., 2013, A&A, 556, A110

Bontemps S., Ward-Thompson D., Andre P., 1996, A&A, 314, 477

Bouvier J., Alencar S. H. P., Harries T. J., Johns-Krull C. M., Romanova M. M., 2007, in Reipurth B., Jewitt D., Keil K., eds, Protostars and Planets V. p. 479 (arXiv:astro-ph/0603498)

Bouvier J., Matt S. P., Mohanty S., Scholz A., Stassun K. G., Zanni C., 2014, in Beuther H., Klessen R. S., Dullemond C. P., Henning T., eds, Protostars and Planets VI. p. 433 (arXiv:1309.7851), doi:10.2458/azu_uapress_9780816531240-ch019

Boyajian T. S., et al., 2012, ApJ, 757, 112

Cantiello M., Langer N., Brott I., de Koter A., Shore S. N., Vink J. S., Voegler A., Yoon S. C., 2009, Communications in Asteroseismology, 158, 61

Castelli F., Kurucz R. L., 2003, in Piskunov N., Weiss W. W., Gray D. F., eds, Vol. 210, Modelling of Stellar Atmospheres. p. A20 (arXiv:astro-ph/0405087)

Charbonneau D., Irwin J., Nutzman P., Falco E. E., 2008, in AAS/Division for Planetary Sciences Meeting Abstracts #40. p. 11.12

Christensen-Dalsgaard J., 2021, Living Reviews in Solar Physics, 18, 2

Cifuentes C., et al., 2020, A&A, 642, A115

Claudi R., et al., 2017, European Physical Journal Plus, 132, 364

Clough S. A., Iacono M. J., 1995, J. Geophys. Res., 100, 16,519

Code A. D., Davis J., Bless R. C., Brown R. H., 1976, ApJ, 203, 417

Cortés-Contreras M., 2016, PhD thesis, Universidad Complutense de Madrid, Spain
Cretignier M., Francfort J., Dumusque X., Allart R., Pepe F., 2020, A&A, 640, A42
Cristofari P. I., et al., 2022a, MNRAS, 511, 1893
Cristofari P. I., et al., 2022b, MNRAS, 516, 3802
Crutcher R. M., 2012, ARA&A, 50, 29
Donati J. F., 2003, in Trujillo-Bueno J., Sanchez Almeida J., eds, Astronomical Society of the Pacific Conference Series Vol. 307, Solar Polarization. p. 41
Donati J. F., Brown S. F., 1997, A&A, 326, 1135
Donati J. F., Catala C., Landstreet J. D., Petit P., 2006, in Casini R., Lites B. W., eds, Astronomical Society of the Pacific Conference Series Vol. 358, Solar Polarization 4. p. 362
Donati J. F., et al., 2008, MNRAS, 390, 545
Donati J. F., et al., 2020, MNRAS, 498, 5684
Dotter A., Chaboyer B., Jevremović D., Kostov V., Baron E., Ferguson J. W., 2008, ApJS, 178, 89
Doughty N. A., Fraser P. A., 1966, MNRAS, 132, 267
Doughty N. A., Fraser P. A., McEachran R. P., 1966, MNRAS, 132, 255
Dressing C. D., Charbonneau D., 2015, ApJ, 807, 45
Durrant C. J., 1979, A&A, 76, 208
Edmunds M. G., 1978, A&A, 64, 103
Feiden G. A., Chaboyer B., 2014, in Petit P., Jardine M., Spruit H. C., eds, Vol. 302, Magnetic Fields throughout Stellar Evolution. pp 150–153 (arXiv:1309.7668), doi:10.1017/S174392131400194X
Figueira P., Kerber F., Chacon A., Lovis C., Santos N. C., Lo Curto G., Sarazin M., Pepe F., 2012, MNRAS, 420, 2874
Flores C., Connelley M. S., Reipurth B., Boogert A., 2019, ApJ, 882, 75
Folsom C. P., Bagnulo S., Wade G. A., Alecian E., Landstreet J. D., Marsden S. C., Waite I. A., 2012, MNRAS, 422, 2072
Folsom C. P., et al., 2016, MNRAS, 457, 580
Folsom C. P., et al., 2018, MNRAS, 474, 4956
Folsom C. P., Ó Fionnagáin D., Fossati L., Vidotto A. A., Moutou C., Petit P., Dragomir D., Donati J. F., 2020, A&A, 633, A48
Folsom C. P., et al., 2022, A&A, 658, A105
Foreman-Mackey D., Hogg D. W., Lang D., Goodman J., 2013, PASP, 125, 306
Fouqué P., et al., 2018, MNRAS, 475, 1960
Fuhrmann K., 1998, A&A, 338, 161

Fuhrmann K., 2008, MNRAS, 384, 173
Gaia Collaboration et al., 2016, A&A, 595, A1
Gaia Collaboration et al., 2022, arXiv e-prints, p. arXiv:2208.00211
Gallenne A., Desgrange C., Milli J., Sanchez-Bermudez J., Chauvin G., Kraus S., Girard J. H., Boccaletti A., 2022, arXiv e-prints, p. arXiv:2207.04116
Gardner J. P., et al., 2006, Space Sci. Rev., 123, 485
Gerber J. M., Magg E., Plez B., Bergemann M., Heiter U., Olander T., Hoppe R., 2022, arXiv e-prints, p. arXiv:2206.00967
Gilmozzi R., Spyromilio J., 2007, The Messenger, 127, 11
Gizis J. E., 1997, AJ, 113, 806
Gomes da Silva J., Santos N. C., Bonfils X., Delfosse X., Forveille T., Udry S., Dumusque X., Lovis C., 2012, A&A, 541, A9
Gray D. F., 1975, ApJ, 202, 148
Gray D. F., 2005, The Observation and Analysis of Stellar Photospheres, 3 edn. Cambridge University Press, doi:10.1017/CBO9781316036570
Gray R. O., Corbally C. J., 1994, AJ, 107, 742
Gray R. O., Corbally Christopher J., 2009, Stellar Spectral Classification
Gray D. F., Johanson H. L., 1991, PASP, 103, 439
Guenther E. W., 2022, MNRAS, 511, 1115
Gullikson K., Dodson-Robinson S., Kraus A., 2014, AJ, 148, 53
Gustafsson B., Bell R. A., Eriksson K., Nordlund A., 1975, A&A, 42, 407
Gustafsson B., Edvardsson B., Eriksson K., Jørgensen U. G., Nordlund Å., Plez B., 2008, A&A, 486, 951
Hale G. E., 1908, ApJ, 28, 315
Hall J. C., 2008, Living Reviews in Solar Physics, 5, 2
Hathaway D. H., 2015, Living Reviews in Solar Physics, 12, 4
Hauschildt P. H., 1992, J. Quant. Spectrosc. Radiative Transfer, 47, 433
Hauschildt P. H., Baron E., Allard F., 1997, ApJ, 483, 390
Hauschildt P. H., Allard F., Baron E., 1999, ApJ, 512, 377
Henry T. J., Jao W.-C., Subasavage J. P., Beaulieu T. D., Ianna P. A., Costa E., Méndez R. A., 2006, AJ, 132, 2360
Hughes A. M., Duchêne G., Matthews B. C., 2018, ARA&A, 56, 541
Hummer D. G., Berrington K. A., Eissner W., Pradhan A. K., Saraph H. E., Tully J. A., 1993, A&A, 279, 298
Husser T. O., Wende-von Berg S., Dreizler S., Homeier D., Reiners A., Barman T., Hauschildt P. H., 2013, A&A, 553, A6

Ikeda Y., et al., 2022, PASP, 134, 015004
Ishikawa H. T., Aoki W., Kotani T., Kuzuhara M., Omiya M., Reiners A., Zechmeister M., 2020, PASJ, 72, 102
Ishikawa H. T., et al., 2022, AJ, 163, 72
Jackson R. J., Deliyannis C. P., Jeffries R. D., 2018, MNRAS, 476, 3245
Johns-Krull C. M., 2007, ApJ, 664, 975
Johns M., et al., 2012, in Stepp L. M., Gilmozzi R., Hall H. J., eds, Society of Photo-Optical Instrumentation Engineers (SPIE) Conference Series Vol. 8444, Ground-based and Airborne Telescopes IV. p. 84441H, doi:10.1117/12.926716
Jönsson H., et al., 2020, AJ, 160, 120
Kippenhahn R., Weigert A., Weiss A., 2013, Stellar Structure and Evolution, doi:10.1007/978-3-642-30304-3.
Klein B., et al., 2021, MNRAS, 502, 188
Klein B., et al., 2022, MNRAS, 512, 5067
Kochukhov O., 2021, A&ARv, 29, 1
Kochukhov O., Reiners A., 2020, ApJ, 902, 43
Kochukhov O., Makaganiuk V., Piskunov N., 2010, A&A, 524, A5
Kopparapu R. K., et al., 2013, ApJ, 765, 131
Kotani T., et al., 2014, in Ramsay S. K., McLean I. S., Takami H., eds, Society of Photo-Optical Instrumentation Engineers (SPIE) Conference Series Vol. 9147, Ground-based and Airborne Instrumentation for Astronomy V. p. 914714, doi:10.1117/12.2055075
Kotani T., et al., 2018, in Evans C. J., Simard L., Takami H., eds, Society of Photo-Optical Instrumentation Engineers (SPIE) Conference Series Vol. 10702, Ground-based and Airborne Instrumentation for Astronomy VII. p. 1070211, doi:10.1117/12.2311836
Kupka F. G., Ryabchikova T. A., Piskunov N. E., Stempels H. C., Weiss W. W., 2000, Baltic Astronomy, 9, 590
Kurucz R. L., 1970, SAO Special Report, 309
Kurucz R. L., 1979, ApJS, 40, 1
Kurucz R. L., 2005, Memorie della Societa Astronomica Italiana Supplementi, 8, 14
Kurucz R. L., 2017, ATLAS9: Model atmosphere program with opacity distribution functions, Astrophysics Source Code Library, record ascl:1710.017 (ascl:1710.017)
Lada E. A., 1992, ApJ, 393, L25
Lallement R., Bertin P., Chassefiere E., Scott N., 1993, A&A, 271, 734
Landi Degl'Innocenti E., Landi Degl'Innocenti M., 1981, Nuovo Cimento B Serie, 62B, 1
Landi Degl'Innocenti E., Landi Degl'Innocenti M., 1985, Sol. Phys., 97, 239

Landi Degl'Innocenti E., Landolfi M., 2004, Polarization in Spectral Lines. Vol. 307, doi:10.1007/978-1-4020-2415-3,

Landstreet J. D., 1988, ApJ, 326, 967

Lee Y. S., et al., 2011, ApJ, 738, 187

López-Valdivia R., et al., 2019, ApJ, 879, 105

López-Valdivia R., et al., 2021, ApJ, 921, 53

Mac Low M.-M., Klessen R. S., 2004, Reviews of Modern Physics, 76, 125

Machida M. N., Matsumoto T., 2011, MNRAS, 413, 2767

Maeder A., 2009, Physics, Formation and Evolution of Rotating Stars, doi:10.1007/978-3-540-76949-1.

Magic Z., Collet R., Asplund M., Trampedach R., Hayek W., Chiavassa A., Stein R. F., Nordlund Å., 2013, A&A, 557, A26

Mahadevan S., et al., 2012, in McLean I. S., Ramsay S. K., Takami H., eds, Society of Photo-Optical Instrumentation Engineers (SPIE) Conference Series Vol. 8446, Ground-based and Airborne Instrumentation for Astronomy IV. p. 84461S (arXiv:1209.1686), doi:10.1117/12.926102

Maldonado J., et al., 2020, A&A, 644, A68

Mann A. W., Brewer J. M., Gaidos E., Lépine S., Hilton E. J., 2013, AJ, 145, 52

Mann A. W., Feiden G. A., Gaidos E., Boyajian T., von Braun K., 2015, ApJ, 804, 64

Mann A. W., et al., 2019, ApJ, 871, 63

Marfil E., et al., 2020, MNRAS, 492, 5470

Marfil E., et al., 2021, arXiv e-prints, p. arXiv:2110.07329

Marois C., Zuckerman B., Konopacky Q. M., Macintosh B., Barman T., 2010, Nature, 468, 1080

Martin B., Wickramasinghe D. T., 1979, MNRAS, 189, 883

Martioli E., et al., 2020, A&A, 641, L1

Martioli E., Hébrard G., Correia A. C. M., Laskar J., Lecavelier des Etangs A., 2021, A&A, 649, A177

Masunaga H., Inutsuka S.-i., 2000, ApJ, 531, 350

Mayor M., Queloz D., 1995, Nature, 378, 355

Mayor M., et al., 2003, The Messenger, 114, 20

McLaughlin D. B., 1924, ApJ, 60, 22

Morin J., 2012, in Reylé C., Charbonnel C., Schultheis M., eds, EAS Publications Series Vol. 57, EAS Publications Series. pp 165–191 (arXiv:1208.3363), doi:10.1051/eas/1257005

Morin J., et al., 2008, MNRAS, 390, 567

Morin J., Donati J. F., Petit P., Delfosse X., Forveille T., Jardine M. M., 2010, MNRAS, 407, 2269

Moutou C., et al., 2017, MNRAS, 472, 4563

Nakamura F., Li Z.-Y., 2005, ApJ, 631, 411

Nakano T., Nakamura T., 1978, PASJ, 30, 671

Neves V., Bonfils X., Santos N. C., Delfosse X., Forveille T., Allard F., Udry S., 2013, A&A, 551, A36

Neves V., Bonfils X., Santos N. C., Delfosse X., Forveille T., Allard F., Udry S., 2014, A&A, 568, A121

Newton E. R., Irwin J., Charbonneau D., Berta-Thompson Z. K., Dittmann J. A., West A. A., 2016, ApJ, 821, 93

Newton E. R., Irwin J., Charbonneau D., Berlind P., Calkins M. L., Mink J., 2017, ApJ, 834, 85

Olander T., Heiter U., Kochukhov O., 2021, A&A, 649, A103

Pakhomov Y. V., Ryabchikova T. A., Piskunov N. E., 2019, Astronomy Reports, 63, 1010

Parker E. N., 1955, ApJ, 122, 293

Passegger V. M., et al., 2018, A&A, 615, A6

Passegger V. M., et al., 2019, A&A, 627, A161

Passegger V. M., et al., 2022, A&A, 658, A194

Peach G., 1970, Mem. RAS, 73, 1

Pecaut M. J., Mamajek E. E., 2013, ApJS, 208, 9

Petit P., et al., 2021, A&A, 648, A55

Pineda J. S., Bottom M., Johnson J. A., 2013, ApJ, 767, 28

Piskunov N. E., Kupka F., Ryabchikova T. A., Weiss W. W., Jeffery C. S., 1995, A&AS, 112, 525

Plez B., 2008, Physica Scripta Volume T, 133, 014003

Plez B., 2011, Journal of Physics: Conference Series, 328, 012005

Preibisch T., Brown A. G. A., Bridges T., Guenther E., Zinnecker H., 2002, AJ, 124, 404

Press W. H., Teukolsky S. A., Vetterling W. T., Flannery B. P., 1992, Numerical Recipes in C (2nd Ed.): The Art of Scientific Computing. Cambridge University Press, USA

Quirrenbach A., et al., 2014, in Ramsay S. K., McLean I. S., Takami H., eds, Society of Photo-Optical Instrumentation Engineers (SPIE) Conference Series Vol. 9147, Ground-based and Airborne Instrumentation for Astronomy V. p. 91471F, doi:10.1117/12.2056453

Rajpurohit A. S., Reylé C., Allard F., Homeier D., Schultheis M., Bessell M. S., Robin A. C., 2013, A&A, 556, A15

Rajpurohit A. S., Allard F., Rajpurohit S., Sharma R., Teixeira G. D. C., Mousis O., Kamlesh R., 2018, A&A, 620, A180

Rauer H., et al., 2014, Experimental Astronomy, 38, 249

Rayner J., et al., 2016, in Evans C. J., Simard L., Takami H., eds, Society of Photo-Optical Instrumentation Engineers (SPIE) Conference Series Vol. 9908, Ground-based and Airborne Instrumentation for Astronomy VI. p. 990884, doi:10.1117/12.2232064

Reddy B. E., Lambert D. L., Allende Prieto C., 2006, MNRAS, 367, 1329

Reiners A., Basri G., 2007, ApJ, 656, 1121

Reiners A., et al., 2022, arXiv e-prints, p. arXiv:2204.00342

Ricci L., Testi L., Natta A., Scholz A., de Gregorio-Monsalvo I., Isella A., 2014, ApJ, 791, 20

Rice K., 2014, Challenges, 5, 296

Richert A. J. W., Getman K. V., Feigelson E. D., Kuhn M. A., Broos P. S., Povich M. S., Bate M. R., Garmire G. P., 2018, MNRAS, 477, 5191

Ricker G. R., et al., 2015, Journal of Astronomical Telescopes, Instruments, and Systems, 1, 014003

Robles J. A., Lineweaver C. H., Grether D., Flynn C., Egan C. A., Pracy M. B., Holmberg J., Gardner E., 2008, ApJ, 684, 691

Rojas-Ayala B., Covey K. R., Muirhead P. S., Lloyd J. P., 2010, ApJ, 720, L113

Rojas-Ayala B., Covey K. R., Muirhead P. S., Lloyd J. P., 2012, ApJ, 748, 93

Rossiter R. A., 1924, ApJ, 60, 15

Rothman L. S., et al., 2009, J. Quant. Spectrosc. Radiative Transfer, 110, 533

Rothman L. S., et al., 2013, J. Quant. Spectrosc. Radiative Transfer, 130, 4

Route M., 2016, ApJ, 830, L27

Rudolf N., Günther H. M., Schneider P. C., Schmitt J. H. M. M., 2016, A&A, 585, A113

Ruiz-Dern L., Babusiaux C., Arenou F., Turon C., Lallement R., 2018, A&A, 609, A116

Sarkis P., et al., 2018, AJ, 155, 257

Sarmento P., Rojas-Ayala B., Delgado Mena E., Blanco-Cuaresma S., 2021, arXiv e-prints, p. arXiv:2103.04848

Sbordone L., Bonifacio P., Castelli F., 2007, in Kupka F., Roxburgh I., Chan K. L., eds, Vol. 239, Convection in Astrophysics. pp 71–73, doi:10.1017/S1743921307000142

Schöfer P., et al., 2019, A&A, 623, A44

Schrijver C. J., Cote J., Zwaan C., Saar S. H., 1989, ApJ, 337, 964

Schweitzer A., et al., 2019, A&A, 625, A68

Seaton M. J., Yan Y., Mihalas D., Pradhan A. K., 1994, MNRAS, 266, 805

Seifahrt A., Käufl H. U., Zängl G., Bean J., Richter M., Siebenmorgen R., 2010, The Messenger, 142, 21

Semel M., 1989, A&A, 225, 456

Shulyak D., Reiners A., Seemann U., Kochukhov O., Piskunov N., 2014, A&A, 563, A35

Shulyak D., Reiners A., Engeln A., Malo L., Yadav R., Morin J., Kochukhov O., 2017, Nature Astronomy, 1, 0184

Skilling J., Bryan R. K., 1984, MNRAS, 211, 111

Skrutskie M. F., et al., 2006, AJ, 131, 1163

Smette A., et al., 2015, A&A, 576, A77

Sneden C., Bean J., Ivans I., Lucatello S., Sobeck J., 2012, MOOG: LTE line analysis and spectrum synthesis (ascl:1202.009)

Somerville W. B., 1964, ApJ, 139, 192

Souto D., et al., 2022, arXiv e-prints, p. arXiv:2201.00891

Steenbeck M., Krause F., Rädler K. H., 1966, Zeitschrift Naturforschung Teil A, 21, 369

Stift M. J., Leone F., 2003, A&A, 398, 411

Struve O., Elvey C. T., 1934, ApJ, 79, 409

Takeda Y., UeNo S., 2017, PASJ, 69, 46

Taniguchi D., et al., 2021, MNRAS, 502, 4210

Teixeira G. D. C., Sousa S. G., Tsantaki M., Monteiro M. J. P. F. G., Santos N. C., Israelian G., 2016, A&A, 595, A15

Tilley D. A., Pudritz R. E., 2007, MNRAS, 382, 73

Tinetti G., et al., 2016, in MacEwen H. A., Fazio G. G., Lystrup M., Batalha N., Siegler N., Tong E. C., eds, Society of Photo-Optical Instrumentation Engineers (SPIE) Conference Series Vol. 9904, Space Telescopes and Instrumentation 2016: Optical, Infrared, and Millimeter Wave. p. 99041X, doi:10.1117/12.2232370

Tomida K., Tomisaka K., Matsumoto T., Hori Y., Okuzumi S., Machida M. N., Saigo K., 2013, ApJ, 763, 6

Trampedach R., Asplund M., Collet R., Nordlund Å., Stein R. F., 2013, ApJ, 769, 18

Tuomi M., et al., 2019, arXiv e-prints, p. arXiv:1906.04644

Ulmer-Moll S., Figueira P., Neal J. J., Santos N. C., Bonnefoy M., 2019, A&A, 621, A79

Vacca W. D., Cushing M. C., Rayner J. T., 2003, PASP, 115, 389

Valenti J. A., Fischer D. A., 2005, ApJS, 159, 141

Valenti J. A., Piskunov N., 1996, A&AS, 118, 595

Villanueva G. L., Smith M. D., Protopapa S., Faggi S., Mandell A. M., 2018, J. Quant. Spectrosc. Radiative Transfer, 217, 86

Vines J. I., Jenkins J. S., 2022, MNRAS, 513, 2719

Wade G. A., Bagnulo S., Kochukhov O., Landstreet J. D., Piskunov N., Stift M. J., 2001, A&A, 374, 265

White R. J., et al., 2015, in American Astronomical Society Meeting Abstracts #225. p. 348.12

Wildi F., et al., 2017, in Society of Photo-Optical Instrumentation Engineers (SPIE) Conference Series. p. 1040018, doi:10.1117/12.2275660

Wilson R. W., Jefferts K. B., Penzias A. A., 1970, ApJ, 161, L43

Winters J. G., et al., 2015, AJ, 149, 5

Woolf V. M., Wallerstein G., 2005, MNRAS, 356, 963

Wright N. J., Drake J. J., Mamajek E. E., Henry G. W., 2011, ApJ, 743, 48

Yee S. W., Petigura E. A., von Braun K., 2017, ApJ, 836, 77

Zeeman P., 1897, Nature, 55, 347

Glossary

⋆ ALMA: Atacama Large Millimeter Array
⋆ APOGEE: Apache Point Observatory Galactic Evolution Experiment
⋆ ARIEL: Atmospheric Remote-sensing Infrared Exoplanet Large-survey
⋆ BERV: Barycentric Earth Radial Velocity
⋆ CARMENES: Calar Alto high-Resolution search for M dwarfs with Exoearths with Near-infrared and optical Échelle Spectrographs
⋆ CFHT: Canada-France-Hawaï Telescope
⋆ cTTS: classical T Tauri Star
⋆ DSEP: Dartmouth Stellar Evolution Program
⋆ ELT: Extremely Large Telescope
⋆ FWHM: Full-Width at Half-Maximum
⋆ GMT: Giant Magellan Telescope
⋆ HARPS: High Accuracy Radial velocity Planet Searcher
⋆ JWST: James Webb Telescope
⋆ LTE: Local Thermodynamic Equilibrium
⋆ $\log g$: Surface gravity
⋆ MAD: Median Absolute Deviation
⋆ [M/H]: Metallicity
⋆ MS: Main-Sequence
⋆ nIR: near-Infrared
⋆ NLTE: Non-Local Thermodynamic Equilibrium
⋆ PLATO: PLanetary Transits and Oscillations of stars
⋆ PMS: Pre-Main-Sequence
⋆ R: Resolving power
⋆ RMS: Root-Mean-Square
⋆ RV: Radial Velocity
⋆ SED: Spectral Energy Distribution
⋆ SLS: SPIRou Legacy Survey
⋆ SNR: Signal-to-Noise Ratio
⋆ SPICE: SPIRou Legacy Survey - Consolidation and Enhancement

- ⋆ TESS: Transiting Exoplanet Survey Satellite
- ⋆ $T_{\rm eff}$: Effective temperature
- ⋆ VLA: Very Large Array
- ⋆ wTTS: weak-line T Tauri Star
- ⋆ 2MASS : Two-Micron All-Sky Survey

List of Figures

Appendix A

Publications

First-author publications

- "Estimating fundamental parameters of nearby M dwarfs from SPIRou spectra"
  Cristofari P. I., et al., 2022a, MNRAS, 511, 1893
- "Estimating the atmospheric properties of 44 M dwarfs from SPIRou spectra"
  Cristofari P. I., et al., 2022b, MNRAS, 516, 3802
- "Constraining atmospheric parameters and magnetic fields with `ZeeTurbo` from SPIRou spectra"
  Cristofari P. I., et al., in prep

Co-author publications

- "A transiting sub-Neptune around a low mass star characterized with SPIRou and TESS"
  Martioli E., et al., 2022 A&A, 660, A86
- "Direct characterization of young giant exoplanets at high spectral resolution by coupling SPHERE and CRIRES+"
  Otten G. P. P. L., et al., 2021, A&A, 646, A150
- "A sub-Neptune planet around TOI-1695 discovered and characterized with SPIRou and TESS"
  Kiefer, F., et al., submitted to A&A

Monthly Notices of the ROYAL ASTRONOMICAL SOCIETY

MNRAS **511,** 1893–1912 (2022) https://doi.org/10.1093/mnras/stab3679
Advance Access publication 2021 December 17

Estimating fundamental parameters of nearby M dwarfs from SPIRou spectra

P. I. Cristofari [1★] J.-F. Donati [1] T. Masseron,[2,3] P. Fouqué,[1,4] C. Moutou,[1] X. Delfosse,[5] E. Artigau,[6] C. P. Folsom [7] A. Carmona,[5] E. Gaidos [8] J.-D. do Nascimento, Jr. [9,10] F. Jahandar[6] and G. Hébrard[11,12]

[1] *Univ. de Toulouse, CNRS, IRAP, 14 av. Belin, F-31400 Toulouse, France*
[2] *Instituto de Astrofísica de Canarias, E-38205 La Laguna, Tenerife, Spain*
[3] *Departamento de Astrofísica, Universidad de La Laguna, E-38206 La Laguna, Tenerife, Spain*
[4] *Canada-France-Hawaii Telescope, CNRS, Kamuela, HI 96743, USA*
[5] *Univ. Grenoble Alpes, CNRS, IPAG, F-38000 Grenoble, France*
[6] *Université de Montréal, Département de Physique, IREX, Montréal, QC H3C 3J7, Canada*
[7] *Tartu Observatory, University of Tartu, Observatooriumi 1, Tõravere, 61602 Tartumaa, Estonia*
[8] *Department of earth sciences, University of Hawai'i at Mānoa, Honolulu, HI 96822, USA*
[9] *Department of Physics, University Federal of Rio Grande do Norte (UFRN), 59078-970 Natal, RN, Brazil*
[10] *Center for Astrophysics, Harvard and Smithsonian, 60 Garden Street, Cambridge, MA 02138, USA*
[11] *Institut d'astrophysique de Paris, UMR7095 CNRS, Universitée Pierre & Marie Curie, 98bis boulevard Arago, F-75014 Paris, France*
[12] *Observatoire de Haute-Provence, CNRS, Universitée d'Aix-Marseille, F-04870 Saint-Michel-l'Observatoire, France*

Accepted 2021 December 10. Received 2021 December 10; in original form 2021 November 8

ABSTRACT

We present the results of a study aiming at retrieving the fundamental parameters of M dwarfs from spectra secured with SPIRou, the near-infrared high-resolution spectropolarimeter installed at the Canada–France–Hawaii Telescope (CFHT), in the framework of the SPIRou Legacy Survey (SLS). Our study relies on comparing observed spectra with two grids of synthetic spectra, respectively, computed from PHOENIX and MARCS model atmospheres, with the ultimate goal of optimizing the precision at which fundamental parameters can be determined. In this first step, we applied our technique to 12 inactive M dwarfs with effective temperatures ($T_{\rm eff}$) ranging from 3000 to 4000 K. We implemented a benchmark to carry out a comparison of the two models used in this study. We report that the choice of model has a significant impact on the results and may lead to discrepancies in the derived parameters of 30 K in $T_{\rm eff}$ and 0.05 dex to 0.10 dex in surface gravity ($\log g$) and metallicity ([M/H]), as well as systematic shifts of up to 50 K in $T_{\rm eff}$ and 0.4 dex $\log g$ and [M/H]. The analysis is performed on high signal-to-noise ratio template SPIRou spectra, averaged over multiple observations corrected from telluric absorption features and sky lines, using both a synthetic telluric transmission model and principal component analysis. With both models, we retrieve $T_{\rm eff}$, $\log g$, and [M/H] estimates in good agreement with reference literature studies, with internal error bars of about 30 K, 0.05 dex, and 0.1 dex, respectively.

Key words: techniques: spectroscopic – stars: fundamental parameters – stars: low-mass – infrared: stars.

1 INTRODUCTION

M dwarfs are the most numerous stars of the solar vicinity (Reylé et al. 2021), and have recently attracted increasing attention in the search for exoplanets located in the habitable zone of their host stars (Bonfils et al. 2013; Dressing & Charbonneau 2013; Gaidos et al. 2016). Determining the fundamental parameters of host stars is a mandatory step for characterizing planets orbiting M dwarfs (Mann et al. 2015; Passegger et al. 2019).

In particular, the goal is to estimate as accurately as possible the effective temperature ($T_{\rm eff}$), surface gravity ($\log g$), and metallicity ([M/H]) of the host stars. These parameters are essential to derive accurate masses and radii of the orbiting companions, as these depend on the masses and radii of the stars when relying on indirect detection methods.

Multiple techniques have been developed to study these parameters by, e.g. adjusting equivalent widths of spectral lines (Rojas-Ayala et al. 2010; Neves et al. 2014; Fouqué et al. 2018), fitting spectral energy distributions (SEDs) to low to mid-resolution spectra (Mann, Gaidos & Ansdell 2013), or fitting synthetic models to high resolution spectra (Passegger et al. 2018, 2019; Schweitzer et al. 2019). For instance, Mann et al. (2015, hereafter M15) derived $T_{\rm eff}$, [Fe/H], masses, and radii of M dwarfs using empirical mass–magnitude relations, equivalent widths, and BT-settl PHOENIX models with low resolution spectra ($R \simeq 1000$). In contrast, Passegger et al. (2019, hereafter P19) performed fits of synthetic models on high-resolution CARMENES spectra, computing $\log g$ from empirical

★ E-mail: paul.cristofari@irap.omp.eu

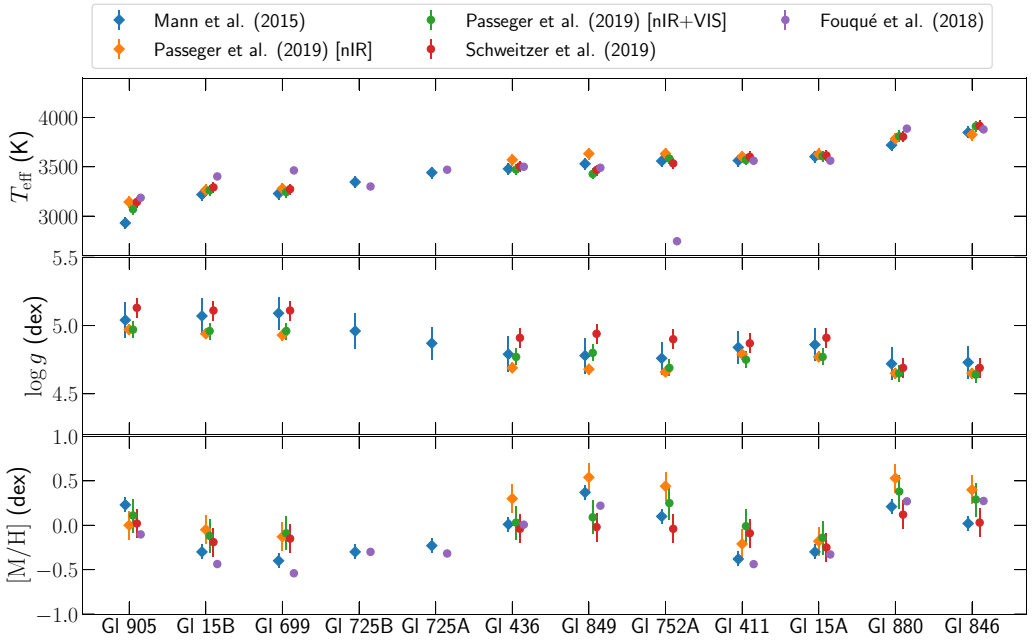

Figure 1. $T_{\rm eff}$, log g, and [M/H] values extracted from the reference studies of Mann et al. (2015), Passegger et al. (2019), Schweitzer et al. (2019), and Fouqué et al. (2018). The typical RMS with respect to the mean is of 45 K in $T_{\rm eff}$, 0.07 dex in log g, and 0.15 dex in [M/H].

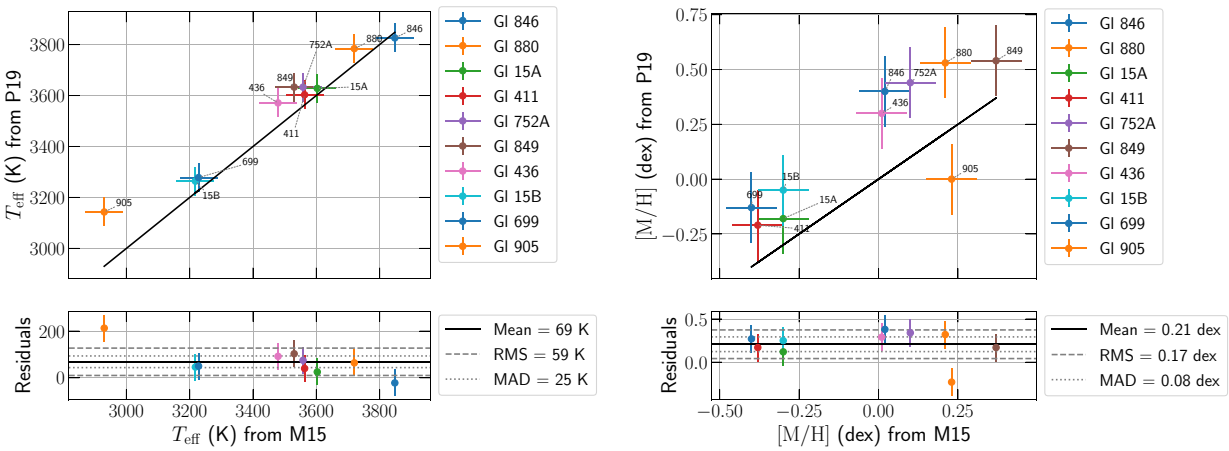

Figure 2. Comparison between parameters published by P19 (using near-infrared regions only) and M15. Top plots present the values retrieved by P19 plotted against the values retrieved by M15 for effective temperature (left-hand panel) and metallicity (right-hand panel). Bottom plots present the residuals, i.e. values retrieved by P19 minus values retrieved by M15. We additionally display the mean value, standard deviation, and median absolute deviation of the residuals.

$T_{\rm eff}$–log g relations. These different approaches typically result in different parameter values, as illustrated in Fig. 1 for the 12 inactive nearby M dwarfs which this paper will focus on. In particular, we compare the values published by M15 and P19 in Fig. 2, and recall the estimates derived by these two references in Table 1.[1]

The ultimate goal of the study we embark on, of which this paper is a first step, is to optimize the determination of these fundamental parameters taking advantage of the large homogeneous collection of SPIRou spectra recorded in the framework of the SPIRou Legacy Survey (SLS). Comparing high-resolution spectra of observed M dwarfs to dense grids of synthetic spectra derived from theoretical model atmospheres is presumably the most promising approach to this problem. However, the high complexity of the spectra, featuring large amounts of molecular and atomic lines, renders this approach challenging. For such studies to be attempted, high-resolution spectroscopy is mandatory, in order to resolve individual spectral features and their profile shapes, and thereby guide us to a more reliable spectral modelling of M dwarfs.

In practice, this requires accurate synthetic spectra that can be compared with observations. Throughout the last decade, multiple codes have been developed to produce synthetic spectra based on observational and experimental data (e.g. the properties of atomic and molecular lines). Codes such as MOOG (Sneden et al. 2012), SME (Valenti & Piskunov 2012), SYNTHE (Kurucz 2005), or Turbospectrum (Alvarez & Plez 1998; Plez 2012) can compute

[1]In this paper, we assume that the overall metallicity [M/H] = [Fe/H], considering no alpha enhancement as a simplifying assumption, and we therefore use the label [M/H] in all circumstances.

Table 1. Stellar properties of the studied targets. For each target, column 2 presents the spectral type and columns 3–6 respectively list the distance, the absolute K magnitude, the mass derived from the mass–luminosity relation of Mann et al. (2019), and the corresponding radius using Baraffe et al. (2015) models. Column 7 lists the surface gravity derived from columns 5 and 6. Column 8 reports $\log g$ values from angular diameters $\theta_{\rm LD}$ computed from interferometric data (Boyajian et al. 2012), assuming the distances and masses reported in columns 3 and 5. Columns 9–11 list the stellar properties from literature; (1): M15, (2): P19 (nIR), (3): P19 (nIR + optical). Spectral types, magnitudes, and parallaxes where obtained through SIMBAD (http://simbad.u-strasbg.fr/simbad/) and used to compute absolute magnitudes.

Star	Spectral type	Distance (pc)	$M_{\rm K}$	$M_\star/{\rm M}_\odot$	$R_\star/{\rm R}_\odot$	$\log g$ (dex) from $M_\star$ and $R_\star$	$\log g$ (dex) from interferometry	$T_{\rm eff}$ (K)	$\log g$ (dex)	[M/H] (dex)	Ref.
Gl 846	M0.5V	10.555 ± 0.016	5.205 ± 0.023	0.444 ± 0.004	0.416 ± 0.007	4.846 ± 0.004		3848 ± 60	4.73 ± 0.12	0.02 ± 0.08	(1)
								3826 ± 56	4.65 ± 0.04	0.40 ± 0.16	(2)
								3911 ± 54	4.64 ± 0.06	0.29 ± 0.19	(3)
Gl 880	M1.5V	6.868 ± 0.002	5.339 ± 0.016	0.422 ± 0.002	0.397 ± 0.004	4.866 ± 0.003	4.584 ± 0.005	3720 ± 60	4.72 ± 0.12	0.21 ± 0.08	(1)
								3784 ± 56	4.65 ± 0.04	0.53 ± 0.16	(2)
								3810 ± 60	4.65 ± 0.06	0.38 ± 0.19	(3)
Gl 15A	M2V	3.563 ± 0.001	6.261 ± 0.020	0.301 ± 0.002	0.300 ± 0.004	4.963 ± 0.003	4.745 ± 0.005	3603 ± 60	4.86 ± 0.12	-0.30 ± 0.08	(1)
								3628 ± 56	4.77 ± 0.04	-0.18 ± 0.16	(2)
								3606 ± 54	4.77 ± 0.06	-0.14 ± 0.19	(3)
Gl 411	M2V	2.547 ± 0.004	6.310 ± 0.050	0.295 ± 0.005	0.295 ± 0.009	4.968 ± 0.008	4.722 ± 0.011	3563 ± 60	4.84 ± 0.12	-0.38 ± 0.08	(1)
								3603 ± 56	4.79 ± 0.04	-0.21 ± 0.16	(2)
								3569 ± 54	4.75 ± 0.06	-0.01 ± 0.19	(3)
Gl 752A	M3V	5.912 ± 0.002	5.814 ± 0.020	0.355 ± 0.003	0.342 ± 0.004	4.921 ± 0.003		3558 ± 60	4.76 ± 0.12	0.10 ± 0.08	(1)
								3633 ± 56	4.66 ± 0.04	0.44 ± 0.16	(2)
								3583 ± 54	4.69 ± 0.06	0.25 ± 0.19	(3)
Gl 849	M3.5V	8.803 ± 0.004	5.871 ± 0.017	0.347 ± 0.002	0.336 ± 0.003	4.927 ± 0.003		3530 ± 60	4.78 ± 0.13	0.37 ± 0.08	(1)
								3633 ± 56	4.68 ± 0.04	0.54 ± 0.16	(2)
								3427 ± 54	4.80 ± 0.06	0.09 ± 0.19	(3)
Gl 436	M3.5V	9.756 ± 0.009	6.127 ± 0.016	0.316 ± 0.002	0.312 ± 0.003	4.951 ± 0.003		3479 ± 60	4.79 ± 0.13	0.01 ± 0.08	(1)
								3571 ± 56	4.69 ± 0.04	0.30 ± 0.16	(2)
								3472 ± 54	4.77 ± 0.06	0.03 ± 0.19	(3)
Gl 725A	M3V	3.522 ± 0.001	6.698 ± 0.020	0.256 ± 0.002	0.263 ± 0.003	5.005 ± 0.003	4.746 ± 0.008	3441 ± 60	4.87 ± 0.12	-0.23 ± 0.08	(1)
Gl 725B	M3.5V	3.523 ± 0.001	7.266 ± 0.023	0.208 ± 0.002	0.224 ± 0.003	5.054 ± 0.004	4.739 ± 0.016	3345 ± 60	4.96 ± 0.13	-0.30 ± 0.08	(1)
Gl 699	M4V	1.827 ± 0.001	8.216 ± 0.020	0.150 ± 0.001	0.175 ± 0.001	5.128 ± 0.002	5.071 ± 0.005	3228 ± 60	5.09 ± 0.12	-0.40 ± 0.08	(1)
								3278 ± 56	4.93 ± 0.04	-0.13 ± 0.16	(2)
								3243 ± 54	4.96 ± 0.06	-0.09 ± 0.19	(3)
Gl 15B	M3.5V	3.561 ± 0.001	8.190 ± 0.024	0.151 ± 0.001	0.176 ± 0.002	5.127 ± 0.003		3218 ± 60	5.07 ± 0.13	-0.30 ± 0.08	(1)
								3264 ± 56	4.94 ± 0.04	-0.05 ± 0.16	(2)
								3261 ± 54	4.96 ± 0.06	-0.12 ± 0.19	(3)
Gl 905	M5.0V	3.155 ± 0.001	8.434 ± 0.020	0.142 ± 0.001	0.167 ± 0.001	5.143 ± 0.002		2930 ± 60	5.04 ± 0.13	0.23 ± 0.08	(1)
								3143 ± 56	4.97 ± 0.04	0.00 ± 0.16	(2)
								3069 ± 54	4.97 ± 0.06	0.11 ± 0.19	(3)

synthetic spectra for different types of stars. These tools typically rely on pre-computed atmosphere models, such as MARCS (Gustafsson et al. 2008), or ATLAS (Kurucz 1970), and use radiative transfer codes to compute the emergent high-resolution spectra. In contrast, PHOENIX performs the computation of both the model atmosphere and the emergent spectrum. These models are usually based on a number of assumptions, such as local thermodynamic equilibrium (LTE) or non-local thermodynamic equilibrium (NLTE), plane-parallel atmospheres or spherical geometry, and the way the microturbulence is taken into account.

PHOENIX is widely considered as one of the most advanced tool for computing stellar atmospheres of M dwarfs and the corresponding emergent spectra. The most recent grid of atmosphere models and synthetic spectra, baptized PHOENIX-ACES models, was published in 2013 (Husser et al. 2013), updated in 2015, and covers a temperature range from 2300 to 12 000 K, suitable for the studies of various objects, such as M dwarfs and giants. MARCS models have been used in several studies focusing on FGK stars (Blanco-Cuaresma et al. 2014; Tabernero et al. 2019), and more recently on M dwarfs (Sarmento et al. 2021). In particular, recent publications (Passegger et al. 2018, 2019; Rajpurohit et al. 2018; Flores et al. 2019; Sarmento et al. 2021) have reported the use of PHOENIX and MARCS models to derive stellar properties of M dwarfs and young low-mass stars from high-resolution spectra secured with various instruments such as CARMENES (Nowak et al. 2020), iSHELL (Rayner et al. 2016), or APOGEE (Wilson et al. 2019), in the near-infrared (nIR) and/or optical domains. The study of the nIR domain, and the development of high-resolution spectrographs working in this spectral range, is mainly motivated by the hunt for planets orbiting very–low–mass stars that are often too faint to be observed in the optical domain. The most up-to-date models are however quite far from precisely reproducing every single line across the entire wavelength range. This is particularly true for the nIR domain, for which data are still limited.

In this study, we analyse nIR high-resolution spectra acquired with the SpectroPolarimètre Infra-Rouge (SPIRou; Donati et al. 2020) installed at the Canada–France–Hawaii Telescope (CFHT) to determine the fundamental parameters of twelve M dwarfs with effective temperatures ranging from about 3000 to 4000 K, using both PHOENIX-ACES and MARCS synthetic spectra. With this work, we push forward the efforts of previous studies and try to improve the accuracy on parameters measurements from nIR spectroscopy. In particular, we take advantage of the high resolving power ($R\sim$70 000) of SPIRou, which covers a spectral range in a single exposure spanning 980–2350 nm, allowing us to observe spectral lines in nIR bands for which few high-resolution observations are currently available. By collecting spectra of M dwarfs at different epochs, we are able to accurately correct for telluric absorption features and sky lines throughout the nIR domain, and to obtain high quality stellar spectra even in regions dominated by telluric absorption lines. Furthermore, SPIRou monitored about 70 M dwarfs, which will allow us to construct a self-consistent data base of stellar parameters for these targets. In the rest of the paper, we typically choose to confront our results to those published by M15, because this reference study based its results on techniques that are largely different from ours, reducing the risk of potential biases.

In Section 2 we outline the SPIRou observations used in this paper, and detail in Section 3 the way reference stellar spectra (called 'template spectra' in this paper) are derived from 40 to 80 individual spectra recorded at different epochs and corrected for telluric absorption and sky lines. In Section 4, we present the method we developed to retrieve the fundamental parameters of the host stars from their template SPIRou spectra. We discuss our results in Section 5, and conclude on the performances of

Table 2. Number of spectra and typical SNR per pixel in the *H* band used to build template spectra.

Star	Number of spectra	Median SNR [SNR range]
Gl 846	54	160 [150–220]
Gl 880	47	220 [150–245]
Gl 15A	38	285 [185–505]
Gl 411	36	385 [310–435]
Gl 752A	38	200 [145–230]
Gl 849	51	125 [105–140]
Gl 436	37	150 [100–225]
Gl 725A	64	230 [190–255]
Gl 725B	56	180 [160–190]
Gl 699	46	210 [165–240]
Gl 15B	77	105 [80–180]
Gl 905	79	125 [90–130]

our method and future steps to further extend its application (see Section 6).

2 SPIROU OBSERVATIONS

2.1 Targets selection

We focus our study on the 12 inactive targets outlined in Section 1, selected on the basis of three main criteria. More specifically, we chose stars that were observed at least 40 times with SPIRou, for which the parameters were determined by previous studies in order to have reference values for comparison, and whose effective temperatures range from 3000 to 4000 K. The sample also include two binary stars for which [M/H] values are expected to be similar.

For each M dwarf of our sample, we select 40 to 80 spectra among the best quality ones collected with SPIRou at different Barycentric Earth Radial Velocities (BERV). This data set allows us to construct high signal-to-noise ratio (SNR) telluric-corrected template spectra of the selected targets from sets of SPIRou observations (see Section 3). The number of SPIRou spectra used to build the templates of each star, and the typical SNR levels of these spectra, are listed in Table 2.

2.2 Observations

Observations were collected using SPIRou, mostly in the framework of the large programme called the SPIRou Legacy Survey (SLS) that was allocated 300 nights at CFHT over 3.5 yr. The two main science goals of the SLS are the search for exoplanets orbiting nearby M dwarfs, and the study of the impact of magnetic fields on star / planet formation. Data are processed through the SPIRou reduction pipeline, APERO (version 0.6.131; Cook et al., in preparation). APERO also provides a blaze function estimated from flat-field exposures acquired prior to observations, which is used to flatten observation spectra. Circularly polarized spectra were also recorded for the 12 stars in our sample but were not used in this analysis.

The spectra are then normalized using a low order polynomial fitted through the points of the continuum. Because SPIRou spectra are not flux calibrated, the normalization steps are mandatory to properly compare the acquired spectra to the synthetic ones. Both telluric correction steps (described in Section 3) and normalization steps are performed independently from APERO.

2.3 Alternative log *g* estimation

As estimating log *g* from stellar spectra is notoriously tricky (e.g. P19), we also summarized alternative estimates obtained with two independent techniques.

The first method consists in computing log *g* from the radius and mass of the stars derived from empirical relations and models. This particular approach presents the advantage of not relying on the retrieved $T_{\rm eff}$ or [M/H]. For the twelve stars in our sample, we obtained photometric measurements from the SIMBAD service.[2] We compute log *g* from the mass–luminosity relation of Mann et al. (2019) in the Ks band and theoretical mass–radius relations from Baraffe et al. (2015) assuming an age of 5 Gyr for all stars in our sample. The mass–radius relations show little deviation with respect to metallicity for low mass stars, and solar metallicity is therefore assumed. The log *g* values thus computed show little deviation from those estimated by M15 (RMS of 0.02 dex).

A second option is to compute log *g* from interferometry (Boyajian et al. 2012). This technique allows us to accurately determine the radius of a given star, and to therefore derive log *g* for a given mass. However, interferometric data of M dwarfs remain rare, and Boyajian et al. (2012) published angular diameters for only six stars in our sample. A comparison between the values obtained using interferometry and those derived from evolutionary models leads us to an RMS of the residuals of 0.06 dex and a median absolute deviation (MAD) of 0.04 dex, smaller than the typical computed uncertainties on log *g*.

All log *g* values mentioned above are reported in Table 1.

3 CONSTRUCTING TEMPLATES FROM SPIROU SPECTRA

Template spectra of our target stars are constructed through an iterative two-step process. We first correct tellurics from observed spectra, then derive the template spectra by computing the median of individual corrected spectra in the barycentric reference frame. This step is repeated until proper convergence is achieved (see Section 3.2). In a second step, we apply Principal Component Analysis (PCA) to the residuals of all individual spectra with respect to the median, to refine the telluric correction and remove emission lines from atmospheric airglow.

3.1 TAPAS correction of telluric lines

To correct telluric lines, we use TAPAS (Transmissions of the AtmosPhere for AStronomical data; Bertaux et al. 2014), a tool capable of computing the atmosphere transmission in the line of sight of a given target. The computation of the transmission relies on the LBLRTM software (Clough & Iacono 1995), using line lists provided by the HITRAN data base (Rothman et al. 2009, 2013).

The TAPAS web-server provides the transmission spectrum for a given epoch, site, and airmass, and for individual atmospheric molecules. For our purpose, we retrieved a typical theoretical spectrum for the six molecules primarily responsible for telluric absorption, i.e. O_2, H_2O, O_3, CO_2, CH_4, and NO_2. Each contribution is adjusted by a power law, and the resulting atmospheric transmission *T* is expressed as follows:

$$T = \left(T_1^{p_1}\ T_2^{p_2}\ T_3^{p_3}\ T_4^{p_4}\ T_5^{p_5}\ T_6^{p_6}\right) * G_\sigma \quad , \tag{1}$$

[2] http://simbad.u-strasbg.fr/simbad/

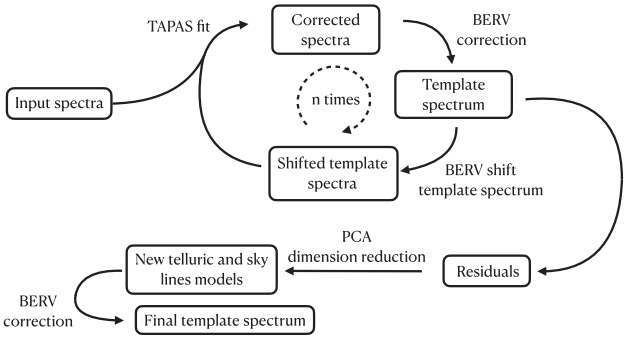

Figure 3. Dual-step iterative scheme used to derive template spectra from individual SPIRou spectra. TAPAS models are fitted on the input spectra using an iterative procedure. A PCA analysis is then applied on the residuals to improve upon the initial TAPAS correction. The stellar template is obtained by taking the median on the full set of TAPAS and PCA corrected spectra.

where T_X is the absorption spectrum, p_X is the adjusting exponent for molecule of index X (1: H_2O, 2: CH_4, 3: CO_2, 4: NO_2, 5: O_2, 6: O_3). G_σ is a Gaussian broadening function of standard deviation $\sigma = 1.83$ km s^{-1} (corresponding to a full-width at half-maximum of 4.3 km s^{-1}) appropriate for the instrumental broadening of SPIRou (Donati et al. 2020).

We also allow for radial velocity shifts of the entire telluric spectrum, as well as for a specific velocity shift of water lines with respect to the rest of the spectrum because of the less homogeneous spatial distribution of this molecule within the atmosphere and thereby its higher sensitivity to weather conditions (Ulmer-Moll et al. 2019). The synthetic telluric transmission model therefore depends on eight parameters.

To minimize the number of free parameters, we use the simplifying assumption that the powers p_{O_2}, p_{CO_2}, and p_{CH_4} are proportional to the airmass so that $p_X = a_X A$, with A denoting the airmass. We derived the values and error bars of the a_X slopes for the three molecules by fitting the model on telluric standards spectra acquired at various epochs, yielding:

$$\begin{cases} a_{CH_4} = 1.027 \pm 0.004 \\ a_{CO_2} = 1.059 \pm 0.003 \\ a_{O_2} = 0.998 \pm 0.006 \end{cases} \quad (2)$$

NO_2 and O_3 having negligible impact on the resulting telluric absorption spectrum in the SPIRou domain, we chose to set these coefficients to a standard value (of 1). The resulting model thus requires us to fit three parameters: p_{H_2O} and the two radial velocities.

3.2 Template construction procedure

The template spectra are built through the iterative procedure illustrated in Fig. 3. We fit TAPAS models on the input spectra with a Levenberg Mardquardt algorithm, and correct the template spectra with the resulting transmissions. The corrected spectra are shifted to account for the BERV, interpolated on the SPIRou wavelength grid, and a first template spectrum is computed by taking the median of the corrected spectra in the barycentric frame. For each value of the BERV, the template is shifted back in the observer frame and used to correct the original spectra from the stellar spectrum itself. The resulting spectra contain less stellar features and mostly telluric lines, allowing us to perform a better fit of the TAPAS model. The process can be repeated multiple times, and we find that five iterations are sufficient to reach satisfactory convergence for the stars in our sample i.e. for the coefficients to remain stable from iteration to iteration.

At the end of the iterative process, residuals are computed by correcting the original spectra by the TAPAS models and the template spectrum shifted to the geocentric frame. PCA is then applied to the residuals to extract the components accounting for most of the spectrum-to-spectrum variations. We found that the three components associated with the highest eigenvalues typically contain most of the variance and spectral line features. We therefore filter the residuals using these three components only and obtain improved model spectra of non-stellar features to correct stellar spectra with. In particular, this last PCA step allows one to correct for emission lines from the sky (atmospheric airglow) that are not included in the TAPAS models, but show up in the SPIRou spectra. All corrected spectra are then shifted to the barycentric reference frame, and the final stellar template is obtained by taking the median of all corrected spectra. The stellar templates computed with the described procedure have a typical SNR per pixel in the *H*-band in the range 500–2000.

We assess the quality of the telluric correction by performing cross–correlations between telluric absorption line masks and residuals. The cross–correlation profile shows a peak in the case of non-corrected spectra, which mostly vanishes with a proper correction of telluric and sky lines (see Fig. 4 for example). Fig. 5 illustrates the successive correction steps for one of our Gl 15A spectra.

We checked that the telluric- and sky-line-corrected template spectra generated with our direct approach, only applicable to stars for which tens of spectra are available for a wide range of BERV values, agree well with the nominal ones produced by the (more general) correction procedure implemented within APERO.

4 SPECTRAL ANALYSIS OF SPIROU TEMPLATE SPECTRA

Our analysis then consists in comparing template spectra (derived as outlined in Section 3) to grids of synthetic spectra computed from model atmospheres and radiative transfer codes. In this section, we describe how this comparison is achieved (Section 4.1), how spectral regions to be compared are selected (Section 4.2), and how the parameters of interest (i.e. $T_{\rm eff}$, $\log g$, and [M/H]) are obtained along with their associated error bars (Section 4.3).

4.1 Comparing observed template spectra with synthetic spectra

For this study, we gathered synthetic spectra computed with two different model atmospheres, namely PHOENIX (Allard & Hauschildt 1995) and MARCS (Gustafsson et al. 2008). We rely on the most recent grid of PHOENIX spectra available in the published literature (Husser et al. 2013), computed with a sampling rate of about 0.6 km s^{-1} for various $T_{\rm eff}$, $\log g$, and [M/H]. MARCS synthetic spectra were computed from the latest available MARCS model atmospheres and the Turbospectrum radiative transfer code (Alvarez & Plez 1998; Plez 2012), for a spectral sampling of 0.0025 nm (corresponding to about 0.5 km s^{-1} at 1400 nm). The range of parameters covered by the computed grid of PHOENIX and MARCS synthetic spectra is summarized in Table 3. The latest version of PHOENIX was specifically developed to improve the modelling of M dwarfs spectra at temperatures 3000 K and below, and is therefore expected to be more reliable than MARCS models on the low side of our temperature range.

To compare the models to template spectra, the synthetic spectra are integrated on the wavelength grid associated with the template

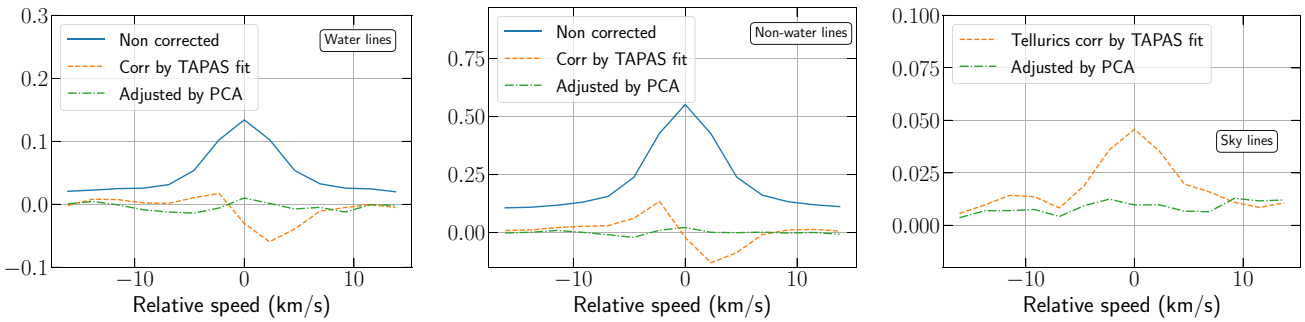

Figure 4. Left-hand panel: cross–correlation profile computed between the residuals for one of our Gl 699 spectra and a mask of water absorption lines. Middle: same as left-hand panel but with a mask containing lines for all the telluric absorbers but water. Right-hand panel: same as left-hand panel but with a mask containing OH emission lines.

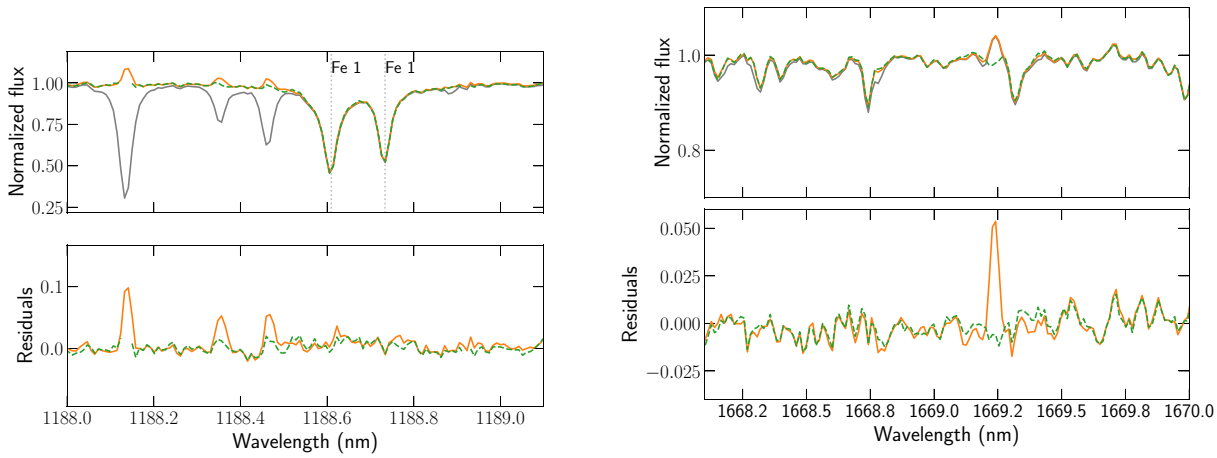

Figure 5. Examples of one of our Gl 15A spectra before and after correction of telluric and sky lines, the left-hand and right-hand panels showing examples of telluric and sky line correction, respectively. Top panel: The uncorrected spectrum (grey) features telluric lines approximately removed following the TAPAS correction (orange). Applying PCA on the residuals yields an improved correction (green). Spectral points with telluric absorption larger than 60 per cent of the local continuum (like those around 1188.14 nm) are excluded prior to applying PCA, to optimize correction on the weak to medium-strength telluric features. Bottom panel: Corresponding residuals before (orange) and after (green) applying PCA.

Table 3. Parameter range covered by the PHOENIX and MARCS synthetic spectral grids. The interpolation factor are chosen based on the typical uncertainties retrieved with our analysis, and indicate the level to which the models are interpolated for the analysis.

Variable	Range (and step size) PHOENIX	Range (and step size) MARCS	Interpolation factor PHOENIX/MARCS	Final step size
$T_{\rm eff}$ (K)	2300–7000 (100)	3000–4000 (100)	20/20	5
log g (dex)	0.0 – +6.0 (0.5)	3.5–5.5 (0.5)	50/50	0.01
[M/H] (dex)	−2.0 – +1.0 (0.5)	−1.5 – +1.0 (0.25)	50/25	0.01

spectra. We then adjust the continuum of the observed spectrum locally by matching the continuum points (defined as the highest 5 per cent points of each spectral window) of the observed spectrum to those of the synthetic spectrum.

We consider four main spectral-line broadeners: one of them to account for the instrument itself, and three associated with the star (microturbulence $v_{\rm mic}$, macroturbulence $v_{\rm mac}$ and rotation). We account for the instrumental broadening by applying a convolution with a Gaussian profile of full-width at half-maximum (FWHM) of 4.3 km.s^{-1} (Donati et al. 2020). The value of $v_{\rm mic}$ is set to 1 km s^{-1} for MARCS models. The PHOENIX models were computed with values of $v_{\rm mic}$ varying from 0.04 km.s^{-1} to 0.6 km.s^{-1} for the range of parameters covered in this study (with the lowest values of $v_{\rm mic}$ corresponding to the coolest stars). Subsequent tests involving the computation of MARCS models with a $v_{\rm mic}$ set to 0.3 km.s^{-1} showed that the influence of microturbulence is small compared to the differences observed between the two models. The effect of rotation is expected to be small compared to the other line broadeners for the inactive M dwarfs in our sample (Reiners et al. 2018), and difficult to disentangle from macroturbulence (Brewer et al. 2016). We chose to account for the joint contribution of rotation and macroturbulence by convolving all the synthetic spectra of the grid with a Gaussian profile of FWHM $v_{\rm b}$. In the rest of the paper, we will be assigning to $v_{\rm b}$ the value of the FWHM of the Gaussian profile, which may differ

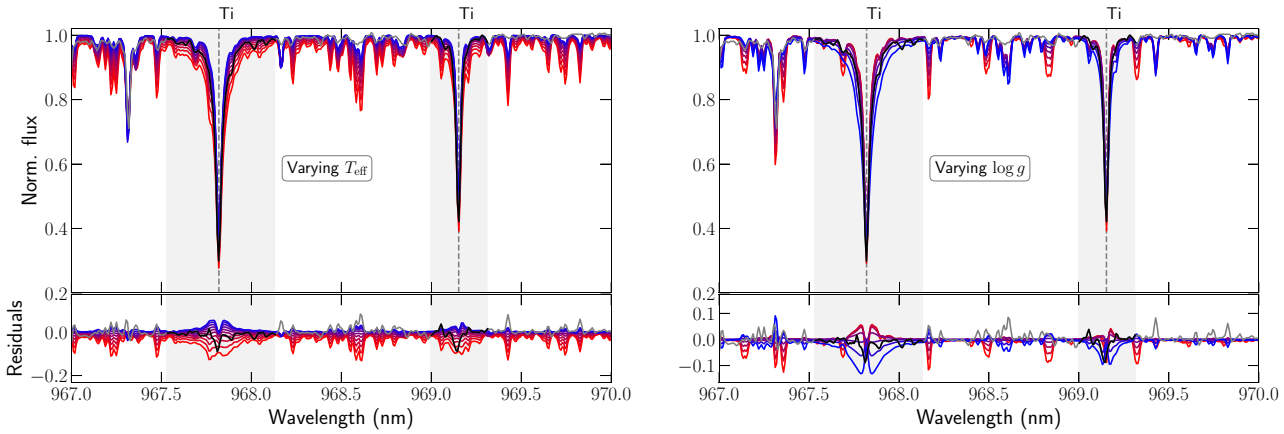

Figure 6. Comparison between PHOENIX synthetic spectra and the template spectrum of Gl 15A (grey). In the regions selected for the analysis, outlined with a grey background, the observed spectrum is displayed as a black line. The coloured spectra correspond to synthetic spectra for different values of the parameters, with red being the lowest and blue the highest. The associated parameters vary from 3000 K to 4000 K in steps of 100 K in $T_{\rm eff}$ (left-hand panel), and from 3. to 6.0 dex in steps of 0.5 dex in $\log g$ (right-hand panel). The bottom plots show the residuals, i.e. the synthetic spectra and template spectrum minus the synthetic spectrum corresponding to the parameters of M15.

from conventional values reported for macroturbulence, often given as $\xi = \mathrm{FWHM}/(2\sqrt{\ln 2}) \simeq 0.6$ FWHM.

The radial velocity (RV) of each star is first estimated by performing a cross–correlation of each template spectrum with a line mask generated from the VALD data base (Pakhomov, Ryabchikova & Piskunov 2019). The RV is then finely adjusted by minimizing a χ^2 with the help of a Levenberg–Marquardt algorithm for each individual synthetic spectrum.

4.2 Selecting spectral windows

Prior to the analysis, we need to identify the lines that are best reproduced by the models that are sensitive to a least one of the fundamental parameters we aim at characterizing (i.e. $T_{\rm eff}$, $\log g$, and [M/H]), and for which the correction of telluric and sky lines is reliable. A number of such lines were identified in previous studies (Rajpurohit et al. 2018; Flores et al. 2019; López-Valdivia et al. 2019; Passegger et al. 2019), and we used them as a starting point for the line selection. This was achieved by comparing SPIRou spectra to synthetic spectra, assuming the parameters published by M15. We began by selecting the lines that deviate from the observed spectrum by less than an arbitrary RMS threshold of 0.02, and for which the depth with respect to the continuum is expected to be greater than 20 per cent. A visual inspection was then carried out on each line to reject those heavily blended with nearby features. We also looked at the effect of varying $T_{\rm eff}$, $\log g$, and [M/H] on the lines to investigate how strong a role they can play for pinpointing these parameters (see Fig. 6 for example). The final list of selected lines is given in Table 4. This list contains about 30 atomic lines, and about 40 molecular lines, the latter being primarily CO lines redwards of 2293 nm. Table A1 summarizes the fundamental properties of the lines used with the PHOENIX and MARCS models, when available. Significant differences can be found in the line lists, which may partially explain the observed differences illustrated in Fig. 7.[3] Fig. A1 shows a comparison of the SPIRou template spectra for the 12 M dwarfs in our sample along with the best-fitting MARCS and PHOENIX models, for four selected lines. Fig. A2 (available as supplementary material) presents a similar comparison for all the lines used for the analysis.

[3]We double checked that adjusting the van der Waals coefficients of the lines used in our study to the values proposed by Petit et al. (2021) have little to no impact on the results detailed below.

Table 4. Selected lines for the analysis. Vacuum wavelengths were extracted from the VALD data base.

Species	Wavelength (nm)
Ti I	967.8198, 969.15274, 970.83269, 972.16252
	1058.7534, 1066.4544, 1189.6132, 1197.7124
	1281.4983, 1571.9867, 2296.9597
Ca I	1034.6654
Fe I	1169.3173, 1197.6323
K I	1169.342, 1177.2861, 1177.6061, 1243.5675, 1516.7211
Mn I	1297.9459
Al I	1315.435, 1672.3524, 1675.514
Mg I	1504.4357
Na I	2206.242, 2208.969
OH	1672.3418, 1675.3831, 1675.6299
CO	2293.5233, 2293.5291, 2293.5585, 2293.5754
	2293.6343, 2293.6627, 2293.7511, 2293.7900
	2293.9094, 2293.9584, 2294.1089, 2294.1668
	2294.3494, 2294.4163, 2294.6311, 2294.7059
	2294.9544, 2295.3195, 2295.4059, 2295.7263
	2295.8159, 2296.1743, 2296.2671, 2296.6648
	2296.7576, 2297.1971, 2297.2884, 2297.7719
	2297.8596, 2298.3888, 2298.4707, 2299.0488
	2299.1222, 2311.2404, 2312.4542, 2315.0029, 2316.3381

4.3 Determining stellar parameters

Each template spectrum is then compared to the whole grid of synthetic spectra following the procedure described in Section 4.1. We end up with a χ^2 landscape over the full 3D grid of stellar parameters from which we derive the optimal ones and the associated error bars.

More specifically, we begin by comparing the template spectra to the original grid of synthetic spectra sampled in steps of 100 K in $T_{\rm eff}$, 0.5 dex in $\log g$, and 0.5 (resp. 0.25 dex) in [M/H] with the grid of PHOENIX (resp. MARCS) synthetic spectra, to find a

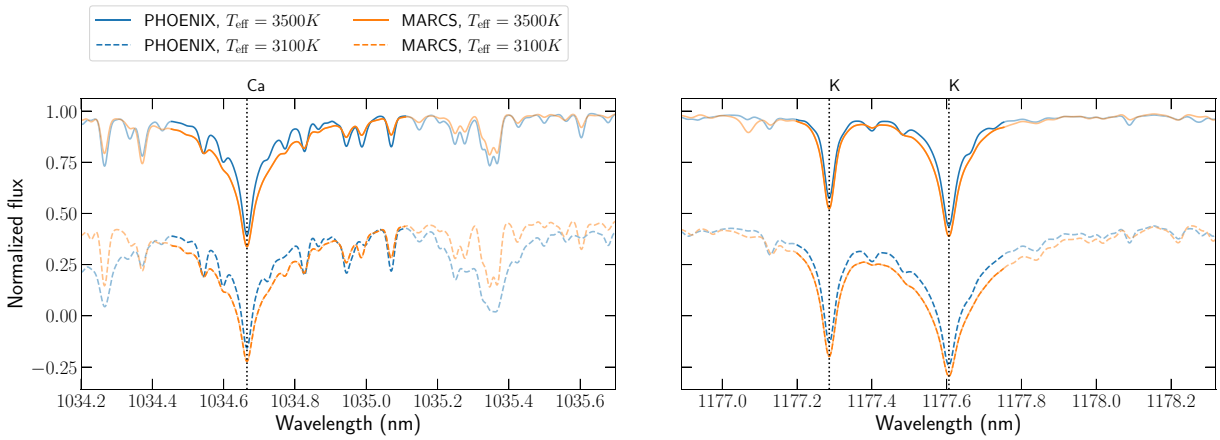

Figure 7. Comparison between synthetic spectra computed from PHOENIX and MARCS model atmospheres. The spectra are compared for two temperatures, and an offset is applied to the spectra for better readability. For all the models, $\log g = 5.0$ dex and [M/H] $= 0.0$ dex.

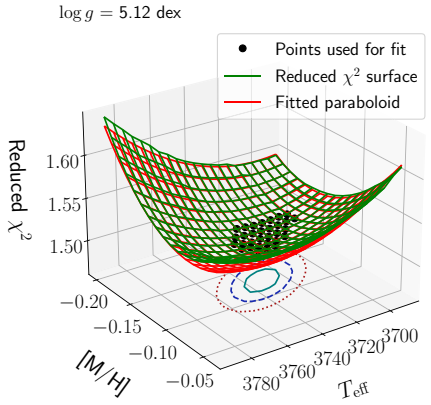

Figure 8. Example of a 2D section of the 3D χ^2 landscape (green) along with the fitted paraboloid (red) derived by comparing our Gl 15A template and the grid of PHOENIX spectra. The projected ellipses mark the contours defined by an increase in χ^2 of 1 (solid green), 4 (dashed blue), and 9 (dotted red) from the minimum. The value of $\log g$ is equal to 5.12 dex in this particular $T_{\rm eff}$, [M/H] slice of the 3D χ^2 landscape.

rough minimum χ^2. We then build a finer grid of synthetic spectra by linear interpolation covering 100 K in $T_{\rm eff}$ and 0.2 dex in $\log g$ and [M/H] around this minimum, in order to reach steps of 5 K in $T_{\rm eff}$ and 0.01 dex in $\log g$ and [M/H]. The interpolation factors and final step sizes are also reported in Table 3. The optimal parameters and error bars are computed by fitting a 3D paraboloid on the 500 points of smallest χ^2 values. Error bars are estimated by measuring the curvature of the 3D paraboloid around its minimum. We derive the 3D confidence ellipsoid in which χ^2 increases by no more than 1 with respect to its minimum value, and project it on each parameters axes. The projected intervals should contain 68.3 per cent of the retrieved values for each parameter assuming the noise obeys a Gaussian distribution (Press et al. 1992). An example 2D section of a 3D paraboloid fit, along with the 2D confidence ellipsoid is presented in Fig. 8. These error bars correspond to the minimum uncertainties of our parameter determination process, i.e. the error bars associated to the photon noise. If the minimum reduced χ^2 reached over the map is larger than 1, i.e. if systematic differences exist between the observations and the models, we scale up all the error bars in the spectra to enforce the minimum reduced χ^2 to be 1; this correction should in principle ensure that the derived error bars on the fitted parameters incorporate some of the systematic differences between the observations and the model, assuming that these differences can be treated as uncorrelated noise. The error bars computed in this way will be referred to as formal error bars in the rest of the paper, and are expected to account for the photon noise and some of the systematics.

4.4 Benchmarking the precision of our parameter determination

To better assess the precision of the derived parameters, and the reliability of the derived error bars, we carried out a benchmark using synthetic spectra to simulate SPIRou templates that we analysed in a second step with the procedure outlined in Sections 4.1 to 4.3.

To achieve this, we randomly generated 100 spectra with parameters ranging from 3000 K to 4000 K in $T_{\rm eff}$, from 3.5 dex to 5.5 dex in $\log g$ and from -0.5 dex to 0.5 dex in [M/H]. We added Gaussian noise to these spectra to simulate a signal-to-noise ratio (SNR) of $\sim$100 in the H-band, accounting for both the blaze in each order and the throughput of SPIRou (Donati et al. 2020). We then ran the procedure described in Section 4.3 on the simulated spectra to recover optimal values and corresponding error bars for $T_{\rm eff}$, $\log g$, and [M/H] for each of these spectra. The test was performed with either PHOENIX or MARCS models to simulate SPIRou templates and carry out the analysis, leading to four cases to study. Fig. 9 presents the results of the different cases along with the corresponding residuals. Linear trends are fitted on the retrieved parameters, with the slopes and intercepts listed in Table 5.

Performing the simulations with the same model (PHOENIX or MARCS) used to produce the input spectra and to run the analysis, we compute a minimum reduced χ^2 close to 1, and we are able to assess the precision of the formal error bars computed as described in Section 4.3. With the PHOENIX (respectively MARCS) synthetic spectra, we compute an RMS on the residuals of 8.2 K in $T_{\rm eff}$, 0.019 dex in $\log g$, and 0.015 dex in [M/H] (respectively 8.4 K in $T_{\rm eff}$, 0.020 dex in $\log g$, and 0.018 dex in [M/H]), slightly larger than the formal error bars of the order of 7.9 K in $T_{\rm eff}$, 0.017 dex in $\log g$, and 0.012 dex in [M/H] (respectively, 7.7 K in $T_{\rm eff}$, 0.017 dex in $\log g$, and 0.010 dex in [M/H]). These results tend to indicate that the formal error bars are overestimated by about 10–20 per cent, maybe up to 60 per cent on the metallicity with the MARCS models.

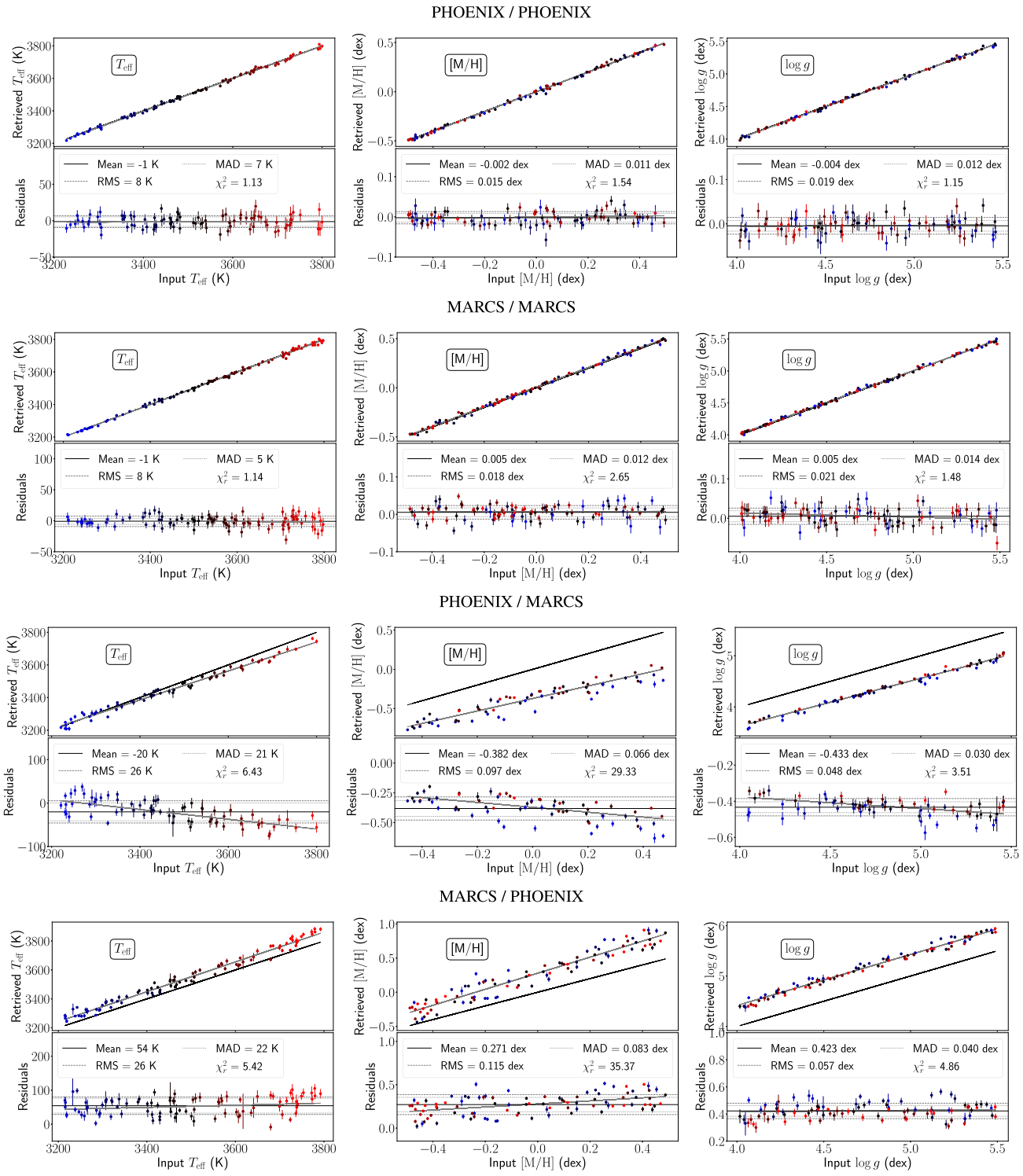

Figure 9. Simulations of parameters determination. The recovered $T_{\rm eff}$, $\log g$, and [M/H] are plotted against the values used to generate the model spectra. The black solid line marks the equality, and a grey solid line is the result of the linear fit performed on the data points. The coefficients and intercepts of the fits are reported in Table 5. All data points are colour coded as a function of $T_{\rm eff}$, blue corresponding to the smallest temperature (3200 K), red to the highest temperature (3800 K), and black corresponding to the median $T_{\rm eff}$ of 3500 K. RMS and MAD values are given with respect to the average of the residuals. The models are generated either from PHOENIX (first and third rows) or MARCS (second and fourth rows) synthetic spectra, which parameters chosen randomly, and a Gaussian noise is added to simulate an SNR of ∼100 in the *H*-band, accounting for both the blaze function in each order and the SPIRou throughput. For each model the analysis was performed with either the PHOENIX or MARCS grid of synthetic spectra.

Table 5. Slope and intercepts for the fits obtained on the data presented in Fig. 9.

	$T_{\rm eff}$ (K)		log g (dex)		[M/H] (dex)	
	Slope	Intercept at 3500 K	Slope	Intercept at 4.7 dex	Slope	Intercept at 0.0 dex
PHOENIX / PHOENIX	1.002 ± 0.005	3498 ± 19	1.002 ± 0.005	4.69 ± 0.02	1.007 ± 0.005	−0.0006 ± 0.0014
MARCS / MARCS	0.996 ± 0.005	3499 ± 17	0.989 ± 0.005	4.70 ± 0.02	1.002 ± 0.005	0.0070 ± 0.0016
PHOENIX / MARCS	0.887 ± 0.014	3473 ± 48	0.935 ± 0.012	4.27 ± 0.06	0.794 ± 0.030	−0.3716 ± 0.0082
MARCS / PHOENIX	1.031 ± 0.015	3552 ± 52	1.00 ± 0.013	5.12 ± 0.064	1.175 ± 0.030	0.2788 ± 0.0096

Table 6. Retrieved fundamental parameters using the grid of PHOENIX (cols. 2–7) and MARCS (cols 8–13) synthetic spectra with and without fixing log g to the values presented column 6 of Table 1.

	PHOENIX			PHOENIX (Fixed log g)			MARCS			MARCS (Fixed log g)		
Star	$T_{\rm eff}$ (K)	log g (dex)	[M/H] (dex)	$T_{\rm eff}$ (K)	log g (dex)	[M/H] (dex)	$T_{\rm eff}$ (K)	log g (dex)	[M/H] (dex)	$T_{\rm eff}$ (K)	log g (dex)	[M/H] (dex)
Gl 846	3902 ± 31	5.07 ± 0.05	0.37 ± 0.10	3861 ± 30	4.85 ± 0.09	0.34 ± 0.10	3815 ± 31	4.65 ± 0.05	0.04 ± 0.10	3867 ± 30	4.85 ± 0.09	0.08 ± 0.10
Gl 880	3773 ± 32	5.05 ± 0.05	0.54 ± 0.10	3732 ± 30	4.87 ± 0.05	0.52 ± 0.10	3674 ± 31	4.60 ± 0.05	0.18 ± 0.10	3745 ± 30	4.87 ± 0.05	0.23 ± 0.10
Gl 15A	3673 ± 32	5.09 ± 0.05	−0.25 ± 0.10	3632 ± 30	4.96 ± 0.07	−0.26 ± 0.10	3622 ± 31	4.61 ± 0.05	−0.45 ± 0.10	3721 ± 30	4.96 ± 0.07	−0.42 ± 0.10
Gl 411	3563 ± 31	4.91 ± 0.05	−0.25 ± 0.10	3583 ± 30	4.97 ± 0.15	−0.24 ± 0.10	3548 ± 31	4.49 ± 0.05	−0.50 ± 0.10	3706 ± 30	4.97 ± 0.15	−0.43 ± 0.10
Gl 752A	3588 ± 32	5.05 ± 0.05	0.36 ± 0.10	3561 ± 30	4.92 ± 0.08	0.34 ± 0.10	3530 ± 31	4.57 ± 0.05	0.05 ± 0.10	3605 ± 30	4.92 ± 0.08	0.11 ± 0.10
Gl 849	3513 ± 34	5.10 ± 0.06	0.54 ± 0.10	3493 ± 30	4.93 ± 0.08	0.51 ± 0.10	3475 ± 31	4.70 ± 0.06	0.22 ± 0.10	3525 ± 30	4.93 ± 0.08	0.27 ± 0.10
Gl 436	3539 ± 31	5.06 ± 0.05	0.18 ± 0.10	3520 ± 30	4.95 ± 0.08	0.17 ± 0.10	3497 ± 31	4.61 ± 0.05	−0.09 ± 0.10	3575 ± 30	4.95 ± 0.08	−0.04 ± 0.10
Gl 725A	3467 ± 31	4.93 ± 0.05	−0.27 ± 0.10	3491 ± 30	5.01 ± 0.08	−0.26 ± 0.10	3459 ± 31	4.55 ± 0.05	−0.46 ± 0.10	3601 ± 30	5.01 ± 0.08	−0.39 ± 0.10
Gl 725B	3346 ± 31	4.88 ± 0.05	−0.37 ± 0.10	3402 ± 30	5.05 ± 0.11	−0.33 ± 0.10	3349 ± 31	4.53 ± 0.05	−0.55 ± 0.10	3523 ± 30	5.05 ± 0.11	−0.43 ± 0.10
Gl 15B	3254 ± 32	5.01 ± 0.06	−0.58 ± 0.10	3295 ± 30	5.13 ± 0.09	−0.52 ± 0.10	3257 ± 31	4.66 ± 0.05	−0.67 ± 0.10	3404 ± 30	5.13 ± 0.09	−0.54 ± 0.10
Gl 699	3190 ± 32	4.71 ± 0.06	−0.70 ± 0.10	3329 ± 30	5.13 ± 0.14	−0.61 ± 0.10	3259 ± 41	4.58 ± 0.12	−0.80 ± 0.11	3440 ± 30	5.13 ± 0.14	−0.62 ± 0.11
Gl 905	2994 ± 32	4.99 ± 0.06	−0.07 ± 0.11	3028 ± 30	5.14 ± 0.11	0.04 ± 0.10	3023 ± 35	4.67 ± 0.08	−0.09 ± 0.11	3140 ± 30	5.14 ± 0.11	−0.22 ± 0.11

These error bars are those one could expect if the only source of uncertainty on the spectrum was the photon noise.

When using the PHOENIX models to simulate the template-like spectra and running the analysis with the grid of MARCS spectra, or vice-versa, we compute a typical minimum reduced χ^2 of 1.8. Ensuring a reduced χ^2 of 1 as described in Section 4.3, we compute formal error bars of the order of about 10 K in $T_{\rm eff}$, 0.025 dex in log g, and 0.015 dex in [M/H]. The RMS of the residuals is of the order of 30 K in $T_{\rm eff}$, 0.05 dex in log g, and 0.1 dex in [M/H], significantly larger than the computed formal error bars, which demonstrates that rescaling the χ^2 to 1 is not a sufficient correction to fully account for the uncertainty added by the systematic differences between the models. We therefore define updated error bars, which we will refer to as empirical error bars, as the quadratic sum of the formal error bars and estimates of the RMS computed when comparing the models, i.e. 30 K in $T_{\rm eff}$, 0.05 dex in log g, and 0.1 dex in [M/H].

We additionally observe systematic shifts and trends when comparing the retrieved parameters to the expected values. In particular, the grid of MARCS spectra leads us to systematic underestimates of log g (by about 0.4 dex) and [M/H] (by about 0.3 dex) when compared to the values adopted for the PHOENIX models, and vice-versa.

5 RESULTS

We performed the analysis described in Section 4 for the twelve stars in our sample assuming a broadening kernel of FWHM $v_{\rm b} = 3$ km s^{-1} (corresponding to a velocity of $\xi = 1.8$ km s^{-1} if the broadening is fully attributed to macroturbulence). The retrieved parameters are reported in Table 6, and presented among literature values in Fig. B1.

We find that, for each SPIRou template, the minimum χ^2 value ($\chi^2_{\rm min}$) retrieved for the best fit is systematically larger than the number of used data points (N, typically 1200), reflecting systematic differences between observations and synthetic spectra that are not accounted for. More specifically, the reduced χ^2 computed when comparing SPIRou templates to observation is on average of 250, much larger than the 1.8 found when comparing synthetic models (see Section 4). Here again, we ensure that our formal error bars account for some of these differences by forcing the χ^2 to 1, as described in Section 4.3.

The typical level to which our template spectra are fitted is equal to 2 to 3 per cent of the continuum.

5.1 Effective temperature

Fig. 10 presents a comparison between the $T_{\rm eff}$ values derived using the grid of PHOENIX and MARCS synthetic spectra and the values published in M15. Fig. B2 presents the same results compared to the values published by P19. With both models, we found $T_{\rm eff}$ values in good agreement with the values published by M15, with empirical error bars of the order of 30 K. We also compute an RMS value of the order of 40 K, smaller that the typical uncertainties reported by M15. Additionally, we find that the values recovered with the grid of PHOENIX models are on average about 30 K higher than with the MARCS models, comparable to the difference observed when running the simulations (see Section 4.4).

Looking more specifically at how our $T_{\rm eff}$ values derived with the grids of PHOENIX and MARCS spectra vary with those of M15, we find trends whose slopes are not exactly one, but rather 1.02 ± 0.04 and 0.85 ± 0.03, respectively, and with RMS dispersion about this trend equal to 33 K and 21 K, respectively, close to the computed empirical error bars. These trends are in fair agreement with those computed when comparing the two models with simulated data (see Section 4.4).

5.2 Metallicity

The values of [M/H] estimated from both the PHOENIX and MARCS spectral grids are compared to the values published by M15 in Fig. 11. Fig. B3 presents a similar comparison of our results to the values published by P19. The typical empirical error bars obtained for [M/H] are about 0.10 dex with the two grids, i.e. about 1.5 to 2.5 times smaller than the RMS between our values and those of M15 (equal to 0.14 dex with the grid of MARCS spectra and 0.23 dex with the grid of PHOENIX spectra), and of the order of the [M/H] uncertainties derived by M15 (equal to 0.08 dex). We also find that the estimated [M/H] derived with the MARCS spectra are

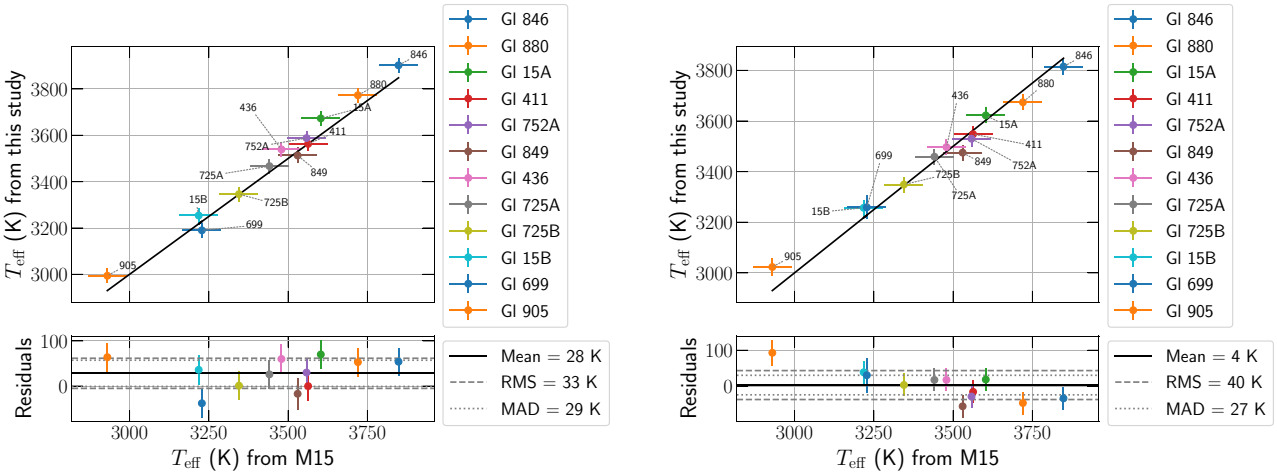

Figure 10. Retrieved $T_{\rm eff}$ using the grid of PHOENIX (left-hand panel) and MARCS (right-hand panel) spectra plotted against values published by M15. The bottom plot presents the residuals, i.e. the retrieved values minus literature values. RMS and MAD values are computed after application of a sigma clipping function on the residuals with a threshold at 5 σ.

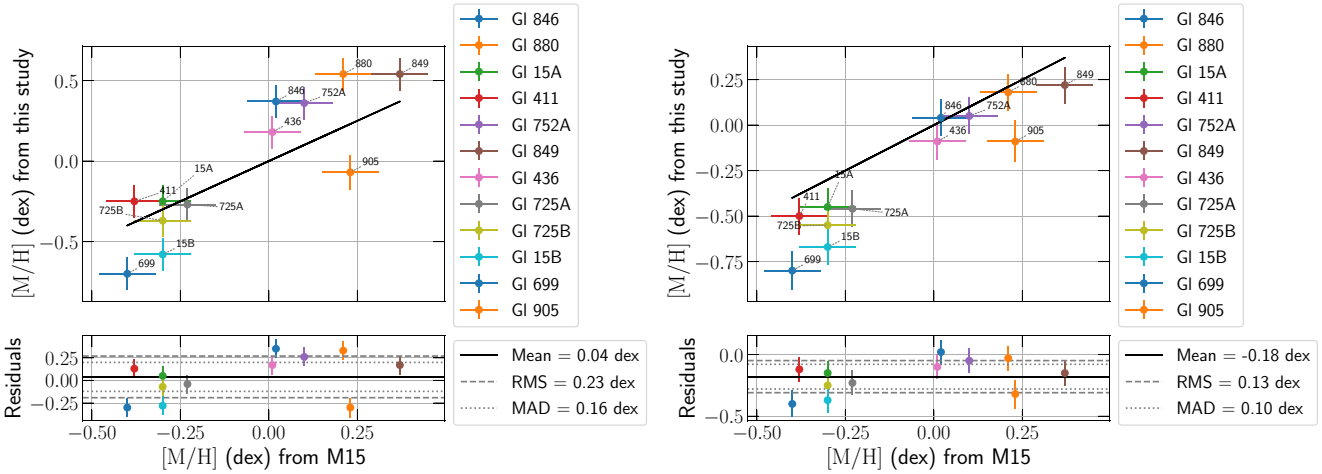

Figure 11. Same as Fig. 10 but for [M/H].

on average 0.18 dex smaller than the values published by M15. The large offset in the average values retrieved with the PHOENIX and MARCS models, of about 0.4 dex, is in good agreement with the offsets computed in our simulations introduced in Section 4.4

For the two binary stars in our sample, we compare the metallicities of both components. With the grid of MARCS spectra, for the Gl 15AB and the Gl 725AB binaries, we find differences in the metallicities of 0.21 and 0.09 dex, respectively. The values derived with this model agree at a 2σ level with the computed empirical error bars. With the grid of PHOENIX spectra, the retrieved [M/H] values differ by 0.10 dex for Gl 725A and Gl 725B, again in good agreement with our empirical error bars; but the difference in [M/H] values reaches 0.33 dex for Gl 15A and Gl 15B, i.e. 3.3 times our empirical error bars.

5.3 Surface gravity

Fig. 12 presents a comparison between the $\log g$ estimates derived with the grid of PHOENIX and MARCS spectra and the values published by M15. The $\log g$ values recovered with the grid of PHOENIX spectra are largely scattered around the equality line, with a computed RMS of the residuals of about 0.2 dex, 3 to 4 times the typical empirical error bars. With the grid of MARCS spectra, the values of $\log g$ appear to be systematically underestimated by about 0.30 dex with respect to M15, and the RMS of residuals is of 0.16 dex, close to the uncertainties published by M15 for these parameters (of 0.12 dex). We also notice that the retrieved $\log g$ values do not fully agree with those expected from the mass luminosity relations and interferometric data (see Section 2.3), although we remind that they span only a small range of values (smaller than the step size in $\log g$ within the grid of synthetic spectra, equal to 0.5 dex).

Given that $\log g$ is apparently difficult to constrain reliably, at least from the list of stellar lines used, we attempted to improve the precision on the other parameters by fixing the value of $\log g$ to the values derived from mass–radius relations and evolutionary models (see Section 2.3). Our approach is similar to that used by Mann et al. (2015), who derived masses from mass–luminosity relations and radii from bolometric flux and parallaxes. The estimated $T_{\rm eff}$ and [M/H] with both the PHOENIX and MARCS spectral grids are listed in Table 6.

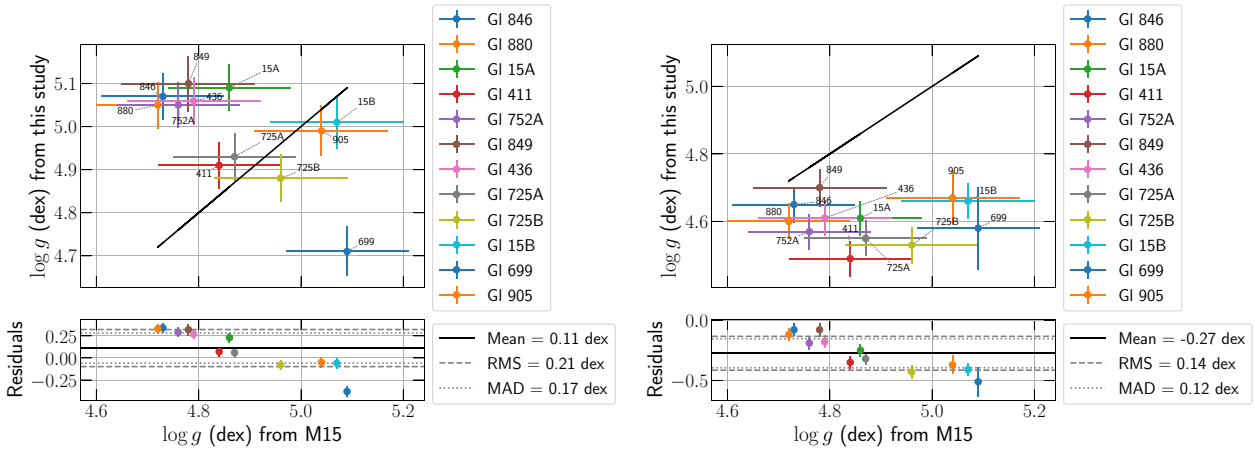

Figure 12. Same as Fig. 10 but for $\log g$.

Table 7. Mean, RMS, and MAD values of the residuals – i.e. parameter values of this study minus values published by M15 – derived with the PHOENIX and MARCS spectral grids. The label 'Fixed $\log g$' specifies that we adopted the values presented column 6 of Table 1 for this parameter, and the values in parentheses therefore do not originate from fits.

Model used	$T_{\rm eff}$ (K)			$\log g$			[M/H]		
	MEAN	RMS	MAD	MEAN	RMS	MAD	MEAN	RMS	MAD
PHOENIX	28	33	29	0.11	0.21	0.17	0.04	0.23	0.16
MARCS	4	40	27	− 0.27	0.14	0.12	− 0.18	0.13	0.10
PHOENIX (Fixed $\log g$)	21	48	36	0.04	0.03	0.02	0.04	0.19	0.13
MARCS (Fixed $\log g$)	111	82	72	0.04	0.03	0.02	− 0.11	0.09	0.06

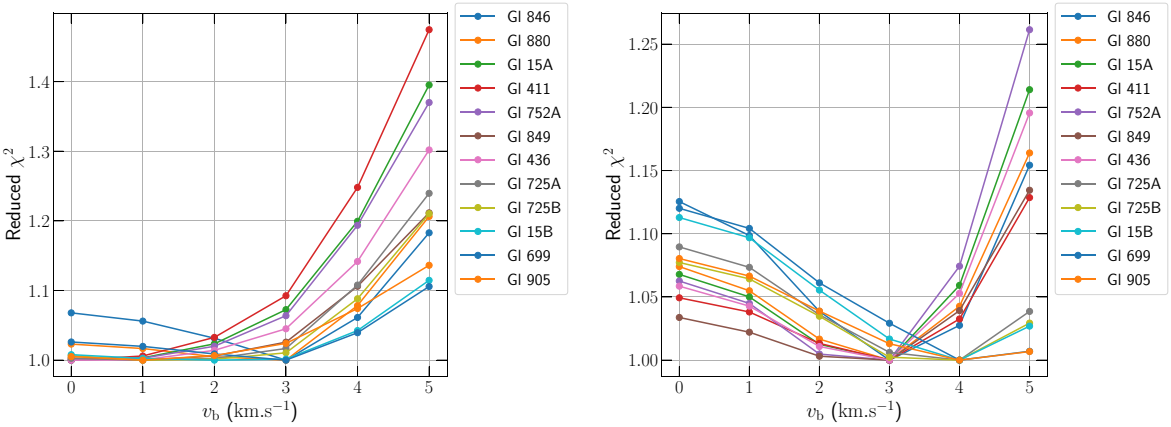

Figure 13. Reduced χ^2 as a function of the FWHM of the considered Gaussian profile, $v_{\rm b}$, obtained with the grid of PHOENIX (left-hand panel) and MARCS (right-hand panel) synthetic spectra, for each target of our sample. The reduced χ^2 for each star are rescaled to the minimum value reached over the range of $v_{\rm b}$, to ease comparison.

This additional constraint has little impact on the $T_{\rm eff}$ and [M/H] derived with the grid of PHOENIX spectra. With this grid, the most notable change is a trend in the recovered $T_{\rm eff}$ of slope 0.83 ± 0.03 with respect to the values of M15, which causes an increase in the computed RMS for this parameter. With the grid of MARCS spectra, we observe a significant offset of about 100 K in the retrieved $T_{\rm eff}$ values, along with an RMS of about 85 K, about twice the RMS computed when fitting all three parameters. Moreover, we observe that fixing $\log g$ does not reduce significantly the gap between the recovered [M/H] for Gl 15A and Gl 15B with the grid of PHOENIX spectra.

All RMS and MAD values are listed in Table 7.

5.4 Assessing the influence of $v_{\rm b}$ on the recovered parameters

We repeated our analysis for several values of the FWHM ($v_{\rm b}$) considered for the Gaussian profile used to broaden the synthetic spectra, which accounts for the joint contributions of $v\sin i$, $v_{\rm mac}$, and any other underestimated broadening effect. As shown in Fig. 13, we find that the value of $v_{\rm b}$ providing an optimal fit to the observed spectra falls in the range 1–3 km s^{-1} for most of the stars in our sample, and is lower with the grid of PHOENIX spectra than with the grid of MARCS spectra. As already stressed, being FWHM, these values should be compared with care to $v\sin i$ or $v_{\rm mac}$ estimates reported in the literature. We also report that the assumed value of

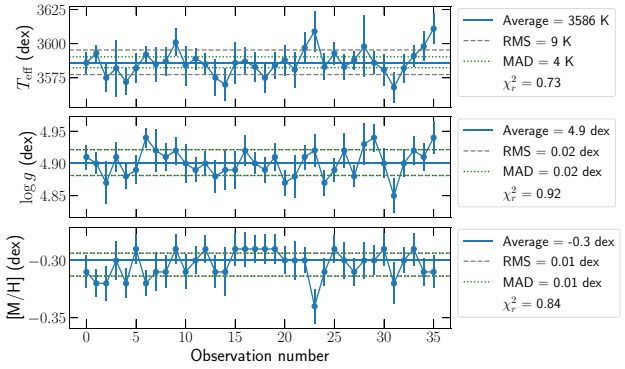

Figure 14. Optimal estimates and corresponding error bars retrieved for a series of SPIRou spectra of Gl 411. The mean value, standard deviation, and median absolute deviation are indicated for each series. We also compute the reduced χ^2 to the mean value of each series.

v_b has no more than a weak impact on the retrieved parameters. The mean, RMS, and MAD computed for different values of v_b are presented in Table C1.

5.5 Estimating the precision of formal error bars

To further assess the precision of the method, we performed the analysis on numerous SPIRou spectra acquired for a single target. Fig. 14 presents the parameters retrieved for our series of Gl 411 spectra along the computed formal error bars, which only account for photon noise and part of the systematics. We observe fluctuations in the retrieved parameters, and estimate their deviation to the mean with respect to our formal error bars by computing the reduced χ^2 on the series of retrieved values. The computed reduced χ^2 show that the formal error bars on the retrieved parameters seem to provide a reliable value on the internal measurement precision. We repeated this test on a series of high-SNR spectra of Gl 699 and recovered a reduced χ^2 of 0.66 for $T_{\rm eff}$, 0.85 on log g, and 0.89 on [M/H], again suggesting that our formal error bars properly account for the deviation found in the parameters for a given star, i.e. at a given point of the $T_{\rm eff}$-log g-[M/H] parameter space. As a sanity check, we performed MCMC computations to explore the χ^2 grid, performing linear interpolation within the grid to retrieve the χ^2 values at each MCMC step. We find that the derived parameters and error bars are in good agreement with those obtained with our main method (described in Section 4.3).

6 DISCUSSION AND CONCLUSIONS

In this paper, we presented the results of a method aimed at determining the fundamental parameters of M dwarfs (i.e. $T_{\rm eff}$, log g, [M/H]) from nIR high-resolution spectra acquired with SPIRou.

We built high-SNR template spectra of 12 inactive M dwarfs from 40 to 80 observed SPIRou spectra collected for each star at a wide range of BERV values, allowing us to reliably correct these spectra for telluric features and sky lines. The correction is performed by iteratively fitting a synthetic model of the Earth atmosphere's transmission (TAPAS) on each observed spectrum, and taking advantage of the numerous observations acquired at various epochs for each target. PCA is also used to further improve telluric correction and remove emission lines from the sky at the same time. We then selected spectral regions that are sensitive to the stellar parameters to be retrieved and best reproduced by two sets of synthetic spectra derived from PHOENIX and MARCS model atmospheres.

The analysis of the template spectra relies on their direct comparison to the synthetic spectra in the selected regions. Only small regions of the synthetic spectra reproduce observed features well enough to constrain parameters because of the lack of precision of the models and line lists currently used, especially in the nIR. We were therefore led to restrict our analysis to about 30 atomic lines, 2 OH lines, and 40 CO lines from the bands redwards of 2293 nm, in spite of the thousands of spectral lines present in the SPIRou spectra. Moreover, remaining discrepancies are observed between the models and template spectra, even for the selected lines, leading to differences between the parameters recovered with both models. The MARCS models rely on the most recent VALD line lists, updated since the publication of the PHOENIX models, which may partially explain the observed differences.

To assess the reliability and precision of our method, we carried out a benchmark, substituting the template spectra with synthetic spectra generated for random parameters, and adding Gaussian noise to simulate an SNR per pixel of $\sim$ 100 in the H-band. These simulations allowed us to confirm that the formal error bars computed with our procedure provide a fair estimate of the uncertainties associated with photon noise. By confronting the PHOENIX synthetic spectra to the MARCS synthetic spectra through our simulations, we observed a larger dispersion on the retrieved parameters than our formal error bars can account for, which can be attributed to the systematic differences between the models. We therefore chose to provide a more realistic estimation of the error bars by taking the quadratic sum of these systematic error bars and our computed formal error bars. Performing the analysis on our SPIRou templates, we derive empirical error bars of the order of 30 K in $T_{\rm eff}$, 0.05 dex in log g, and 0.10 dex in [M/H], smaller than the typically published uncertainties on these parameters.

In order to estimate the accuracy of our method with respect to values published in the literature, we compared our results to the pseudo-empirical parameters estimated by Mann et al. (2015). In particular, we compute a standard deviation of about 30 K to 50 K in $T_{\rm eff}$, and 0.15 dex to 0.20 dex in log g, and [M/H] with the two grids of synthetic spectra, about twice larger than our empirical error bars, and comparable to the typical uncertainties published by P19.

Additionally, we find significant differences in the results obtained with the two grids of synthetic spectra, of about 30 K in $T_{\rm eff}$, 0.2 dex in [M/H], and 0.4 dex in log g. These observed offsets are in good agreement with these observed when comparing the PHOENIX and MARCS synthetic spectra through our simulations, and can therefore be attributed to the systematic differences in the line profiles predicted by the two models. We also find trends between our retrieved $T_{\rm eff}$ and those of M15, with slopes that are not exactly equal to one (1.04 ± 0.04 and 0.86 ± 0.04 with the grids of PHOENIX and MARCS spectra, respectively) and with RMS about these trends very close to the empirical error bars computed with both models ($\sim$30 K). These trends are also in good agreement with those retrieved when comparing the two models through our simulations.

Because constraining the surface gravity appears to be difficult, we investigated the effect of fixing the values of log g to derive $T_{\rm eff}$ and [M/H]. This constraint caused a significant increase in the average and scattering of $T_{\rm eff}$ values derived with the grid of MARCS spectra, and did not bring significant improvement to the analysis relying on the grid of PHOENIX spectra.

Binary stars provide an additional way of testing the precision of our method, as we expect to retrieve similar metallicities for both components. For the two binaries included in our study and with both

synthetic grids, these discrepancies tend to be of the order of 0.2 dex or lower, in rough agreement with our empirical error bars, except for the Gl 15AB binary when modelled with PHOENIX spectra, for which we find a difference of about 0.33 dex. We also report that fixing $\log g$ to derive [M/H] does not significantly reduce this gap.

The results presented in this paper demonstrate the viability of the approach, i.e. of extracting stellar parameters from nIR SPIRou spectra, and show that the necessary assumptions on which this study relies (such as the choice of broadening kernel and normalization strategies) have a much smaller impact on the results than the discrepancies found between synthetic models and observations. A close comparison of the line parameters used by PHOENIX and MARCS (when available) shows significant differences for some lines. Our line selection procedure is however based on a comparison of both models, which likely led us to select lines for which parameters best agree between the two lists. Large differences however remain between the PHOENIX and MARCS synthetic spectra, even for the selected lines, which may indicate that the choice of model atmospheres, and modelling assumptions, may be responsible for most of the observed discrepancies. A subsequent work will attempt to better understand these differences, in order to improve our modelling strategies and the accuracy of our analysis.

In a future study, we will attempt to produce PHOENIX spectra using the latest line lists available. This will allow us to carry out a more precise comparison of the PHOENIX and MARCS models and to assess the impact of the line lists on the produced spectra. In parallel, we plan to improve the analysis by identifying more lines capable of constraining the stellar parameters, in particular $\log g$ and [M/H]. A second step will include the modification of the line list in the regions selected for the analysis, guided by the SPIRou high resolution spectra of reference stars, allowing us to further calibrate the analysis method.

Following works will then aim at applying the procedure discussed in this paper to all M dwarfs observed with SPIRou as part of the SLS, in order to build a self-consistent data base of stellar properties. We will also focus on other classes of stars of interest for the SLS, in particular active pre-main-sequence (PMS) low-mass stars. These stars are known to be difficult to model because of the presence of large star spots and strong magnetic fields at their surface, for which a 2-temperature model seems to be required to obtain a proper fit to the spectra (Gully-Santiago et al. 2017). By improving the spectral modelling of low-mass stars, we should be able to pinpoint their stellar properties with a higher precision than what is currently achieved, directly from nIR SPIRou spectra. In turn, such constraints will help us to better characterize planets orbiting these stars, and to guide us towards more reliable atmospheric models of M dwarfs and PMS stars.

ACKNOWLEDGEMENTS

This project received funding from the European Research Council under the H2020 research and innovation programme (grant #740651 NewWorlds).

This work is based on observations obtained at the Canada–France–Hawaii Telescope (CFHT) which is operated by the National Research Council (NRC) of Canada, the Institut National des Sciences de l'Univers of the Centre National de la Recherche Scientifique (CNRS) of France, and the University of Hawaii. The observations at the CFHT were performed with care and respect from the summit of Maunakea which is a significant cultural and historic site.

This work made use of TAPAS (Transmissions of the AtmosPhere for AStronomical data) models acquired through the ETHER French Atmospheric Chemistry Data Centre (http://ether.ipsl.jussieu.fr/tapas/).

This research has made use of the SIMBAD (Set of Identifications, Measurements, and Bibliography for Astronomical Data) data base (Wenger et al. 2000), operated at CDS, Strasbourg, France

This work has made use of the VALD (Vienna Atomic Line Database) data base, operated at Uppsala University, the Institute of Astronomy RAS in Moscow, and the University of Vienna. We also acknowledge funding from the French National Research Agency (ANR) under contract number ANR-18-CE31-0019 (SPlaSH)

TM acknowledges financial support from the Spanish Ministry of Science and Innovation (MICINN) through the Spanish State Research Agency, under the Severo Ochoa Program 2020-2023 (CEX2019-000920-S).

We thank an anonymous referee for suggesting modifications that improved the manuscript.

DATA AVAILABILITY

The data used in this work was acquired in the context of the SLS, and will be publicly available from the Canadian Astronomy Data Center one year following the completion of the SLS.

REFERENCES

Allard F., Hauschildt P. H., 1995, ApJ, 445, 433
Alvarez R., Plez B., 1998, A&A, 330, 1109
Baraffe I., Homeier D., Allard F., Chabrier G., 2015, A&A, 577, A42
Barklem P. S., Piskunov N., O'Mara B. J., 2000, A&AS, 142, 467
Bertaux J. L., Lallement R., Ferron S., Boonne C., Bodichon R., 2014, A&A, 564, A46
Blanco-Cuaresma S., Soubiran C., Heiter U., Jofré P., 2014, A&A, 569, A111
Bonfils X. et al., 2013, A&A, 556, A110
Boyajian T. S. et al., 2012, ApJ, 757, 112
Brewer J. M., Fischer D. A., Valenti J. A., Piskunov N., 2016, ApJS, 225, 32
Clough S. A., Iacono M. J., 1995, J. Geophys. Res., 100, 16,519
Donati J.-F. et al., 2020, MNRAS, 498, 5684
Dressing C. D., Charbonneau D., 2013, ApJ, 767, 95
Flores C., Connelley M. S., Reipurth B., Boogert A., 2019, ApJ, 882, 75
Fouqué P. et al., 2018, MNRAS, 475, 1960
Gaidos E., Mann A. W., Kraus A. L., Ireland M., 2016, MNRAS, 457, 2877
Gully-Santiago M. A. et al., 2017, ApJ, 836, 200
Gustafsson B., Edvardsson B., Eriksson K., Jørgensen U. G., Nordlund Å., Plez B., 2008, A&A, 486, 951
Husser T. O., Wende-von Berg S., Dreizler S., Homeier D., Reiners A., Barman T., Hauschildt P. H., 2013, A&A, 553, A6
Kurucz R. L., 1970, SAO Special Report, 309
Kurucz R. L., 2005, Mem. Soc. Astron. Ital. Suppl., 8, 14
López-Valdivia R. et al., 2019, ApJ, 879, 105
Mann A. W., Gaidos E., Ansdell M., 2013, ApJ, 779, 188
Mann A. W., Feiden G. A., Gaidos E., Boyajian T., von Braun K., 2015, ApJ, 804, 64 (M15)
Mann A. W. et al., 2019, ApJ, 871, 63
Neves V., Bonfils X., Santos N. C., Delfosse X., Forveille T., Allard F., Udry S., 2014, A&A, 568, A121
Nowak G. et al., 2020, A&A, 642, A173
Pakhomov Y. V., Ryabchikova T. A., Piskunov N. E., 2019, Astron. Rep., 63, 1010
Passegger V. M. et al., 2018, A&A, 615, A6
Passegger V. M. et al., 2019, A&A, 627, A161 (P19)
Petit P. et al., 2021, A&A, 648, A55
Plez B., 2012, Turbospectrum: Code for Spectral Synthesis, record ascl:1205.004

Press W. H., Teukolsky S. A., Vetterling W. T., Flannery B. P., 1992, Numerical Recipes in C (2nd Ed.): The Art of Scientific Computing. Cambridge Univ. Press, Cambridge
Rajpurohit A. S., Allard F., Rajpurohit S., Sharma R., Teixeira G. D. C., Mousis O., Kamlesh R., 2018, A&A, 620, A180
Rayner J. et al., 2016, in Evans C. J., Simard L., Takami H., eds, Proc. SPIE Conf. Ser. Vol. 9908, Ground-based and Airborne Instrumentation for Astronomy VI. SPIE, Bellingham, p. 990884
Reiners A. et al., 2018, A&A, 612, A49
Reylé C., Jardine K., Fouqué P., Caballero J. A., Smart R. L., Sozzetti A., 2021, A&A, 650, A201
Rojas-Ayala B., Covey K. R., Muirhead P. S., Lloyd J. P., 2010, ApJ, 720, L113
Rothman L. S. et al., 2009, J. Quant. Spectrosc. Radiat. Transfer, 110, 533
Rothman L. S. et al., 2013, J. Quant. Spectrosc. Radiat. Transfer, 130, 4
Sarmento P., Rojas-Ayala B., Delgado Mena E., Blanco-Cuaresma S., 2021, A&A, 649, A147
Schweitzer A. et al., 2019, A&A, 625, A68
Sneden C., Bean J., Ivans I., Lucatello S., Sobeck J., 2012, MOOG: LTE Line Analysis and Spectrum Synthesis, record ascl:1202.009
Tabernero H. M., Marfil E., Montes D., González Hernández J. I., 2019, A&A, 628, A131
Ulmer-Moll S., Figueira P., Neal J. J., Santos N. C., Bonnefoy M., 2019, A&A, 621, A79
Valenti J. A., Piskunov N., 2012, SME: Spectroscopy Made Easy, record ascl:1202.013
Wenger M. et al., 2000, A&AS, 143, 9
Wilson J. C. et al., 2019, PASP, 131, 055001

SUPPORTING INFORMATION

Supplementary data are available at *MNRAS* online.

Figure A2. Template spectra (grey) along with the fitted PHOENIX model (dashed orange) and MARCS model (dotted green) for the different spectral windows. Selected regions of the template spectra over which the comparison was carried out are shown in black. From top to bottom: Gl 846, Gl 880, Gl 15A, Gl 411, Gl 752A, Gl 849, Gl 436, Gl 725A, Gl 725B, Gl 15B, Gl 699, and Gl 905. Every spectrum but the first one is shifted by a multiple of 0.5 for better readability.

Please note: Oxford University Press is not responsible for the content or functionality of any supporting materials supplied by the authors. Any queries (other than missing material) should be directed to the corresponding author for the article.

APPENDIX A: SELECTED LINES COMPARED SYNTHETIC MODELS

Fig. A1 presents the templates spectra and best-fitting PHOENIX and MARCS models for eight of the selected regions used in the analysis. All the regions used for the analysis are presented in Fig. A2 available as supplementary material. The atomic line parameters considered by the models are presented in Table A1.

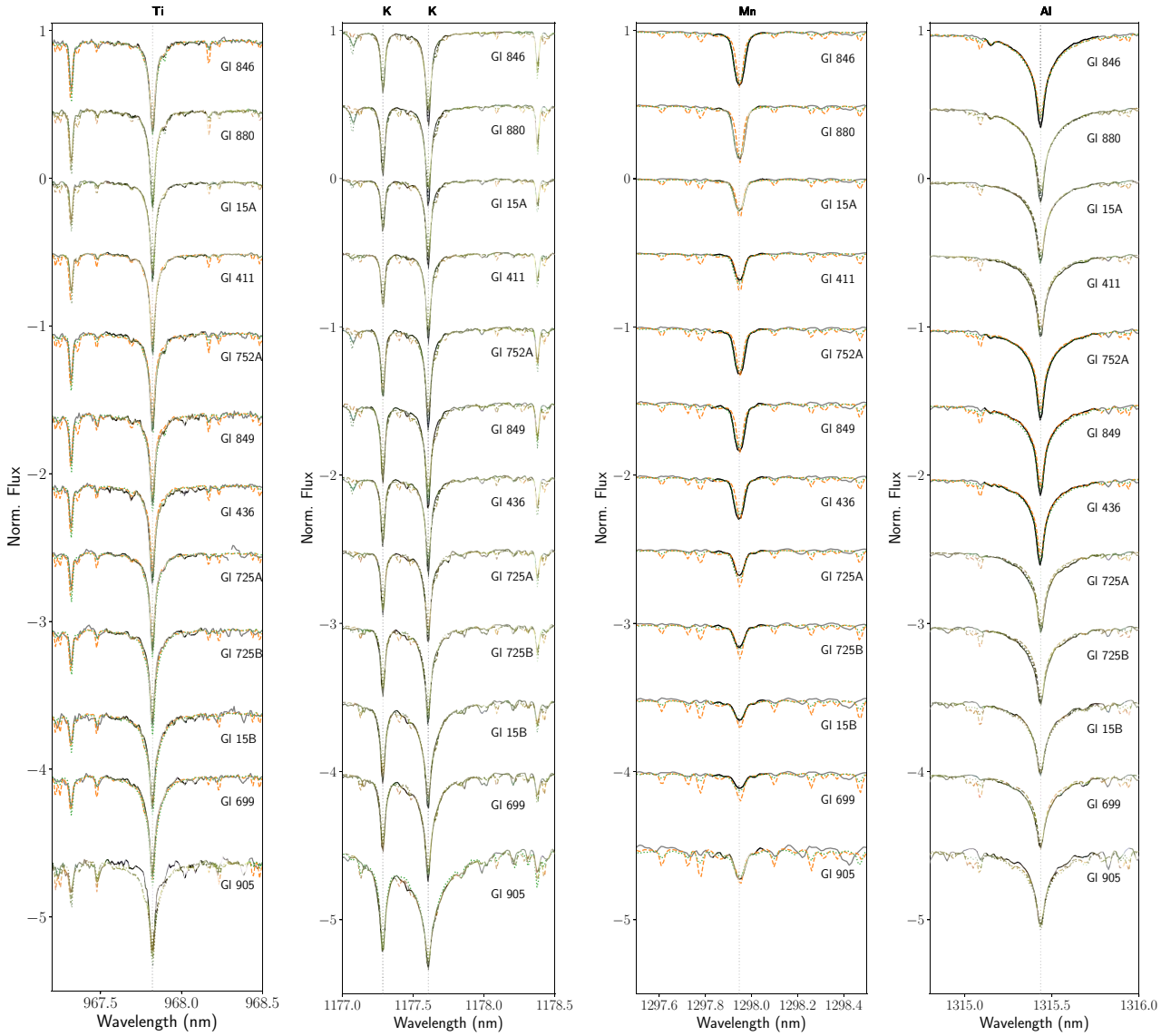

Figure A1. Template spectra (grey) along with the fitted PHOENIX model (dashed orange) and MARCS model (dotted green) for four spectral windows. Selected regions of the template spectra over which the comparison was carried out are shown in black. From top to bottom: Gl 846, Gl 880, Gl 15A, Gl 411, Gl 752A, Gl 849, Gl 436, Gl 725A, Gl 725B, Gl 15B, Gl 699, and Gl 905. Every spectrum but the first one is shifted by a multiple of 0.5 for better readability. Fig. A2 (available as supplementary material) shows all the spectral windows used for the analysis.

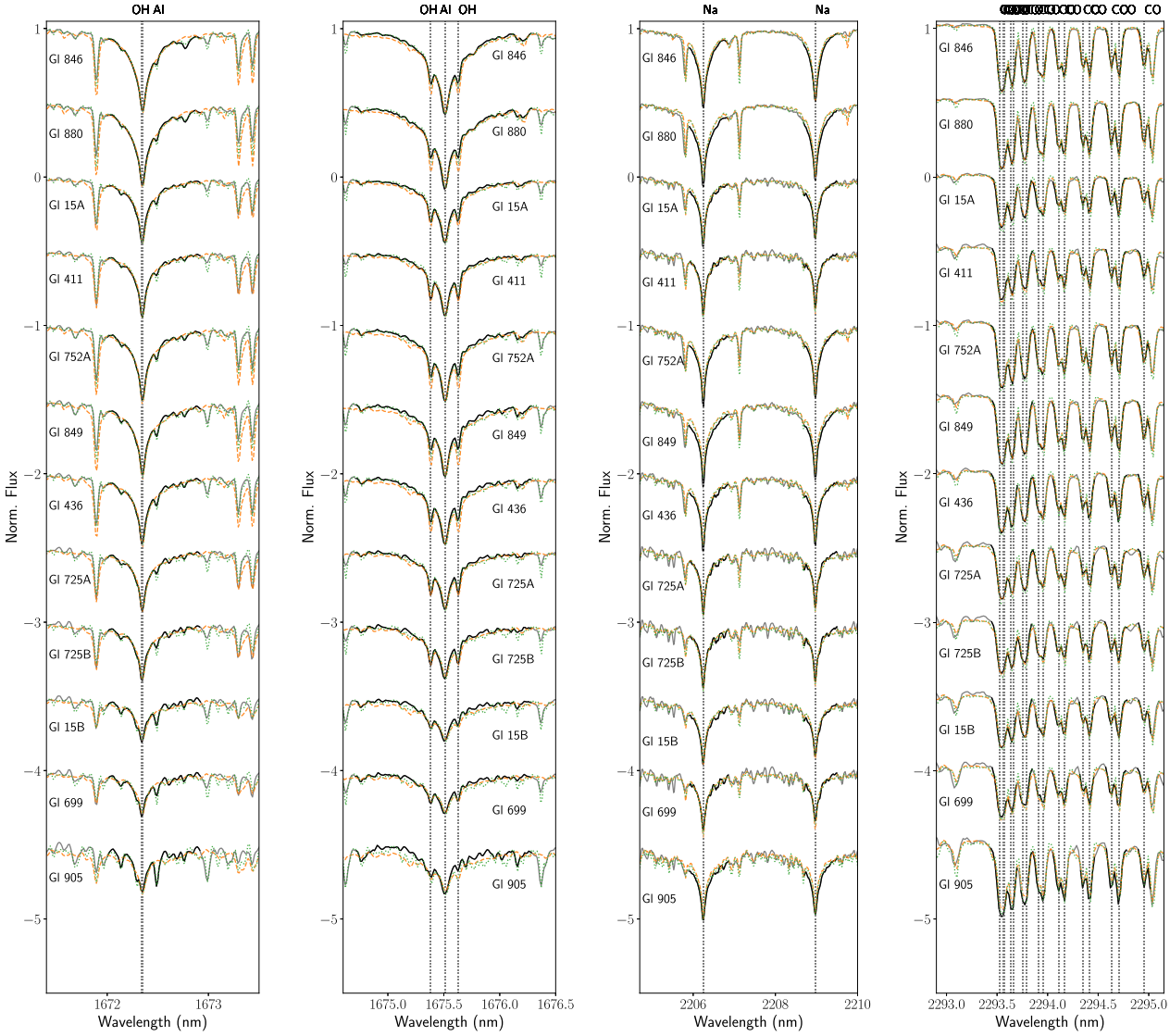

Figure A1 - *continued*

Table A1. Fundamental parameters of the atomic lines included in the analysis as found in the lists used by the PHOENIX and MARCS models. For the lines with hyperfine structure, we display the parameters of all components. For the van der Waals parameter, values below 0 correspond to commonly reported $\log \gamma_6$, values between 0 and 5 correspond to the Uns'old factor, and values above 5 encode the two parameters defined in Barklem, Piskunov & O'Mara (2000), with the integer part being the cross-section for collisions by neutral hydrogen, and the fractional part being the velocity parameter α.

	PHOENIX			MARCS					
							Damping parameters		
Species	Vacuum wavelength (nm)	χ_{low} (eV)	log *gf*	Vacuum wavelength (nm)	χ_{low} (eV)	log *gf*	Van der Waals	Rad.	Stark
Na I	2206.245	3.187	0.289	2206.324	3.191	− 0.519	2.000	5.000	–
Na I	2208.969	3.187	− 0.019	2209.057	3.191	− 0.518	2.000	5.000	–
				2209.052	3.191	− 1.217	2.000	5.000	–
				2209.051	3.191	− 0.518	2.000	5.000	–
				2206.331	3.191	− 1.218	2.000	5.000	–
				2206.331	3.191	− 0.519	2.000	5.000	–
				2206.330	3.191	− 0.072	2.000	5.000	–
				2206.324	3.191	− 0.917	2.000	5.000	–
				2206.324	3.191	− 0.519	2.000	5.000	–
				2209.058	3.191	− 0.518	2.000	5.000	–
Mg I	1504.436	5.098	0.119	1504.527	5.108	0.115	− 7.200	8.170	–
Al I	1675.514	4.087	0.407	1675.709	4.087	− 0.506	− 7.220	7.560	–
Al	1672.353	4.077	0.152	1672.547	4.085	− 0.55	− 7.150	7.560	–
Al I	1315.435	3.136	− 0.030	1315.608	3.143	− 0.519	2.500	5.000	–
				1315.609	3.143	− 1.063	2.500	5.000	–
				1315.616	3.143	− 0.519	2.500	5.000	–
				1315.615	3.143	− 0.616	2.500	5.000	–
K I	1177.606	1.616	0.509	1177.866	1.617	− 1.87	649.270	7.810	− 5.170
				1177.866	1.617	0.084	649.270	7.810	− 5.170
				1177.866	1.617	− 0.724	649.270	7.810	− 5.170
K I	1243.568	1.608	− 0.438	1243.781	1.610	− 0.944	1258.183	7.790	− 4.880
				1243.781	1.610	− 1.643	1258.183	7.790	− 4.880
				1243.782	1.610	− 0.944	1258.183	7.790	− 4.880
				1177.866	1.617	− 1.694	649.270	7.810	− 5.170
				1243.781	1.610	− 0.944	1258.183	7.790	− 4.880
				1177.866	1.617	− 0.627	649.270	7.810	− 5.170
				1177.866	1.617	− 0.694	649.270	7.810	− 5.170
				1177.866	1.617	− 0.74	649.270	7.810	− 5.170
K I	1169.342	1.608	0.249	1169.609	1.610	− 0.556	648.269	7.810	− 5.170
				1169.609	1.610	− 0.556	648.269	7.810	− 5.170
				1169.609	1.610	− 0.954	648.269	7.810	− 5.170
				1169.609	1.610	− 0.109	648.269	7.810	− 5.170
				1169.609	1.610	− 0.556	648.269	7.810	− 5.170
				1169.609	1.610	− 1.255	648.269	7.810	− 5.170
K I	1177.286	1.616	− 0.449	1177.546	1.617	− 1.654	649.270	7.810	− 5.170
				1177.866	1.617	− 0.122	649.270	7.810	− 5.170
				1177.546	1.617	− 1.45	649.270	7.810	− 5.170
				1177.546	1.617	− 1.654	649.270	7.810	− 5.170
				1177.546	1.617	− 1.508	649.270	7.810	− 5.170
				1177.546	1.617	− 1.353	649.270	7.810	− 5.170
				1177.546	1.617	− 1.45	649.270	7.810	− 5.170
				1177.546	1.617	− 0.906	649.270	7.810	− 5.170
				1177.546	1.617	− 1.508	649.270	7.810	− 5.170
K I	1516.721	2.669	− 0.660	1516.802	2.670	0.632	− 6.820	7.640	–
				1177.866	1.617	− 0.372	649.270	7.810	− 5.170
				1177.546	1.617	− 2.052	649.270	7.810	− 5.170
				1516.802	2.670	− 1.04	− 6.980	7.640	–
Ca I	1034.665	2.927	− 0.407	1035.145	2.932	− 0.3	− 7.480	8.500	− 5.060
Ti I	967.820	0.834	− 0.898	968.633	0.836	− 0.804	− 7.800	6.250	− 6.090
Ti I	1281.498	2.160	− 1.364	1281.692	2.160	− 1.39	− 7.750	7.990	− 6.010
Ti I	1197.712	1.460	− 1.443	1197.956	1.460	− 1.39	− 7.790	6.870	− 6.100
Ti	1189.613	1.427	− 1.739	1189.863	1.430	− 1.73	− 7.790	6.930	− 6.100
Ti I	1066.454	0.817	− 1.996	1066.857	0.818	− 1.915	− 7.810	5.130	− 6.090
Ti I	1058.753	0.825	− 1.858	1059.172	0.826	− 1.775	− 7.810	5.130	− 6.090
Ti	972.162	1.501	− 1.257	972.941	1.503	− 1.181	− 7.780	6.161	− 6.110
Ti I	970.833	0.825	− 1.100	971.622	0.826	− 1.009	− 7.800	6.241	− 6.090
Ti I	969.153	0.812	− 1.707	969.955	0.813	− 1.61	− 7.800	6.241	− 6.090
Ti I	1571.987	1.872	− 1.287	1571.950	1.873	− 1.28,	− 7.440	6.380	–
Ti I	2296.961	1.885	− 1.616	2297.041	1.887	− 1.53	− 7.790	6.810	− 6.060
Mn I	1297.948	2.886	− 0.940	1298.133	2.888	− 1.797	2.500	5.000	–
Fe I	1197.632	2.175	− 1.499	1197.877	2.176	− 1.483	− 7.820	7.190	− 6.220
Fe I	1169.317	2.220	− 2.076	1169.584	2.223	− 2.068	− 7.820	7.149	− 6.220

APPENDIX B: RESULTS COMPARED TO OTHER REFERENCES

Fig. B1 presents the $T_{\rm eff}$, $\log g$, and [M/H] values published by several authors (Mann et al. 2015; Fouqué et al. 2018; Passegger et al. 2019; Schweitzer et al. 2019) along with the parameters derived in this study. Figs B2 and B3 present a comparison of the retrieved $T_{\rm eff}$ and [M/H] values and those of P19.

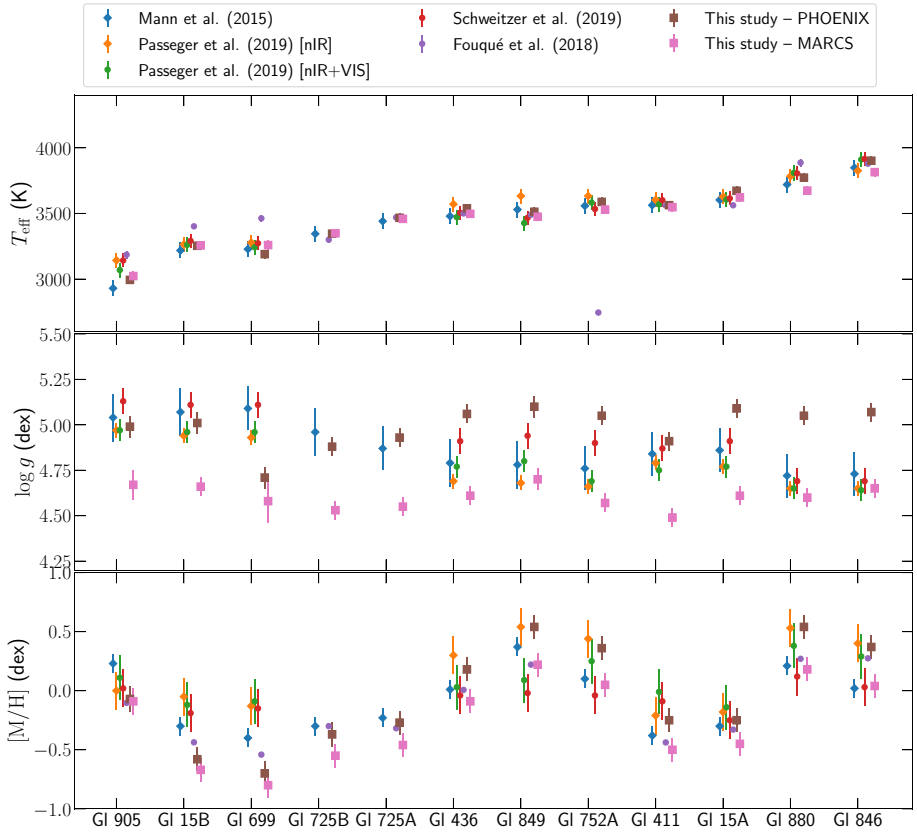

Figure B1. $T_{\rm eff}$, $\log g$, and [M/H] values derived in this work, along with the values published by various studies for the stars in our sample.

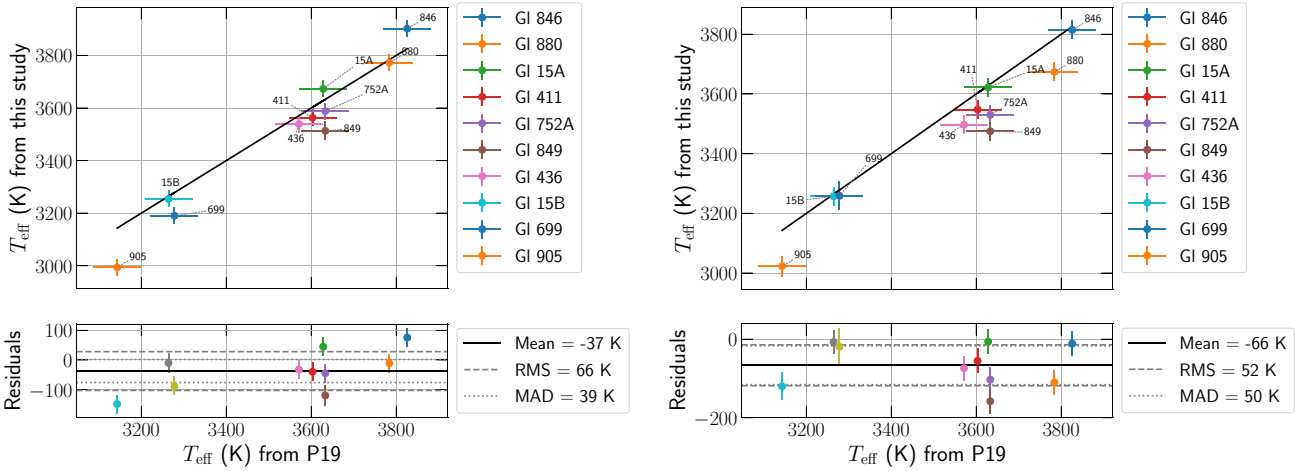

Figure B2. Retrieved $T_{\rm eff}$ using the grid of PHOENIX (top) and MARCS (bottom) spectra plotted against values published by P19. The bottom plot presents the residuals, i.e. the retrieved values minus literature values. RMS and MAD values are computed after application of a sigma clipping function on the residuals with a threshold at 5 σ.

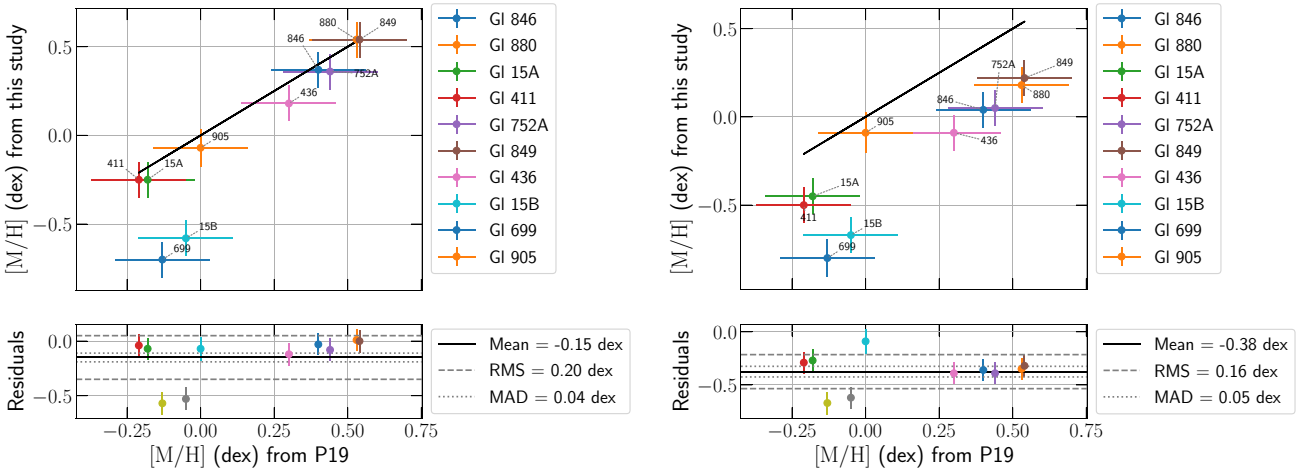

Figure B3. Same as Fig. 10 but for [M/H].

APPENDIX C: RECOVERED PARAMETERS AS A FUNCTION OF v_B

Table C1 presents the mean, RMS, and MAD values of the residuals obtained with various values of v_b.

Table C1. Mean, standard deviation, and median absolute deviation values of the residuals for various values of v_b.

Model used	T_{eff} (K)			log g			[M/H]			v_b (km s^{-1})
	MEAN	RMS	MAD	MEAN	RMS	MAD	MEAN	RMS	MAD	
PHOENIX	56	33	34	0.16	0.23	0.21	−0.03	0.21	0.15	0
	52	29	24	0.17	0.24	0.21	0.01	0.23	0.16	1
	43	31	28	0.15	0.23	0.19	0.02	0.22	0.16	2
	28	33	29	0.11	0.21	0.17	0.04	0.23	0.16	3
	19	35	28	0.08	0.22	0.18	0.06	0.23	0.16	4
	10	42	27	0.08	0.21	0.11	0.11	0.21	0.17	5
	−11	43	36	0.0	0.21	0.13	0.1	0.23	0.14	6
MARCS	32	40	24	−0.2	0.15	0.13	−0.21	0.14	0.11	0
	28	41	24	−0.21	0.15	0.13	−0.2	0.13	0.1	1
	17	40	26	−0.24	0.15	0.12	−0.2	0.13	0.1	2
	4	40	27	−0.27	0.14	0.12	−0.18	0.13	0.1	3
	−17	40	25	−0.33	0.15	0.12	−0.16	0.13	0.1	4
	−30	47	30	−0.36	0.16	0.12	−0.14	0.12	0.07	5
	−47	45	36	−0.4	0.16	0.12	−0.11	0.12	0.06	6

This paper has been typeset from a TEX/LATEX file prepared by the author.

Monthly Notices of the ROYAL ASTRONOMICAL SOCIETY

MNRAS **516,** 3802–3820 (2022) https://doi.org/10.1093/mnras/stac2364
Advance Access publication 2022 August 29

Estimating the atmospheric properties of 44 M dwarfs from SPIRou spectra

P. I. Cristofari [1★] J.-F. Donati [1] T. Masseron,[2,3] P. Fouqué,[1,4] C. Moutou,[1] A. Carmona,[5] E. Artigau,[6] E. Martioli,[7,8] G. Hébrard,[7,9] E. Gaidos [10] X. Delfosse[5] and the SLS consortium

[1]*Université de Toulouse, CNRS, IRAP, 14 av. Belin, F-31400 Toulouse, France*
[2]*Instituto de Astrofísica de Canarias, E-38205 La Laguna, Tenerife, Spain*
[3]*Departamento de Astrofísica, Universidad de La Laguna, E-38206 La Laguna, Tenerife, Spain*
[4]*Canada–France–Hawaii Telescope, CNRS, Kamuela, HI 96743, USA*
[5]*Université Grenoble Alpes, CNRS, IPAG, F-38000 Grenoble, France*
[6]*Département de Physique, Université de Montréal, IREX, Montréal, QC H3C 3J7, Canada*
[7]*Institut d'Astrophysique de Paris, CNRS, UMR 7095, Sorbonne Université, F-75014 Paris, France*
[8]*Laboratório National de Astrofísica, Itajubá, MG 37504-364, Brazil*
[9]*Observatoire de Haute Provance, CNRS,Université´ d'Aix-Marseille, F-04870 Saint-Michel-l'Observatoire, France*
[10]*Department of Earth Sciences, University of Hawai'i at Mānoa, Honolulu, HI 96822, USA*

Accepted 2022 August 18. Received 2022 August 12; in original form 2022 June 17

ABSTRACT

We describe advances on a method designed to derive accurate parameters of M dwarfs. Our analysis consists in comparing high-resolution infrared spectra acquired with the near-infrared spectro-polarimeter SPIRou to synthetic spectra computed from MARCS model atmospheres, in order to derive the effective temperature ($T_{\rm eff}$), surface gravity ($\log g$), metallicity ([M/H]), and alpha-enhancement ([α/Fe]) of 44 M dwarfs monitored within the SPIRou Legacy Survey (SLS). Relying on 12 of these stars, we calibrated our method by refining our selection of well-modelled stellar lines, and adjusted the line list parameters to improve the fit when necessary. Our retrieved $T_{\rm eff}$, $\log g$, and [M/H] are in good agreement with literature values, with dispersions of the order of 50 K in $T_{\rm eff}$ and 0.1 dex in $\log g$ and [M/H]. We report that fitting [α/Fe] has an impact on the derivation of the other stellar parameters, motivating us to extend our fitting procedure to this additional parameter. We find that our retrieved [α/Fe] are compatible with those expected from empirical relations derived in other studies.

Key words: techniques: spectroscopic – stars: fundamental parameters – stars: low-mass – infrared: stars.

1 INTRODUCTION

M dwarfs are obvious targets of interest to look for exoplanets, especially those located in the habitable zones of their host stars (Bonfils et al. 2013; Dressing & Charbonneau 2013; Gaidos et al. 2016), as they dominate the stellar population of the solar neighbourhood. In order to accurately characterize these planets, and derive their masses and radii, it is essential to obtain reliable estimates of the fundamental parameters of the host stars. In particular, the effective temperature ($T_{\rm eff}$), surface gravity ($\log g$), and overall metallicity ([M/H]) of M dwarfs must be determined as accurately as possible.

Several techniques have been developed to characterize atmospheric parameters of low-mass stars. Some rely on the adjustment of equivalent widths (Rojas-Ayala et al. 2010; Neves et al. 2014; Fouqué et al. 2018). Others attempt to fit spectral energy distributions (SEDs) on low- to mid-resolution spectra (Mann et al. 2013). More recently, advances in spectral modelling and the advent of new high-resolution spectrographs in the near-infrared (NIR) domain allowed some authors to perform direct fits of synthetic spectra on high-resolution spectroscopic observations (Passegger et al. 2018; Schweitzer et al. 2019; Marfil et al. 2021).

Of these techniques, the latter is presumably the best option to retrieve precise estimates of the atmospheric parameters by modelling individual spectral lines rather than integrated quantities such as equivalent width or bandpass fluxes. To succeed, this approach however requires accurate high-resolution synthetic spectra on the one hand, and high-resolution and high signal-to-noise ratio (SNR) spectroscopic observations on the other hand. To this end, model atmospheres of low-mass stars such as MARCS (Gustafsson et al. 2008), ATLAS (Kurucz 1970), or PHOENIX (Allard & Hauschildt 1995) were developed and refined over the last few decades. While PHOENIX also performs the radiative transfer to produce synthetic spectra, other codes are used to compute emergent spectra from model atmospheres, such as Turbospectrum (Alvarez & Plez 1998; Plez 2012) or SYNTHE (Kurucz 2005), in the case of MARCS and ATLAS atmospheric models, respectively. In parallel, instruments such as SPIRou (Donati et al. 2020), CARMENES (Quirrenbach et al. 2014), iSHELL (Rayner et al. 2016), IRD (Kotani et al. 2018), or HPF (Mahadevan et al. 2012) have provided the community with high-quality and high-resolution spectra in the NIR domain.

★ E-mail: paul.cristofari@irap.omp.eu

For M dwarfs in the NIR domain, the modelling of stellar spectra is particularly challenging because of the high density of atomic and molecular lines, forming deep absorption bands. Furthermore, telluric features, extremely abundant in the NIR domain, often blend with stellar lines and forces one to carry out extra processing steps to extract the stellar spectrum. In spite of these challenges, the NIR domain remains an abundant source of information, particularly for M dwarfs that are brighter in the NIR than in the optical.

In this paper, we pursue the work initiated in Cristofari et al. (2022, hereafter C22) with the ultimate goal of providing the community with accurate stellar parameters for most M dwarfs observed with SPIRou. Over 70 of them have been monitored with this instrument in the context of the SPIRou Legacy Survey (SLS, Donati et al. 2020), an ongoing observation program for which 310 nights were allocated on the 3.6-m Canada–France–Hawaii Telescope (CFHT). M dwarfs within the SLS are typically monitored tens of times over successive seasons, allowing us to produce high-quality median spectra for our analysis (C22), which we call 'template spectra' in the following. In this work, we focus on the 44 M dwarfs that were most intensively observed with SPIRou.

In contrast with C22, we focus in this paper on MARCS model atmospheres to derive stellar parameters, and bring several improvements to our method. More specifically, we extend our tools to constrain the abundance of alpha elements (O, Ne, Mg, Si, S, Ar, Ca, and Ti) for the studied targets, and demonstrate the importance of considering the alpha-enhancement parameter ([α/Fe]) when modelling spectra of M dwarfs.

In Section 2, we introduce the selected targets and the processing steps undertaken to produce template spectra from SPIRou observations. We recall the main steps of our analysis in Section 3 along with the implemented improvements. We then discuss the impact of [α/Fe] on the retrieved parameters in Section 4, outline the modifications brought to the parameters of some of the atomic lines used in our work (see Section 5), and present the results of our analysis of 44 M dwarfs in Section 6. We conclude and discuss the results of our work in Section 7.

2 OBSERVATIONS AND REDUCTION

2.1 Selecting targets

Most stars were monitored several tens of times over successive seasons with the widest possible range of Barycentric Earth Radial Velocites (BERV). In this work, we focus on 44 M dwarfs for which at least 20 SPIRou spectra were collected in order to build high-SNR stellar templates (see Section 2.2, Table 1). For now, we exclude highly active targets, for which stellar line profiles are likely to be impacted by magnetic fields and chromospheric activity. Several publications assessed the activity level from Hα equivalent width for most targets of our sample (Fouqué et al. 2018; Schöfer et al. 2019), confirming that they are no more than weakly active. We further performed visual inspection of the spectra to ensure that the stellar lines were not significantly affected by activity, e.g. with core reversals in strong lines like those seen in the spectra of more active targets (such as GJ 3622).

Out of our 44 stars, we use 12 (the same as in C22, see Table 2) to improve our tools and calibrate our analysis procedure. We consider the parameters published by Mann et al. (2015, hereafter M15) as a reference for these stars, given that this study relies on methods that are largely independent from ours (e.g. SED fits to low-resolution spectra, equivalent widths, and empirical mass–magnitude relations), and agree well with other literature studies. Table 3 presents the stellar parameters for 16 additional stars included in our sample for which M15 reported stellar properties.

Table 1. Number of spectra, visits, and typical SNR of the collected observations.

Star	Nb. spectra	Nb. epochs	Med. SNR [SNR range]
Gl 338B	124	31	250 [150–300]
Gl 410	472	112	130 [50–150]
Gl 846	792	194	160 [50–230]
Gl 205	593	143	290 [50–350]
Gl 880	634	155	200 [70–250]
Gl 514	740	152	160 [50–280]
Gl 382	238	59	150 [50–220]
Gl 412A	884	148	180 [60–350]
Gl 15A	1040	198	280 [60–360]
Gl 411	592	143	360 [200–440]
Gl 752A	523	129	170 [50–230]
Gl 48	786	195	130 [60–150]
Gl 617B	546	133	120 [50–150]
Gl 480	283	70	110 [60–120]
Gl 436	188	38	150 [70–220]
Gl 849	771	189	120 [50–140]
Gl 408	495	117	140 [50–170]
Gl 687	898	214	200 [60–240]
Gl 725A	889	213	210 [50–260]
Gl 317	108	27	100 [70–130]
Gl 251	749	175	140 [50–170]
GJ 4063	784	190	100 [50–120]
Gl 581	124	31	120 [60–150]
Gl 725B	855	211	160 [70–200]
PM J09553−2715	172	43	110 [80–140]
Gl 876	369	88	160 [70–220]
GJ 1012	522	129	100 [50–120]
GJ 4333	734	181	100 [50–120]
Gl 445	171	43	110 [50–140]
GJ 1148	399	98	100 [50–110]
PM J08402+3127	462	115	100 [50–110]
GJ 3378	725	179	100 [50–130]
GJ 1105	515	128	100 [50–130]
Gl 699	950	231	200 [60–240]
Gl 169.1A	673	165	100 [50–130]
PM J21463+3813	718	177	100 [50–120]
Gl 15B	755	188	100 [50–120]
GJ 1289	812	202	100 [50–110]
Gl 447	180	45	120 [60–170]
GJ 1151	568	141	100 [50–120]
GJ 1103	254	62	100 [50–110]
Gl 905	484	117	110 [50–130]
GJ 1002	524	130	100 [60–120]
GJ 1286	438	113	100 [50–120]

2.2 Building templates from SPIRou spectra

All SPIRou spectra are processed through the SPIRou reduction pipeline, APERO (version 0.6.132, Cook et al., in preparation). A correction of the telluric absorption and emission lines is performed by APERO, relying on telluric templates built from telluric standards (Artigau et al., in preparation). A blaze profile estimated from flat-field exposures is used to flatten the extracted spectra, and each order is normalized using a third-degree polynomial.

Stellar templates are built by taking the median of the telluric corrected spectra in the barycentric reference frame. Because of the relative motion of telluric lines with respect to spectral features due to the Earth revolution around the Sun, having spectra observed at

Table 2. Parameters derived by M15 for 12 calibration stars used in this study. log g values are computed from reported masses and radii.

Star	Spectral type	$T_{\rm eff}$	[M/H]	Radius	Mass	log g
Gl 846	M0.5V	3848 ± 60	0.02 ± 0.08	0.546 ± 0.019	0.590 ± 0.059	4.74 ± 0.05
Gl 880	M1.5V	3720 ± 60	0.21 ± 0.08	0.549 ± 0.018	0.574 ± 0.057	4.72 ± 0.05
Gl 15A	M2V	3603 ± 60	−0.30 ± 0.08	0.388 ± 0.013	0.398 ± 0.040	4.86 ± 0.05
Gl 411	M2V	3563 ± 60	−0.38 ± 0.08	0.389 ± 0.013	0.386 ± 0.039	4.84 ± 0.05
Gl 752A	M3V	3558 ± 60	0.10 ± 0.08	0.474 ± 0.016	0.475 ± 0.047	4.76 ± 0.05
Gl 849	M3.5V	3530 ± 60	0.37 ± 0.08	0.470 ± 0.018	0.482 ± 0.048	4.78 ± 0.06
Gl 436	M3V	3479 ± 60	0.01 ± 0.08	0.449 ± 0.019	0.445 ± 0.044	4.78 ± 0.06
Gl 725A	M3V	3441 ± 60	−0.23 ± 0.08	0.351 ± 0.013	0.334 ± 0.033	4.87 ± 0.05
Gl 725B	M3.5V	3345 ± 60	−0.30 ± 0.08	0.273 ± 0.011	0.248 ± 0.025	4.96 ± 0.06
Gl 699	M4V	3228 ± 60	−0.40 ± 0.08	0.186 ± 0.007	0.155 ± 0.015	5.09 ± 0.05
Gl 15B	M3.5V	3218 ± 60	−0.30 ± 0.08	0.192 ± 0.008	0.159 ± 0.016	5.07 ± 0.06
Gl 905	M5.0V	2930 ± 60	0.23 ± 0.08	0.189 ± 0.008	0.145 ± 0.015	5.04 ± 0.06

Table 3. Same as Table 2 for 16 additional stars included in both M15 and this study.

Star	Spectral type	$T_{\rm eff}$	[M/H]	Radius	Mass	log g
Gl 205	M1.5V	3801 ± 60	0.49 ± 0.08	0.581 ± 0.019	0.633 ± 0.063	4.71 ± 0.05
Gl 514	M1.0V	3727 ± 60	−0.09 ± 0.08	0.483 ± 0.016	0.527 ± 0.053	4.79 ± 0.05
Gl 382	M2V	3623 ± 60	0.13 ± 0.08	0.522 ± 0.019	0.525 ± 0.053	4.72 ± 0.05
Gl 412A	M1.0V	3619 ± 60	−0.37 ± 0.08	0.383 ± 0.013	0.390 ± 0.039	4.86 ± 0.05
Gl 480	M3.5V	3463 ± 60	0.26 ± 0.08	0.466 ± 0.025	0.467 ± 0.047	4.77 ± 0.06
Gl 251	M3V	3448 ± 60	−0.02 ± 0.08	0.358 ± 0.013	0.352 ± 0.035	4.88 ± 0.05
Gl 687	M3.0V	3439 ± 60	0.050 ± 0.080	0.414 ± 0.015	0.405 ± 0.041	4.81 ± 0.05
Gl 581	M3V	3395 ± 60	−0.150 ± 0.080	0.311 ± 0.012	0.292 ± 0.029	4.92 ± 0.06
PM J09553−2715	M3V	3346 ± 60	0.01 ± 0.080	0.321 ± 0.016	0.299 ± 0.030	4.90 ± 0.06
GJ 3378	M4.0V	3340 ± 60	−0.09 ± 0.08	0.269 ± 0.011	0.245 ± 0.024	4.97 ± 0.06
GJ 4333	M3.5V	3324 ± 60	0.24 ± 0.08	0.416 ± 0.020	0.391 ± 0.039	4.79 ± 0.06
GJ 1148	M4.0V	3304 ± 61	0.07 ± 0.08	0.376 ± 0.018	0.336 ± 0.034	4.81 ± 0.06
Gl 876	M3.5V	3247 ± 60	0.17 ± 0.08	0.363 ± 0.014	0.328 ± 0.033	4.83 ± 0.06
Gl 447	M4V	3192 ± 60	−0.020 ± 0.080	0.197 ± 0.008	0.168 ± 0.017	5.08 ± 0.06
GJ 1289	M4.5V	3173 ± 60	0.05 ± 0.08	0.238 ± 0.013	0.202 ± 0.020	4.99 ± 0.06
GJ 1151	M4.5V	3118 ± 60	0.03 ± 0.08	0.190 ± 0.009	0.154 ± 0.015	5.07 ± 0.06

various BERV (with typical maximum difference between observations ranging from 10 to 30 km s^{-1}) allows one to minimize telluric correction errors, and to obtain a template spectrum even in regions where telluric lines are deep enough to render a single observation hardly usable over the corresponding range. All telluric-corrected spectra recorded with an SNR per 2 km s^{-1} pixel in the H band exceeding 50 are used to build the stellar templates. The typical SNR per pixel of these template spectra reaches up to 2000.

3 DERIVING FUNDAMENTAL STELLAR PARAMETERS FROM SPIROU TEMPLATE SPECTRA

In C22, we described and tested a method for determining atmospheric parameters from SPIRou template spectra. We discussed the use of two different models, PHOENIX-ACES (Husser et al. 2013) and MARCS, the differences in the synthetic spectra computed with both models, and their impact on the results. In this work, we update the method to improve the framework and produce more reliable results. Some of these improvements include the implementation of a new continuum normalization procedure and an empirical revision of line parameters for some of the atomic lines used (see Section 3.3). We then further improve the method to retrieve the alpha enhancement ([α/Fe]) as an additional free parameter of our model (see Section 4). We concentrate our efforts on MARCS model atmospheres, readily available for different values of [α/Fe] and computed with up-to-date line lists.[1]

Table 4. Parameter range covered by the computed grid of MARCS synthetic spectra. The range and initial step size are listed along with the level to which the grid is interpolated to reach the final step size.

Variable	Range (and step size)	Interp. factor (and final step size)
$T_{\rm eff}$ (K)	3000–4000 (100)	20 (5)
log g (dex)	3.5–5.5 (0.5)	50 (0.01)
[M/H] (dex)	−1.5–+1.0 (0.25)	25 (0.01)
[α/Fe] (dex)	−0.25–+0.5 (0.25)	25 (0.01)

3.1 The grid of synthetic spectra

We use a grid of synthetic spectra computed from MARCS model atmospheres with Turbospectrum for several $T_{\rm eff}$, log g, and [M/H] values. This grid is the same as that used in C22, augmented with models computed for [α/Fe] values ranging from −0.25 to 0.50 dex in steps of 0.25 dex (see Table 4). Spectra were computed for all

[1]The grid of PHOENIX-ACES synthetic spectra was not published with multiple [α/Fe] values for $T_{\rm eff}$ > 3500 K, and updating the line list is not an easy task, hence why we focused on MARCS models in this new study.

available $\log g$, although values below 4.5 dex are not expected to be used in the case of main sequence (Baraffe et al. 2015).

3.2 Stellar analysis procedure

The parameter determination procedure used in this paper is similar to that described in C22. In this section, we briefly summarize the main steps of this process.

3.2.1 Comparison of models to observation templates

SPIRou template spectra are compared to synthetic spectra in order to identify the best-fitting model. Prior to this comparison, the synthetic spectra are binned on the wavelength grid of the SPIRou template. This binning operation is performed through a cubic interpolation and convolution with a rectangular function of width 2 km s^{-1} (representing pixels). The synthetic spectra are also convolved with a Gaussian profile of full width at half-maximum (FWHM) of 4.3 km s^{-1} to account for instrumental broadening (resolving power 70 000). We finally consider the effect of both rotation and macroturbulence on stellar spectra, which we approximate as a Gaussian broadening of FWHM $v_{\rm b} = 3$ km s^{-1} as in C22. We then extract 400-bin windows around selected lines and adjust the local continuum of the synthetic spectra to match that of the observation template spectrum. This step is particularly challenging in the NIR spectra of M dwarfs, where the large density of atomic and molecular lines renders the pseudo continuum hard to locate. The comparison of synthetic spectra and observation templates is performed on a total of ∼70 lines, found to be more or less adequately reproduced in synthetic spectra, and sensitive to the atmospheric parameters of interest.

3.2.2 χ^2 minimization

Synthetic spectra for a given range of $T_{\rm eff}$, $\log g$, [M/H], and [α/Fe] are compared to the SPIRou template for a given star of our sample, yielding a 4D grid of χ^2 values. Given the rough step size of this initial grid (see Section 3.1), we interpolate the synthetic spectra to reach steps of 5 K in $T_{\rm eff}$ and 0.01 dex in $\log g$ and [M/H] around the grid minimum in order to locate the grid minimum and determine the curvature at this position as accurately as possible. A new 4D χ^2 landscape is computed, and a 4D second-degree polynomial is fitted on the 3000 points with smallest χ^2 values.

3.2.3 Error estimation

To estimate error bars on the retrieved parameters, we measure the curvature of the fitted paraboloid. More specifically, we search for the ellipsoid where the χ^2 increases by 1 from the minimum, and project it on each parameter axis. The projected intervals should contain 68.3 per cent of normally distributed data (Press et al. 1992), which we refer to as formal error bars. In C22, we observed that the choice of model has a significant impact on the results, introducing systematics that are not accounted for by our formal error bars computation. To take this effect into account, C22 introduced a second error bar, derived from the root mean square (RMS) difference between the parameters retrieved with both sets of atmospheric models.

In this work, we consider a single model and thus cannot perform a similar operation. We therefore rely on the results of C22 to increase our error bars, by quadratically adding 30 K, 0.05 dex, and 0.1 dex to the computed formal error bars on $T_{\rm eff}$, $\log g$, and [M/H], respectively, and refer to these as empirical error bars.

Since we have no means to retrieve an empirical error bar for [α/Fe], we estimate it from those derived on [M/H]. We typically compute smaller formal error bars on [α/Fe] than on [M/H], with average values of about 0.015 and 0.005 dex, respectively. The median of the ratio between our formal error bars on [M/H] and on [α/Fe] is of 2.5. To account for some of the systematics and provide a conservative estimate of the error bars on [α/Fe], we choose to quadratically add 0.04 dex to our formal error bars for this parameter. This is consistent with the dispersion of the retrieved [α/Fe] values for stars having [M/H] > -0.1 dex, for which thin and thick disc populations blend together.

3.3 Adjustment of the continuum

In this paper, we also revised our continuum adjustment procedure. We extract 400-bin windows around all selected lines for both the SPIRou template and the synthetic spectrum. In each window, we exclude all points of the SPIRou template that fall above the 98th percentile, and may correspond to the poorly corrected telluric emission lines. We then subdivide the 400-bin windows into 40-bin windows, in which we consider all points above the 90th percentile as tracing the continuum. We then fit a straight line through these points to retrieve two continua, one for the template spectrum and one for the synthetic spectrum, which are then used to bring the continua of the template and model spectra to the same level. This procedure sets in the local continuum of both the template and the synthetic spectrum to unity.

4 THE IMPACT OF [α/Fe] ON THE RECOVERED FUNDAMENTAL PARAMETERS

Several studies (Passegger et al. 2019; Schweitzer et al. 2019) assume that the abundances of elements with respect to those of the Sun all differ by the same amount, and typically report values of [M/H] where [X/H] = [M/H] for all elements X with atomic numbers ≥3. This assumption simplifies the modelling but likely affects the estimation of the other parameters. In particular, the abundance of alpha elements (O, Ne, Mg, Si, S, Ar, Ca, and Ti) was shown to depend on the considered stellar population (Fuhrmann 1998; Adibekyan et al. 2013), and models were modified to incorporate an alpha-enhancement parameter ([α/Fe], Gustafsson et al. 2008; Allard, Homeier & Freytag 2011; Husser et al. 2013). In the rest of the paper, [M/H] is used to designate the overall metallicity of all elements but the alpha elements, whose abundances are set to [α/H] = [M/H] + [α/Fe].

The effect of [α/Fe] is visible across the entire SPIRou domain where molecular lines are numerous, and where variations in the abundances of alpha elements, in particular oxygen, leads to significant changes of the model atmospheres.

4.1 [α/Fe]–[M/H] relations

Previous publications analysing M dwarfs analysis adopted a unique [α/Fe]–[M/H] relations for their analysis (Rajpurohit et al. 2018; Marfil et al. 2021). These assume that [α/Fe] $= -0.4$[Fe/H] for $-1 \leq$ [Fe/H] < 0, [α/Fe] $= 0$ for [Fe/H] ≥ 0, and [α/Fe] $= -1$ for [Fe/H] < -1. This relation was also used for the PHOENIX BT-Settl grid of synthetic spectra (Allard et al. 2011).

Due to ongoing spectroscopic large surveys, such relations can nowadays be refined more empirically. For example, this relation

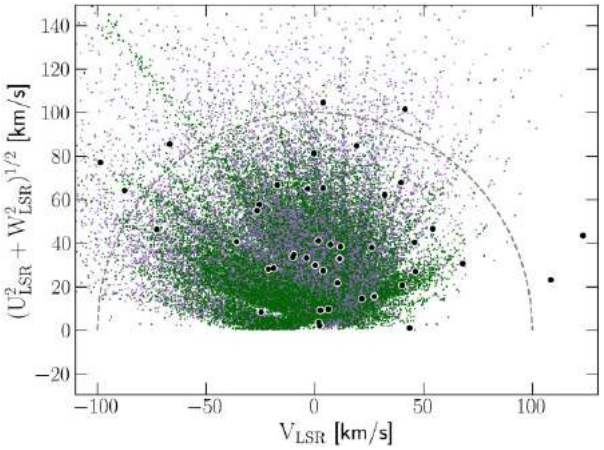

Figure 1. Toomre diagram for the giant stars studied with APOGEE. U, V, and W are the velocities in the Galactic coordinate system, corrected for solar motion (LSR). The purple and green pixels show stars from the thick and thin disc, respectively, distinguished from their elemental abundances. The grey dashed line marks a fiducial boundary at 100 km s^{-1}. The stars studied in this work are marked with a black dot. An alternative figure with labels identifying the stars is presented in Fig. A1.

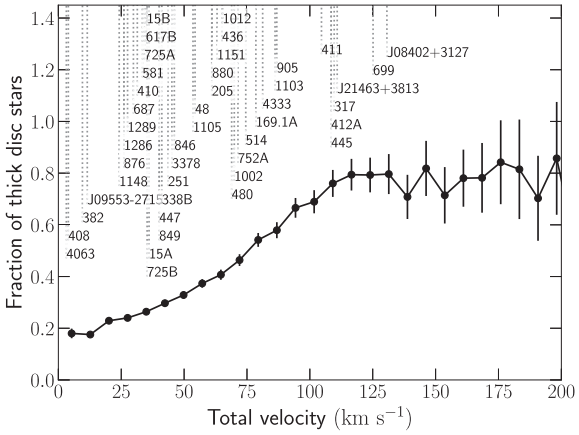

Figure 2. Thick-to-thin disc stars ratio per total velocity bin. The labels mark the velocities of the stars in our sample. This ratio suggests that stars with total velocities >100 km s^{-1} have a probability >70 per cent to belong to the thick disc.

can be derived by looking at abundances in giants (4000 K < $T_{\rm eff}$ < 5000 K and $\log g$ < 3.5 dex) estimated from the APOGEE survey (Jönsson et al. 2020). These stars can be split into two groups corresponding to two Galactic populations, with the ones from the thick Galactic disc having typically larger [α/Fe] values than those from the thin Galactic disc. This suggests that distinct [α/Fe]–[M/H] relations should be considered for thin and thick disc stars. It is however still unclear whether these relations also apply to M dwarfs, due to the lack of accurate data for these stars. In this work, we place a fiducial boundary between the low-[α/Fe] and high-[α/Fe] stars to define the thin and thick disc populations, respectively. This simplistic classification aims at providing an a posteriori verification that our derived [α/Fe] values for the targets in our sample are consistent with the literature, rather than investigating the distribution of the stars across the Galactic populations.

Several studies attempted to estimate individual abundances of elements in M dwarfs spectra, from fits of synthetic spectra (Jahandar et al., in preparation; Souto et al. 2022) or equivalent widths (Ishikawa et al. 2020, 2022). In particular, Souto et al. (2022) derived the element abundances for several targets included in our study (Gl 411, Gl 15A, Gl 725A, Gl 725B, and Gl 880) and obtained [α/Fe]–[M/H] trends suggesting that [α/Fe] increases for metal-poor stars, consistent with the relations derived for giant stars from APOGEE data.

4.2 Classification of stellar populations from dynamics

Placing the giants studied with APOGEE on a Toomre diagram, we find that the thick disc stars tend to have higher total velocity than thin disc stars (see Figs 1 and A1), and that most of the stars in our sample are found to feature a peculiar velocity below 100 km s^{-1}. Besides, looking at the proportion of thin and thick disc giants with a given velocity (see Fig. 2) provides an estimate of the probability for a star to belong to either population based on its velocity. In particular, stars with a total velocity above 100 km s^{-1} likely belong to the thick disc with a probability > 70 per cent. Assuming that M dwarfs behave as giant stars in this respect suggests that most of ours stars, featuring velocities < 75 km s^{-1}, are likely to belong to the thin disc. Only seven of our stars (PM J08402+3127, PM J21463+3813, Gl 699, Gl 411, Gl 317, Gl 445, and Gl 412A) have a total velocity > 100 km s^{-1}, and are thus more likely to belong to the thick disc. We come back on this point further in the paper.

Because the choice of [α/Fe] has a strong impact on the other three parameters, and because we cannot arbitrarily set its value for each star, we chose to fit [α/Fe] in our analysis procedure.

5 LINE SELECTION AND ADJUSTMENT

The analysis must rely on well-modelled spectral lines in order to provide accurate stellar parameters. Selecting such lines is particularly challenging in the NIR where molecular lines may blend with atomic features, and where models may not accurately reproduce line profiles. SPIRou allows us to select several lines from multiple bands due to its large wavelength coverage. In this work, we revised the line selection performed in C22 and adjusted the properties of some lines, assuming known stellar parameters for three of our calibration stars: Gl 699, Gl 15A, and Gl 411.

5.1 Selecting the stellar lines of interest

Stellar lines are selected by comparing observation templates to synthetic spectra assuming atmospheric parameters as derived from M15, identifying those that are well reproduced by the models, and sensitive to the fundamental parameters we want to constrain. This selection is performed by comparing spectra of calibration stars to model spectra computed for expected parameters. In C22, we selected a set of 26 atomic lines and 40 molecular lines, mainly located in the CO band between 2290 and 2300 nm. In this new study, we added several atomic and OH lines, and rejected some atomic lines that are found to be poorly informative, leading to a new line list containing 17 atomic lines, nine OH lines, and CO lines from the aforementioned (see Table 5). The selected atomic lines are reported in Table 6, and include seven lines from non-alpha elements (Fe, Mn, Al, K, and Na). The table also lists the parameters of the atomic lines, with the hyperfine structure when included in our line lists. These data are used to compute the emergent spectra with the Turbospectrum radiative transfer code.

To exclude some lines, we compared the χ^2 values computed for the expected model (assuming the parameters of M15) and the best

Table 5. Full list of spectral lines used. Lines were identified by depth and wavelength using the VALD data base.

Species	Wavelength (Å)
Ti I	9678.198, 9691.527, 9708.327, 9721.626
	22969.597
Fe I	10343.719
Ca I	16201.500
K I	15167.211
Mn I	12979.459
Al I	13126.964, 16723.524, 16755.203
Mg I	15044.357, 15051.818
Na I	22062.420, 22089.692
OH	1672.3418, 1675.3831, 1675.6299
CO	22935.233, 22935.291, 22935.585, 22935.754
	22936.343, 22936.627, 22937.511, 22937.900
	22939.094, 22939.584, 22941.089, 22941.668
	22943.494, 22944.163, 22946.311, 22947.059
	22949.544, 22953.195, 22954.059, 22957.263
	22958.159, 22961.743, 22962.671, 22966.648
	22967.576, 22971.971, 22972.884, 22977.719
	22978.596, 22983.888, 22984.707, 22990.488
	22991.222, 23112.404, 23124.542, 23150.029, 23163.381

fit obtained (whose parameters may differ from the expected values). Whenever, for our calibration stars, the computed χ^2 is found to be much larger for the expected atmospheric parameters than for those derived with our process, we adjusted the line parameters (see Section 5.2) or excluded the region from our analysis.

5.2 Adjusting line parameters on reference stars

The adjustments were performed on three of our best calibration stars (Gl 699, Gl 15A, Gl 411), by comparing the modelled spectra with various values of the Van Der Waals broadening parameter and oscillator strengths to the SPIRou stellar template spectra. For this step, the parameters published by M15 are assumed for our calibration stars, and [α/Fe] values were set to 0.2 dex for Gl 699 and Gl 411 and 0.08 dex for Gl 15A, assuming thick and thin disc populations based on velocity.

Significant differences are observed between models and observations, in particular for Ti lines, whose wings appear wider in the models than in observations; this is likely to affect determinations of $\log g$ if not corrected for. Since the wings of these lines are very sensitive to the Van Der Waals collisional broadening parameter, as illustrated on Fig. 3, we decreased the value of this parameter for these lines until a good fit was achieved for all three reference stars, and re-computed a grid of spectra with these adjustments. All corrections applied to the line list are specified in Table 6. Some lines were attributed an Unsöld factor (Unsold 1955) when no value of the Van der Waals damping parameter (γ_6) was reported in the VALD (Pakhomov, Ryabchikova & Piskunov 2019) line lists.

5.3 Consequence on retrieved parameters

To assess the impact of our adjustments on the retrieved stellar parameters, we perform the analysis on our calibration stars with the new set of synthetic models computed with these adjustments, and derived for each star the four atmospheric parameters of interest with the corresponding error bars. We compare these results to those obtained with the original line list (see Fig. B1). The [M/H] and $\log g$ estimates of a few stars are found to be in better agreement with M15. The influence of the correction remains however small on the retrieved $T_{\rm eff}$, $\log g$, and [M/H] for most stars. Similarly, we look at the effect of the correction on our estimated [α/Fe] (see Fig. B2), and retrieve values closer to those expected from empirical relations for a few stars, such as Gl 849, Gl 880, or Gl 905.

Table 6. Line list used for the analysis. Columns 1 to 5 present the parameters found in the original list. Modifications to the oscillator strength (Δlggf) and Van de Waals parameter (ΔVdW) are specified in columns 6 and 7, when applicable. When the hyperfine structure (HFS) is available, we display data for all subcomponents. Two distinct prescriptions are found in the Van der Waals column: the commonly reported Van der Waals damping parameter γ_6 is considered if the value is negative; values between 0 and 20 give the value of the fudge factor within the Unsöld approximation.

	Vac. wvl. (Å)	$\chi_{\rm low}$	lggf	VdW	species	Δlggf	ΔVdW
	9678.198	0.84	−0.80	−7.80	Ti I	–	−0.3
	9691.527	0.81	−1.61	−7.80	Ti I	–	−0.2
	9708.327	0.83	−1.01	−7.80	Ti I	–	−0.2
	9721.626	1.50	−1.18	−7.78	Ti I	−0.1	−0.2
	10343.719	2.20	−3.58	−7.80	Fe I	–	–
	10968.389	5.93	−2.16	2.50	Mg I	–	–
HFS	12979.260	2.89	−2.65	2.50	Mn I	–	–
HFS	12979.277	2.89	−2.36	2.50	Mn I	–	–
HFS	12979.295	2.89	−2.62	2.50	Mn I	–	–
HFS	12979.320	2.89	−2.14	2.50	Mn I	–	–
HFS	12979.347	2.89	−2.44	2.50	Mn I	–	–
HFS	12979.364	2.89	−3.39	2.50	Mn I	–	–
HFS	12979.387	2.89	−1.96	2.50	Mn I	–	–
HFS	12979.423	2.89	−2.37	2.50	Mn I	–	–
HFS	12979.450	2.89	−3.31	2.50	Mn I	–	–
HFS	12979.478	2.89	−1.80	2.50	Mn I	–	–
HFS	12979.524	2.89	−2.40	2.50	Mn I	–	–
HFS	12979.560	2.89	−3.44	2.50	Mn I	–	–
HFS	12979.592	2.89	−1.66	2.50	Mn I	–	–
HFS	12979.647	2.89	−2.58	2.50	Mn I	–	–
HFS	12979.692	2.89	−3.79	2.50	Mn I	–	–
HFS	13126.957	3.14	−0.62	2.50	Al I	–	–
HFS	13126.962	3.14	−0.52	2.50	Al I	–	–
HFS	13126.965	3.14	−0.63	2.50	Al I	–	–
HFS	13127.024	3.14	−0.16	2.50	Al I	–	–
HFS	13127.030	3.14	−0.52	2.50	Al I	–	–
HFS	13127.035	3.14	−1.06	2.50	Al I	–	–
	15044.357	5.11	0.12	−7.20	Mg I	–	–
	15051.818	5.11	−0.40	−7.19	Mg I	–	–
	15167.211	2.67	0.63	−6.82	K I	–	–
	16201.500	4.54	0.09	−6.59	Ca I	–	–
HFS	16723.478	4.08	−0.66	−7.15	Al I	–	–
HFS	16723.492	4.08	−0.55	−7.15	Al I	–	–
HFS	16723.510	4.08	−1.09	−7.15	Al I	–	–
HFS	16723.512	4.08	−0.65	−7.15	Al I	–	–
HFS	16723.530	4.08	−0.55	−7.15	Al I	–	–
HFS	16723.557	4.08	−0.19	−7.15	Al I	–	–
HFS	16755.031	4.09	−0.02	−7.22	Al I	–	–
HFS	16755.115	4.09	−0.23	−7.22	Al I	–	–
HFS	16755.126	4.09	−0.71	−7.22	Al I	–	–
HFS	16755.183	4.09	−0.51	−7.22	Al I	–	–
HFS	16755.192	4.09	−0.56	−7.22	Al I	–	–
HFS	16755.203	4.09	−1.66	−7.22	Al I	–	–
HFS	16755.236	4.09	−0.92	−7.22	Al I	–	–
HFS	16755.241	4.09	−0.58	−7.22	Al I	–	–
HFS	16755.249	4.09	−1.28	−7.22	Al I	–	–
HFS	16755.274	4.09	−0.74	−7.22	Al I	–	–
HFS	16755.279	4.09	−1.11	−7.22	Al I	–	–
HFS	16755.293	4.09	−1.06	−7.22	Al I	–	–
HFS	22062.379	3.19	−0.52	2.00	Na I	–	–
HFS	22062.381	3.19	−0.52	2.00	Na I	–	–
HFS	22062.381	3.19	−0.92	2.00	Na I	–	–
HFS	22062.442	3.19	−0.07	2.00	Na I	–	–
HFS	22062.446	3.19	−0.52	2.00	Na I	–	–
HFS	22062.448	3.19	−1.22	2.00	Na I	–	–
HFS	22089.645	3.19	−0.52	2.00	Na I	–	–
HFS	22089.655	3.19	−1.22	2.00	Na I	–	–
HFS	22089.712	3.19	−0.52	2.00	Na I	–	–
HFS	22089.721	3.19	−0.52	2.00	Na I	–	–
	22969.597	1.89	−1.53	−7.79	Ti I	–	–

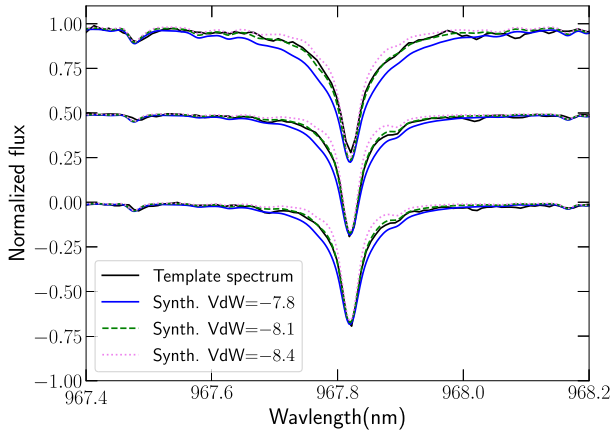

Figure 3. Example of Ti line. The black lines present the template spectra of three stars, from top to bottom: Gl 699, Gl 15A, and Gl 411. Synthetic spectra with three different values of Van der Waals damping parameter are plotted for each star. The initial value found in the list was −7.8, and we adopt a value −8.1 for our analysis.

We also perform a comparison between the results obtained while fitting [α/Fe] or if the parameter is set to 0 (see Fig. B3). We find that fitting [α/Fe] allows us to significantly reduce the scatter on the retrieved $\log g$, and to obtain [M/H] estimates in better agreement with our reference study, with the exception of Gl 905, for which [M/H] is found about 0.2 dex smaller than that reported by M15, who relied on empirically calibrated relations between equivalent widths of some atomic features and metallicity. Subsequent tests showed that a variation of [α/Fe] of 0.05 dex can lead to a 0.2 dex variation on [M/H] for this star.

Two binaries are included in our study: Gl 725 and Gl 15. For both systems, we retrieve [M/H] for each component that are in good agreement, with differences of 0.02 dex for Gl 725 and 0.09 dex for Gl 15, thereby improving over our initial study where this difference reached 0.21 dex in the case of Gl 15A (C22). For Gl 15, we also observe a small difference in the [α/Fe] values of 0.06 dex, again consistent with the estimated empirical error bars.

6 RESULTS

We performed the analysis described in Section 3 with the updated list presented in Section 5, on our 44 selected targets (see Section 2.1). Figs 4 and A2 present a comparison between the results and the parameters published by M15 for the 28 stars common to both samples. Fig. C1 (available as supplementary material) presents the best fit obtained on all lines for five stars in our sample. The retrieved $T_{\rm eff}$, $\log g$, [M/H], and [α/Fe] are listed in Table 7 along with an estimate of the stellar masses and radii.

6.1 Effective temperature

For the 28 stars also studied by M15, we compare our results to the reported effective temperatures (Fig. 4). The overall retrieved $T_{\rm eff}$ are in good agreement with M15 with an RMS on the residuals of the order of 45 K, compatible with the error bars reported by M15. We observe a tendency to derive higher $T_{\rm eff}$ for cooler stars, with a deviation of up to 140 K for Gl 905. This trend may reflect discrepancies in the physics used in the MARCS models at the lowest side of their temperature range, or alternatively probe systematics in M15. To assess the internal dispersion of our results, we fit a line

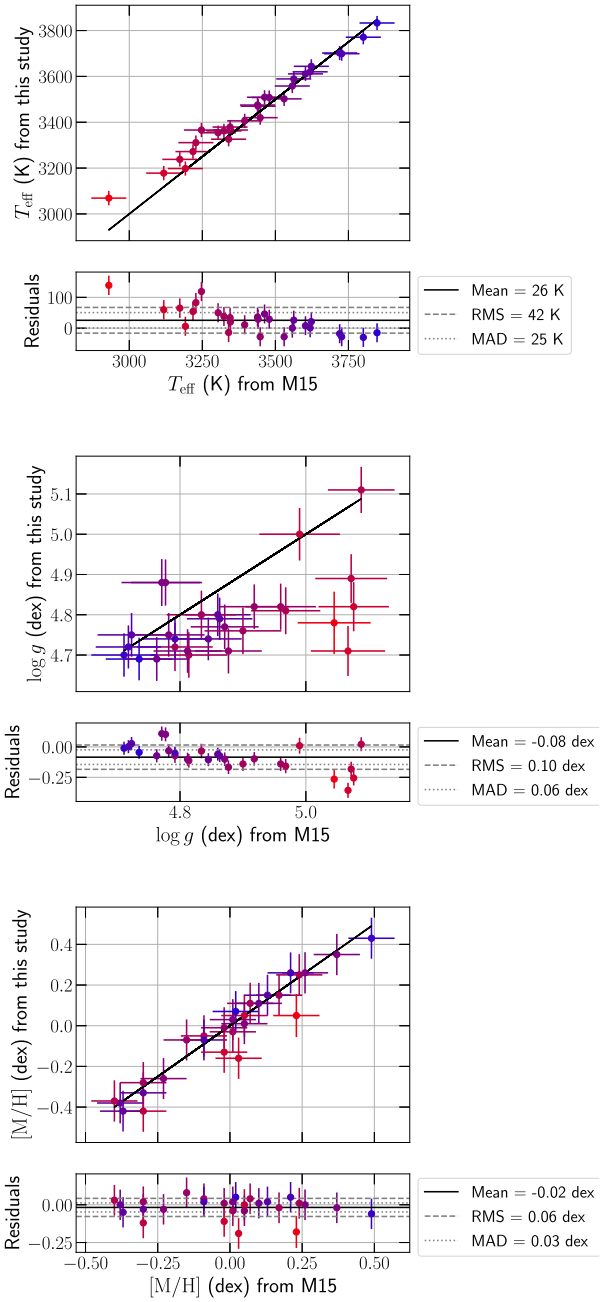

Figure 4. Comparison between retrieved parameters and value published by M15 for 23 stars common to both samples. The temperature is colour coded from red (coolest) to blue (hottest). An alternative figure with labels identifying the stars is presented in Fig. A2.

through our retrieved results (of slope 0.85 ± 0.02). For these 28 stars, the RMS about the trend in $T_{\rm eff}$ is of about 25 K, of the order of our estimated error bars.

Fig. D1 presents a similar comparison to the parameters retrieved by Passegger et al. (2019), who performed fits of PHOENIX-ACES synthetic spectra on high-resolution CARMENES data. The RMS on the residuals is then of about 60 K, again, of the order of the typically published error bars. We point out that Passegger et al. (2019), as well as other references such as Marfil et al. (2021), also find higher $T_{\rm eff}$ values than M15 for the coolest star of our sample.

Table 7. Retrieved parameters of the star in our sample. Columns 2 to 5 present the stellar parameters estimated from our fitting procedure. Columns 6 through 9, respectively, present the *Gaia G*-, *J*-, and *K*-band absolute magnitudes and parallaxes extracted from SIMBAD. Column 10 lists the log of the logarithmic bolometric luminosity (with respect to that of the Sun) derived from M_G. Columns 11 and 12 present the radius computed from T_{eff} and M_J and mass derived from M_K–mass relations. Column 13 presents alternative log g estimates computed from columns 11 and 12.

Star	T_{eff}	log g	[M/H]	[α/Fe]	M_G	M_J	M_K	Parallax	log ($L_*/L_\odot$)	Radius	Mass	alt. log g
Gl 338B	3952 ± 30	4.71 ± 0.05	−0.08 ± 0.10	0.05 ± 0.04	8.046 ± 0.003	5.77 ± 0.17	5.13 ± 0.02	157.88 ± 0.02	−1.090 ± 0.011	0.609 ± 0.012	0.58 ± 0.02	4.63 ± 0.02
Gl 410	3842 ± 31	4.87 ± 0.05	0.05 ± 0.10	0.05 ± 0.04	8.426 ± 0.003	6.14 ± 0.02	5.30 ± 0.02	83.76 ± 0.02	−1.239 ± 0.002	0.543 ± 0.009	0.55 ± 0.02	4.71 ± 0.02
Gl 846	3833 ± 31	4.69 ± 0.05	0.07 ± 0.10	−0.01 ± 0.04	8.282 ± 0.003	6.07 ± 0.02	5.20 ± 0.02	94.56 ± 0.05	−1.204 ± 0.002	0.568 ± 0.009	0.57 ± 0.02	4.68 ± 0.02
Gl 205	3771 ± 31	4.70 ± 0.05	0.43 ± 0.10	−0.08 ± 0.04	8.327 ± 0.003	6.05 ± 0.06	5.12 ± 0.06	175.31 ± 0.02	−1.202 ± 0.004	0.588 ± 0.010	0.58 ± 0.02	4.66 ± 0.02
Gl 880	3702 ± 31	4.72 ± 0.05	0.26 ± 0.10	−0.04 ± 0.04	8.611 ± 0.003	6.18 ± 0.02	5.34 ± 0.02	145.62 ± 0.03	−1.272 ± 0.001	0.563 ± 0.009	0.55 ± 0.02	4.67 ± 0.02
Gl 514	3699 ± 31	4.74 ± 0.05	−0.07 ± 0.10	0.04 ± 0.04	8.793 ± 0.003	6.49 ± 0.02	5.62 ± 0.03	131.10 ± 0.03	−1.382 ± 0.001	0.497 ± 0.008	0.50 ± 0.02	4.74 ± 0.02
Gl 382	3644 ± 31	4.75 ± 0.05	0.15 ± 0.10	−0.02 ± 0.04	8.897 ± 0.003	6.45 ± 0.02	5.58 ± 0.02	129.75 ± 0.03	−1.384 ± 0.001	0.511 ± 0.009	0.51 ± 0.02	4.73 ± 0.02
Gl 412A	3620 ± 31	4.79 ± 0.05	−0.42 ± 0.10	0.12 ± 0.04	9.460 ± 0.003	7.08 ± 0.02	6.32 ± 0.02	203.89 ± 0.03	−1.628 ± 0.001	0.391 ± 0.007	0.39 ± 0.02	4.84 ± 0.03
Gl 15A	3611 ± 31	4.80 ± 0.05	−0.33 ± 0.10	0.10 ± 0.04	9.460 ± 0.003	7.49 ± 0.26	6.26 ± 0.02	280.71 ± 0.02	−1.740 ± 0.034	0.345 ± 0.015	0.39 ± 0.02	4.96 ± 0.04
Gl 411	3589 ± 31	4.74 ± 0.05	−0.38 ± 0.10	0.19 ± 0.04	9.522 ± 0.003	7.17 ± 0.24	6.31 ± 0.05	392.75 ± 0.03	−1.659 ± 0.010	0.383 ± 0.008	0.39 ± 0.02	4.86 ± 0.03
Gl 752A	3558 ± 31	4.69 ± 0.05	0.11 ± 0.10	−0.01 ± 0.04	9.240 ± 0.003	6.72 ± 0.03	5.81 ± 0.02	169.06 ± 0.02	−1.500 ± 0.001	0.469 ± 0.008	0.47 ± 0.02	4.77 ± 0.02
Gl 48	3529 ± 31	4.68 ± 0.05	0.08 ± 0.10	0.07 ± 0.04	9.364 ± 0.003	6.72 ± 0.03	5.87 ± 0.02	121.46 ± 0.02	−1.514 ± 0.002	0.469 ± 0.008	0.46 ± 0.02	4.76 ± 0.03
Gl 617B	3525 ± 31	4.84 ± 0.06	0.20 ± 0.10	0.00 ± 0.04	9.459 ± 0.003	6.75 ± 0.02	5.91 ± 0.02	92.90 ± 0.02	−1.532 ± 0.002	0.460 ± 0.008	0.45 ± 0.02	4.77 ± 0.03
Gl 480	3509 ± 31	4.88 ± 0.06	0.26 ± 0.10	−0.01 ± 0.04	9.565 ± 0.003	6.81 ± 0.02	5.92 ± 0.04	70.11 ± 0.03	−1.562 ± 0.002	0.449 ± 0.008	0.45 ± 0.02	4.79 ± 0.03
Gl 436	3508 ± 31	4.75 ± 0.05	0.03 ± 0.10	0.00 ± 0.04	9.631 ± 0.003	6.95 ± 0.02	6.12 ± 0.02	102.30 ± 0.03	−1.609 ± 0.002	0.425 ± 0.008	0.42 ± 0.02	4.80 ± 0.03
Gl 849	3502 ± 31	4.88 ± 0.06	0.35 ± 0.10	−0.04 ± 0.04	9.511 ± 0.003	6.78 ± 0.02	5.87 ± 0.02	113.44 ± 0.03	−1.548 ± 0.002	0.458 ± 0.008	0.46 ± 0.02	4.78 ± 0.03
Gl 408	3487 ± 31	4.79 ± 0.05	−0.09 ± 0.10	0.04 ± 0.04	9.831 ± 0.003	7.17 ± 0.02	6.36 ± 0.01	148.20 ± 0.03	−1.695 ± 0.002	0.390 ± 0.007	0.38 ± 0.02	4.83 ± 0.03
Gl 687	3475 ± 31	4.71 ± 0.05	0.01 ± 0.10	0.06 ± 0.04	9.739 ± 0.003	7.05 ± 0.02	6.26 ± 0.02	219.79 ± 0.02	−1.649 ± 0.002	0.414 ± 0.007	0.39 ± 0.02	4.80 ± 0.03
Gl 725A	3470 ± 31	4.77 ± 0.06	−0.26 ± 0.10	0.15 ± 0.04	10.120 ± 0.003	7.45 ± 0.02	6.70 ± 0.02	283.84 ± 0.02	−1.809 ± 0.002	0.345 ± 0.006	0.33 ± 0.02	4.88 ± 0.03
Gl 317	3421 ± 31	4.71 ± 0.06	0.23 ± 0.10	−0.04 ± 0.04	9.859 ± 0.003	7.03 ± 0.03	6.12 ± 0.02	65.88 ± 0.04	−1.657 ± 0.004	0.423 ± 0.008	0.42 ± 0.02	4.80 ± 0.03
Gl 251	3420 ± 31	4.71 ± 0.06	−0.01 ± 0.10	−0.01 ± 0.04	10.129 ± 0.003	7.37 ± 0.02	6.54 ± 0.02	179.06 ± 0.03	−1.786 ± 0.003	0.365 ± 0.007	0.35 ± 0.02	4.86 ± 0.03
GJ 4063	3419 ± 31	4.77 ± 0.06	0.42 ± 0.10	−0.07 ± 0.04	9.982 ± 0.003	7.00 ± 0.02	— ± —	91.80 ± 0.02	−1.662 ± 0.004	0.422 ± 0.008	— ± —	— ± —
Gl 581	3406 ± 31	4.82 ± 0.06	−0.07 ± 0.10	0.01 ± 0.04	10.425 ± 0.003	7.71 ± 0.03	6.84 ± 0.02	158.72 ± 0.03	−1.917 ± 0.002	0.317 ± 0.006	0.31 ± 0.02	4.92 ± 0.03
Gl 725B	3379 ± 31	4.82 ± 0.06	−0.28 ± 0.10	0.14 ± 0.04	10.790 ± 0.003	7.99 ± 0.02	7.27 ± 0.02	283.84 ± 0.03	−2.038 ± 0.003	0.280 ± 0.005	0.25 ± 0.02	4.95 ± 0.04
Gl 876	3366 ± 31	4.80 ± 0.06	0.15 ± 0.10	−0.04 ± 0.04	10.528 ± 0.003	7.59 ± 0.02	6.66 ± 0.02	214.04 ± 0.04	−1.892 ± 0.004	0.333 ± 0.006	0.33 ± 0.02	4.91 ± 0.03
PM J09553-2715	3366 ± 31	4.76 ± 0.06	−0.03 ± 0.10	−0.02 ± 0.04	10.629 ± 0.003	7.84 ± 0.02	6.96 ± 0.02	91.74 ± 0.04	−1.979 ± 0.003	0.302 ± 0.006	0.29 ± 0.02	4.94 ± 0.04
GJ 1012	3363 ± 31	4.66 ± 0.06	0.07 ± 0.10	0.01 ± 0.04	10.268 ± 0.003	7.40 ± 0.02	6.56 ± 0.02	74.71 ± 0.04	−1.811 ± 0.003	0.367 ± 0.007	0.35 ± 0.02	4.85 ± 0.03
GJ 4333	3362 ± 31	4.72 ± 0.06	0.25 ± 0.10	−0.02 ± 0.04	10.233 ± 0.003	7.27 ± 0.03	6.38 ± 0.02	94.37 ± 0.03	−1.767 ± 0.006	0.386 ± 0.008	0.37 ± 0.02	4.84 ± 0.03
Gl 445	3356 ± 31	4.85 ± 0.06	−0.24 ± 0.10	0.14 ± 0.04	10.949 ± 0.003	8.12 ± 0.02	7.35 ± 0.03	190.33 ± 0.02	−2.094 ± 0.003	0.266 ± 0.005	0.24 ± 0.02	4.97 ± 0.04
GJ 1148	3354 ± 31	4.70 ± 0.06	0.11 ± 0.10	0.01 ± 0.04	10.370 ± 0.003	7.40 ± 0.02	6.61 ± 0.02	90.69 ± 0.03	−1.820 ± 0.004	0.365 ± 0.007	0.34 ± 0.02	4.84 ± 0.03
PM J08402 + 3127	3347 ± 31	4.76 ± 0.06	−0.08 ± 0.10	0.01 ± 0.04	10.739 ± 0.003	7.87 ± 0.02	7.05 ± 0.02	89.07 ± 0.03	−1.998 ± 0.003	0.299 ± 0.006	0.28 ± 0.02	4.93 ± 0.04
GJ 3378	3326 ± 31	4.81 ± 0.06	−0.05 ± 0.10	−0.01 ± 0.04	10.975 ± 0.003	8.02 ± 0.02	7.20 ± 0.02	129.30 ± 0.03	−2.068 ± 0.004	0.279 ± 0.005	0.26 ± 0.02	4.96 ± 0.04
GJ 1105	3324 ± 31	4.63 ± 0.07	−0.04 ± 0.10	−0.05 ± 0.04	10.931 ± 0.003	8.00 ± 0.02	7.14 ± 0.03	112.99 ± 0.03	−2.056 ± 0.004	0.283 ± 0.005	0.27 ± 0.02	4.96 ± 0.04
Gl 699	3311 ± 31	5.11 ± 0.06	−0.37 ± 0.10	0.16 ± 0.04	11.884 ± 0.003	8.93 ± 0.02	8.21 ± 0.02	546.98 ± 0.04	−2.432 ± 0.004	0.185 ± 0.004	0.16 ± 0.02	5.11 ± 0.06
GJ 169.1A	3307 ± 31	4.71 ± 0.06	0.13 ± 0.10	−0.07 ± 0.04	10.994 ± 0.003	7.91 ± 0.02	7.01 ± 0.02	181.24 ± 0.05	−2.037 ± 0.005	0.292 ± 0.006	0.28 ± 0.02	4.96 ± 0.04
PM J21463 + 3813	3305 ± 33	5.06 ± 0.08	−0.38 ± 0.10	0.25 ± 0.04	11.591 ± 0.003	8.71 ± 0.02	7.96 ± 0.02	141.89 ± 0.02	−2.335 ± 0.003	0.208 ± 0.004	0.18 ± 0.02	5.06 ± 0.06
Gl 15B	3272 ± 31	4.89 ± 0.06	−0.42 ± 0.10	0.04 ± 0.04	11.928 ± 0.003	9.03 ± 0.02	8.19 ± 0.02	280.69 ± 0.03	−2.465 ± 0.004	0.182 ± 0.004	0.16 ± 0.02	5.13 ± 0.06
GJ 1289	3238 ± 32	5.00 ± 0.07	0.05 ± 0.10	−0.00 ± 0.04	11.556 ± 0.003	8.50 ± 0.03	7.61 ± 0.02	119.58 ± 0.06	−2.269 ± 0.007	0.233 ± 0.005	0.21 ± 0.02	5.03 ± 0.05
Gl 447	3198 ± 31	4.82 ± 0.06	−0.13 ± 0.10	−0.01 ± 0.04	11.960 ± 0.003	8.86 ± 0.02	8.01 ± 0.02	296.31 ± 0.03	−2.419 ± 0.006	0.201 ± 0.004	0.18 ± 0.02	5.08 ± 0.06
GJ 1151	3178 ± 31	4.71 ± 0.06	−0.16 ± 0.10	−0.03 ± 0.04	12.158 ± 0.003	8.96 ± 0.03	8.11 ± 0.02	124.34 ± 0.05	−2.468 ± 0.009	0.193 ± 0.004	0.17 ± 0.02	5.10 ± 0.06
GJ 1103	3170 ± 31	4.67 ± 0.06	−0.03 ± 0.10	−0.00 ± 0.04	11.818 ± 0.003	8.66 ± 0.02	7.83 ± 0.02	107.85 ± 0.04	−2.344 ± 0.007	0.224 ± 0.005	0.19 ± 0.02	5.03 ± 0.05
Gl 905	3069 ± 31	4.78 ± 0.08	0.05 ± 0.11	−0.06 ± 0.04	12.881 ± 0.003	9.39 ± 0.03	8.43 ± 0.02	316.48 ± 0.04	−2.664 ± 0.012	0.165 ± 0.004	0.15 ± 0.02	5.17 ± 0.07
GJ 1002	2980 ± 33	4.70 ± 0.08	−0.33 ± 0.11	−0.00 ± 0.04	13.347 ± 0.003	9.90 ± 0.02	9.01 ± 0.02	206.35 ± 0.05	−2.864 ± 0.009	0.139 ± 0.003	0.12 ± 0.02	5.22 ± 0.09
GJ 1286	2961 ± 33	4.55 ± 0.12	−0.23 ± 0.10	−0.04 ± 0.04	13.344 ± 0.003	9.87 ± 0.02	8.90 ± 0.02	139.34 ± 0.04	−2.855 ± 0.010	0.142 ± 0.004	0.12 ± 0.02	5.21 ± 0.08

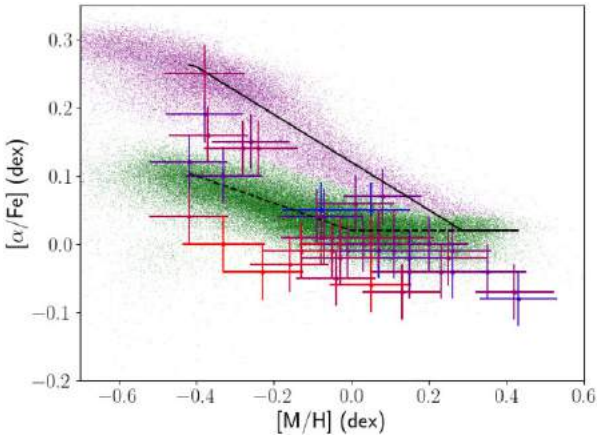

Figure 5. Retrieved [α/Fe] plotted against [M/H] for the 44 targets in our sample. The solid and dashed black lines mark empirical thick and thin disc [M/H]–[α/Fe] relations, respectively. The coloured pixels mark the position of giants studied by APOGEE, with the purple and green colours marking those expected to be from the thick and thin disc, respectively. An alternative figure with labels identifying the stars is presented in Fig. A3.

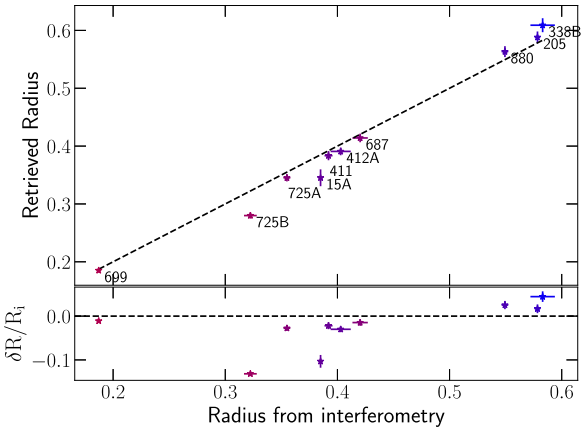

Figure 6. Comparison between radii retrieved from fits and computed from interferometric measurements (Boyajian et al. 2012) for nine stars. The symbol colour depicts the temperature from red (cool) to blue (hot). The larger error bars originate from uncertainties on the M_J measurements published by the 2MASS survey. The bottom plot displays the relative difference between our estimated radii and those computed from interferometric measurements.

6.2 Metallicity and alpha-enhancement

For the 28 stars studied in this work and in M15, the [M/H] values recovered with our analysis are in good agreement, with an RMS on the residuals of about 0.1 dex, of the order of our estimated empirical error bar for this parameter. Here again, the largest deviation is observed for the coolest stars in our sample, for which we find lower [M/H] than M15, but for which other studies (Passegger et al. 2019; Marfil et al. 2021) also find different values than M15 (see Figs D1 and D2).

Comparing our results to the values published by Passegger et al. (2019, Fig. D1), we find a much larger RMS on the residuals of about 0.16 dex. These results illustrate the difficulty to estimate the accuracy of the parameters derived from fits of synthetic spectra which depends on the assumed reference on which to rely.

Fitting [α/Fe] as an additional dimension in our process allowed us to significantly improve the estimate of [M/H] for cool metal-poor stars. Because our line list contains several features sensitive to [α/Fe] variations, we are able to obtain reliable estimates of this parameter without the need to set priors. Figs 5 and A3 present the retrieved [α/Fe] as a function of the recovered [M/H] for the 44 stars of our sample. These results are globally consistent with the expected trends estimated from the APOGEE data for giants and suggest that most of our stars belong to the thin Galactic disc, with a few exception such as Gl 699, Gl 411, PM J21463+3813, and Gl 445 which would more likely belong to the thick Galactic disc. Gl 725 A and B are found at the limit of the fiducial boundary between thick and thin disc, and are therefore difficult to classify.

6.3 Masses and radii

Mann et al. (2019) derived a *K*-band magnitude (M_K) – mass–metallicity empirical relation. We use this relation to derive the masses of the targets in our sample. Radii for the studied stars can be computed from the recovered $T_{\rm eff}$ and the bolometric luminosity using Stefan–Boltzmann law. Bolometric luminosities are directly computed from 2MASS *J*- and *Gaia* (DR2) *G*-band absolute magnitudes (M_J and M_G, respectively) and bolometric corrections (Cifuentes et al. 2020). All magnitudes used in this work were extracted from SIMBAD.[2] In this work, we chose to derive the luminosities from bolometric corrections and absolute magnitudes rather than to rely on bolometric luminosities reported by authors such as Cifuentes et al. (2020) or M15. This allows us to produce self-consistent results for all the stars in our sample as these studies do not typically report values for all our targets. Several tests allowed to verify that the reported values and those derived from bolometric corrections are in fair agreement for most stars (see Fig. E1). One should note that the 2MASS survey attributes a quality flag to the reported magnitudes, which may not systematically be accounted for by reported uncertainties. We compare our retrieved radii (R_f) to those computed from interferometry (R_i) by Boyajian et al. (2012, see Fig. 6). We find values that are consistent with interferometric measurements for the nine stars studied by Boyajian et al. (2012), with a dispersion on $\delta R/R_i \approx 5$ per cent, with $\delta R = R_f - R_i$.

We note that the radius retrieved from interferometry for Gl 725B is significantly larger than the one we estimate with this method; coupled with the measured magnitude, it would yield an effective temperature of $T_{\rm eff} = 3145 \pm 10$ K, i.e. 200 K cooler than the values derived by most studies (M15, C22 Fouqué et al. 2018; Marfil et al. 2021) and ours. This discrepancy was also observed and reported by M15. The apparent inconsistency in these results calls for an in-depth investigation of Gl 725B.

We locate our stars in a Hertzsprung–Russell (HR) diagram (see Figs 7 and A4). We compare our results to the isochrone computed by Baraffe et al. (2015). Our results tend to be in good agreement with the model, with points scattered around the isochrone, which can be attributed to metallicity. Isochrones computed with the Dartmouth stellar evolution program (DSEP, Dotter et al. 2008) for different metallicities confirm the dependency on [M/H]. We also observe a strong divergence between the DSEP models and those of Baraffe et al. (2015), in particular for stars with masses lower than 0.3 $M_\odot$.

Our estimated radii and masses are found in good agreement with mass–radius relations expected from stellar evolution models (see Figs 8 and A5, Feiden & Chaboyer 2012). We further note a good agreement between our derived masses and radii and those reported

[2] http://simbad.cds.unistra.fr/simbad/

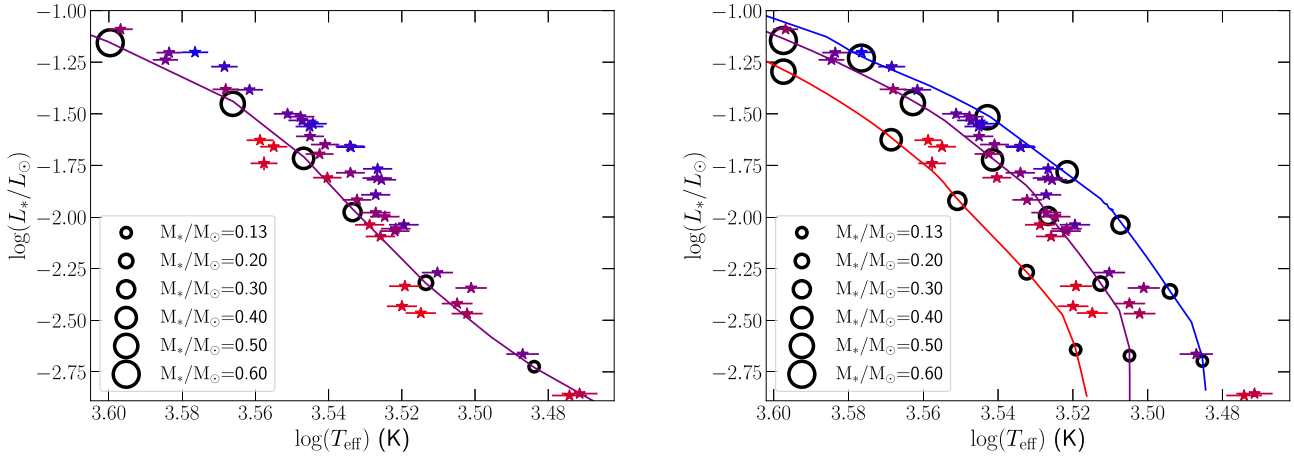

Figure 7. HR diagram showing the position of the stars in our sample. Luminosity was computed from *G*-band magnitude retrieved through SIMBAD. The metallicity is colour coded from red to blue (low to high metallicity, respectively). On the left-hand panel, the purple solid line presents the isochrone computed by Baraffe et al. (2015) at solar metallicity. On the right-hand panel, the red, purple, and blue solid lines present the DSEP stellar isochrones for [M/H] = −0.5 dex, [M/H] = 0.0 dex, and [M/H] = 0.5 dex, respectively. An age of 5 Gyr is assumed for all isochrones. The black circles mark the position of different stellar masses for each metallicity. An alternative figure with labels identifying the stars is presented in Fig. A4.

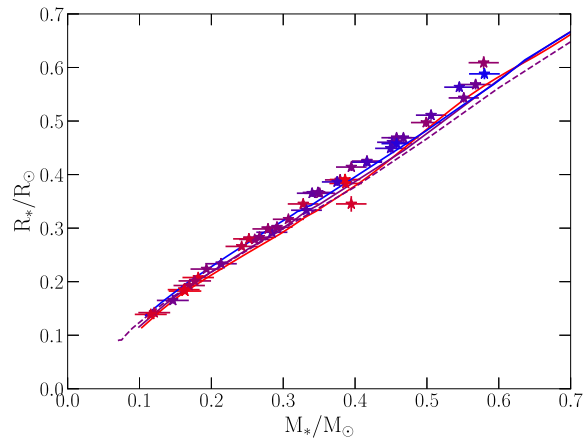

Figure 8. Mass–radius diagram showing the position of the stars in our sample. The metallicity is colour coded from red to blue (low to high metallicity, respectively). The red, purple, and blue solid lines present the mass–radius relation predicted by the DSEP models for [M/H] = −0.5 dex, [M/H] = 0.0 dex, and [M/H] = 0.5 dex, respectively. The purple dashed line presents the mass–radius relationship predicted by the models of Baraffe et al. (2015), at solar metallicity. An age of 5 Gyr is assumed for all models. An alternative figure with labels identifying the stars is presented in Fig. A5.

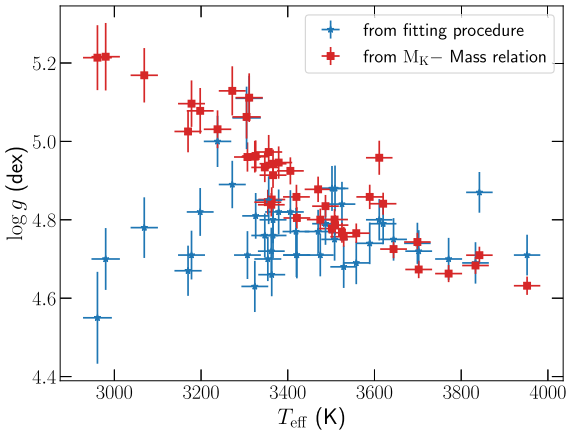

Figure 9. Comparison of the log g derived from our fitting procedure and those computed from M$_K$–mass relation. An alternative figure with labels identifying the stars is presented in Fig. A6.

by M15 (see Fig. F1), with a relative dispersion of 4 per cent on both parameters.

6.4 Surface gravity

Surface gravity is known to be difficult to constrain for M dwarfs. Several studies chose to fix this parameter from semi-empirical relations or evolutionary models (Rajpurohit et al. 2018; Passegger et al. 2019). Following C22, we fit this parameter. Our new estimates are in better agreement with M15 than those of C22, showing that the various improvements brought to our analysis (see Section 3–5) helped solving the issue.

From the masses and radii derived in Section 6.3 we compute new log g values, and compare these to the values obtained from the spectral fitting procedure (see Figs 9 and A6). We observe significant differences between the two sets of log g values, and compute an RMS on the residuals of about 0.2 dex. This dispersion is also the result of larger discrepancies at low $T_{\rm eff}$ and the RMS value computed when ignoring the six coolest stars in our sample falls to 0.11 dex. This may suggest that, for some yet unclear reason, we underestimate the log g of the coolest stars with our fitting procedure.

7 DISCUSSION AND CONCLUSIONS

In this work, we improved and extended a method designed to retrieve the atmospheric parameters of M dwarfs from high-resolution spectroscopic observations using state-of-the-art synthetic spectra computed with Turbospectrum from MARCS model atmospheres. Our analysis consists in comparing these models to high-SNR template spectra built from tens to hundreds of observations collected with SPIRou. We extend the work initiated in C22 and applied our new tool to our SLS sample of 44 M dwarfs.

Recent publications (Rajpurohit et al. 2018; Marfil et al. 2021) included empirical [α/Fe]–[M/H] relations in their analysis, or relied on models that did so, in order to constrain $T_{\rm eff}$ or [M/H]. In this

work, the fitting procedure, initially developed to constrain $T_{\rm eff}$, $\log g$, and [M/H], was extended to also include a fit of [α/Fe], motivated by the large impact this parameter has on the derivation of the other stellar parameters. We retrieve [α/Fe] values that are consistent with empirical trends observed when studying giants (Adibekyan et al. 2013). We find that the coolest low-metallicity stars in our sample are the most sensitive to [α/Fe]. This is likely due to the presence of strong O-bearing molecular bands (e.g. CO) in the NIR spectra at low $T_{\rm eff}$, strongly impacted by variations in the abundances of alpha elements, in particular oxygen.

In this paper, we revised the line list used in C22, and updated the continuum adjustment procedure to improve the fit quality. This updated list contains 17 atomic lines, nine OH lines, and about 40 molecular lines found in the CO band redward of 2293 nm, which represents a very small subset of the lines that are included in the models and those present in the observed template spectra (which in most cases do not match well). Previous studies have attempted to refine the parameters of some atomic lines for their analysis (Petit et al. 2021). Here, we tried to improve the fits of synthetic spectra to SPIRou templates by adjusting the values of Van Der Waals broadening parameters and oscillator strengths for a few of the selected lines. We assumed the parameters published by M15 for three calibration stars (Gl 699, Gl 15A, and Gl 411) to perform this step. These corrections, and in particular those applied to the Van Der Waals parameter of Ti lines, helped to bring our $\log g$ estimates closer to those of M15 for some targets. One should note that these corrections may not be the sole result of uncertainties in the line parameters, and may also reflect inaccuracies of the atmospheric models.

With the implemented improvements and updated line list, we recover parameters in good agreement with M15 for 28 stars included in both studies. We retrieve $T_{\rm eff}$ with a typical dispersion of about 45 K, lower that the uncertainties reported by M15, although larger than our estimated error bars of about 30 K. This difference is also the result of a trend observed in the retrieved $T_{\rm eff}$ values, as we tend to derive larger $T_{\rm eff}$ for cool stars than M15. The dispersion about this trend is of the order of 25 K, of the order of our empirical error bars. We also obtain [M/H] values with a dispersion of 0.06 dex, consistent with our error bars estimated to about 0.1 dex. Finally, $\log g$ is in better agreement with M15 compared to the values reported in C22, although we tend to recover smaller estimates than M15 for the coolest stars in our sample.

For our 44 targets, we extracted *Gaia G*-, *J*-, and *K*-band magnitudes from SIMBAD, along with parallaxes, when available. We computed the radii for our sample from $T_{\rm eff}$, absolute *J*-band magnitude ($M_{\rm J}$), and bolometric corrections (Cifuentes et al. 2020). Interferometric data published by Boyajian et al. (2012) for nine of these stars reported angular diameters that are consistent with our retrieved radii, with a relative dispersion of about 5 per cent. Additionally, we derive the masses of the stars in our sample from $M_{\rm K}$–mass relations (Mann et al. 2019). Our derived masses and radii tend to be in good agreement with mass–radius relationships predicted by evolutionary models. We note a slight tendency to estimate larger radii that those predicted by the DSEP models and those of Baraffe et al. (2015). This tendency was reported in the literature (Feiden & Chaboyer 2013; Jackson, Deliyannis & Jeffries 2018) and different hypothesises were proposed, attributing the phenomenon to metallicity, modelling assumptions, or radius inflation induced by the presence of magnetic fields. From our masses and radii estimates, we compute new $\log g$ values, and compare them to those derived from the fitting procedure. We find significant discrepancies between the two sets of $\log g$ values, especially at the lowest temperatures. This difference suggests that we tend to underestimate $\log g$ for the coolest stars in our sample with our fitting procedure. Fixing $\log g$ to higher values for the coolest stars in our sample results in an increase in $T_{\rm eff}$ of 20–50 K, an increase in [M/H] of up to 0.2 dex, and slight increases in [α/Fe] by less than 0.04 dex. This may reflect MARCS models being less accurate at temperatures close to 3000 K, i.e. close to the lower limit of our model temperature grid.

We also retrieved [α/Fe] values for the 44 stars in our sample, but lack references for most of these targets. Given that $T_{\rm eff}$, $\log g$, and [M/H] are very sensitive to small variations in [α/Fe], the latter should be carefully considered when fitting models to spectra of M dwarfs. To assess the quality of the constraint on this parameter, we place our stars in a [α/Fe]–[M/H] plane, and find that the recovered [α/Fe] are in good agreement with values expected from empirical relations. We find that a few stars, in particular Gl 699, Gl 445, PM J21463+3813, and Gl 411, have relatively large retrieved [α/Fe] values and are likely to belong to the thick Galactic disc, while most of our stars are likely to belong to thin disc, with lower [α/Fe] values. These results are somewhat consistent with the computed velocities, larger than 100 km s^{-1} for these four stars. Although Gl 317 and PM J09553-2715 also feature high velocities, their supersolar metallicities make it difficult to reliably conclude about the disc population these stars belong to. Gl 412A also has a velocity above 100 km s^{-1}, but we derive an [α/Fe] value smaller than that expected for the thick disc. These results are compatible with previous classification of these stars (Cortés-Contreras 2016; Schöfer et al. 2019), in which PM J09553−2715, PM J21463+3813, Gl 699, Gl 445, and Gl 411 were identified as belonging to the thick disc, and Gl 412A labelled as within the transition between thin and thick discs. Most other stars studied by Cortés-Contreras (2016) and included in our work were classified as belonging to the thin or young disc, with a few exceptions such as Gl 880, Gl 905, and GJ 1151, placed either in the thick of transition between thick and thin discs. One should note that the boundary between thin and thick disc from [α/Fe] remains fuzzy even for giants making it tricky to clearly split the stars of our sample into two distinct populations.

In subsequent works, we will perform a similar analysis with other models, such as PHOENIX, which will require to compute new grids of synthetic spectra for different [α/Fe] values, and with up-to-date line lists. As our models evolve, we will revise the modifications performed on the line lists and identify additional stellar features to use for our purposes. This will allow us to further investigate the differences between models, and to identify the modelling assumptions that are best suited to the computation of synthetic spectra of M dwarfs and cool stars. Additionally, we will try to perform the same kind of analysis on more active targets that were excluded from our sample, and on the pre-main-sequence stars also observed with SPIRou in the framework of the SLS. The spectra of such stars may be impacted by activity, with effects from the chromosphere (Hintz et al. 2019) or Zeemann broadening (Deen 2013) and radius inflation due to stronger magnetic fields (Feiden & Chaboyer 2013). This may require the addition of extra steps to the modelling process. Spots are indeed likely to be present at the surface of active targets, which may require implementing a two-temperature model to reproduce their spectra (Gully-Santiago et al. 2017).

ACKNOWLEDGEMENTS

We acknowledge funding from the European Research Council under the H2020 & innovation program (grant #740651 NewWorlds).

This work is based on observations obtained at the Canada–France–Hawaii Telescope (CFHT), which is operated by the National

Research Council (NRC) of Canada, the Institut National des Sciences de l'Univers of the Centre National de la Recherche Scientifique (CNRS) of France, and the University of Hawaii. The observations at the CFHT were performed with care and respect from the summit of Maunakea, which is a significant cultural and historic site.

This research used the SIMBAD data base (Wenger et al. 2000), operated at CDS, Strasbourg, France.

TM acknowledges financial support from the Spanish Ministry of Science and Innovation (MICINN) through the Spanish State Research Agency, under the Severo Ochoa Program 2020-2023 (CEX2019-000920-S) as well as support from the ACIISI, Consejería de Economía, Conocimiento y Empleo del Gobiernode Canarias and the European Regional Development Fund (ERDF) under grant with reference PROID2021010128. 777.

We acknowledge funding from the French National Research Agency (ANR) under contract number ANR18CE310019 (SPlaSH). XD and AC acknowledge support in the framework of the Investissements d'Avenir program (ANR-15-IDEX-02), through the funding of the 'Origin of Life' project of the Grenoble-Alpes University.

DATA AVAILABILITY

The data used in this work were acquired in the context of the SLS, and will be publicly available at the Canadian Astronomy Data Center one year after the completion of the program.

REFERENCES

Adibekyan V. Z. et al., 2013, A&A, 554, A44
Allard F., Hauschildt P. H., 1995, ApJ, 445, 433
Allard F., Homeier D., Freytag B., 2011, in Johns-Krull C., Browning M. K., West A. A., eds, ASP Conf. Ser. Vol. 448, 16th Cambridge Workshop on Cool Stars, Stellar Systems, and the Sun. Astron. Soc. Pac., San Francisco, p. 91
Alvarez R., Plez B., 1998, A&A, 330, 1109
Baraffe I., Homeier D., Allard F., Chabrier G., 2015, A&A, 577, A42
Bonfils X. et al., 2013, A&A, 556, A110
Boyajian T. S. et al., 2012, ApJ, 757, 112
Cifuentes C. et al., 2020, A&A, 642, A115
Cortés-Contreras M., 2016, PhD thesis, Univ. Complutense de Madrid
Cristofari P. I. et al., 2022, MNRAS, 511, 1893 (C22)
Deen C. P., 2013, AJ, 146, 51
Donati J. F. et al., 2020, MNRAS, 498, 5684
Dotter A., Chaboyer B., Jevremović D., Kostov V., Baron E., Ferguson J. W., 2008, ApJS, 178, 89
Dressing C. D., Charbonneau D., 2013, ApJ, 767, 95
Feiden G. A., Chaboyer B., 2012, ApJ, 757, 42
Feiden G. A., Chaboyer B., 2013, ApJ, 779, 183
Fouqué P. et al., 2018, MNRAS, 475, 1960
Fuhrmann K., 1998, A&A, 338, 161
Gaidos E., Mann A. W., Kraus A. L., Ireland M., 2016, MNRAS, 457, 2877
Gully-Santiago M. A. et al., 2017, ApJ, 836, 200
Gustafsson B., Edvardsson B., Eriksson K., Jørgensen U. G., Nordlund, Å., Plez B., 2008, A&A, 486, 951
Hintz D. et al., 2019, A&A, 623, A136
Husser T. O., Wende-von Berg S., Dreizler S., Homeier D., Reiners A., Barman T., Hauschildt P. H., 2013, A&A, 553, A6
Ishikawa H. T., Aoki W., Kotani T., Kuzuhara M., Omiya M., Reiners A., Zechmeister M., 2020, PASJ, 72, 102
Ishikawa H. T. et al., 2022, AJ, 163, 72
Jackson R. J., Deliyannis C. P., Jeffries R. D., 2018, MNRAS, 476, 3245
Jönsson H. et al., 2020, AJ, 160, 120
Kotani T. et al., 2018, in Evans C. J., Simard L., Takami H., eds, Proc. SPIE Conf. Ser. Vol. 10702, Ground-based and Airborne Instrumentation for Astronomy VII. SPIE, Bellingham, p. 1070211
Kurucz R. L., 1970, SAO Special Report, 309
Kurucz R. L., 2005, Memorie della Societa Astronomica Italiana Supplementi, 8, 14
Mahadevan S. et al., 2012, in McLean I. S., Ramsay S. K., Takami H., eds, Proc. SPIE Conf. Ser. Vol. 8446, Ground-based and Airborne Instrumentation for Astronomy IV. SPIE, Bellingham, p. 84461S
Mann A. W., Brewer J. M., Gaidos E., Lépine S., Hilton E. J., 2013, AJ, 145, 52
Mann A. W., Feiden G. A., Gaidos E., Boyajian T., von Braun K., 2015, ApJ, 804, 64 (M15)
Mann A. W. et al., 2019, ApJ, 871, 63
Marfil E. et al., 2021, A&A, 656, A162
Neves V., Bonfils X., Santos N. C., Delfosse X., Forveille T., Allard F., Udry S., 2014, A&A, 568, A121
Pakhomov Y. V., Ryabchikova T. A., Piskunov N. E., 2019, Astron. Rep., 63, 1010
Passegger V. M. et al., 2018, A&A, 615, A6
Passegger V. M. et al., 2019, A&A, 627, A161
Petit P. et al., 2021, A&A, 648, A55
Plez B., 2012, Astrophysics Source Code Library, record ascl: 1205.004
Press W. H., Teukolsky S. A., Vetterling W. T., Flannery B. P., 1992, Numerical Recipes in C (2nd Ed.): The Art of Scientific Computing. Cambridge University Press, USA
Quirrenbach A. et al., 2014, in Ramsay S. K., McLean I. S., Takami H., eds, Proc. SPIE Conf. Ser. Vol. 9147, Ground-based and Airborne Instrumentation for Astronomy V. SPIE, Bellingham, p. 91471F
Rajpurohit A. S., Allard F., Teixeira G. D. C., Homeier D., Rajpurohit S., Mousis O., 2018, A&A, 610, A19
Rayner J. et al., 2016, in Evans C. J., Simard L., Takami H., eds, Proc. SPIE Conf. Ser. Vol. 9908, Ground-based and Airborne Instrumentation for Astronomy VI. SPIE, Bellingham, p. 990884
Rojas-Ayala B., Covey K. R., Muirhead P. S., Lloyd J. P., 2010, ApJ, 720, L113
Schöfer P. et al., 2019, A&A, 623, A44
Schweitzer A. et al., 2019, A&A, 625, A68
Souto D. et al., 2022, ApJ, 927, 123
Unsold A., 1955, Physik der Sternatmospharen, MIT besonderer Berucksichtigung der Sonne. Springer-Verlag, Berlin
Wenger M. et al., 2000, A&AS, 143, 9

SUPPORTING INFORMATION

Supplementary data are available at *MNRAS* online.

Figure S1. Best-fitting models obtained for five stars in our sample.

Please note: Oxford University Press is not responsible for the content or functionality of any supporting materials supplied by the authors. Any queries (other than missing material) should be directed to the corresponding author for the article.

APPENDIX A: FIGURES WITH LABELS

Figs A1 to A6 present alternative plots to Figs 1, 4, 5, 7, 8, and 9 with labels identifying the stars.

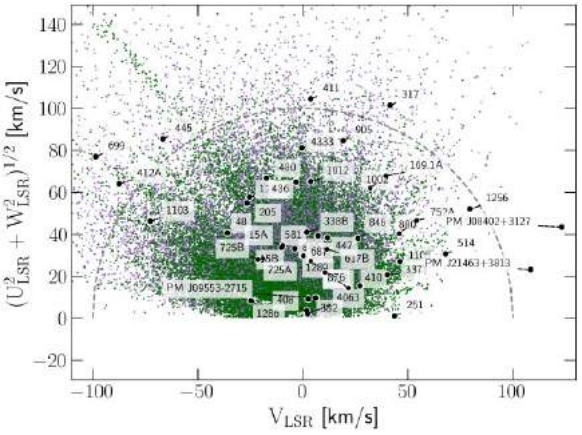

Figure A1. Same as Fig. 1 with labels identifying the stars.

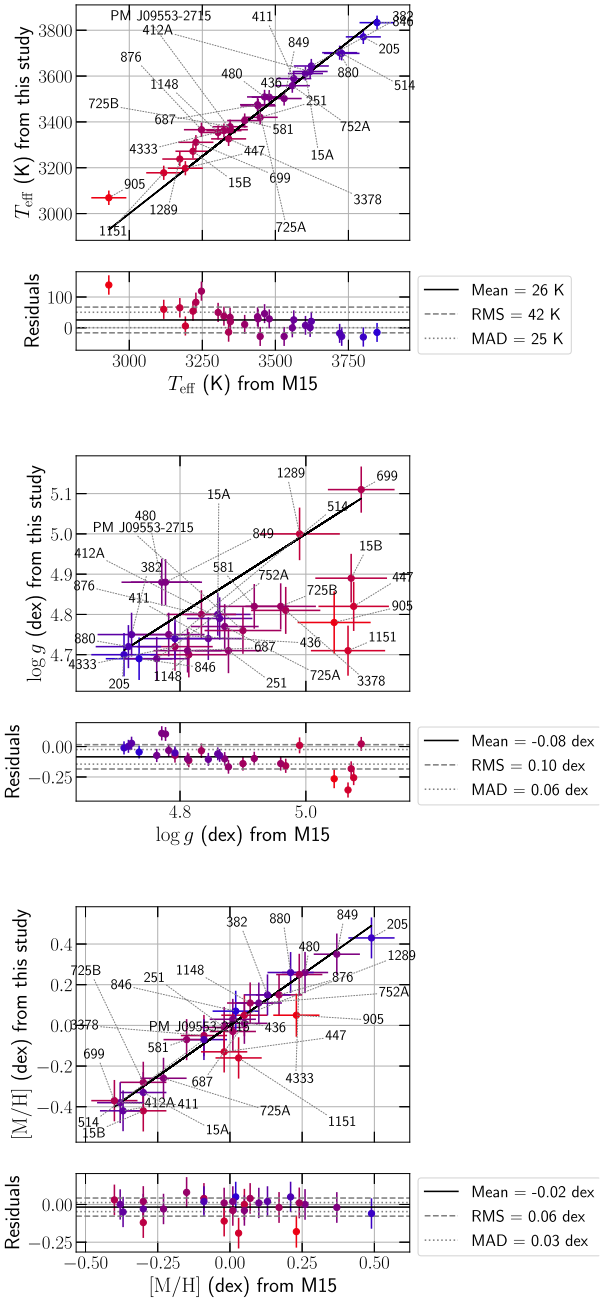

Figure A2. Same as Fig. 4 with labels identifying the stars.

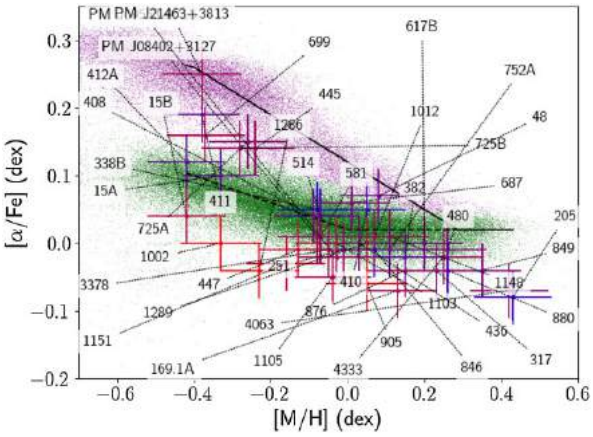

Figure A3. Same as Fig. 5 with labels identifying the stars.

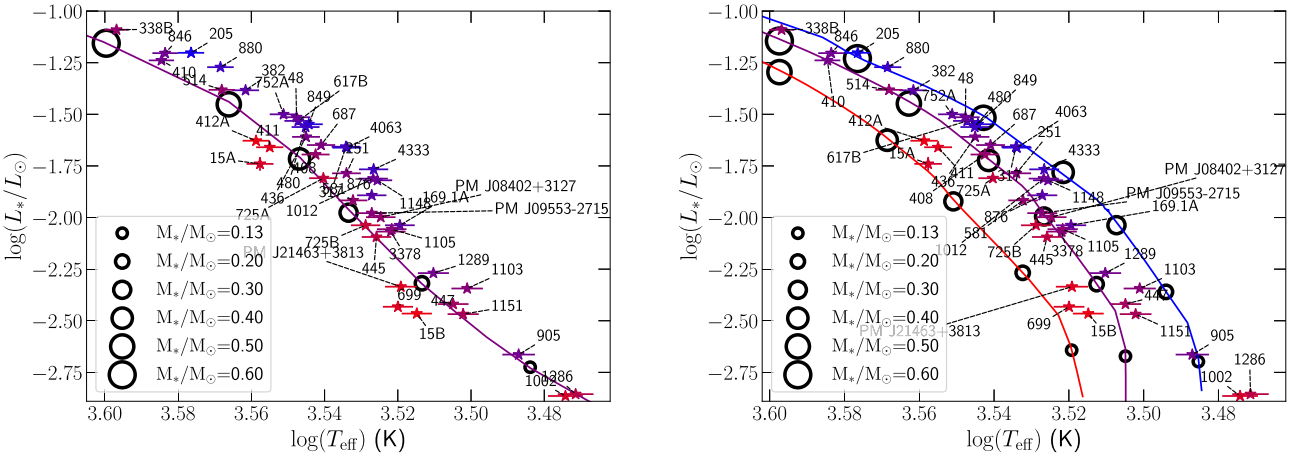

Figure A4. Same as Fig. 7 with labels identifying the stars.

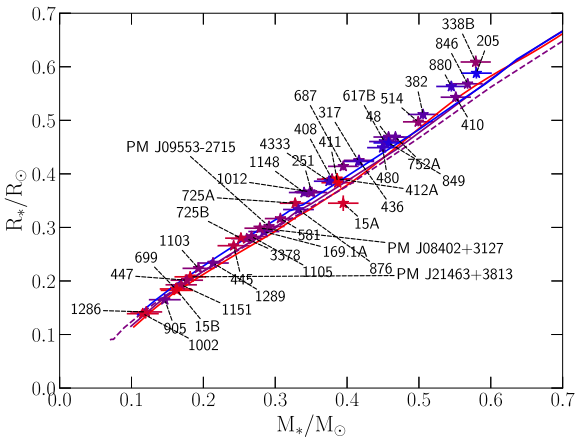

Figure A5. Same as Fig. 8 with labels identifying the stars.

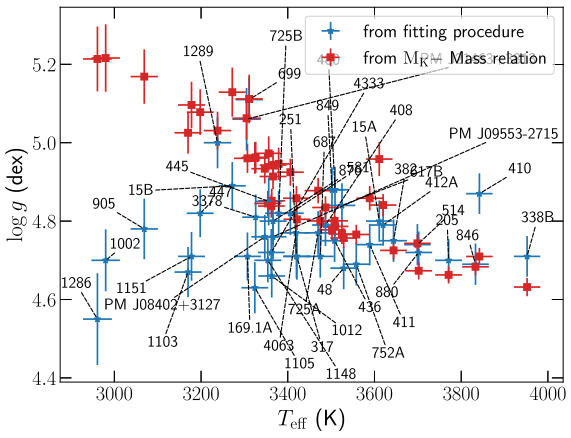

Figure A6. Same as Fig. 9 with labels identifying the stars.

APPENDIX B: RESULTS ON CALIBRATION STARS

Figs B1 and B2 present a comparison of the results obtained with and without corrections applied to the line list parameters (see Section 5).

Fig. B3 illustrates the effect of fitting on [α/Fe] on the retrieved parameters of our calibration stars.

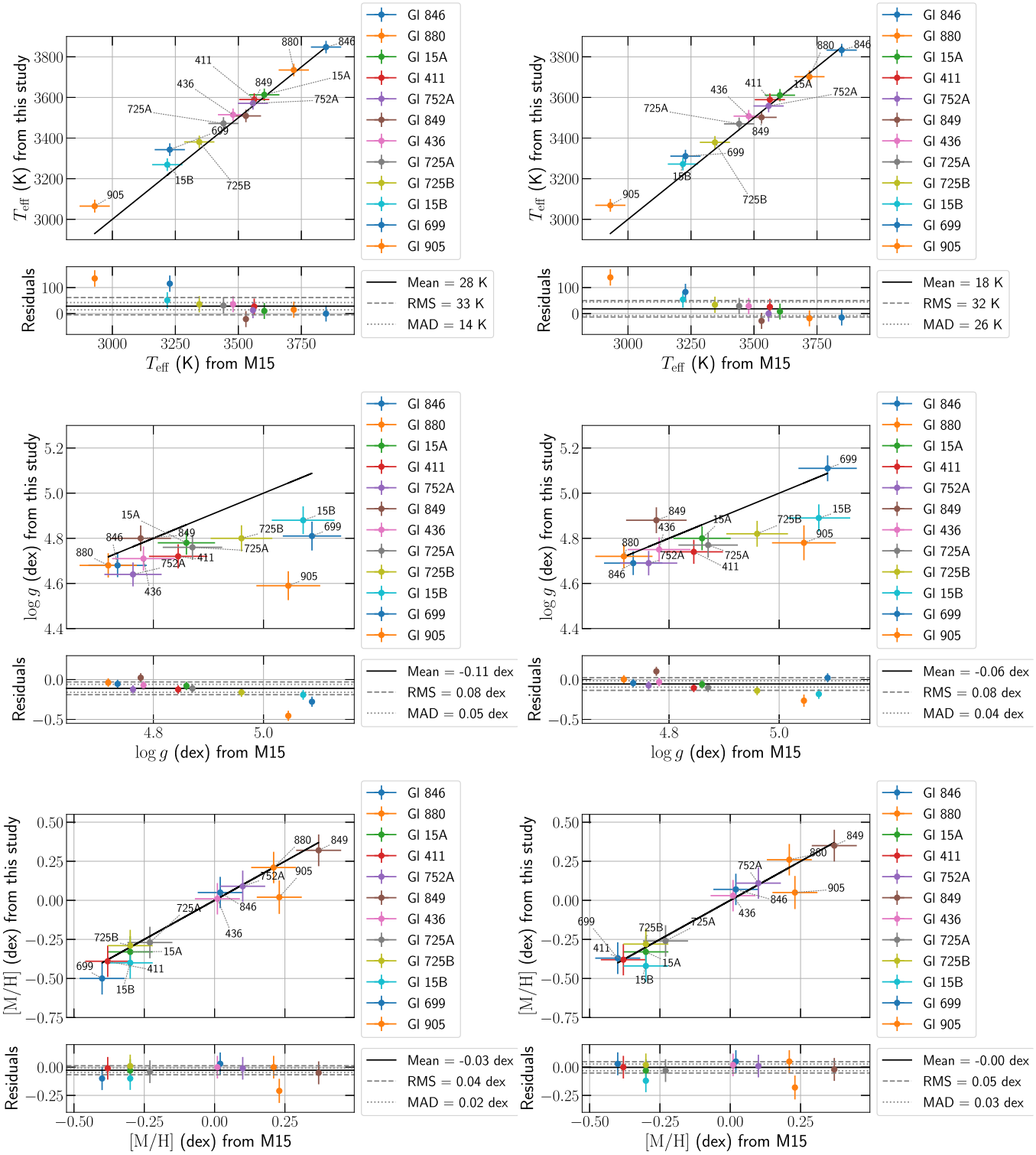

Figure B1. Comparisons between the retrieved $T_{\rm eff}$, log g, and [M/H] for our 12 calibration stars. The left- and right-hand panels present the results obtained before and after the corrections applied to the line list parameters listed in Section 5.

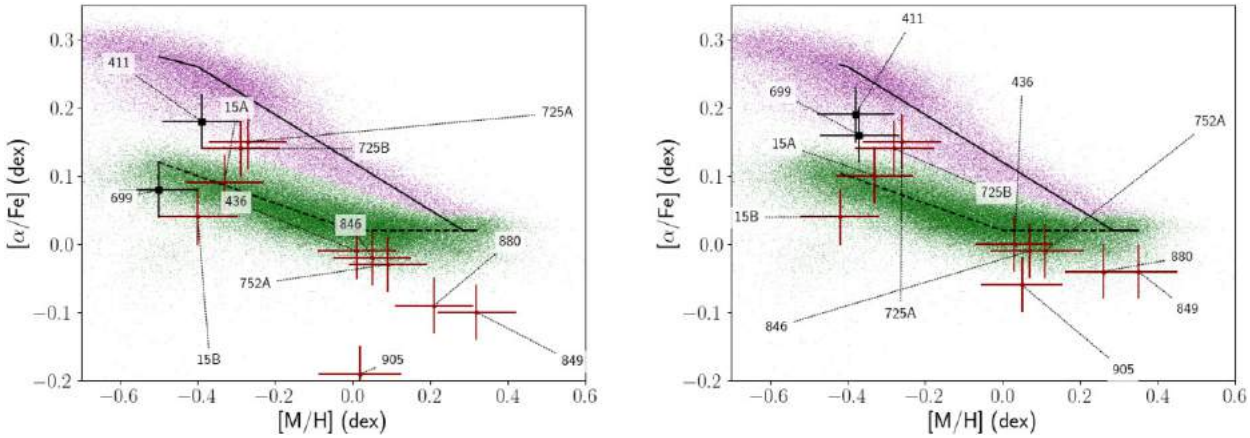

Figure B2. Retrieved [α/Fe] and [M/H] values for our 12 calibration stars. The purple and green pixels depict APOGEE data for giants of the thick and thin disc, respectively. The stars in our sample expected to belong to the thick disc from their velocity are marked with a black square symbol. The solid and dashed black lines mark empirical thick and thin disc [M/H]–[α/Fe] relations, respectively. The left- and right-hand panels present the results obtained before and after correction on some line parameters (see Section 5), respectively.

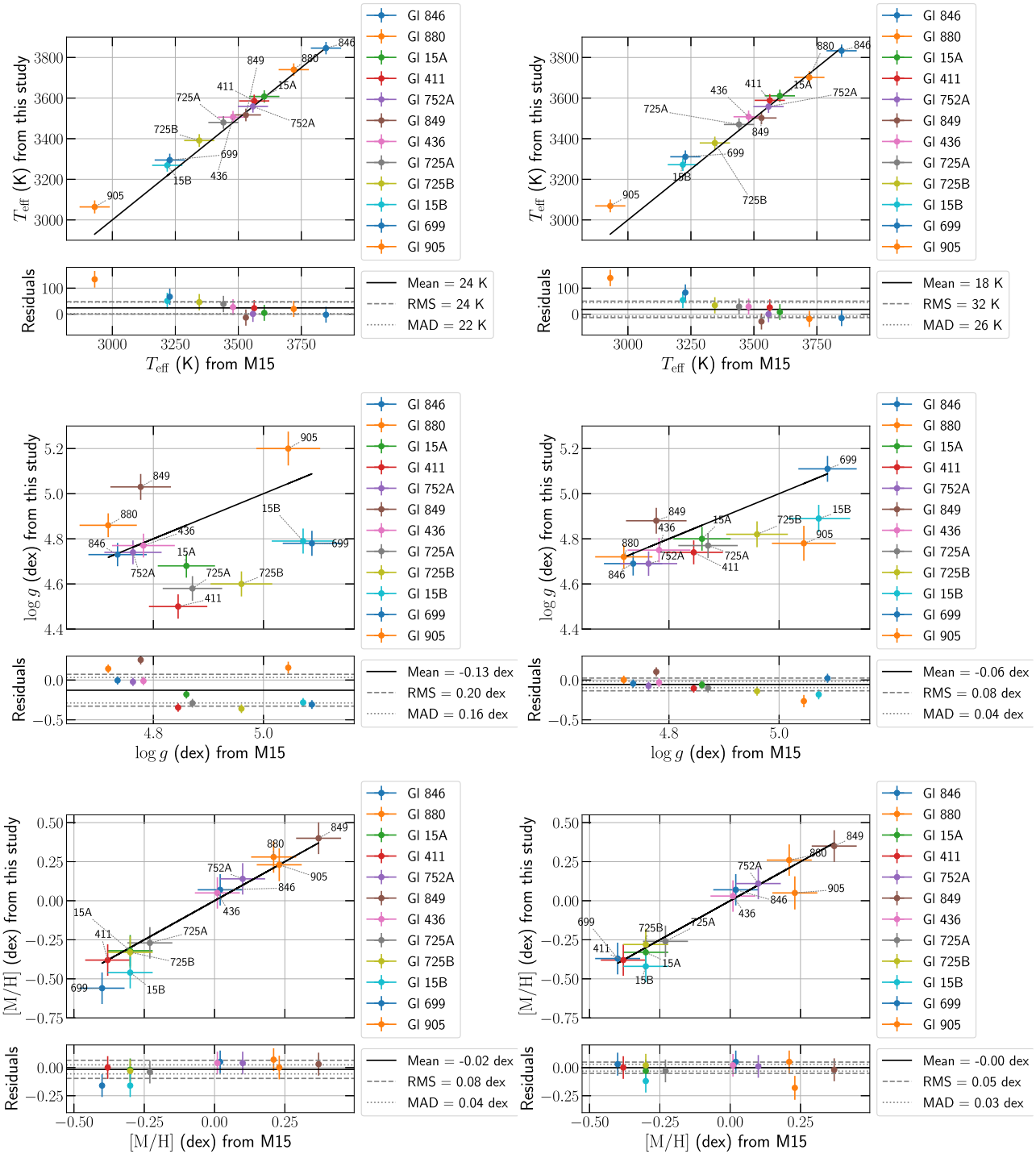

Figure B3. Same as Fig. B1 but comparing the results obtained with [α/Fe] = 0 dex (left-hand panels) and while fitting [α/Fe] (right-hand panels). These results are obtained with corrections of the line list described in Section 5.

APPENDIX C: BEST FITS ON ALL SPECTRAL LINES

Fig. C1 available as supplementary material presents the best fits obtained for five stars in our sample.

APPENDIX D: LITERATURE PARAMETERS COMPARISON

We present comparisons of parameters recovered by several studies. Figs D1 and D2 present the results for 32 and 35 stars studied by Passegger et al. (2019) and Marfil et al. (2021), respectively.

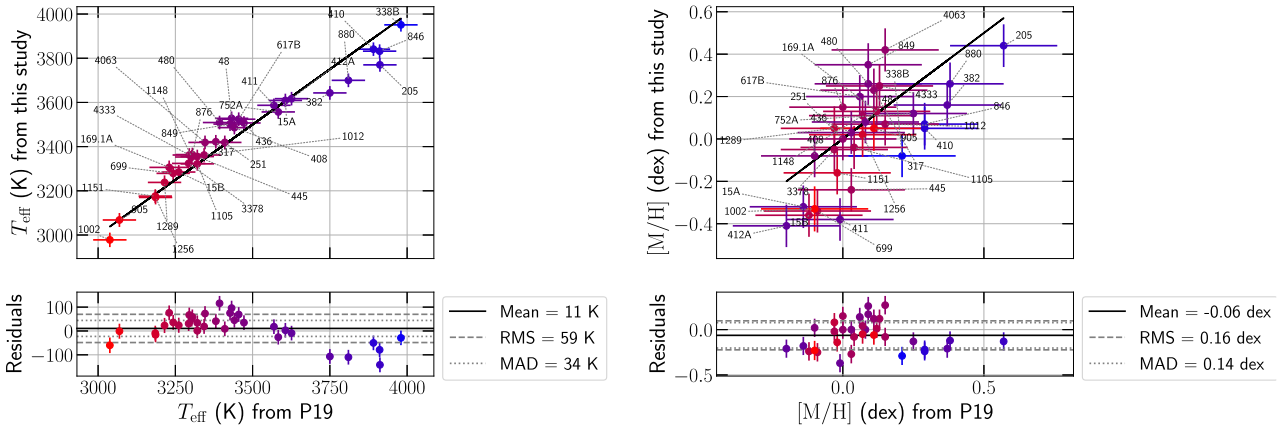

Figure D1. Comparison between retrieved parameters of 32 stars and the values published by Passegger et al. (2019).

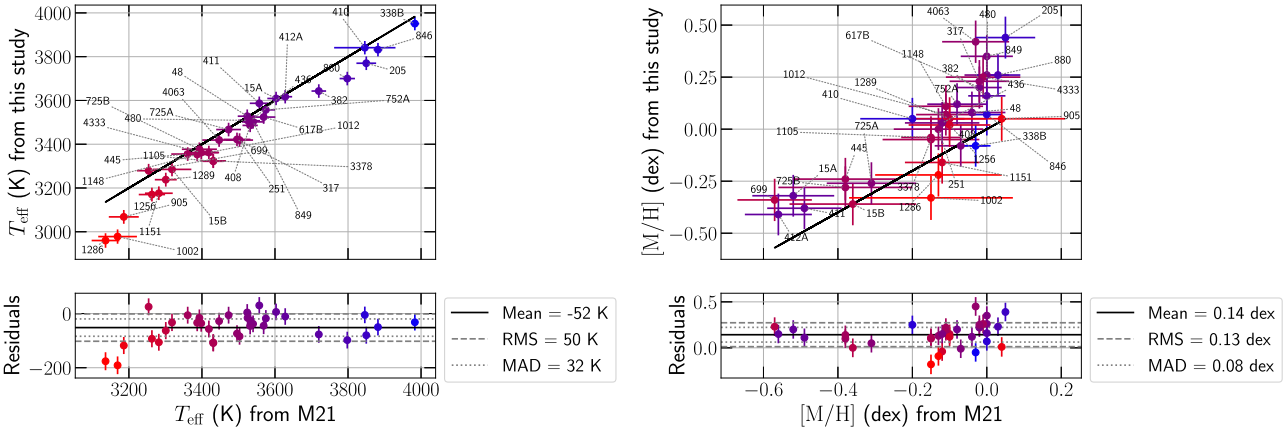

Figure D2. Same as Fig. D1 for 35 stars and values published by Marfil et al. (2021).

APPENDIX E: ESTIMATION OF LUMINOSITY

Fig. E1 presents a comparison between the luminosities estimated from *G* and *J*-band magnitudes using bolometric corrections (Cifuentes et al. 2020) and these reported by Cifuentes et al. (2020).

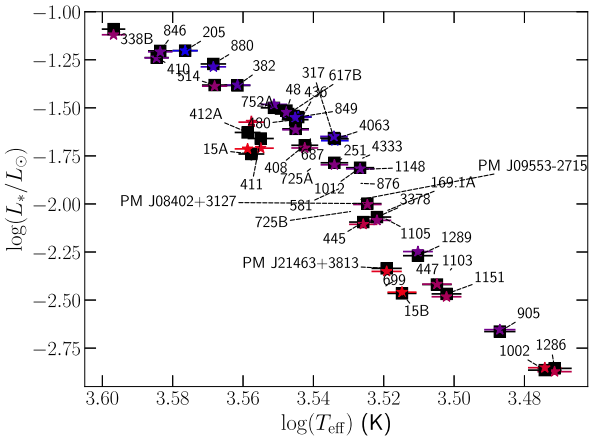

Figure E1. Comparison between the luminosities computed from bolometric corrections using the relation proposed by Cifuentes et al. (2020) (black squares), and those reported by Cifuentes et al. (2020) (coloured symbols) for 33 stars included in our sample. One should note that the $T_{\rm eff}$ values used by the authors to estimate the luminosities may differ from those estimated in this work. The symbol colours display the metallicity from low (red) to high (blue).

APPENDIX F: MASS–RADIUS RELATION

Fig. F1 presents a comparison between the masses and radii derived in this study and these reported by M15.

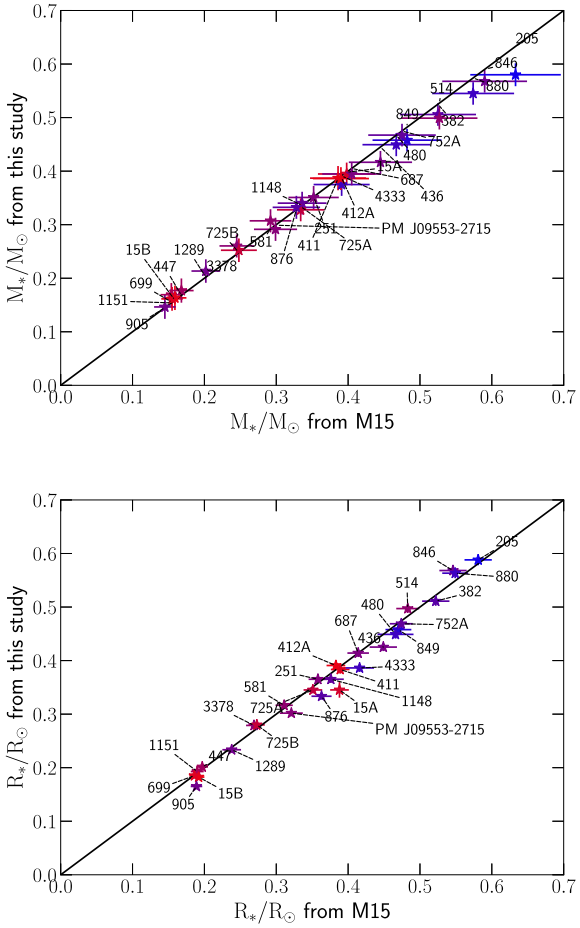

Figure F1. Comparison between our derived masses and radii and these reported by M15 for the 28 stars included in both studies (top and bottom panels, respectively). The black solid lines represent the equality.

This paper has been typeset from a TEX/LATEX file prepared by the author.

MNRAS 000, 1–12 (2015) Preprint 26 February 2023 Compiled using MNRAS LATEX style file v3.0

Constraining atmospheric parameters and surface magnetic fields with ZeeTurbo: an application to SPIRou spectra

P. I. Cristofari[1]★ J.-F. Donati[1], C. P. Folsom[2,3], T. Masseron[4], P. Fouqué[1,5], C. Moutou[1], E. Artigau[6], A. Carmona[7], P. Petit[1], X. Delfosse[7], E. Martioli[8,9], and the SLS consortium
[1]*Univ. de Toulouse, CNRS, IRAP, 14 av. Belin, 31400 Toulouse, France*
[2]*Tartu Observatory, University of Tartu, Observatooriumi 1, Tõravere, 61602 Tartumaa, Estonia*
[3]*University of Western Ontario, Department of Physics & Astronomy, London, ON, N6A 3K7, Canada*
[4]*Departamento de Astrofísica, Universidad de La Laguna, E-38206 La Laguna, Tenerife, Spain*
[5]*Canada–France–Hawaii Telescope, CNRS, Kamuela, HI 96743, USA*
[6]*Université de Montréal, Département de Physique, IREX, Montréal, QC, H3C 3J7, Canada*
[7]*Univ. Grenoble Alpes, CNRS, IPAG, 38000 Grenoble, France* [8]*Institut d'Astrophysique de Paris, CNRS, UMR 7095, Sorbonne Université, F-75014 Paris, France*
[9]*Laboratório National de Astrofísica, Itajubá, MG 37504-364, Brazil*

Accepted XXX. Received YYY; in original form ZZZ

ABSTRACT

We report first results on a method aimed at simultaneously characterising atmospheric parameters and magnetic properties of M dwarfs from high-resolution nIR spectra recorded with SPIRou in the framework of the SPIRou Legacy Survey. Our analysis relies on fitting synthetic spectra computed from `MARCS` model atmospheres to selected spectral lines, both sensitive and insensitive to magnetic fields. We introduce a new code, `ZeeTurbo`, obtained by including the Zeeman effect and polarised radiative transfer capabilities to `Turbospectrum`. We compute a grid of synthetic spectra with `ZeeTurbo` for different magnetic field strengths and develop a process to simultaneously constrain $T_{\rm eff}$, $\log g$, [M/H], [α/Fe] and the average surface magnetic flux. In this paper, we present our approach and assess its performance using simulations, before applying it to six targets observed in the context of the SPIRou Legacy Survey (SLS), namely AU Mic, EV Lac, AD Leo, CN Leo, PM J18482+0741, and DS Leo. Our method allows us to retrieve atmospheric parameters in good agreement with the literature, and simultaneously yields surface magnetic fluxes in the range 2–4 kG with a typical precision of 0.05 kG, in agreement with literature estimates, and consistent with the saturated dynamo regime in which most of these stars are.

Key words: techniques: spectroscopic – stars: fundamental parameters – stars: low-mass – infrared: stars – stars: magnetic fields

1 INTRODUCTION

M dwarfs are known to harbour magnetic fields (Saar & Linsky 1985; Johns-Krull & Valenti 1996; Shulyak et al. 2014; Kochukhov 2021) and thus trigger activity that can impact the detection and characterisation of the planets they may host (Hébrard et al. 2016; Dumusque et al. 2021; Bellotti et al. 2022). One direct consequence of magnetic fields in the stellar photosphere is the splitting of energy levels caused by the Zeeman effect, affecting the shape of spectral lines (Landi Degl'Innocenti & Landolfi 2004; Reiners & Basri 2007; Reiners 2012; Shulyak et al. 2014). Some authors have estimated the surface magnetic flux of cool stars by modelling synthetic spectra including magnetic fields, and fitting them to observed unpolarised near-infrared spectra, that are ideal for characterising the broadening impact of magnetic fields on spectral lines (Valenti et al. 1995; Johns-Krull et al. 2004; Shulyak et al. 2014; Lavail et al. 2017; Kochukhov & Reiners 2020; Reiners et al. 2022).

Several tools have been developed for the synthesis of magnetic stars spectra, such as COSSAM (Stift 1985; Stift & Leone 2003), INVERS (Piskunov & Kochukhov 2002), `Synmast` (Kochukhov 2007), `MOOGStokes` (Deen 2013) or `Zeeman` (Landstreet 1988; Wade et al. 2001; Folsom et al. 2016). The latter, in particular, computes spectra from `MARCS` model atmospheres but does not consider molecules in the computed chemical equilibrium, which limits its application for cool stars. Given that `Turbospectrum` (Alvarez & Plez 1998; Plez 2012) allowed us to obtain good constraints on the stellar parameters of M dwarfs (Cristofari et al. 2022b), we undertook to build a new tool, called `ZeeTurbo`, by merging `Turbospectrum` and `Zeeman`, allowing us to synthesise spectra of magnetic M dwarfs.

With this paper, we report first results with an updated version of our tools to characterise M dwarfs (Cristofari et al. 2022a,b) monitored with SPIRou (Donati et al. 2020). Our goal is to provide the community with reliable constraints on the atmospheric parameters of targets observed in the context of the SPIRou Legacy Survey (SLS, Donati et al. 2020) and its follow-up program called SPICE, respectively allocated 310 and 174 nights on the 3.6-m Canada-France-Hawaii Telescope (CFHT). In the present work, we focus on a few very active M dwarfs already known to host strong magnetic fields (AU Mic = Gl 803, AD Leo = Gl 388, EV Lac = Gl 873, CN Leo = Gl 406, and PM J18482+0741) thereby ideal targets for assessing the

★ E-mail: paul.cristofari@irap.omp.eu (IRAP)

capabilities of our new atmospheric characterisation tool, and on one moderately active star (DS Leo = Gl 410), in order to confirm that our tool also performs adequately for such stars. We use `ZeeTurbo` to compute synthetic spectra for different magnetic field strengths, in order to simultaneously constrain the atmospheric parameters and magnetic field strengths of our 6 targets.

In Sec 2 we describe the data used in this work, and introduce `ZeeTurbo` in Sec. 3. We then discuss a revised procedure inspired by our previous work (Cristofari et al. 2022b) and assess its performance through simulations in Sec. 4, before presenting applications to SPIRou spectra in Sec. 5. In Sec. 6, we discuss our results, and lay our conclusions and perspectives.

2 OBSERVATIONS AND REDUCTION

In this paper, we analyse SPIRou spectra (covering a domain of 0.95-2.5 μm at a resolving power of 70,000, Donati et al. 2020) of AU Mic, AD Leo, EV Lac, DS Leo, CN Leo, and PM J18482+0741 monitored in the context of the SLS. For these targets, spectra were acquired over 100 to 200 nights. Data were processed through the SPIRou reduction pipeline `APERO` (version 0.7.254, Cook et al. 2022). `APERO` provides a calibrated wavelength solution and blaze functions estimated from flat field exposure, used to correct observations. `APERO` also performs the correction of telluric lines.

Each spectral order is normalised with a third-degree polynomial fitted on continuum points. For each star, we correct all observed spectra for the barycentric Earth radial velocity (BERV), use a cubic interpolation to bin all spectra on a common wavelength grid, and take the median of the telluric corrected spectra in the barycentric reference frame. These median spectra are referred to as templates in the rest of the paper and provide reference stellar spectra of typical signal-to-noise ratio (SNR) per 2 km s^{-1} pixel in the H band reaching up to about 2000.

3 ZEETURBO, POLARISED RADIATIVE TRANSFER WITH TURBOSPECTRUM

`ZeeTurbo` was built directly from `Turbospectrum` and includes most of the its capabilities while solving the polarised radiative transfer equation with routines adapted or inspired from the `Zeeman` code.

3.1 General description and functionalities

The general scheme of `ZeeTurbo` is described in Fig. 1. For a given model atmosphere, the continuous opacities are computed by `Turbospectrum`. The stellar disk is divided into concentric rings, each divided into cells. For each disk element, we compute the local field strength, orientation with respect to the line-of-sight, and its projection on the line-of-sight. The computation of line opacities is also performed by `Turbospectrum`, but called for each σ and π Zeeman components, and adapted to support anomalous dispersion. The line list format used by `ZeeTurbo` is inspired by that of `Turbospectrum`, but also stores Landé factors for the lower and upper energy levels of each transition. For lines with no tabulated Landé factors, we compute the lower and upper Landé factors from the atomic structures assuming LS coupling. The solution of the polarised radiative transfer equation is carried out by a routine adapted from that of the `Zeeman` code, with the implementation of the quasi-analytic technique proposed by Martin & Wickramasinghe (1979) and discussed in Wade et al. (2001).

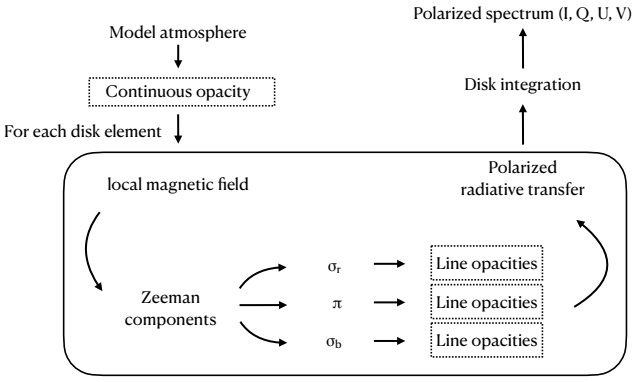

Figure 1. Schematic of the ZeeTurbo implementation.

`ZeeTurbo` was implemented on the latest published version of `Turbospectrum` (version 20, with NLTE capabilities, Gerber et al. 2022). Most modifications of the `Turbospectrum` code where kept in separate routines and files whenever possible. Consequently, the modification to the code mostly affects the bsyn.f file of the `Turbospectrum` source code. We implemented a trigger to bypass any added feature and use the original `Turbospectrum` functions only. Currently, `ZeeTurbo` does not support NLTE computations for line list formatting reasons, but minor modifications to the code will allow us to implement this capability in the future. For the time being, rotation, and macroturbulence are applied as post-processing steps by convolving the spectra with rotation or macroturbulence profiles (Gray 1975; Gray 2005). In this work, we focus on the analysis of Stokes I spectra, although `ZeeTurbo` is also able to compute Stokes Q, U and V spectra. The analysis of polarised spectra will be treated in subsequent studies.

3.2 Verification and validation

In order to ensure that the spectra synthesised with `ZeeTurbo` are reliable, we compared them to those computed with `Turbospectrum` and `Zeeman`. We find that `ZeeTurbo` and `Turbospectrum` produce similar spectra when no magnetic field is considered. The `Zeeman` and `Turbospectrum` codes, however, were found to produce significantly different outputs, both in the continuum levels and in the shape of spectral lines. These discrepancies are particularly obvious at temperatures lower than 3500 K. In order to ensure that `ZeeTurbo` produces Zeeman patterns in agreement with the `Zeeman` code, we synthesised spectra at higher temperatures (e.g. 6000 K, see Fig. 2) and compared the Zeeman patterns modelled by both codes. We found that the Zeeman patterns computed with `ZeeTurbo` are consistent with those computed with the `Zeeman` code. Several comparisons allowed us to validate that `ZeeTurbo` behaves as expected (see Fig. 2 for an example).

3.3 Computing a grid of synthetic spectra with ZeeTurbo

We computed a new grid of synthetic spectra with `ZeeTurbo` for the analysis of our 6 M dwarfs. The parameters covered by our grid are presented in Table 1. This grid was extended to cover lower temperatures than in our previous studies (Cristofari et al. 2022a,b) in order to analyse cooler targets. All models are computed assuming

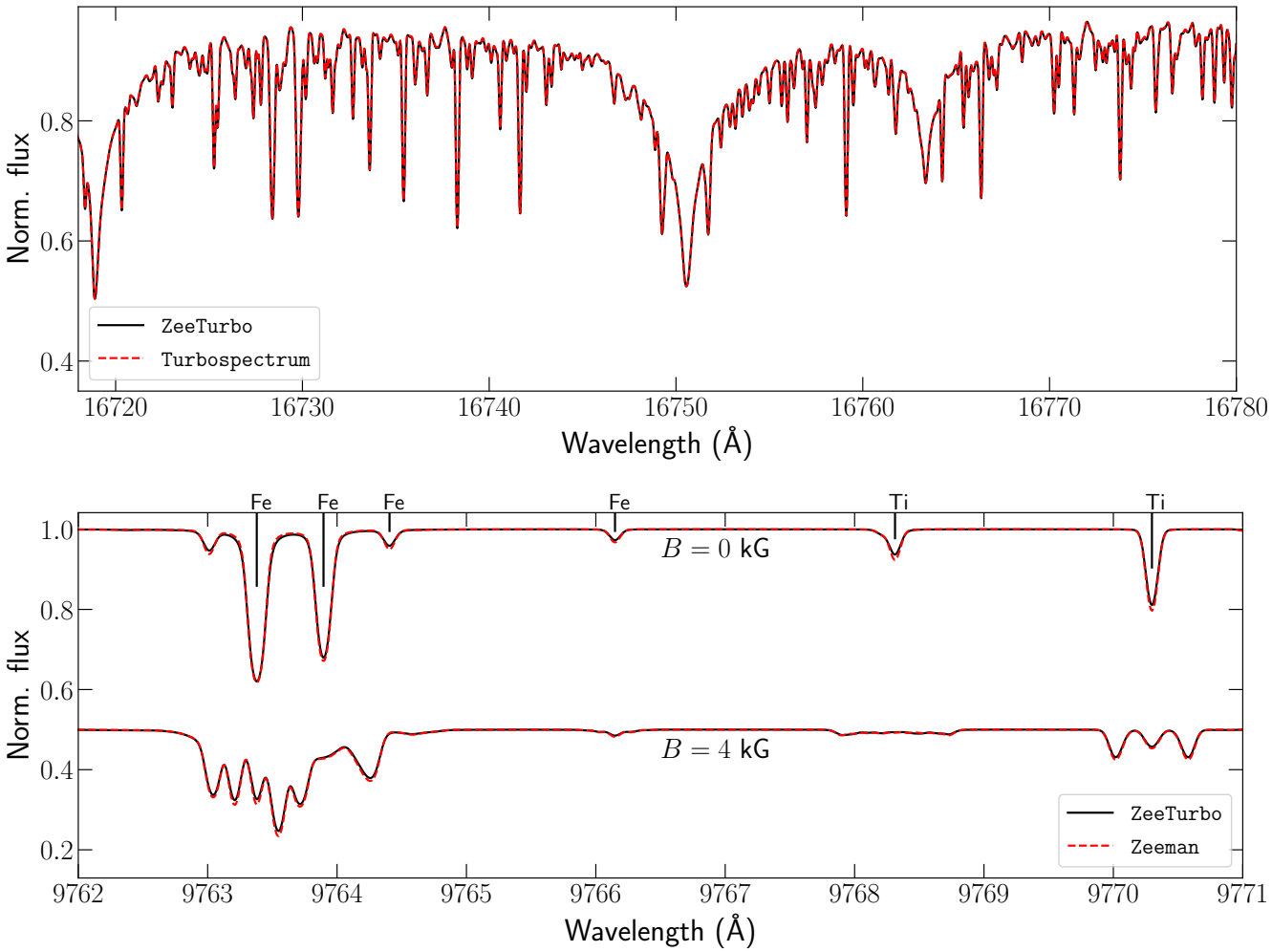

Figure 2. Top panel: comparison between spectra computed for a 0 kG field with `ZeeTurbo` and `Turbospectrum` for models with $T_{\rm eff}$ = 3500 K, $\log g$ = 5.0 dex, [M/H] = 0.0 dex, and [α/Fe] = 0.0 dex. Bottom panel: comparison between spectra computed with `ZeeTurbo` and `Zeeman` for $T_{\rm eff}$ = 6000 K, $\log g$ = 5.0 dex, [M/H] = 0.0 dex, and [α/Fe] = 0.0 dex. The spectra were computed assuming that the magnetic field is radial in all points of the photosphere.

Table 1. Coverage and step size of the computed grid of `ZeeTurbo` spectra.

$T_{\rm eff}$ (K)	2700 – 4000 (100)
$\log g$ (dex)	4.0 – 5.5 (0.5)
[M/H] (dex)	−1.0 – +1.0 (0.5)
[α/Fe] (dex)	−0.25 – +0.50 (0.25)
B (kG)	0 – 10 (2)

that the magnetic field is radial and of equal strength for all surface grid cells. Our coverage in $T_{\rm eff}$, $\log g$, [M/H], and [α/Fe] is expected to be sufficient for most stars observed in the context of the SLS, and the step and span in magnetic field strengths are inspired from previous studies (e.g., Kochukhov & Reiners 2020; Reiners et al. 2022).

4 CHARACTERISING M DWARFS WITH ZEETURBO

4.1 Modelling magnetic activity – filling factors

Following the results of previous studies (Shulyak et al. 2010, 2014; Kochukhov & Reiners 2020; Reiners et al. 2022), we choose to model the stellar spectra as a combination of spectra computed for various magnetic field strengths. This allows us to obtain better fits of the observed spectra by assuming a simple N-component model (with magnetic and non-magnetic regions at the surface of the star). Considering the spectrum S_X computed with a field of X kG, the modelled spectrum S is then

$$S = a_0 S_0 + a_2 S_2 + a_4 S_4 + a_6 S_6 + a_8 S_8 + a_{10} S_{10} \quad (1)$$

where a_X is the filling factor for the field of X kG, verifying that $a_0 + a_2 + a_4 + a_6 + a_8 + a_{10} = 1$ with all $a_X \geq 0$.

Modelling the spectrum then amounts to finding the filling factors that lead to the best fit to our observations.

4.2 Analysis

4.2.1 Constraining atmospheric parameters and magnetic fields

Our analysis is inspired by Cristofari et al. (2022a,b), searching for the model that provides the best fit to observations. However, unlike our previous studies, we now carry out a MCMC analysis, relying on

the emcee package[1] (Foreman-Mackey et al. 2013) to estimate the atmospheric parameters from posterior distributions. Prior to their comparison to observations, synthetic spectra are broadened to account for instrumental resolution, macroturbulence and rotation, and shifted to match the observed radial velocity. We then perform an adjustment of the continuum following the steps described in Cristofari et al. (2022b). Fixing both the instrumental width and either the macroturbulence or the rotation velocity to their known values, we end up with 11 parameters to be estimated with our MCMC process. Macroturbulent velocity and rotation are typically difficult to disentangle due to the similar effect they have on spectral lines (see e.g. Gray 2005; Valenti & Fischer 2005). In the present paper, we chose to set the value of $v \sin i$ and fit the macroturbulent velocity. We found that fixing macroturbulence and fitting the rotational velocity lead to very similar results in atmospheric parameters and magnetic field strengths.

Priors set on atmospheric parameters are meant to prevent walkers to run outside the boundaries of our grid. Priors are also set to ensure that the filling factors remain positive. To ensure that the sum of the filling factors is one, we compute $a_0 = 1 - (a_2 + a_4 + a_6 + a_8 + a_{10})$. For each walker, if one of the filling factors differs from 1, or if the atmospheric parameters fall out of the grid, we set the likelihood value to -infinity.

4.2.2 *Deriving error bars*

Error bars on atmospheric parameters and filling factors are estimated from posterior distributions. In practice, we find that the minimum reduced χ^2 ($\chi^2_{\rm r,min}$) derived from fitting the observed spectrum is larger than 1, because of systematic differences between the model and observations, which impacts the results of our MCMC analysis. In order to overcome the issue, we artificially expand the error bars on each pixel by $\sqrt{\chi^2_{\rm r,min}}$ before running our analysis, to ensure that the best fit corresponds to a unit $\chi^2_{\rm r}$. The factor used to expand the error bars is estimated after a preliminary run.

In our previous work (Cristofari et al. 2022a), formal error bars on atmospheric parameters were found to be smaller than the dispersion between parameters derived using different grids of synthetic spectra. Following Cristofari et al. (2022a,b) we chose to further enlarge these errors again by quadratically adding to our formal error bars 30 K for $T_{\rm eff}$, 0.05 dex for $\log g$, 0.10 dex for [M/H] and 0.04 dex in [α/Fe]. The resulting error bars are referred to as 'empirical error bars' in the rest of the paper.

4.3 Line list

For this analysis, we start from the same atomic and molecular line list used in Cristofari et al. (2022b), adding several Ti, K, and Mg lines included in previous studies (Kochukhov & Reiners 2020; Reiners et al. 2022), and shown to be useful for estimating magnetic fields. Atomic data, including Landé factors, were extracted from the VALD database (Piskunov et al. 1995; Kupka et al. 2000; Ryabchikova et al. 2015; Pakhomov et al. 2019). For a few Ti lines, corrections to the Van Der Waals parameters were applied following Cristofari et al. (2022b). Our line list also contains a number of OH and CO lines, assumed to be insensitive to magnetic fields. This assumption was supported by comparing the spectra of weakly and strongly magnetic targets, as well as by the results of previous studies (e.g. López-Valdivia et al. 2021). The lines used in the present analysis are listed in Table 2.

[1] https://emcee.readthedocs.io/en/stable/

Table 2. List of lines used for our analysis. The identification relied on wavelengths and depths extracted from the VALD database. Effective Landé factors are given for atomic lines. For each atomic line in the table, if two values of effective Landé factors are given, the first is that listed in the VALD database, and the second was computed assuming LS coupling. When effective Landé factors were missing from the VALD database, we display a single value computed assuming LS coupling.

Species	Wavelength (Å) [effective Landé factor]
Ti I	9678.20 [1.35 – 1.35], 9708.33 [1.26 – 1.25], 9721.63 [0.95 – 1.00], 9731.07 [1.00 – 1.00], 9746.28 [0.00 – 0.00], 9785.99 [1.48 – 1.50], 9786.27 [1.49 – 1.50], 9790.37 [1.50 – 1.50], 22217.28 [2.08 – 2.00], 22238.91 [1.66 – 1.67], 22280.09 [1.58 – 1.58], 22316.70 [2.50 – 2.50], 22969.60 [1.11 – 1.10],
Fe I	10343.72 [0.68 – 0.67],
Mg I	10968.42 [1.33], 15044.36 [1.75], 15051.83 [2.00],
K I	12435.67 [1.33], 12525.56 [1.17], 15167.21 [1.07 – 1.07],
Mn I	12979.46 [1.21 – 1.21],
Al I	13127.00 [1.17], 16723.52 [0.83], 16755.14 [1.10],
Na I	22062.42 [1.17], 22089.69 [1.33],
OH	16073.91, 16539.10, 16708.92, 16712.08, 16753.83, 16756.30, 16907.35, 16908.89, 16910.25,
CO	22935.23, 22935.29, 22935.58, 22935.75, 22936.34, 22936.63, 22937.51, 22937.90, 22939.09, 22939.58, 22941.09, 22943.49, 22944.16, 22946.31, 22947.06, 22949.54, 22950.36, 22953.19, 22954.06, 22957.26, 22958.16, 22961.74, 22962.67, 22966.65, 22967.58, 22971.97, 22972.88, 22977.72, 22978.60, 22983.89, 22984.71, 22990.49

4.4 Benchmarking `ZeeTurbo`

4.4.1 *Building model templates*

We ran a benchmark, to ensure that our new tool is indeed capable of constraining atmospheric parameters and filling factors. To this end, we generated a set of model template spectra as follows. From a set of atmospheric parameters and filling factors, we computed a synthetic spectrum. We then broadened this spectrum with a Gaussian profile of full width at half maximum (FWHM) 4.3 km s^{-1} to account for the instrumental width of SPIRou, and optionally applied convolution with rotation and/or macroturbulence profiles. The spectrum was then convolved with a 2 km s^{-1}-wide rectangular function representing pixels, and re-sampled on a typical SPIRou wavelength solution. Noise was added to the spectrum, accounting for the typical SPIRou throughput (Donati et al. 2020) and the typical blaze function for a SPIRou observation. The modelled spectrum, therefore, resembles template spectra in that the noise varies throughout each order, and from order to order.

4.4.2 *Simulating the estimation of the atmospheric parameters and filling factors.*

We performed our analysis on 50 modelled templates computed for the same atmospheric parameters and filling factors but different noise realisations with the process described in Sec. 4.2. The modelled templates were computed assuming an SNR in the H band of ~500, $T_{\rm eff}$ = 3400 K, $\log g$ = 5.0 dex, [M/H] = 0.0 dex and

[α/Fe] = 0.0 dex. We set the filling factors of the models to a_0=0.10, a_2=0.50, a_4=0.25, a_6=0.05, a_8=0.10 and a_{10} = 0.00 (yielding an average magnetic field strength $< B >$= 3.1 kG), thus adopting values consistent with typically observed targets (see Sec. 5). We simultaneously constrained atmospheric parameters and filling factors and analysed posterior distributions to find out potential correlations and estimate uncertainties. Figure 3 presents the results of our benchmark. We find that the dispersion on the series of 50 points is not fully consistent with our formal error bars, especially for the atmospheric parameters $T_{\rm eff}$, log g, [M/H] and [α/Fe], the reduced χ^2 ($\chi^2_{\rm r}$) on the residuals (the retrieved parameters minus the median) reaching up to 3.2. Subsequent tests showed that most of this excess dispersion can be attributed to the continuum adjustment step. We also find that the effect of the continuum adjustment is sensitive to the SNR, and can introduce systematic offsets in the retrieved atmospheric parameters of up to 0.01 dex in log g or [M/H] and up to 0.5 K in $T_{\rm eff}$ with a SNR ~500. These shifts reach up to 20 K in $T_{\rm eff}$ and 0.1 dex in log g, [M/H] and [α/Fe] if we assume a SNR ~100. In practice, the SPIRou templates usually reach an SNR in the H band of ~2000, implying that our results should not be affected by such biases.

With our benchmark, we explored the impact of magnetic fields on the estimation of atmospheric parameters. We generated templates for magnetic stars, and ran our analysis with non-magnetic models. The recovered atmospheric parameters deviate from the input parameters by up to 30 K in $T_{\rm eff}$ and 0.3 dex log g (see Fig. 4) for this particular magnetic configuration. Smaller biases (< 0.1 dex) are found on [M/H] and [α/Fe]. These systematic shifts can be ~10 times larger than our formal error bars for large values of the magnetic flux.

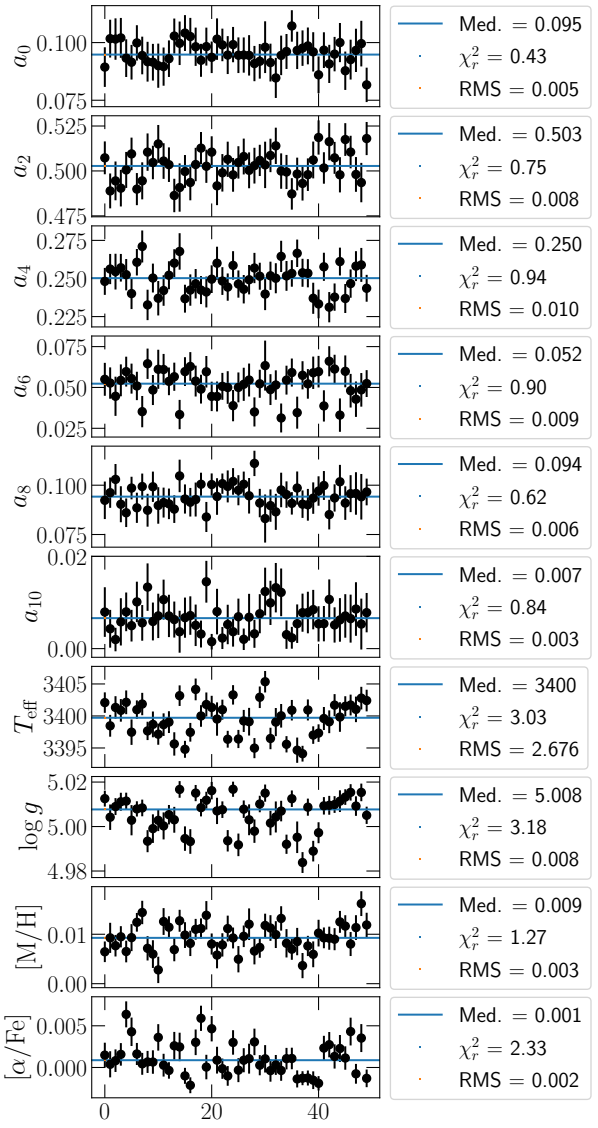

Figure 3. Example of comparison between input and output parameters. The blue horizontal solid line marks the median. For each parameter, we compute the χ^2 of the series of points. The models were computed for $T_{\rm eff}$ = 3400 K, log g = 5.0 dex, [M/H] = 0.00 dex and [α/Fe] = 0.00 dex.

5 APPLICATION TO SPIROU SPECTRA

We applied our new tool to our template SPIRou spectra of AU Mic, AD Leo, EV Lac, DS Leo, CN Leo and PM J18482+0741, relying on models computed for magnetic fields ranging from 0 to 10 kG in steps of 2 kG.

For the coolest targets in our sample (CN Leo and PM J18482+0741), we found discrepancies between the best-fitted model and the SPIRou template for some lines, such as the Ti line at 9678 Å (see Fig. 5). We worked out that the presence of spurious TiO lines in the synthetic spectra were responsible for some of these discrepancies, and that removing this molecule from the spectral synthesis improved the fit quality for the coolest stars in our sample. The results presented in this section were obtained with synthetic spectra computed without TiO, after checking that very similar results (and worse fits) were obtained when keeping TiO in.

The case of AU Mic = Gl 803

The young planetary system AU Mic attracted significant attention in the recent years (Boccaletti et al. 2018; Kochukhov & Reiners 2020; Martioli et al. 2020, 2021; Klein et al. 2021, 2022) and has been monitored by several instruments. The rotation period of this star is $P_{\rm rot}$ = 4.863 ± 0.010 d (Plavchan et al. 2020; Klein et al. 2021) with an angle between the line of sight and the rotation axis close to 90°, and its radius was estimated from interferometric measurements to 0.862 ± 0.052 $R_\odot$ (Gallenne et al. 2022). For this star, we adopt a $v \sin i$ = 8.5 ± 1.0 km s^{-1} (Donati et al., in prep), yielding a radius of 0.82 $R_\odot$. With a mass estimated at 0.60 ± 0.03 $M_\odot$ (Donati et al., in prep), the logarithmic surface gravity of AU Mic is then equal to log g = 4.39 dex.

We performed an analysis of AU Mic fitting $\zeta_{\rm RT}$ and fixing $v \sin i$ = 8.5 km s^{-1} (see Table 4). Figure 6 presents a corner plot with all fitted parameters. We find some correlations between a_2 and a_4, and between a_4 and a_6. Similar correlations were also reported in previous studies (Kochukhov & Reiners 2020; Reiners et al. 2022). From posterior distributions, we estimate a $T_{\rm eff}$ = 3677 ± 31 K, log g = 4.54 ± 0.05 dex, [M/H] = 0.12 ± 0.10 dex and [α/Fe] = 0.00 ± 0.04 dex. These estimates are listed Table 4. The temperature is consistent with that estimated from SEDs (Afram & Berdyugina 2019). Our log g is significantly larger than that estimated from mass and radius. We attempted to perform the analysis by fixing the value of log g to 4.40 dex. In that case, we retrieve a $T_{\rm eff}$ = 3648 ± 31 K and [M/H] = 0.09 ± 0.10 dex, and $\zeta_{\rm RT}$ = 5.3 ± 0.2 km s^{-1}, still consistent with literature values.

The derived filling factors amount to an average field strength $< B >$= 2.63 ± 0.05 kG (see Fig. 8), which compares well to values

Table 3. Literature parameters for the stars in our sample. For all stars but AU Mic, masses were obtained from the mass-K band magnitude proposed by Mann et al. (2019), and radii were computed from the mass with the models of Baraffe et al. (2015) assuming an age of 5 Gyr for all stars but AU Mic. K band magnitudes were extracted from the SIMBAD database (Wenger et al. 2000). For each star, we report $v \sin i$ estimates from the literature, or our adopted values if rotation period and radius estimates suggested that the literature $v \sin i$ was overestimated. The convective turnover time (τ) is taken from Reiners et al. (2022). The Rossby number (R_O) is computed from the rotation period (P_{rot}) and τ. Ref. – *a*: Plavchan et al. (2020), *b*: Donati et al., (in prep), *c*: Gallenne et al. (2022), *d*: Morin et al. (2008), *e*: Díez Alonso et al. (2019a), *f*: Donati et al. (2008) *g*: Reiners et al. (2018) *h*: Reiners & Basri (2007) .

Star	GJ ID	Spectral type	P_{rot} (d)	M ($M_\odot$)	R ($R_\odot$)	$v \sin i$ (km s^{-1})	τ (d)	R_O
AU Mic	Gl 803	M1V	4.863 ± 0.010^a	0.60 ± 0.03^b	0.82 ± 0.05^b	8.5 ± 1.0^b	39	0.125
EV Lac	Gl 873	M4.0V	4.3715 ± 0.0006^d	0.32 ± 0.02	0.31 ± 0.02	3 ± 1	110	0.040
AD Leo	Gl 388	M3V	2.2399 ± 0.0006^d	0.42 ± 0.02	0.39 ± 0.02	3 ± 1^d	80	0.028
CN Leo	Gl 406	M6V	2.704 ± 0.003^e	0.11 ± 0.02	0.13 ± 0.02	2 ± 1	387	0.007
PM J18482+0741	–	M5.0V	2.76 ± 0.01^e	0.14 ± 0.02	0.17 ± 0.02	2.4 ± 1.5^g	230	0.012
DS Leo	Gl 410	M1.0V	14.0 ± 0.1^f	0.57 ± 0.02	0.53 ± 0.02	1.5 ± 1.0	60	0.233

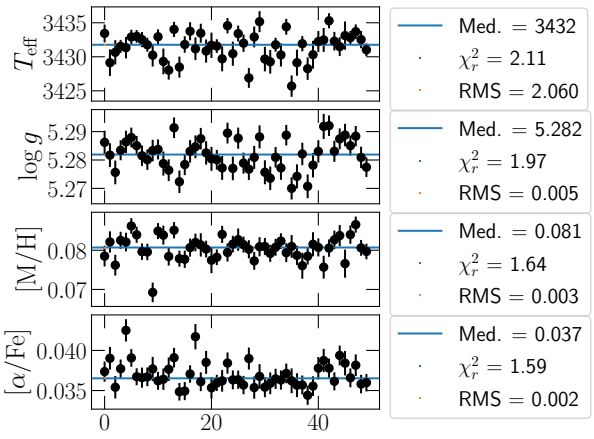

Figure 4. Same as Fig. 3 but with no magnetic field considered for the analysis.

reported in the literature of, for example, 2.1–2.3 kG (Kochukhov & Reiners 2020) and 3.01 ± 0.22 kG (Reiners et al. 2022). When fixing $\log g$ to 4.40 dex, the average field strength rises up to $< B >= 2.74 \pm 0.05$ kG, still consistent with the values reported in the literature.

We repeated our analysis assuming a Gaussian macroturbulence. With this kernel, we recovered $T_{\rm eff}$, $\log g$, [M/H], [α/Fe] and $< B >$ very close to those assuming a radial-tangential macroturbulence profile (see Table 4). The strong constraint derived for $< B >$ can be explained by the dependence of line shapes on the magnetic field, as illustrated in Fig. 7 and Fig. B1 (available as supplementary material). We note that the filling factors a_2 and a_4 associated with the 2 and 4 kG components account for most of the surface field of AU Mic (see Fig. 8). To diagnose the influence of the higher-field components on the results, we performed a second analysis, omitting the 8 and 10 kG models. We find no change in the atmospheric parameters, and that the average magnetic field is lowered by a negligible amount, with a difference of 0.01 kG on $< B >$, thus confirming that keeping the 8 and 10 kG components do not generate additional errors when characterizing the surface magnetic field of AU Mic.

The case of AD Leo = Gl 388

We performed a similar analysis on AD Leo (Gl 388). This star was included in the sample of previous studies studies (Morin et al. 2008; Reiners et al. 2022), and its projected rotational velocity was estimated to $v \sin i = 3 \pm 1$ km s^{-1} (Morin et al. 2008). The mass and radius of this star were estimated from the mass-K band magnitude relation of (Mann et al. 2019) and the models of (Baraffe et al. 2015) (see Table 3). These yield a $\log g \sim 4.88 \pm 0.05$ dex. The rotation period of AD Leo is $P_{\rm rot} = 2.2399 \pm 0.0006$ d (Morin et al. 2008, see Table 3).

We chose to fix the value of $v \sin i$ and fit a radial-tangential macroturbulence in this analysis. With these constraints, we derive an average magnetic field of 3.03 ± 0.06 kG, consistent with some previous estimates, e.g. 2.9 ± 0.2 kG (Reiners & Basri 2007) and 3.57 ± 0.09 kG (Reiners et al. 2022). Just like for AU Mic, we find the largest filling factors for the 2 and 4 kG components for this star. The retrieved atmospheric parameters, i.e. $T_{\rm eff} = 3467 \pm 31$, $\log g = 4.90 \pm 0.05$, [M/H] = 0.24 ± 0.10 and [α/Fe] = 0.00 ± 0.04 compare well with previous estimates (Mann et al. 2015), with the exception of a few recent studies suggesting that this star may be metal-poor (Marfil et al. 2021). Our $\log g$ is in good agreement with the mass and radius estimates.

With $v \sin i = 3$ km s^{-1}, we retrieve a radial-tangential macroturbulence $\zeta_{\rm RT} = 1.7 \pm 0.2$ km s^{-1}. We repeat the analysis, this time with a Gaussian macroturbulence, and retrieve a FWHM of $\zeta_{\rm G} = 2.0 \pm 0.2$ km s^{-1}. We find that changing the macroturbulence model has a negligible impact on the derived atmospheric parameters and filling factors (see Table 4).

The case of EV Lac = Gl 873

EV Lac (Gl 873) is another very well-known magnetic M dwarf observed in the context of the SLS, with a rotation period of $P_{\rm rot} = 4.3715 \pm 0.0006$ d (Morin et al. 2008). We estimated its mass and radius to $M = 0.32 \pm 0.02$ M$_\odot$ and $R = 0.31 \pm 0.02$ R$_\odot$ (see Table 3), thus implying $\log g = 4.96 \pm 0.06$ dex. The projected rotational velocity of this star was estimated to about 4 ± 1 km s^{-1} (Morin et al. 2008). The radius and rotation period of this star would suggest that this value is slightly over-estimated, and we therefore choose to fix its value to $v \sin i = 3$ km s^{-1}.

We fixed $v \sin i$, and fitted the radial-tangential macroturbulent velocity $\zeta_{\rm RT}$. For this star we derive $T_{\rm eff} = 3340 \pm 31$ K, $\log g = 4.87 \pm 0.05$ dex, [M/H] = 0.04 ± 0.10 dex and [α/Fe] = 0.01 ± 0.04 dex. These atmospheric parameters are in good agreement with those reported by previous studies (Maldonado et al. 2020). Our $\log g$ estimate is also in good agreement with the estimated mass and radius for this star. We compute an average magnetic field of $< B >= 4.53 \pm 0.07$ kG, consistent with estimates reported in the literature, of 3.8 ± 0.5 kG (Johns-Krull & Valenti 2000) or 4.32 ± 0.11 kG (Reiners et al. 2022). For this star, we note that the filling factors associated to the 6, 8 and 10 kG components

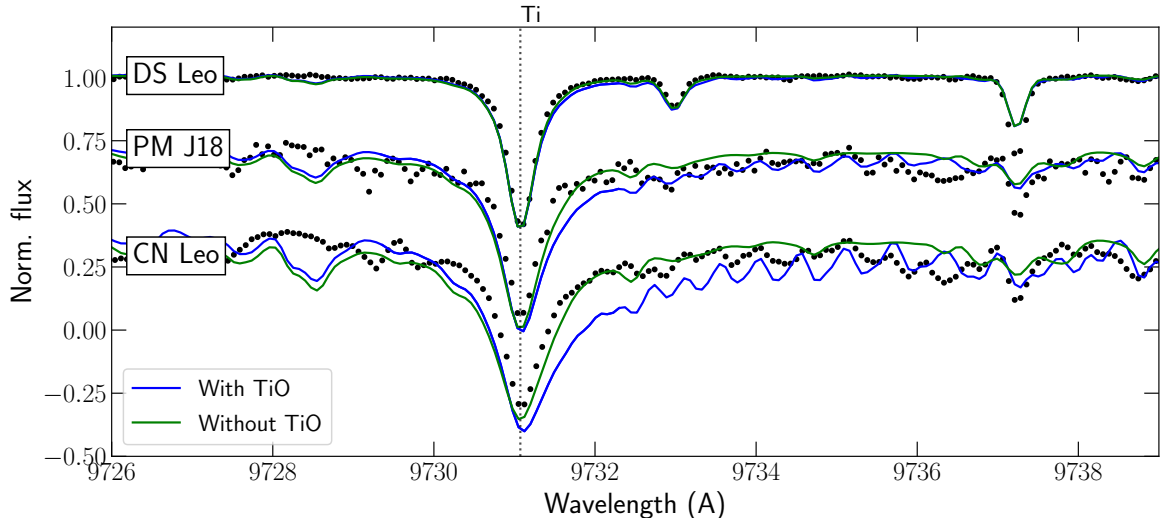

Figure 5. Best obtained fit with synthetic spectra computed with and without TiO for the two coolest stars in our sample (CN Leo and PM J18482+0741) and DS Leo. The black points show the SPIRou templates.

The label of PM J18482+0741 was abbreviated PM J18 for better readability.

are not close to 0, but rather account for 30 % of the total magnetic flux (see Fig. A1).

We retrieved a macroturbulent velocity $\zeta_{RT} = 4.2 \pm 0.2$ km s^{-1}. We repeat the analysis, this time fitting a Gaussian macroturbulence model, and retrieve a FWHM of $\zeta_G = 4.6 \pm 0.3$ km s^{-1}. We further checked that changing the adopted value of $v \sin i$ by 1 km s^{-1} had negligible impact on the retrieved atmospheric parameters and magnetic field strength. Here again, the choice of model for the macroturbulence profile has negligible impact on the derived atmospheric parameters and magnetic field strength (see Table 4).

The case of CN Leo = Gl 406

We then performed our analysis on the SPIRou template of CN Leo (Gl 406), an active late-type M dwarf. The rotation period of this star is $P_{rot} = 2.704 \pm 0.003$ d (Díez Alonso et al. 2019a), and we estimate its mass and radius to $M = 0.11 \pm 0.02$ M$_\odot$ and $R = 0.13 \pm 0.02$ R$_\odot$ (see Table 3). The projected rotational velocity of CN Leo was previously estimated to $v \sin i = 3 \pm 1$ km s^{-1} (Reiners & Basri 2007). Given the rotation period and radius for this star, we find that $v \sin i = 3$ km s^{-1} is likely overestimated, and we chose to fix its value to $v \sin i = 2$ km s^{-1}.

We retrieve $T_{eff} = 2898 \pm 31$ K, in good agreement with previously reported estimates (Mann et al. 2015). Our estimate of $\log g = 4.82 \pm 0.08$ dex is significantly lower than that computed from mass and radius, of $\log g = 5.25 \pm 0.17$ dex. We derive [M/H] $= 0.17 \pm 0.12$ dex, consistent with previous estimates (Rojas-Ayala et al. 2012; Mann et al. 2015).

We recover an average magnetic field strength $< B >= 3.45 \pm 0.20$ kG, consistent with previously reported values ($< B >= 3.01 \pm 0.16$ kG, Reiners et al. 2022). Again, we find that fitting the data with a Gaussian macroturbulence profile yields almost identical parameters (see Table 4).

The case of PM J18482+0741

PM J18482+0741 is another cool M dwarf observed in the context of the SLS, with a projected rotational velocity estimated to $v \sin i = 2.4 \pm 1.5$ km s^{-1} (Reiners et al. 2018), and a mass and radius estimated to $M = 0.14 \pm 0.02$ M$_\odot$ & $R = 0.17 \pm 0.02$ R$_\odot$ (see Table 3), yielding $\log g = 5.12 \pm 0.13$ dex. The rotation period of this star was estimated by (Díez Alonso et al. 2019b) to 2.76 ± 0.01 d.

For this target, we retrieve $T_{eff} = 3078 \pm 32$ K, consistent with previously reported effective temperatures for this target (Gaidos et al. 2014; Passegger et al. 2019). Our recovered $\log g = 4.72 \pm 0.06$ is lower than that reported by (Passegger et al. 2019) and that implied by our radius and mass estimates. With our process, we retrieve an average magnetic field $< B >= 1.99 \pm 0.15$ kG, almost twice that of Reiners et al. (2022, $< B >= 1.19 \pm 0.23$ kG). We find that for this star too, fitting the data with a Gaussian instead of a radial-tangential macroturbulence profile has negligible impact on the results (see Table 4).

The case of DS Leo = Gl 410

Finally, we run our process on the moderately active DS Leo (Gl 410). The rotation period of this star, of $P_{rot} = 14 \pm 0.1$ d (Donati et al. 2008), is the largest in our sample. The mass and radius of DS Leo, estimated to $M = 0.57 \pm 0.02$ M$_\odot$ and $R = 0.53 \pm 0.02$ R$_\odot$ (see Table 3), implies a surface gravity of $\log g = 4.74 \pm 0.04$ dex. For this star, $v \sin i$ was estimated to 2 ± 1 km s^{-1} by Morin et al. (2008).

With a fixed value of $v \sin i$, we retrieved $T_{eff} = 3818 \pm 30$ K, $\log g = 4.79 \pm 0.05$ dex, [M/H] $= 0.01 \pm 0.10$ dex and $[\alpha/Fe] = 0.03 \pm 0.04$ dex (see Table 4). These values are in good agreement with previous estimates, including ours (Mann et al. 2015; Cristofari et al. 2022b). Our $\log g$ is also comparable to that implied by previous mass and radius estimates. We derive $< B >= 0.73 \pm 0.03$ kG, lower than that reported by Reiners et al. (2022), of $< B >= 1.04 \pm 0.06$ kG. For DS Leo, we find a_4, a_6 and a_8 to be close to 0. We repeat our analysis process, only using models computed for 0 and 2 kG, and find that removing the 4, 6, 8 and 10 kG

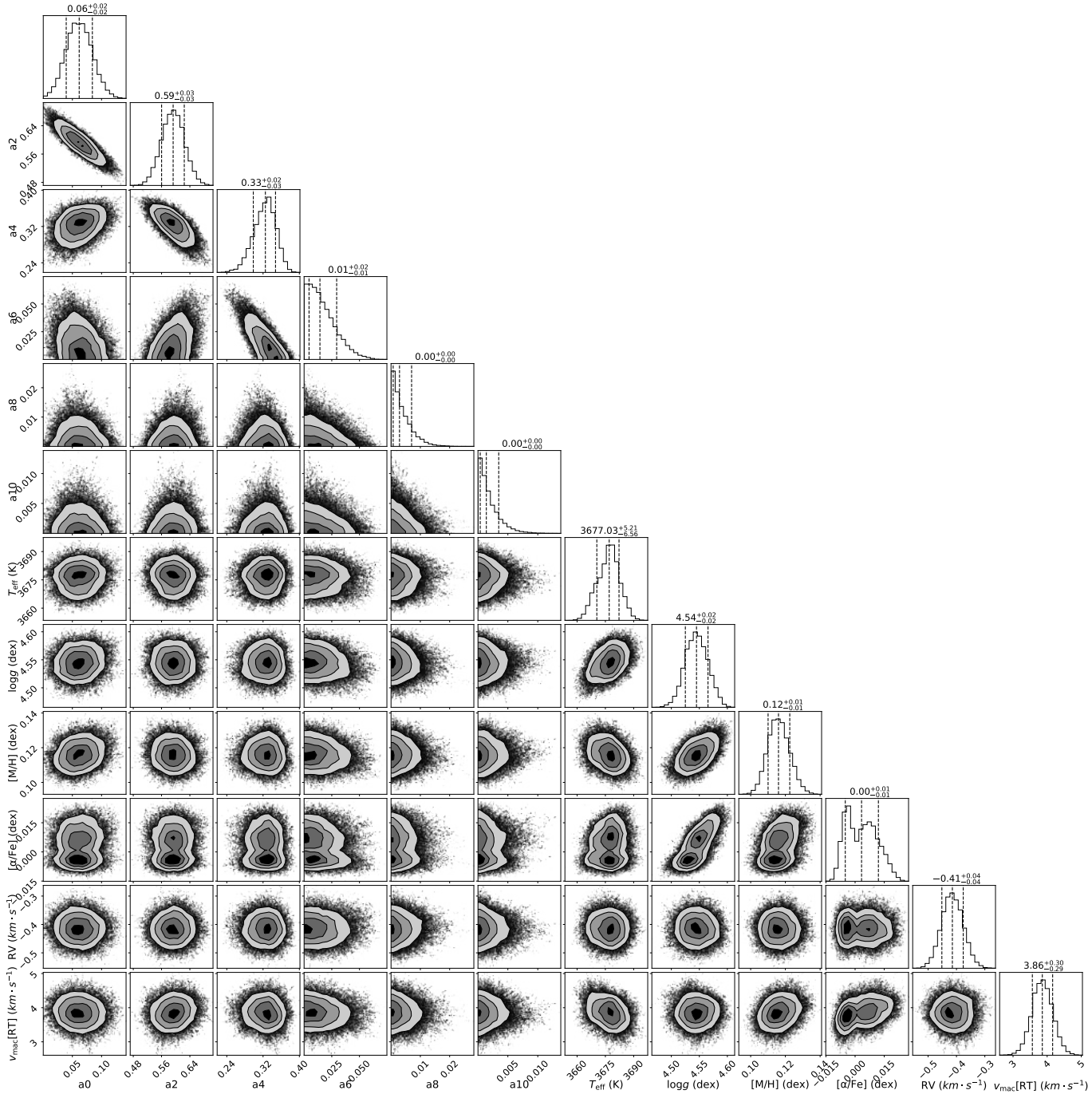

Figure 6. Corner plot presenting posterior distributions for filling factors and atmospheric parameters for AU Mic.

components has negligible impact on the estimation of atmospheric parameters and filling factors.

Comparison with the literature

Figure 9 presents a comparison between our retrieved $< B >$ estimates and those reported by Reiners et al. (2022). We find an overall good agreement between the two sets of values. $< B >$ is expected to evolve with time, which can at least partly account for some of the observed differences. Figure 10 presents the position of the stars in a $< B >$ vs Rossby number ($R_{\rm O}$) diagram. Most active M dwarfs included in our sample fall within the saturated dynamo regime, with the exception of DS Leo. These results are also in good agreement with those reported in Reiners et al. (2022). Comparisons between our retrieved $T_{\rm eff}$, $\log g$ and literature estimates are presented in Figs. C1 & C2.

6 DISCUSSION AND CONCLUSIONS

In this paper, we present our first results with our new tools aimed at characterising M dwarfs from SPIRou spectra. Our process relies on

Table 4. Retrieved stellar parameter and magnetic fields for our sample of targets. Values given with no associated uncertainties were fixed. For each star, multiple lines present the results obtained when fixing different parameters.

Star (GJ ID)	$T_{\rm eff}$	$\log g$	[M/H]	[α/Fe]	$v \sin i$	$\zeta_{\rm RT}$	$\zeta_{\rm G}$	$< B >$	f_0, f_2, f_4, f_6, f_8, f_{10}
AU Mic (Gl 803)	3677 ± 31	4.54 ± 0.05	0.12 ± 0.10	0.00 ± 0.04	8.5	3.9 ± 0.3	–	2.63 ± 0.05	0.07 ± 0.02, 0.59 ± 0.03, 0.32 ± 0.03,
									0.02 ± 0.01, 0.00 ± 0.00, 0.00 ± 0.00
AU Mic (Gl 803)	3678 ± 31	4.55 ± 0.05	0.12 ± 0.10	0.00 ± 0.04	8.5	–	4.4 ± 0.4	2.63 ± 0.05	0.06 ± 0.02, 0.59 ± 0.03, 0.32 ± 0.03,
									0.02 ± 0.01, 0.00 ± 0.00, 0.00 ± 0.00
AU Mic (Gl 803)	3648 ± 31	4.40	0.09 ± 0.10	−0.01 ± 0.04	8.5	5.3 ± 0.2	–	2.74 ± 0.05	0.04 ± 0.02, 0.61 ± 0.03, 0.31 ± 0.03,
									0.03 ± 0.01, 0.01 ± 0.00, 0.00 ± 0.00
AU Mic (Gl 803)	3650 ± 31	4.40	0.09 ± 0.10	−0.01 ± 0.04	8.5	–	6.2 ± 0.4	2.74 ± 0.05	0.05 ± 0.02, 0.60 ± 0.03, 0.31 ± 0.03,
									0.03 ± 0.01, 0.01 ± 0.00, 0.00 ± 0.00
EV LAC (Gl 873)	3340 ± 31	4.87 ± 0.05	0.04 ± 0.10	0.01 ± 0.04	3.0	4.2 ± 0.2	–	4.53 ± 0.07	0.02 ± 0.04, 0.29 ± 0.03, 0.38 ± 0.04,
									0.09 ± 0.04, 0.13 ± 0.04, 0.08 ± 0.02
EV LAC (Gl 873)	3342 ± 31	4.88 ± 0.05	0.03 ± 0.10	0.01 ± 0.04	3.0	–	4.6 ± 0.2	4.52 ± 0.07	0.02 ± 0.04, 0.29 ± 0.03, 0.39 ± 0.04,
									0.09 ± 0.05, 0.13 ± 0.04, 0.08 ± 0.02
AD Leo (Gl 388)	3467 ± 31	4.90 ± 0.05	0.24 ± 0.10	−0.00 ± 0.04	3.0	1.7 ± 0.2	–	3.03 ± 0.06	0.04 ± 0.02, 0.50 ± 0.03, 0.41 ± 0.03,
									0.04 ± 0.02, 0.01 ± 0.01, 0.00 ± 0.00
AD Leo (Gl 388)	3467 ± 31	4.89 ± 0.05	0.24 ± 0.10	−0.01 ± 0.04	3.0	–	2.0 ± 0.3	3.04 ± 0.06	0.03 ± 0.02, 0.50 ± 0.03, 0.41 ± 0.03,
									0.04 ± 0.02, 0.01 ± 0.01, 0.00 ± 0.00
CN Leo (Gl 406)	2898 ± 31	4.82 ± 0.08	0.17 ± 0.12	−0.04 ± 0.04	2.0	4.3 ± 0.3	–	3.45 ± 0.20	0.10 ± 0.07, 0.44 ± 0.11, 0.29 ± 0.10,
									0.07 ± 0.06, 0.07 ± 0.05, 0.03 ± 0.03
CN Leo (Gl 406)	2899 ± 31	4.82 ± 0.07	0.16 ± 0.11	−0.04 ± 0.04	2.0	–	4.8 ± 0.3	3.45 ± 0.19	0.10 ± 0.07, 0.44 ± 0.11, 0.29 ± 0.10,
									0.07 ± 0.06, 0.07 ± 0.05, 0.03 ± 0.03
DS Leo (Gl 410)	3818 ± 30	4.79 ± 0.05	0.01 ± 0.10	0.03 ± 0.04	1.5	2.7 ± 0.1	–	0.73 ± 0.03	0.65 ± 0.00, 0.34 ± 0.02, 0.00 ± 0.00,
									0.00 ± 0.00, 0.00 ± 0.00, 0.00 ± 0.00
DS Leo (Gl 410)	3818 ± 33	4.79 ± 0.06	0.01 ± 0.10	0.03 ± 0.04	1.5	–	3.0 ± 0.3	0.82 ± 0.10	0.66 ± 0.01, 0.32 ± 0.04, 0.01 ± 0.01,
									0.01 ± 0.01, 0.00 ± 0.00, 0.00 ± 0.00
PM J18482+0741	3078 ± 32	4.72 ± 0.06	−0.02 ± 0.10	−0.05 ± 0.04	2.4	4.8 ± 0.4	–	1.99 ± 0.16	0.23 ± 0.04, 0.65 ± 0.09, 0.08 ± 0.05,
									0.02 ± 0.02, 0.01 ± 0.01, 0.01 ± 0.01
PM J18482+0741	3081 ± 34	4.72 ± 0.08	−0.03 ± 0.11	−0.05 ± 0.04	2.4	–	5.2 ± 0.5	2.08 ± 0.24	0.25 ± 0.05, 0.63 ± 0.13, 0.07 ± 0.06,
									0.02 ± 0.02, 0.02 ± 0.02, 0.01 ± 0.01

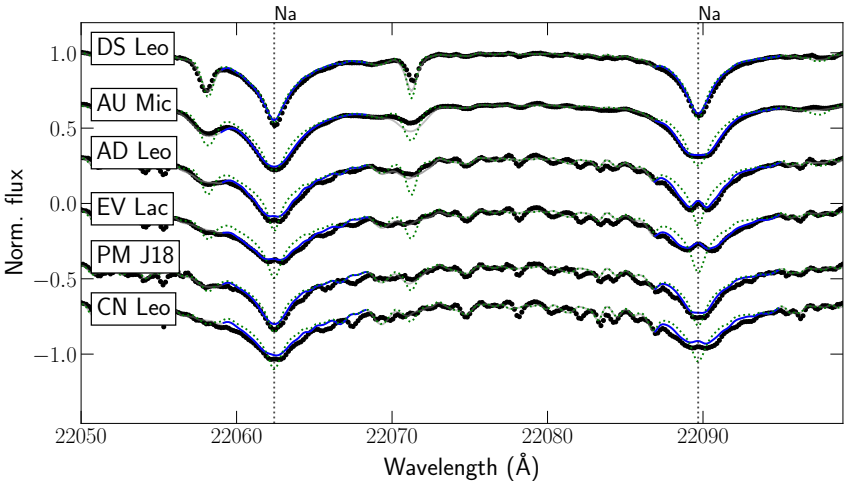

Figure 7. Best fit obtained for the seven stars included in our study with `ZeeTurbo` for two Na lines (22062.4 and 22089.7 Å). Black points present the data. The grey solid line shows the best fit, and the blue solid blue line presents the part of the windows used for the fit. The green dotted line shows the model obtained for the same atmospheric parameters but with a zero magnetic field. The name PM J18482+0741 was replaced by PM J18 for better readability.

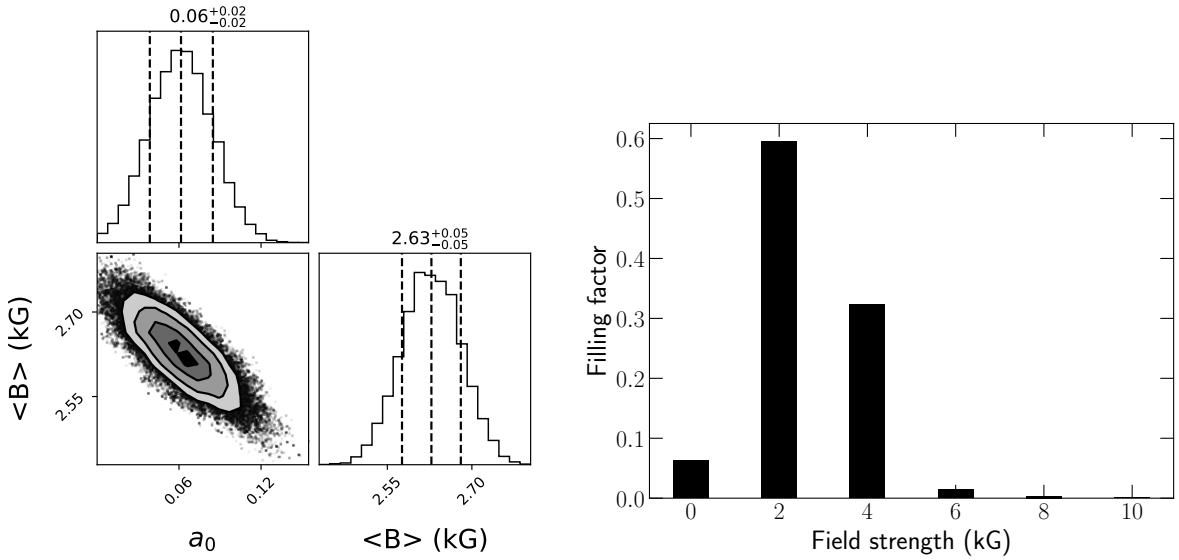

Figure 8. Left panel: non-magnetic component against average field strength for AU Mic. Right panel: distribution of the filling factors over magnetic field components for AU Mic.

the comparison of high-resolution synthetic spectra computed from state-of-the-art `MARCS` model atmospheres to data, and is used to constrain $T_{\rm eff}$, $\log g$, [M/H], [α/Fe] and the average magnetic field strengths for 4 targets observed in the context of the SLS.

We introduce a new code, `ZeeTurbo`, built from the `Turbospectrum` and `Zeeman` codes, allowing us to synthesise spectra of magnetic stars from `MARCS` model atmospheres. We compared the output spectra computed with `ZeeTurbo`, `Zeeman` and `Turbospectrum` and found that our new code allows us to properly synthesise spectra for magnetic M dwarfs. Our code also allowed us to synthesise molecular lines, assumed to be insensitive to magnetic fields in the present work. This assumption holds for the lines our analysis relies on, namely the few OH lines and the CO lines at 2.28 μm. Modelling molecular lines is particularly critical to the analysis of M dwarfs spectra since they are numerous and blend with atomic features.

With our newly implemented code, we computed a grid of synthetic spectra assuming a constant magnetic field, radial in all points of the photosphere. We modelled the spectra by a linear combination of profiles computed for different magnetic strengths, and fitted our model to SPIRou templates to constrain $T_{\rm eff}$, $\log g$, [M/H], [α/Fe], the filling factors and thereby the surface magnetic flux. Our analysis relies on a MCMC process, and the atmospheric parameters and filling factors are estimated from posterior distributions. We performed a benchmark, designed to assess the performances of our new tool, and found that it was capable of simultaneously constraining magnetic fields and atmospheric parameters. We then applied our tool to a few well-known magnetic stars observed in the context of the SLS (AU Mic, AD Leo, EV Lac, DS Leo, CN Leo and

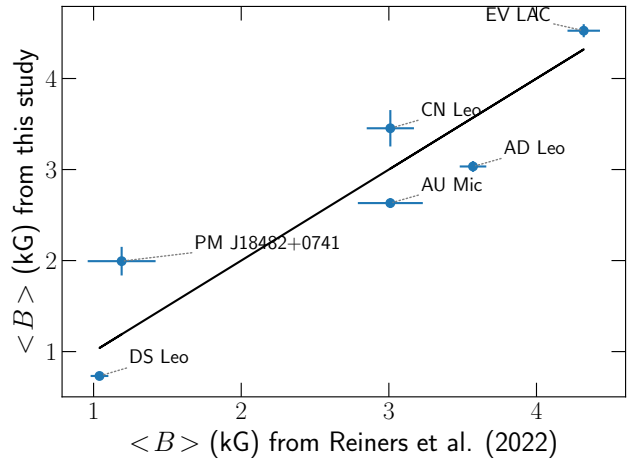

Figure 9. Comparison between our derived $< B >$ values and those of Reiners et al. (2022). The black line marks the equality

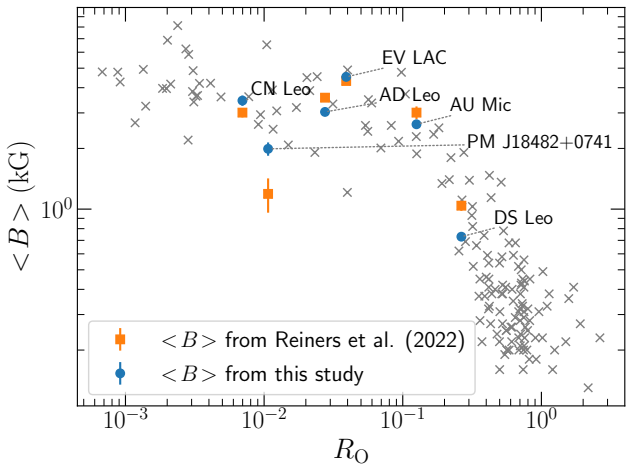

Figure 10. Comparison Rossby number (R_O) and $< B >$ values derived from our study (blue dots) and reported by Reiners et al. (2022, orange squares). The grey symbols mark the position of all the stars studied by Reiners et al. (2022).

PM J18482+0741). Our recovered atmospheric parameters and magnetic field estimates are found in good agreement with the literature for most stars. The largest discrepancies between our results and the literature are found for the two coolest stars in our sample (CN Leo and PM J18482+0741), with $\log g$ estimates significantly lower than those computed from masses and radii.

The average surface magnetic flux retrieved with our process for the six targets in our sample are in good agreement with previous estimates reported by Reiners et al. (2022, see Fig. 9). Our estimates are also consistent with most of our stars being in the saturated dynamo regime, with the exception of DS Leo, whose rotation period is significantly longer than that of the other stars. The differences in the values reported in the literature and those derived in this study may partly arise from the evolution of the surface magnetic flux with time.

We find that the way the surface magnetic flux is distributed across the magnetic field strengths differs from star to star. In particular, we find significantly larger contributions of the 6, 8 and 10 kG components for EV Lac of CN Leo, than for the other targets of our sample. For the quietest star in our sample, DS Leo, the best fit relies almost entirely on the 0 and 2 kG components. Moreover, the contribution of the 0 kG component also differs from star to star, and is not necessarily smallest for the most magnetic targets (e.g. the case of CN Leo, where $a_0 = 0.10$, see Fig. A4). These results illustrate the variety of magnetic topologies encountered in our sample, and the possibility to distinguish them using unpolarised spectra.

`ZeeTurbo` will allow us to analyse all stars observed in the context of the SLS in a self-consistent way. In particular, we will reprocess the M dwarfs included in our previous studies, to measure their surface magnetic fluxes and assess their impact on the atmospheric characterisation. We will also look for temporal evolution in the average magnetic flux of stars monitored over several years, in order to find new means of constraining rotation, activity cycles, and help disentangle activity jitters from radial velocity signals (Haywood et al. 2016; Suárez Mascareño et al. 2020, Donati et al., in prep). We will also expand our analysis to PMS stars, whose modelling may require to account for veiling and starspots, and whose characterisation is essential to the study of stars and planets formation (Flores et al. 2021; López-Valdivia et al. 2021).

ACKNOWLEDGEMENTS

This project received funding from the European Research Council (ERC) under the H2020 research and innovation programme (grant #740651, NewWorlds). TM acknowledges financial support from the Spanish Ministry of Science and Innovation (MICINN) through the Spanish State Research Agency, under the Severo Ochoa Program 2020-2023(CEX2019-000920-S) as well as support from the ACIISI, Consejería de Economía, Conocimiento y Empleo del Gobiernode Canarias and the European Regional Development Fund (ERDF) under grant with reference PROID2021010128

This work is based on observations obtained at the Canada–France–Hawaii Telescope (CFHT), operated by the National Research Council (NRC) of Canada, the Institut National des Sciences de l'Univers of the Centre National de la Recherche Scientifique (CNRS) of France, and the University of Hawaii. The observations at the CFHT were performed with care and respect from the summit of Maunakea, which is a significant cultural and historic site.

We acknowledge B. Plez for his implication in developing the freely available `Turbospectrum` code which allowed us to develop `ZeeTurbo`.

We acknowledge funding from the French ANR under contract number ANR18CE310019 (SPlaSH).

DATA AVAILABILITY

The data used in this work were recorded in the context of the SLS, and will be available to the public at the Canadian Astronomy Data Center one year after completion of the program.

REFERENCES

Afram N., Berdyugina S. V., 2019, A&A, 629, A83
Alvarez R., Plez B., 1998, A&A, 330, 1109
Baraffe I., Homeier D., Allard F., Chabrier G., 2015, A&A, 577, A42

Bellotti S., Petit P., Morin J., Hussain G. A. J., Folsom C. P., Carmona A., Delfosse X., Moutou C., 2022, A&A, 657, A107
Boccaletti A., et al., 2018, A&A, 614, A52
Cook N. J., et al., 2022, arXiv e-prints, p. arXiv:2211.01358
Cristofari P. I., et al., 2022a, MNRAS, 511, 1893
Cristofari P. I., et al., 2022b, MNRAS, 516, 3802
Deen C. P., 2013, AJ, 146, 51
Díez Alonso E., et al., 2019a, A&A, 621, A126
Díez Alonso E., et al., 2019b, A&A, 621, A126
Donati J. F., et al., 2008, MNRAS, 390, 545
Donati J. F., et al., 2020, MNRAS, 498, 5684
Dumusque X., et al., 2021, A&A, 648, A103
Flores C., Connelley M. S., Reipurth B., Duchêne G., 2021, arXiv e-prints, p. arXiv:2111.03957
Folsom C. P., et al., 2016, MNRAS, 457, 580
Foreman-Mackey D., Hogg D. W., Lang D., Goodman J., 2013, PASP, 125, 306
Gaidos E., et al., 2014, MNRAS, 443, 2561
Gallenne A., Desgrange C., Milli J., Sanchez-Bermudez J., Chauvin G., Kraus S., Girard J. H., Boccaletti A., 2022, arXiv e-prints, p. arXiv:2207.04116
Gerber J. M., Magg E., Plez B., Bergemann M., Heiter U., Olander T., Hoppe R., 2022, arXiv e-prints, p. arXiv:2206.00967
Gray D. F., 1975, ApJ, 202, 148
Gray D. F., 2005, The Observation and Analysis of Stellar Photospheres, 3 edn. Cambridge University Press, doi:10.1017/CBO9781316036570
Haywood R. D., et al., 2016, MNRAS, 457, 3637
Hébrard É. M., Donati J. F., Delfosse X., Morin J., Moutou C., Boisse I., 2016, MNRAS, 461, 1465
Johns-Krull C. M., Valenti J. A., 1996, ApJ, 459, L95
Johns-Krull C. M., Valenti J. A., 2000, in Pallavicini R., Micela G., Sciortino S., eds, Astronomical Society of the Pacific Conference Series Vol. 198, Stellar Clusters and Associations: Convection, Rotation, and Dynamos. p. 371
Johns-Krull C. M., Valenti J. A., Saar S. H., 2004, ApJ, 617, 1204
Klein B., et al., 2021, MNRAS, 502, 188
Klein B., et al., 2022, MNRAS, 512, 5067
Kochukhov O. P., 2007, in Romanyuk I. I., Kudryavtsev D. O., Neizvestnaya O. M., Shapoval V. M., eds, Physics of Magnetic Stars. pp 109–118 (arXiv:astro-ph/0701084)
Kochukhov O., 2021, A&ARv, 29, 1
Kochukhov O., Reiners A., 2020, ApJ, 902, 43
Kupka F. G., Ryabchikova T. A., Piskunov N. E., Stempels H. C., Weiss W. W., 2000, Baltic Astronomy, 9, 590
Landi Degl'Innocenti E., Landolfi M., 2004, Polarization in Spectral Lines. Vol. 307, doi:10.1007/978-1-4020-2415-3,
Landstreet J. D., 1988, ApJ, 326, 967
Lavail A., Kochukhov O., Hussain G. A. J., Alecian E., Herczeg G. J., Johns-Krull C., 2017, A&A, 608, A77
López-Valdivia R., et al., 2021, ApJ, 921, 53
Maldonado J., et al., 2020, A&A, 644, A68
Mann A. W., Feiden G. A., Gaidos E., Boyajian T., von Braun K., 2015, ApJ, 804, 64
Mann A. W., et al., 2019, ApJ, 871, 63
Marfil E., et al., 2021, arXiv e-prints, p. arXiv:2110.07329
Martin B., Wickramasinghe D. T., 1979, MNRAS, 189, 883
Martioli E., et al., 2020, A&A, 641, L1
Martioli E., Hébrard G., Correia A. C. M., Laskar J., Lecavelier des Etangs A., 2021, A&A, 649, A177
Morin J., et al., 2008, MNRAS, 390, 567
Pakhomov Y. V., Ryabchikova T. A., Piskunov N. E., 2019, Astronomy Reports, 63, 1010
Passegger V. M., et al., 2019, A&A, 627, A161
Piskunov N., Kochukhov O., 2002, A&A, 381, 736
Piskunov N. E., Kupka F., Ryabchikova T. A., Weiss W. W., Jeffery C. S., 1995, A&AS, 112, 525
Plavchan P., et al., 2020, Nature, 582, 497
Plez B., 2012, Turbospectrum: Code for spectral synthesis (ascl:1205.004)
Reiners A., 2012, Living Reviews in Solar Physics, 9, 1
Reiners A., Basri G., 2007, ApJ, 656, 1121
Reiners A., et al., 2018, A&A, 612, A49
Reiners A., et al., 2022, arXiv e-prints, p. arXiv:2204.00342
Rojas-Ayala B., Covey K. R., Muirhead P. S., Lloyd J. P., 2012, ApJ, 748, 93
Ryabchikova T., Piskunov N., Kurucz R. L., Stempels H. C., Heiter U., Pakhomov Y., Barklem P. S., 2015, Phys. Scr., 90, 054005
Saar S. H., Linsky J. L., 1985, ApJ, 299, L47
Shulyak D., Reiners A., Wende S., Kochukhov O., Piskunov N., Seifahrt A., 2010, A&A, 523, A37
Shulyak D., Reiners A., Seemann U., Kochukhov O., Piskunov N., 2014, A&A, 563, A35
Stift M. J., 1985, MNRAS, 217, 55
Stift M. J., Leone F., 2003, A&A, 398, 411
Suárez Mascareño A., et al., 2020, A&A, 639, A77
Valenti J. A., Fischer D. A., 2005, ApJS, 159, 141
Valenti J. A., Marcy G. W., Basri G., 1995, ApJ, 439, 939
Wade G. A., Bagnulo S., Kochukhov O., Landstreet J. D., Piskunov N., Stift M. J., 2001, A&A, 374, 265
Wenger M., et al., 2000, A&AS, 143, 9

APPENDIX A: ADDITIONAL FIGURES

Figures A1, A2 and A3 present the same plots as Fig. 8 for EV Lac, AD Leo, DS Leo, CN Leo and PM J18482+0741 respectively.

APPENDIX B: BEST FITS

Figure B1 available as supplementary material presents the best fits obtained for AU Mic, AD Leo, EV Lac and DS Leo for all lines used in our analysis.

APPENDIX C: COMPARISON OF $T_{\rm eff}$ AND $\log g$ WITH THE LITERATURE

This paper has been typeset from a TEX/LATEX file prepared by the author.

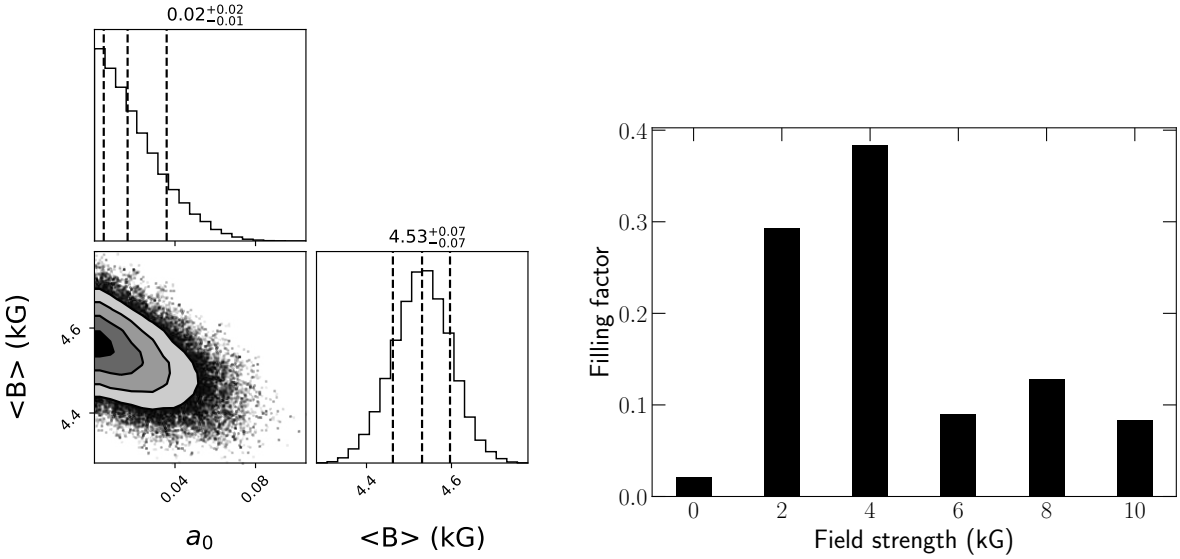

Figure A1. Same as 8 for EV Lac.

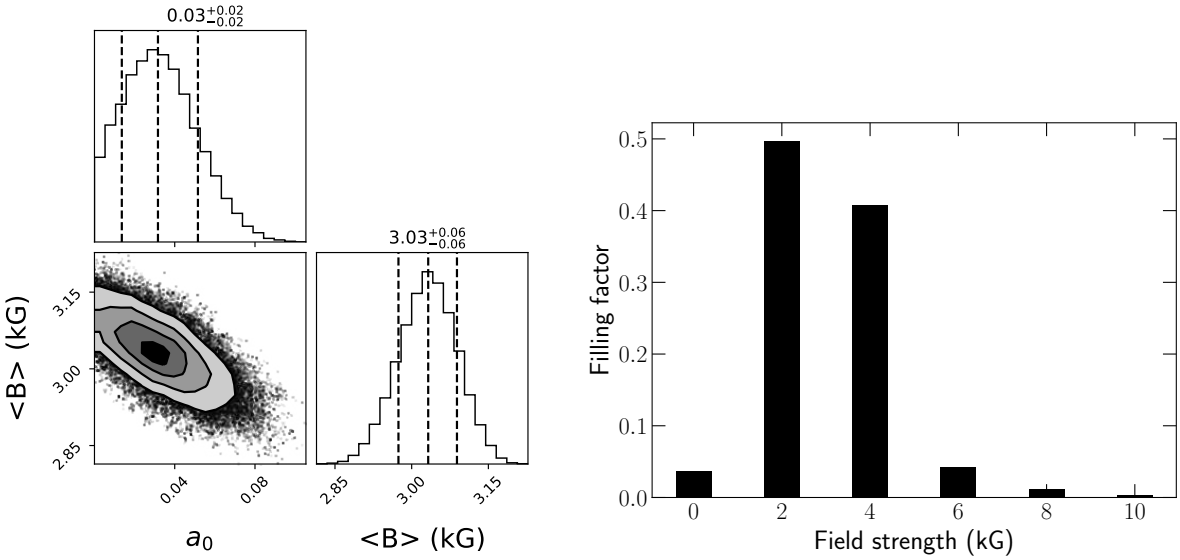

Figure A2. Same as 8 for AD Leo.

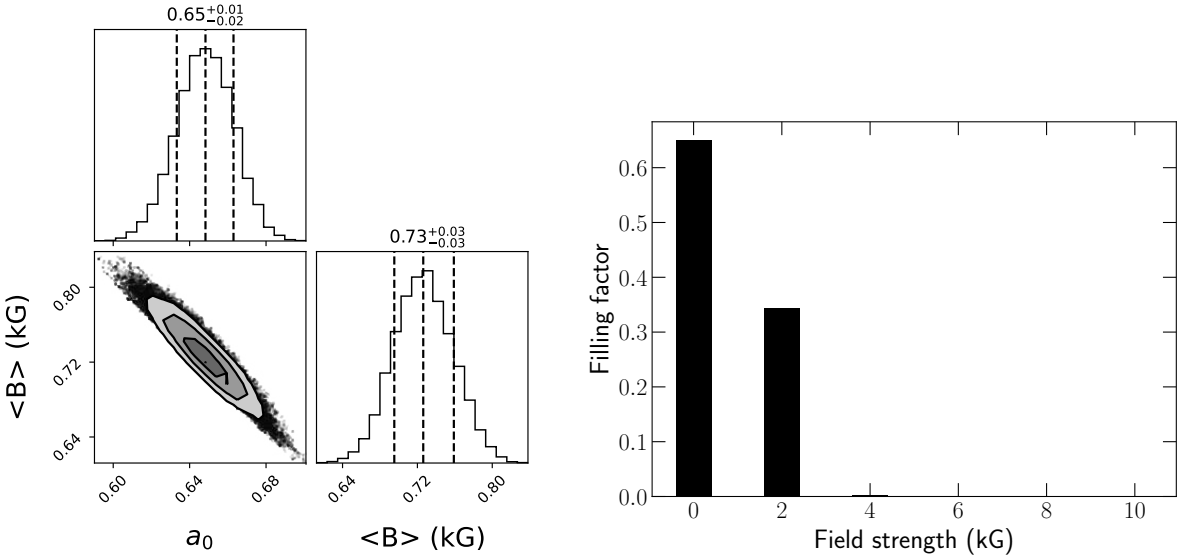

Figure A3. Same as 8 for DS Leo.

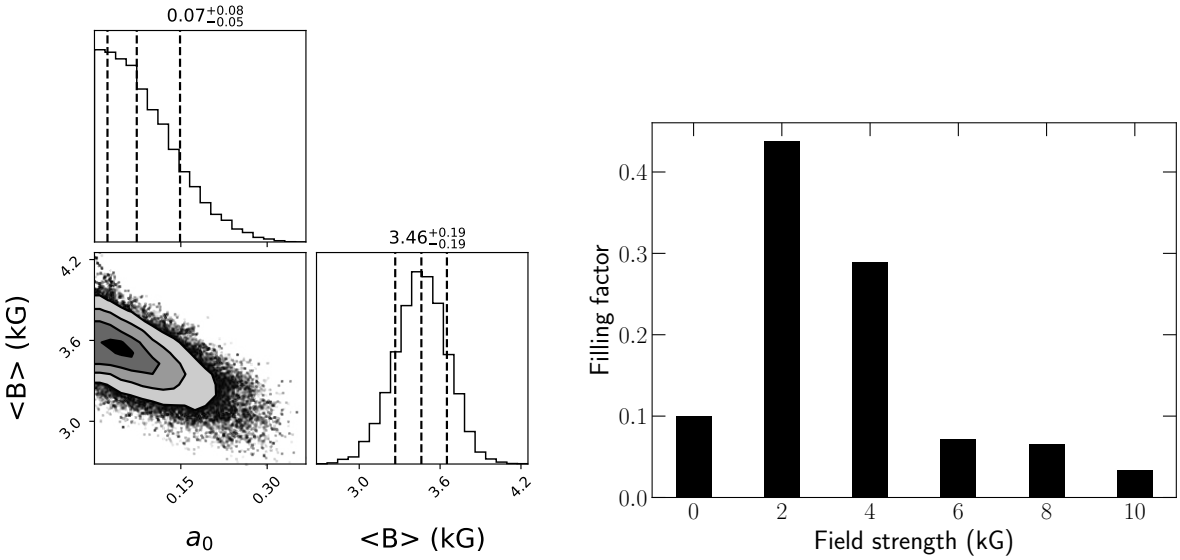

Figure A4. Same as 8 for CN Leo.

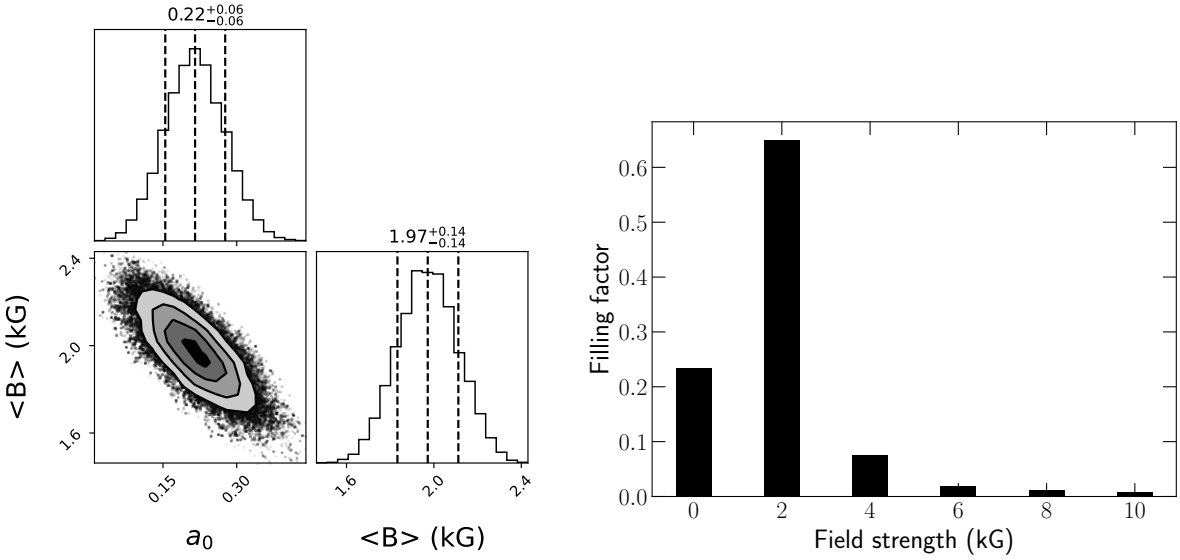

Figure A5. Same as 8 for PM J18482+0741.

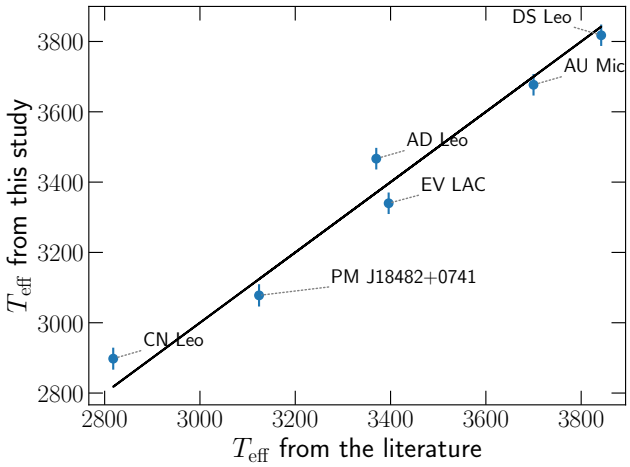

Figure C1. Retrieved $T_{\rm eff}$ compared to literature estimates taken from Afram & Berdyugina (2019, AU Mic), Mann et al. (2015, AD Leo, CN Leo), Maldonado et al. (2020, EV Lac), Cristofari et al. (2022b, DS Leo) and Passegger et al. (2019, PM J18482+0741).

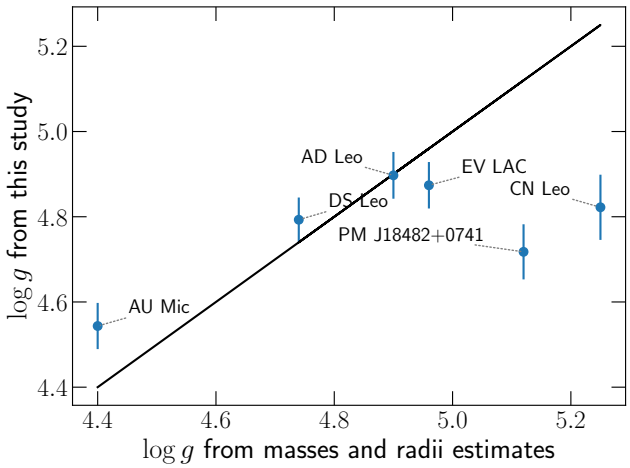

Figure C2. Retrieved $\log g$ compared to estimates derived from masses and radii (see Table 3).